Toward Quantitative Understanding of Compartmentalized NADPH Metabolism in Cancer Cells

by

Sun Jin Moon

B.S. Chemical and Biological Engineering, Korea University, 2016

SUBMITTED TO THE DEPARTMENT OF CHEMICAL ENGINEERING IN PARTIAL FULFILLMENT OF THE REQUIREMENTS FOR THE DEGREE OF

DOCTOR OF PHILOSOPHY IN CHEMICAL ENGINEERING

AT THE

MASSACHUSETTS INSTITUTE OF TECHNOLOGY

MAY 2022

Signature of Author: .....

Department of Chemical Engineering

May 12, 2022

Certified by: .....

Hadley D. Sikes

Associate Professor of Chemical Engineering

Thesis Supervisor

Certified by: .....

Gregory Stephanopoulos

Willard Henry Dow Professor in Chemical Engineering

Thesis Supervisor

Accepted by: .....

Patrick S. Doyle

Robert T. Haslam (1911) Professor of Chemical Engineering

Chairman, Committee of Graduate Student

Toward Quantitative Understanding of Compartmentalized NADPH Metabolism in Cancer Cells

by

Sun Jin Moon

Submitted to the Department of Chemical Engineering
On May 12, 2022, in partial fulfillment of the
Requirements for the degree of
Doctor of Philosophy in Chemical Engineering

Abstract

Reduced nicotinamide adenine dinucleotide phosphate (NADPH) is an essential molecule in living organisms by virtue of its function as electron donor driving reductive biosynthesis and protecting cells against oxidative stress. Over the past decades, extensive research has studied key NADPH regeneration pathways and investigated whether targeting these pathways constitutes an effective cancer therapy. However, fundamental questions still remain unanswered. The pool sizes or dynamics of cytosolic and mitochondrial NADPH are unknown and how they interact through varying metabolic processes.

Assessment of compartmentalized NADPH redox states is important as cytosolic and mitochondrial NADPH levels are known to be different due to its impermeability to intracellular membranes, yet it is known to be transported from one compartment to the other by various mechanisms such as metabolite shuttles. NADPH pool sizes can influence metabolic processes to a varying extent and targeting compartment-specific NADPH-dependent enzymes may result in selective and variable responses. Moreover, various metabolic reactions that rely on NADPH are reversible, meaning that altered NADPH redox states can influence metabolic pathway directions in one compartment first, followed by opposite changes in another compartment. Thus, improved understanding of compartmentalized NADPH pool sizes, interactive dynamics and affected

metabolic pathways can lead to designing effective cancer therapies by targeting NADPH metabolism.

In this thesis, I investigate compartmentalized NADPH metabolism in cancer cells by developing compartmentalized NADPH dynamics and metabolism analysis platform that incorporates genetically encoded NADPH biosensors to explore mitochondrial NADPH dynamics and analyze NADPH-mediated metabolism using ^{13}C-glcucose isotopic tracers and mathematical models. First, using NADPH sensors, we observed mitochondrial NADPH pool decreased in response to mitochondria-specific oxidative stress, whereas the cytosolic NADPH was minimally influenced. Second, the oxidative pentose phosphate pathway activity and TCA cycle intermediate turnover rates increased in response to decrease of mitochondrial NADPH by mitochondrial oxidative stress. Third, utilizing a kinetic model for mitochondrial antioxidant network, we calculated mitochondrial NADPH/$NADP^+$ ratio and documented an activation of indirect NADPH shuttle system that maintained the mitochondrial NADPH pool. Lastly, we found that the compartmentalized NADPH dynamics varied among different cancer cell lines and perturbing compartment-specific NADPH pools led to cell line specific growth inhibitions *in vitro*. Altogether, our mitochondrial NADPH sensor and integrated approach led to findings that enhanced our insight into compartmentalized NADPH metabolism that can help advance more selective anticancer therapies.

Thesis Supervisor: Hadley Sikes

Title: Associate Professor and Esther and Harold E. Edgerton Career Development Professor of Chemical Engineering

Thesis Supervisor: Gregory Stephanopoulos

Title: Willard Henry Dow Professor in Chemical Engineering

Acknowledgements

My past six years were like running a full marathon. I started with full of energy, with ambitious goals and plans organized. However, as I approached to a finish line, I realized that it was not just with my own strength that carried me to the finish line, but it was the runners, coaches and spectators, who gave me unbounded support and encouragement to finish strong. I was grateful to encounter these wonderful people along my journey in Ph.D. and would like to acknowledge them for help.

First of all, I would like to offer my special thanks to my thesis advisors – Professor Hadley Sikes and Professor Greg Stephanopoulos. I am thankful to Hadley throughout my Ph.D. years. She is supportive, caring, and has provided me with great advice on academics and my career paths. Whenever I present new data, which may not be directly related to my project, she is always happy to discuss and gave me feedback. I am thankful that she trust my work and encourage me all the time. These support really help me stay positive and move forward even when I encounter difficult times. Moreover, I thank her for providing me a framework of being a successful scientist, engineer, and a leader of a lab. Throughout numerous one-on-one meetings, subgroup meetings, and group presentations, I learn greatly from her about professional skills needed for a Ph.D. student. She is a wonderful mentor and I am humbled to be a part of a Sikes lab for the past years. Thank you.

Along with Hadley, I am grateful to Greg for being my thesis advisor. Greg has once told me an adage during my group presentation – "There was a man who dropped a coin in darkness. He was looking for a coin where a light was shining by the light stand, but not in a darkness where a coin was actually located." His wisdom guided me how to approach problems during my early years. Moreover, Greg has been curious of my data and has provided wonderful feedback. I particularly thank Greg for his advice on my mathematical works, helping me to think more critically and logically. He has also showed me how to look a forest. Near to the end of my journey, he has provided me with great advice on my career paths. I am grateful for all the advice throughout the years, and will try to remember your wisdom in my heart, and share them with others. Thank you.

I would like to thank my thesis committee members – Professor Vander Heiden, Professor Chung, and Professor Love. I am especially grateful to Professor Vander Heiden for his being my committee member. I have learned deeply from him about cancer biology by taking his class. He has also provided me with valuable feedback on my research work. I am thankful to him especially since I have limited experienced in cancer metabolism before my Ph.D. He has been always supportive and has helped me out whenever needed. I thank for all his support and guidance. I also thank him for generosity in using some of the equipment in the lab, and lastly thank Peter for coordinating multiple schedules with Matt. Thank you.

I also thank to Professor Chung for his great advice on imaging and microscopic technologies. I am grateful to be able to take his pioneering technology class and learn greatly about the cutting-edge imaging techniques used in biological settings in my early Ph.D. stage. His feedback on development of sensors and imaging techniques have been helpful in my earlier years. I also thank him for giving me advice regarding finding postdoc positions and career paths in our final thesis meeting. Thank you.

I also thank Prof Love for providing me valuable advice on my research work throughout thesis committee meetings. I particularly appreciate it for your feedback in our last meeting. Your feedback on

statistical methods and validation experiments. I also thank Mariann for coordinating schedules with him at ease. Thank you.

Moreover, I express special thanks to Dr. Joanne Kelleher. I learn greatly from her about the classic biochemistry approach and her valuable insights on isotopic tracing techniques. From her, I am able to learn how I should think like a biologist and approach problems more quantitatively. I am grateful that she has been always around and help me out along the way. I especially thank her for great feedback on isotopic tracing studies and mathematical models. Her critics and suggestions during the group meetings are something I always appreciated it and will keep in mind. Thank you.

All the lab members of Sikes have helped me to go through my Ph.D. years. I especially thank to Dr. Troy Langford and Dr. Kassi Stein. They have helped me to learn everything from cell culturing to cloning, protein purifications, developing sensors and implementing imaging experiments. Thanks to their help, I am able to complete my research work. I also thank to Dr. Eric Miller for his training on molecular engineering techniques. Besides, I would like to thank all other lab members in the Sikes Lab and the undergraduate researchers who I have been able to assist along the journey. I also thank Andre for helping me out ordering lab materials readily.

I also thank to all the lab members in the Stephanopoulos group. I especially thank to Dr. Wentao Dong, who has trained me in isotopic tracing techniques using GC-MS and how to interpret data critically. I has enjoyed conversing with him on research and the collaborations we have made together along the way. I also thank Dr. Mark Keibler for his general advice, which has helped me to adjust to the cancer metabolism field. He has given me confidence and support that has led me to engage to research smoothly. I am also grateful that I am able to contribute to his research. Besides, I thank to all other lab members I have encountered during my Ph.D., including Dr. Ben Woolston, Dr. Junyoung Park, Dr. Nian Liu, Antonio, Anush, Vincent, Yongshuo, Jingbo, George, Costas, and Jack. I also thank Rosangela, Nicholas, and Hannah for assisting lab orders and administrative support.

Additionally, I thank to Prof. Arthur Tischler and Dr. Jim Powers in Tufts Medical School. I have enjoyed collaboration, working on actual tumor samples. I also thank to Dr. Sooyeon Cho for our collaboration on hydrogen peroxide work. From him, I have been able to learn how my skillsets can be helpful to researchers outside the field. I also thank to MIT chemical engineering community. Outside the lab, I also thank to the members of the Korean Graduate Soccer Team. It has been my joy to be able to play soccer every week with enthusiasm and playing together competitively in intramurals. I thank to my friends from Church. Conversing with them on Sunday refreshed my mind and allowed me to get back to the work. I also thank volunteers in Loaves and Fishes Meal Program and NetPals organizers. Outside activities truly enriched my experience in Cambridge.

Lastly, I thank to my family, who has given me unlimited support and love that has provided me the power to persevere patiently and move forward up to this point. I am grateful to be able to meet with my family nearly every year. I express my deepest gratitude to them.

TABLE OF CONTENTS

LIST OF FIGURES

LIST OF TABLES

Chapter 1

Introduction

1.1. Motivation

In metabolism, NADPH serves as an electron donor that supports reductive biosynthetic pathways and protects cells against oxidative stress[1–4]. Impaired NADPH metabolism perturbs cellular functions and is associated with diseases including diabetes, neurodegeneration, heart failure and cancers[5–8]. Characterized by unregulated growth, cancer cells demand large quantities of NADPH to meet the demands of lipid synthesis and combat against oxidative stress generated by aberrant metabolism. Thus, researchers have studied NADPH generation pathways in the past decade and investigated whether targeting these pathways constitute effective cancer therapy[2,4,8–10]. However, it is still unknown what are the compartmentalized NADPH redox states and their dynamics under varying metabolic conditions. Understanding compartmentalized NADPH redox states is critical because NADPH is known to be impermeable to intracellular membranes and their compartment-specific pool sizes and redox states are likely to be different in subcellular organelles. Furthermore, a wide range of metabolic reactions occurs in different compartments and uses NADPH as a co-factor. Additionally, these reactions are highly reversible, indicating that altered NADPH redox states influence reaction directionality in specific compartments and ultimately metabolic pathway directions. Assessment of compartment-specific NADPH redox states, pool sizes, and dynamics is critical to advance our understanding of compartmentalized redox metabolic reaction network. Ultimately, these understanding will help improve cancer therapies by targeting NADPH metabolism.

1.2. NADPH metabolism

NADPH metabolism refers to biochemical reactions and pathways that generate, consume, or use NADPH as a cofactor to support cellular processes in living organisms. Understanding NADPH

metabolism begins with an examination of NADPH generation and consumption reactions and relevant pathways.

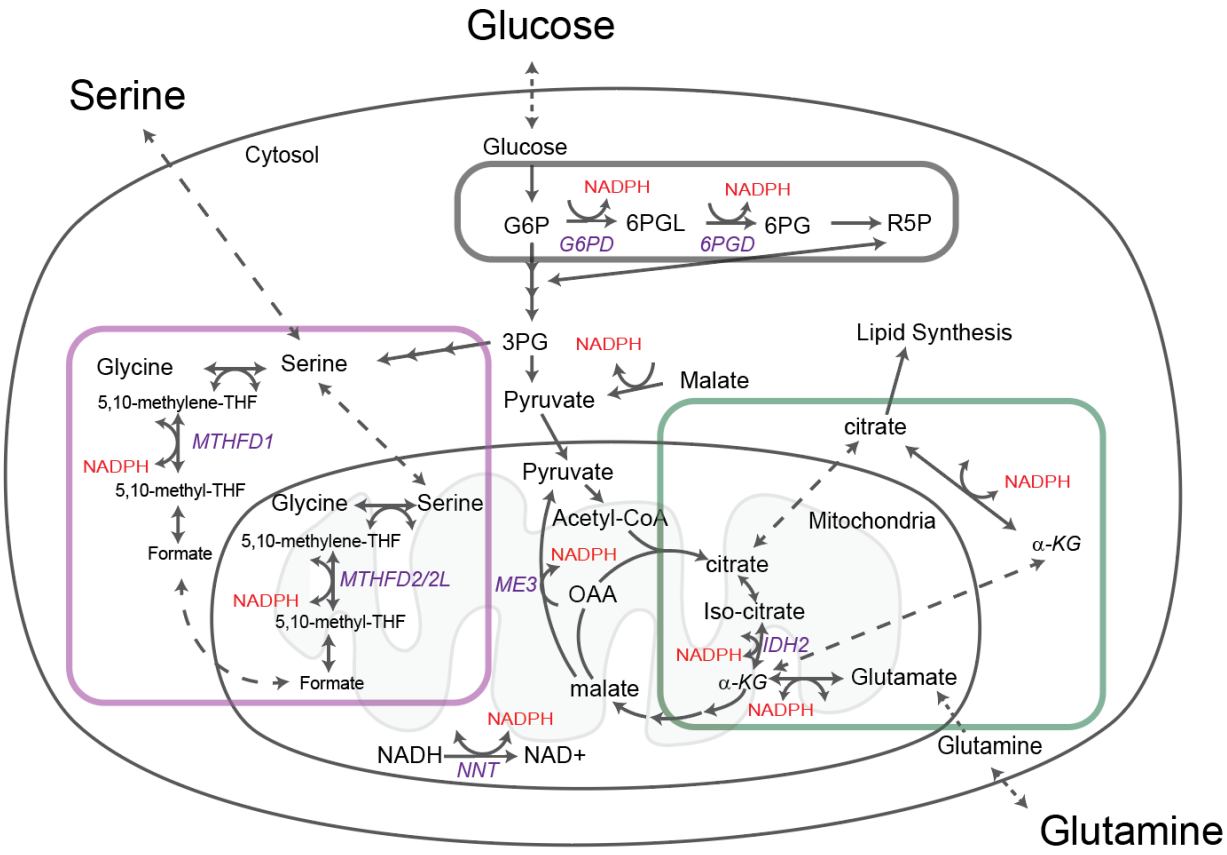

Figure 1.1. Schematics representing the major NADPH generation reactions and pathways in eukaryotes.

1.3. NADPH generation pathways

1.3.1. $NADP^+$ synthesis

To understand the ultimate source of NADPH, it is necessary to assess NAD^+ production pathways as NAD^+ is a precursor of $NADP^+$, which is ultimately a precursor of NADPH. In brief, NAD^+ can be made *de novo* from an essential amino acid tryptophan, or through salvaging pathways that begin with nicotinamide riboside (NR), nicotinamide (NaM), or nicotinamide

riboside (NR), all of which are parts of vitamin B_3 [11]. As *de novo* synthesis of NAD^+ from tryptophan requires eight steps, it is rather a slower process compared to the other three salvaging pathways. Except liver and kidney that could make NAD^+ from tryptophan, other tissues generally were shown to use NAD^+ from nicotinamide. The turnover rate of NAD^+ synthesis varied from 15 minutes by small intestine to 15 hours by adipocytes. 10 % of NAD^+ was shown to be used for synthesis of $NADP^+$ through NAD kinase reactions [12].

1.3.2. Oxidative Pentose phosphate pathway (oxPPP)

Oxidative pentose phosphate pathway has long been regarded as a major source of cytosolic NADPH for lipid synthesis and redox defense in eukaryotes [4,13,14]. The oxidative pentose phosphate pathway includes reactions such as glucose-6-phosphate dehydrogenase (G6PD) and 6-phosphogluconate dehydrogenase (6PGD), which can regenerate two to twelve NADPH moles per one mole of glucose depending on the reversibility of phosphoglucose isomerase and Fructose 1,6-bisphosphatase [15].

1.3.3. Folate-mediated one carbon pathway

Folate-mediated NADPH regeneration pathway has been shown to be another source of NADPH, particularly mitochondrial NADPH [2,9,16]. Folate is a substrate that can be reduced to tetrahydrofolate (THF), which can subsequently accept one carbon from serine, making a 5,10-methylene-THF (5,10-meTHF) via SHMT reaction. 5,10-meTHF can further undergo oxidation reaction via MTHFD2/L, which is a mitochondria-localized enzyme generating NAD(P)H and the 10-formylTHF. 10-formylTHF can be further oxidized to CO_2 through ALDH1L2. 10-

formylTHF can be converted to formate through MTHF(D)1L reaction and can a set of reactions can be recycled. In essence, through folate-mediated one carbon metabolism, MTHFD2/L, ALDH1L2, and ALDH1L1 reactions can regenerate NADPH.

1.3.4. Isocitrate dehydrogenases (IDH)

IDH is an enzyme that can reduce alpha-ketoglutarate (α-KG) to isocitrate using NADPH or reversibly oxidize isocitrate to α-KG while generating NADPH. There are three isoforms – IDH1 for cytosolic enzyme utilizing NADPH, IDH2 for mitochondrial enzyme utilizing mitochondrial NADPH, and IDH3 for mitochondrial enzyme utilizing mitochondrial NADH. Mutations of IDH1 enzyme led to a formation of 2-R-hydroxyglutarate, which is regarded as an oncometabolite [17]. Although IDH1 enzymes could be important source of NADPH production in cytosol, IDH1 was shown to be used for reductive carboxylation in hypoxia, consuming NADPH in the cytosol [18,19]. Knockout of IDH1 enzyme did not also decrease NADPH production in HCT116 cells [20]. During anchorage-independent growth, IDH1-mediated metabolite shuttle systems were shown to transfer reducing equivalents of NADPH from cytosol to mitochondria [21].

1.3.5. Malic enzymes (ME)

ME is one of the enzymes that were reported to generate NADPH in cytosol or mitochondria [22,23]. ME converts malate to pyruvate while using $NADP^+$ and making CO_2 as a byproduct. Malic enzymes have three isoforms – ME1 expressed in cytosol, ME2 expressed in mitochondria while using NAD^+, and ME3 expressed in mitochondria. It was shown that malic enzyme activities are

high in adipocytes and liver, while serving as NADPH source for lipogenesis [10,22]. A correlation between high glucose diets and increased activities of malic enzymes suggested malic enzyme's link to glucose metabolism. Malic enzymes have been proposed to be linked to malate dehydrogenase and pyruvate carboxylase to regenerate NAD^+ and $NADPH^+$ while using ATP [22]. Knockout of ME1 did not induce significant changes in NADPH or NADPH/$NADP^+$ in HCT-116 cells [20].

1.3.6. Glutamate dehydrogenase (GLUD)

GLUD is an enzyme that can oxidize glutamate, making α-KG, NADPH, and NH_4^+. The enzyme is specifically localized to mitochondria and use either NAD^+ or $NADP^+$ as co-factors. Glutamate dehydrogenase was reported to be one of the key NADPH producing enzymes specifically localized in mitochondria and play an important role in urea synthesis [24,25]. However, glutamate could also be directly converted to α-KG through transamination reaction, while transferring the nitrogen to pyruvate and making alanine [26]. It was shown some cancer utilized transaminase reactions rather than glutamate dehydrogenase in some context [27,28]. Whether glutamate is converted to α-KG via GLUD or transaminases, these metabolites are closely followed by other reactions that involve the change of NADH or NADPH, thereby altering the redox states in the end.

1.3.7. Nicotinamide nucleotide transhydrogenase

NNT is an enzyme that is localized to mitochondrial membrane and transfers electrons from NADH to $NADP^+$, while translocating hydrogen atom from intermembrane space to

mitochondrial matrix [29]. The main function of NNT is known to modulate mitochondrial NAD(P)H redox states and protect cells against oxidative stress. The enzymatic reaction is reversible. Therefore, the proton gradient and mitochondrial NAD(P)H redox states influence the directionality of reactions. In cancer cells, NNT was observed to coordinate reductive carboxylation and glucose and glutamine catabolism in Vhl deficient renal cell carcinoma and melanomas. More recently, other researchers demonstrated that knockout of NNT inhibited tumorigenesis of liver and gastric cancers [30,31]. Structure of NNT by cryo-electron microscopy revealed a potential opportunities of developing NNT inhibitors, which can be used for therapeutic purposes in cancers as well as ischemia reperfusion injury and metabolic diseases [32].

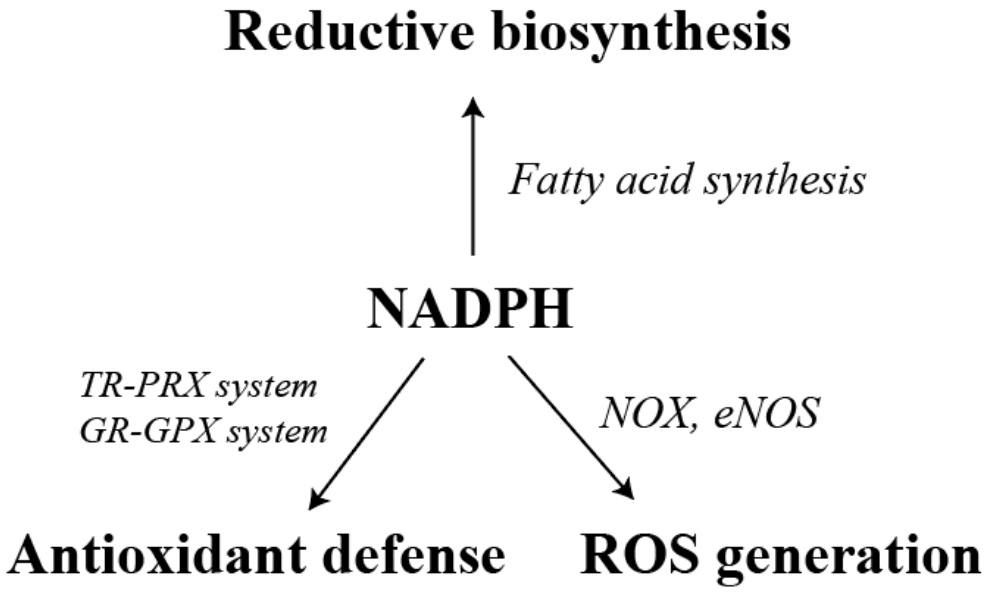

Figure 1.2. Schematics representing NADPH consumption pathways.

1.4. NADPH consumption pathways

1.4.1. Reductive biosynthesis

The major sink of NADPH is anabolic processes, including lipid and non-essential amino acid synthesis. For instance, a synthesis of one mole of palmitate, which is a major component of cellular membrane, requires 14 moles of NADPH. For cholesterol, which regulates the fluidity of membrane, requires 26 moles of NADPH. For non-essential amino acids, proline and arginine synthesis demands one mole of NADPH [33]. Since cancer cells proliferated unregulated and proliferation requires a large quantity of lipid synthesis for cellular membranes, it was hypothesized that cancer cells may be limited by the productions of NADPH [4].

1.4.2. Antioxidant defense

NADPH is essential to regulate oxidative stress in cells. It provides reducing equivalents to maintain H_2O_2 scavenging systems by reducing oxidized thioredoxin (Trx) and glutathione (GSH). The reduced Trx transfer electrons to the oxidized peroxiredoxin (Prx). Prx ultimately react with H_2O_2 to make a water. For GSH, it can directly reacts with H_2O_2 through glutathione peroxidase (GPx) [34]. In this regards, maintaining a proper NADPH redox state is critical to keep cells against accumulation of reactive oxygen species such as H_2O_2.

1.4.3. Reactive oxygen species generation

NADPH also serves as an electron donor to generate reactive oxygen species such as superoxide ($O^{\cdot -}$) via NADPH oxidases or nitric oxide (NO) via endothelial NO synthase (eNOS)[35,36]. NADPH oxidase (NOX) is a membrane-bound enzyme complex that produces a superoxide

radical by transferring electron from NADPH to oxygen [36–38]. Superoxide can be quickly converted to hydrogen peroxide via superoxide dismutase or under at low pH [36]. In humans, seven NOXs were identified including NOX 1-5 and Duox 1-2 [39]. These isoforms were expressed across different tissues such as colon, inner ear, kidney, blood vessels, lymphoid tissues, testis, and thyroids. Depending on cell types and isoforms, NADPH oxidases are expressed in different subcellular localization such as plasma membrane, endoplasmic reticulum membrane, perinuclear cytoskeleton, mitochondrial membrane or nucleus [40–43].

1.5. NADPH in cancer metabolism

One of the new emerging hallmarks of cancer is a rewired cellular metabolism [44,45]. Warburg first reported in 1930 that cancer cells utilized glucose for production of lactate even in presence of oxygen. Ever since, numerous studies revealed different metabolic phenotypes between normal and cancer cells. Altered metabolic pathways included glucose, glutamine, one-carbon, amino acids, and redox metabolism [46]. With respect to NADPH, cancer cells overexpressed NADPH regenerating metabolic enzymes such as G6PD, 6PGD, ME1, and IDH1 through Nrf2 accumulation under constitutive activation of constituent activation of PI3K-Akt signaling pathway [47]. MYC-dependent cancer cells also revealed upregulation of serine-mediated NADPH generation pathways genes [48]. It makes sense that cancer cells upregulate these genes to generate excessive NADPH to support proliferation and fight against oxidative stress. Reprograming of glutamine metabolism by mediated by KRAS revealed production of NADPH not mainly through GLUD but through aspartate transaminases and malic enzymes at least in pancreatic cancer cells [28]. In summary, it is evident cancer cells alter metabolic activities to regulate

NADPH generation and consumption, which is now regarded as one of the six hallmarks of cancer metabolism [49].

1.6. Isotopic tracers for measurement NADPH generation pathways

1.6.1. Deuterium metabolic isotope tracers

Glucose or amino acids with deuterium labeled hydrogen have been used to directly measure the activities of NADPH generation pathways. For instance, a hydrogen positioned at the 3rd carbon of glucose can be replaced to a deuterium. When [3-^{2}H]glucose is catabolized through the oxPPP, a deuterium is transferred to $NADP^+$, making a heavy NADPH. If the glucose tracer catabolized through glycolysis and oxidative phosphorylation, no NADPH generating enzyme allows transfer of deuterium to NADPH. Therefore, [3-^{2}H]glucose can directly probe usage of oxPPP from glucose. [2,9]. There are a variety of deuterium labeled tracers available for measurement of NADPH generation pathway activities, which will be discussed in detail in later chapters.

1.6.2. ^{13}C-glucose tracers

^{13}C-glucose tracers have been widely used to probe the activities of central carbon metabolic pathways. As glucose can be completed oxidized through glycolysis, TCA cycle, and oxidative phosphorylation, ^{13}C-glucose tracers have been used to map the glucose catabolic pathway activities. However, glucose can be shunted to pentose phosphate pathway and [1,2-^{13}C]glucose can be used to measure the pentose phosphate pathway activities.

1.7. Methods for measurement of intracellular NADPH redox states

1.7.1. Classical approaches of estimating free cytosolic NADPH/NADP$^+$

Estimation of free NADPH/NADP$^+$ ratio is important as the ratio determines the directions of metabolic reactions that use NADPH as a cofactor and further the flux of metabolic pathways[1,50]. Measurement of free NADPH concentration is also valuable as NADPH/NADP$^+$ can be directly calculated from NADPH through a mathematical modeling based on the antioxidant network[51]. The concentration further infers the extent of change of NADPH/NADP$^+$ upon perturbation[3]. In kinetically controlled redox systems, NADPH availability was shown to determine the activities of reactive oxygen species generation by NADPH oxidase system[51–55].

Classic measurements of free NADPH/NADP$^+$ was achieved by measuring metabolite ratios and calculating the NADPH ratio assuming the reactions are near equilibrium and the relevant enzymes are localized to the compartment of interest[1,56,57]. Isocitrate dehydrogenase and malic enzymes were used for measurement of cytosolic free NADPH/NADP$^+$ assuming the expressions and activities of isoforms in mitochondria are low. As there is no enzyme that specifically utilize NADPH in mitochondria, this method has been limited to measurement of cytosolic free NADPH/NADP$^+$. Classic measurements revealed free cytosolic NADPH/NADP$^+$ increased under starvation from 84 to 746, partly due to inhibition of lipid synthesis pathway, which required a large amount of NADPH[1,58,59].

1.7.2. Recent approaches of estimating compartmentalized NADPH/NADP$^+$ and NADPH level

More recently, several NADPH, NADP, and NADPH/NADP$^+$ sensors have been developed to allow direct measurement of NADPH redox states in subcellular organelles of living cells [5,60–62]. These sensors are typically designed as a fusion protein that has a binding protein for a target molecule and a reporter fluorescent protein.

A currently available NADPH sensor, called iNap, offers a high dynamic range, selectivity, and multiple versions suitable for cytosolic and mitochondrial analysis. iNap sensor was developed based on a NADH binding *Thermus aquaticus* transcription regulator, whose binding site was engineered to alter its selectivity toward NADPH while a DNA binding domain was truncated to avoid potential interaction with endogenous DNA and to decrease its molecular weight as much as possible [5]. As a reporting system, the sensor incorporated a circularly permuted yellow fluorescent protein (cpYFP). It was previously created by Nagai *et al.*, who connected the original N and C terminus of green fluorescent protein, thereby creating a new N and C terminus while exposing the fluorophore readily accessible to the surrounding environment and thus a greater change in its fluorescence depending on surrounding pH [22]. The cpYFP, due to its fluorophore open to environment, is vulnerable to change of pH as the sensor's fluorophore state can be protonated or deprotonated relying on surrounding available protons. A different state of fluorophore leads to a change of intensities in excitation peaks [24]. Thus, the actual fluorescence response of the sensor can be amplified as a function of pH. In this sense, authors of iNap sensors created another version that does not bind to NADPH to control pH effect. The control iNap sensor, called iNapC, needs to be expressed in parallel to account of pH effect. Detailed information of cpYFP and its pH effect can be found in appendix 7.11.

Additionally, a semisynthetic biosensor for NADPH/$NADP^+$ revealed cytosolic, nucleus, and mitochondrial NADPH/$NADP^+$ in U2OS cells, with mitochondria showing high NADPH redox states compared to cytosol. The oxidative stress generated by H_2O_2 lowered the ratio to 20. Treatment of rotenone, a complex I inhibitor, decreased the ratio by 25% for cytosolic NADPH/$NADP^+$ and 20% for mitochondrial counterpart. On the other hand, the treatment of oligomycin A, an ATP synthase inhibitor, increased the cytosolic ratio by 12% and 36% for mitochondrial ratio.

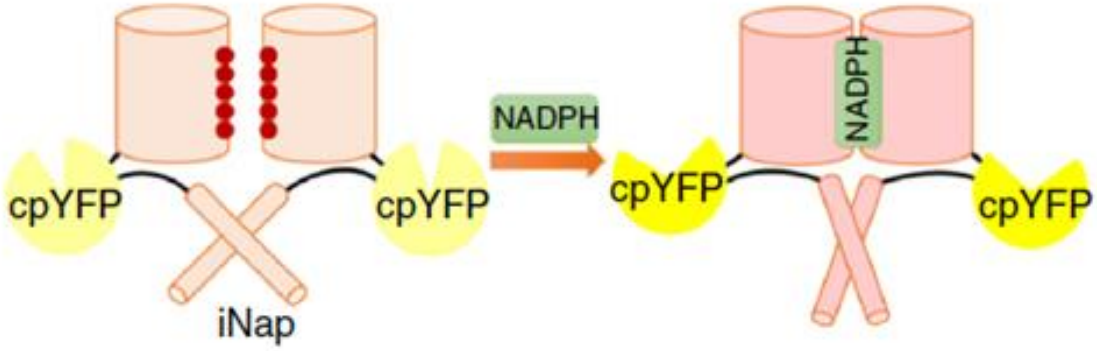

Figure 1.3. Schematics of iNap sensors. Upon binding of NADPH, the sensor induces a conformational change of circularly permuted yellow fluorescent protein, altering fluorescence intensity. (Tao et al., Nat Methods, 2017)

1.7.3. Measurement of bound NADPH

Although free NADPH or $NADP^+$ are the direct substrates that participate redox reactions, NADP(H) can also exist as bounded to enzymes. Cell lysates methods do not differentiate the bound and fee NADPH concentrations and reveal the total NADPH pools. $NADP^+$ are vulnerable to alkaline pH. Therefore, by treating cells with basic solution, only NADPH pools can be measured. On the other hand, NADPH is weak to high temperature and treatment of cells with

heat may destroy NADPH selectively [63]. For measurement of NADPH, ultrafiltration has been used to extract free NADPH and measure free NADPH concentration. It was shown that the total NADPH was approximately 30 μM and the unbounded NADPH was about 6%, which was 2 μM. Similarly, approximately 5% of the $NADP^+$ were freely available.

More recently, using fluorescence lifetime imaging techniques (FLIM), bound NADPH and NADH are separated and their ratios were quantified [64]. FLIM reveals different fluorescence lifetime between bound NADH and NADPH, but not the freely available reducing co-factors.

1.8. Compartmentalized NADPH redox states

NADPH is highly compartmentalized in eukaryotes [3]. From the use of classical methods and mathematical models to the advent of recent genetically biosensors, compartmentalized NADPH redox states have been reported since 1960s to 2022. Although the change of free cytosolic $NADPH/NADP^+$ is agreed to be approximately 100 at the basal state, the values of mitochondrial $NADPH/NADP^+$ are still divergent and no clear consensus has been made. Below is a table that summarizes the literature review of current compartmentalized NADPH, $NADP^+$, and $NADPH/NADP^+$.

Table 1.1. Compartmentalized free NADPH/NADP+ ratio and NADP(H) levels

Name	Compartment	Values (ratio or µM)	Methods	Results	Reference	year
NADPH /$NADP^+$	Cytosol	84 – 746		Starvation increases free NADPH/ $NADP^+$ in cytosol in rat liver	[1]	1969
		78 – 303	Measuring metabolites ratios and using equilibrium constant equation	Chronic ethanol consumption increased the ratio in rat liver	[65]	1985
		27 - 58		Increasing glucose concentration elevates free NADPH/ $NADP^+$ in cytosol in mouse pancreatic cells	[57]	1987
		58 – 128		Lipopolysaccharide (LPS) induced decrease of NADPH/ $NADP^+$ after 24 hours in rat liver	[66]	1995
		20 – 100	Using a $NADP^+$-snifit fluorescent biosensor	H2o2 stress decreased NADPH/ $NADP^+$ ratio from 70 to 20 in U2OS cells	[61]	2018
NADPH /$NADP^+$	Mitochondria	0.1	Measuring metabolites ratios and using equilibrium constant equation	Using the NNT transhydrogenase equilibrium constant	[61]	1969
		47 – 120	Using a $NADP^+$-snifit fluorescent biosensor	Inhibition of complex I decreased NADPH/ $NADP^+$ ratio - Fret-based biosensor in U2OS cells	[61]	2018
		0.2 - 13.4	Using iNap sensor and a mathematical model	Mitochondrial oxidative stress decreases steady state mitochondrial NADPH/ $NADP^+$ ratio in Hela cells	[51]	2020

NADPH	Cytosol	3.1 - 5.5	Using iNap sensors	Overexpression of NAD kinase increases cytosolic NADPH; oxidative stress by diamide decreases cytosolic NADPH in Hela cells	[5]	2017
	Mitochondria	37 - 41				
NADPH	Mitochondria	39 - 42	Using iNap sensors	Mitochondrial oxidative stress decreases mitochondrial NADPH in Hela cells	[51]	2020
NADP	Cytosol	1 - 10	Using Apollo Homo-FRET sensor	Glucose acutely decreases cytosolic $NADP^+$, whereas oxidative stress by diamide increases cytosolic $NADP^+$ in beta TC3 cells (pancreatic cells)	[60]	2016

1.9. Oxidative stress

Oxidative stress, a condition caused by an inadequate clearance of excessive production of H_2O_2, perturbs redox homeostasis and trigger programmed cell death. Although decreased NADPH/$NADP^+$ redox states may allow cells more vulnerable to oxidative stress, but oxidative stress caused by external reagents or some other stimulus are typically cause of decrease of NADPH/$NADP^+$ redox states, NADPH pool and modulate NADP-dependent metabolic fluxes [6,7,67]. Oxidative stress in fibroblast cells led to a shift of glycolytic flux toward the oxidative pentose phosphate pathway to regenerate NADPH [9,46,67,68]. In isolated cardiac myocytes under a pathological workload, the direction of mitochondrial nicotinamide transhydrogenase reaction was reversed, lowering the total NADPH pool and increasing the production of mitochondrial ROS [8]. Similarly, the availability of NADPH in mitochondria along with NADPH-producing

enzymes such as isocitrate dehydrogenase 2 (IDH2) and nicotinamide nucleotide transhydrogenase (NNT) was shown to control the antioxidant network for clearance of H_2O_2 [69].

1.10. Mitochondria-derived oxidative stress

Mitochondria emerge as a major source of reactive oxygen species (ROS), and excessive production of ROS has been linked to various diseases including neurodegeneration, inflammation, aging, diabetes, and cancers via induction of lipid peroxidation, protein oxidation, and DNA damage [70–76]. Of various types of ROS, hydrogen peroxide (H_2O_2) acts as a signaling molecule that can initiate expression of survivor genes such as antioxidant response elements (e.g., Nrf2), induce DNA repair mechanisms (e.g., p53 and ATM), or activate programmed cell death pathways (e.g., NF-κB) [73,77,78]. As accumulation of H_2O_2 can induce toxicity, cells maintain a defensive system to clear H_2O_2 via redox reactions [71,79,80]. Additionally, mitochondria derived reactive oxygen species was also shown to promote increased flux through the pentose phosphate pathway via dimerization of ATM proteins [81].

1.11. Modulation of NADPH redox states for therapeutics

1.12. Thesis overview

The overarching theme of this thesis was to evaluate compartmentalized NADPH dynamics and metabolic pathways under varying stress conditions in cancer cells. In **chapter 2**, I evaluated cytosolic and mitochondrial NADPH dynamics under mitochondrial oxidative stress. In **chapter 3**, I assessed the NADPH generation pathways, particularly oxidative pentose phosphate pathway and glucose metabolic pathways to understand how NADPH was maintained under

mitochondrial stress. In **chapter 4**, I applied a mathematical model based on the system of ordinary differential equations to estimate the NADPH concentration and NADPH/$NADP^+$ ratio. In c**hapter 5**, I explored how nutrient conditions in media influence both cytosolic and mitochondrial NADPH levels across varying cancer cell lines. In **chapter 6**, I studied the role of citrate transport for maintenance of NADPH homeostasis. In **chapter 7**, I related the cytosolic and mitochondrial NADPH indices to cell growth and investigated whether perturbing compartment specific NADPH pools selectively inhibited growth of cancer cell lines. In **chapter 8**, I found a new role NNT enzyme in ketone body metabolism and its function in mitochondrial NADPH homeostasis. Lastly, in **chapter 9**, I developed new NADPH and NADP sensors. Altogether, my thesis work provided new insight on compartmentalized NADPH metabolism, particularly mitochondrial and cytosolic NADPH states, dynamics, and pathways in response to mitochondrial oxidative stress and nutrient stress[4,82].

1.13. References

1. Veech, R. L., Eggleston, L. V & Krebs, H. a. The redox state of free nicotinamide-adenine dinucleotide phosphate in the cytoplasm of rat liver. *Biochem. J.* **115**, 609–619 (1969).

2. Lewis, C. A. *et al.* Tracing Compartmentalized NADPH Metabolism in the Cytosol and Mitochondria of Mammalian Cells. *Mol. Cell* **55**, 253–263 (2014).

3. Goodman, R. P., Calvo, S. E. & Mootha, V. K. Spatiotemporal compartmentalization of hepatic NADH and NADPH metabolism. *J. Biol. Chem.* **293**, 7508–7516 (2018).

4. Heiden, M. G. Vander *et al.* Understanding the Warburg Effect : Cell Proliferation. *Science (80-.).* **324**, 1029 (2009).

5. Tao, R. *et al.* Genetically encoded fluorescent sensors reveal dynamic regulation of NADPH metabolism. *Nat. Methods* **14**, 720–728 (2017).

6. Pollak, N., Dölle, C. & Ziegler, M. The power to reduce: pyridine nucleotides – small molecules with a multitude of functions. *Biochem. J.* **402**, 205–218 (2007).

7. Ying, W. NAD^+/NADH and $NADP^+$/NADPH in Cellular Functions and Cell Death: Regulation and Biological Consequences. *Antioxid. Redox Signal.* **10**, 179–206 (2008).

8. Nickel, A. G. *et al.* Reversal of mitochondrial transhydrogenase causes oxidative stress in heart failure. *Cell Metab.* **22**, 472–484 (2015).

9. Fan, J. *et al.* Quantitative flux analysis reveals folate-dependent NADPH production. *Nature* **510**, 298–302 (2014).

10. Liu, L. *et al.* Malic enzyme tracers reveal hypoxia-induced switch in adipocyte NADPH pathway usage. *Nat. Chem. Biol.* **12**, 345–352 (2016).

11. Katsyuba, E., Romani, M., Hofer, D. & Auwerx, J. NAD+ homeostasis in health and disease. *Nat. Metab.* **2**, 9–31 (2020).

12. Liu, L. *et al.* Quantitative Analysis of NAD Synthesis-Breakdown Fluxes. *Cell Metab.* **27**, 1067-1080.e5 (2018).

13. Hayes, J. D., Dinkova-Kostova, A. T. & Tew, K. D. Oxidative Stress in Cancer. *Cancer Cell* **38**, 167–197 (2020).

14. Wasylenko, T. M., Ahn, W. S. & Stephanopoulos, G. The oxidative pentose phosphate pathway is the primary source of NADPH for lipid overproduction from glucose in Yarrowia lipolytica. *Metab. Eng.* **30**, 27–39 (2015).

15. Stephanopoulos;, G. N., Aristidou, A. A. & Nielsen, J. *Metabolic Engineering: Principles and Methodologies*. *Academic Press* vol. 1 (1998).

16. Ducker, G. S. & Rabinowitz, J. D. One-Carbon Metabolism in Health and Disease. *Cell Metab.* **25**, 27–42 (2017).

17. Dang, L. *et al.* Cancer-associated IDH1 mutations produce 2-hydroxyglutarate. *Nature* **462**, 739–744 (2009).

18. Metallo, C. M. *et al.* Reductive glutamine metabolism by IDH1 mediates lipogenesis under hypoxia. *Nature* **481**, 380–384 (2012).

19. Mullen, A. R. *et al.* Reductive carboxylation supports growth in tumour cells with defective mitochondria. *Nature* **481**, 385–388 (2012).

20. Chen, L. *et al.* NADPH production by the oxidative pentose-phosphate pathway supports folate metabolism. *Nat. Metab.* **1**, 404–415 (2019).

21. Jiang, L. *et al.* Reductive carboxylation supports redox homeostasis during anchorage-independent growth. *Nature* **532**, 255–258 (2016).

22. Wise, E. M. & Ball, E. G. Malic Enzyme and Lipogenesis. *Proc. Natl. Acad. Sci. U. S. A.* **52**, 1255–63 (1964).

23. Nagel, W., Dauchy, R. T. & leonard a. sauer. Mitochondrial Malic Enzymes. **4**, 3849–3854 (1983).

24. Lewis, J. E. *et al.* Genome-scale modeling of NADPH-driven β-lapachone sensitization in head and neck squamous cell carcinoma. *Antioxid. Redox Signal.* **29**, ars.2017.7048 (2017).

25. Petcu, L. G. & Plaut, G. W. NADP-specific isocitrate dehydrogenase in regulation of urea synthesis in rat hepatocytes. *Biochem. J.* **190**, 581–92 (1980).

26. Hosios, A. M. *et al.* Amino Acids Rather than Glucose Account for the Majority of Cell Mass in Proliferating Mammalian Cells. *Dev. Cell* **36**, 540–549 (2016).

27. Moreadith, R. W. & Lehninger, A. L. The pathways of glutamate and glutamine oxidation by tumor cell mitochondria. Role of mitochondrial NAD(P)+-dependent malic enzyme. *J. Biol. Chem.* **259**, 6215–6221 (1984).

28. Son, J. *et al.* Glutamine supports pancreatic cancer growth through a KRAS-regulated metabolic pathway. *Nature* **496**, 101–105 (2013).

29. Rydström, J. Mitochondrial NADPH, transhydrogenase and disease. *Biochim. Biophys. Acta - Bioenerg.* **1757**, 721–726 (2006).

30. Ho, H. Y., Lin, Y. T., Lin, G., Wu, P. R. & Cheng, M. L. Nicotinamide nucleotide transhydrogenase (NNT) deficiency dysregulates mitochondrial retrograde signaling and impedes proliferation. *Redox Biol.* **12**, 916–928 (2017).

31. Li, S. *et al.* Nicotinamide nucleotide transhydrogenase-mediated redox homeostasis promotes tumor growth and metastasis in gastric cancer. *Redox Biol.* **18**, 246–255 (2018).

32. Kampjut, D. & Sazanov, L. A. Structure and mechanism of mitochondrial proton-translocating transhydrogenase. *Nature* **573**, 291–295 (2019).

33. Lunt, S. Y. & Vander Heiden, M. G. Aerobic Glycolysis: Meeting the Metabolic Requirements of Cell Proliferation. *Annu. Rev. Cell Dev. Biol.* **27**, 441–464 (2011).

34. Hanschmann, E. M. *et al.* Both thioredoxin 2 and glutaredoxin 2 contribute to the reduction of the mitochondrial 2-Cys peroxiredoxin Prx3. *J. Biol. Chem.* **285**, 40699–40705 (2010).

35. Förstermann, U. & Münzel, T. Basic Science for Clinicians Endothelial Nitric Oxide Synthase in Vascular Disease. 1708–1714 (2006) doi:10.1161/CIRCULATIONAHA.105.602532.

36. Bedard, K. & Krause, K. The NOX Family of ROS-Generating NADPH Oxidases : Physiology and Pathophysiology. *Am. Physiol. Soc.* **87**, 245–313 (2007).

37. Ushio-fukai, M. Forum Review Article Compartmentalization of Redox Signaling Through

NADPH Oxidase–Derived ROS. **11**, (2009).

38. Zhang, Y., Murugesan, P., Huang, K. & Cai, H. NADPH oxidases and oxidase crosstalk in cardiovascular diseases : novel therapeutic targets. *Nat. Rev. Cardiol.* **17**, 43–55 (2020).

39. Terada, L. S. Specifi city in reactive oxidant signaling : think globally , act locally. **174**, 615–623 (2006).

40. Martyn, K. D., Frederick, L. M., Loehneysen, K. Von, Dinauer, M. C. & Knaus, U. G. Functional analysis of Nox4 reveals unique characteristics compared to other NADPH oxidases. **18**, 69–82 (2006).

41. Chen, K., Craige, S. E. & Keaney, J. F. Downstream Targets and Intracellular Compartmentalization in Nox Signaling. **11**, (2009).

42. J.D. VAN BUUL, M. FERNANDEZ-BORJA, E.C. ANTHONY, and P. L. H. Expression and Localization of NOX2 and NOX4 in Primary Human Endothelial Cells. (2005) doi:10.1089/ars.2005.7.308.

43. Matsushima, S. *et al.* Integrative Physiology Increased Oxidative Stress in the Nucleus Caused by Nox4 Mediates Oxidation of HDAC4 and Cardiac Hypertrophy. 651–663 (2012) doi:10.1161/CIRCRESAHA.112.279760.

44. Pavlova, N. N. & Thompson, C. B. The Emerging Hallmarks of Cancer Metabolism. *Cell Metabolism* (2016) doi:10.1016/j.cmet.2015.12.006.

45. Weinberg. Hallmarks of cancer. *J. Prev. Med. Hyg.* **57**, E41–E46 (2016).

46. Heiden, M. G. Vander & Deberardinis, R. J. Review Understanding the Intersections between Metabolism and Cancer Biology. *Cell* **168**, 657–669 (2017).

47. Mitsuishi, Y. *et al.* Nrf2 Redirects Glucose and Glutamine into Anabolic Pathways in Metabolic Reprogramming. *Cancer Cell* **22**, 66–79 (2012).

48. Ye, J. *et al.* Serine catabolism regulates mitochondrial redox control during hypoxia. *Cancer Discov.* **4**, 1406–1417 (2014).

49. Pavlova, N. N. & Thompson, C. B. The Emerging Hallmarks of Cancer Metabolism. *Cell Metab.* **23**, 27–47 (2016).

50. Fendt, S. M. *et al.* Reductive glutamine metabolism is a function of the α-ketoglutarate to citrate ratio in cells. *Nat. Commun.* **4**, 1–11 (2013).

51. Moon, S. J., Dong, W., Stephanopoulos, G. N. & Sikes, H. D. Oxidative pentose phosphate pathway and glucose anaplerosis support maintenance of mitochondrial NADPH pool under mitochondrial oxidative stress. *Bioeng. Transl. Med.* 1–18 (2020) doi:10.1002/btm2.10184.

52. Clark, R. A., Leidal, K. G., Pearson, D. W. & Nauseef, W. M. NADPH Oxidase of Human Neutrophils. *J. Biol. Chem.* **262**, 4065–4074 (1987).

53. Fisher, A. B. Redox Signaling Across Cell Membranes. *Antioxid. Redox Signal.* **11**, 1349–1356 (2009).

54. Jones, D. P. & Sies, H. The Redox Code. *Antioxid. Redox Signal.* **23**, 734–746 (2015).

55. Adimora, N. J., Jones, D. P. & Kemp, M. L. A Model of Redox Kinetics Implicates the Thiol Proteome in Cellular Hydrogen Peroxide Responses. *Antioxid. Redox Signal.* **13**, 731–743 (2010).

56. Krebs, H. A. & Veech, R. L. Equilibrium relations between pyridine nucleotides and adenine nucleotides and their roles in the regulation of metabolic processes. *Adv. Enzyme Regul.* **7**, 397–413 (1969).

57. Hedeskov, C. J., Capito, K. & Thams, P. Cytosolic ratios of free [NADPH]/[NADP+] and [NADH]/[NAD+] in mouse pancreatic islets, and nutrient-induced insulin secretion. *Biochem. J.* **241**, 161–167 (1987).

58. Vander Heiden, M. G. & DeBerardinis, R. J. Understanding the Intersections between Metabolism and Cancer Biology. *Cell* **168**, 657–669 (2017).

59. Jeon, S. M., Chandel, N. S. & Hay, N. AMPK regulates NADPH homeostasis to promote tumour cell survival during energy stress. *Nature* **485**, 661–665 (2012).

60. Cameron, W. D. *et al.* Apollo-NADP+: A spectrally tunable family of genetically encoded sensors for NADP+. *Nat. Methods* **13**, 352–358 (2016).

61. Sallin, O. *et al.* Semisynthetic biosensors for mapping cellular concentrations of nicotinamide adenine dinucleotides. *Elife* **7**, 1–32 (2018).

62. Zhao, F. L., Zhang, C., Zhang, C., Tang, Y. & Ye, B. C. A genetically encoded biosensor for in vitro and in vivo detection of NADP+. *Biosens. Bioelectron.* **77**, 901–906 (2016).

63. Letizia Canepa, A. M. gerraris. M. M. and G. F. G. Bound and unbound pyridine dinucleotides in normal and glucose-6-phosphate dehydrogenase-deficient erythrocytes. *Biochim. Biophys. Acta.* **1074**, 101–104 (1991).

64. Blacker, T. S. *et al.* Separating NADH and NADPH fluorescence in live cells and tissues using FLIM. *Nat. Commun.* **5**, (2014).

65. Kosenko, E. A. & Yury, G. A COMPARISON BETWEEN EFFECTS ETHANOL CONSUMPTION , ETHANOL AND FASTING IN ETHANOL-FED THE FREE CYTOSOLIC NADP + / NADPH ENZYME IN THE LIVER OF CHRONIC WITHDRAWAL RATS ON RATIO AND ACTIVITIES. **17**, 895–902 (1985).

66. Gitomer, W. L., Miller, B. C. & Cottam, G. L. In Vivo Effects of Lipopolysaccharide on Hepatic Free-NAD(P) + -Linked Redox States and Cytosolic Phosphorylation Potential in 48-Hour-Fasted Rats. **9**, 1170–1174 (1995).

67. Kuehne, A. *et al.* Acute Activation of Oxidative Pentose Phosphate Pathway as First-Line Response to Oxidative Stress in Human Skin Cells. *Mol. Cell* **59**, 359–371 (2015).

68. Dong, W., Keibler, M. A. & Stephanopoulos, G. Review of metabolic pathways activated in cancer cells as determined through isotopic labeling and network analysis. *Metab. Eng.* **43**, 113–124 (2017).

69. Dey, S., Sidor, A. & O'Rourke, B. Compartment-specific control of reactive oxygen species scavenging by antioxidant pathway enzymes. *J. Biol. Chem.* **291**, 11185–11197 (2016).

70. Esposito, L. A., Melov, S., Panov, A., Cottrell, B. A. & Wallace, D. C. Mitochondrial disease in mouse results in increased oxidative stress. *Proc. Natl. Acad. Sci.* **96**, 4820–4825 (1999).

71. Kang, J. & Pervaiz, S. Mitochondria: Redox Metabolism and Dysfunction. *Biochem. Res. Int.* **2012**, 1–14 (2012).

72. Shadel, G. S. & Horvath, T. L. Mitochondrial ROS Signaling in Organismal Homeostasis. *Cell* **163**, 560–569 (2015).

73. Kohen, R. & Nyska, A. Oxidation of Biological Systems: Oxidative Stress Phenomena, Antioxidants, Redox Reactions, and Methods for Their Quantification. *Toxicol. Pathol.* **30**, 470 ou pag cap. 150–180 (2002).

74. Wallace, D. C. A mitochondrial paradigm of metabolic and degenerative diseases, aging, and cancer: a dawn for evolutionary medicine. *Annu. Rev. Genet.* **39**, 359–407 (2005).

75. Reuter, S., Gupta, S. C., Chaturvedi, M. M. & Aggarwal, B. B. Oxidative stress, inflammation, and cancer: How are they linked? *Free Radic. Biol. Med.* **49**, 1603–1616 (2010).

76. Gilgun-Sherki, Y., Melamed, E. & Offen, D. Oxidative stress induced-neurodegenerative diseases: The need for antioxidants that penetrate the blood brain barrier. *Neuropharmacology* **40**, 959–975 (2001).

77. Marnett, L. J. Oxyradicals and DNA damage. *Carcinogenesis* **21**, 361–370 (2000).

78. Paul D. Ray, Bo-Wen Huang, Y. T. Reactive oxygen species (ROS) homeostasis and redox regulation in cellular signaling. *Cell. Signal.* **24**, 981–990 (2012).

79. Lennicke, C., Rahn, J., Lichtenfels, R., Wessjohann, L. A. & Seliger, B. Hydrogen peroxide - Production, fate and role in redox signaling of tumor cells. *Cell Commun. Signal.* **13**, 1–19 (2015).

80. Gough, D. R. & Cotter, T. G. Hydrogen peroxide: a Jekyll and Hyde signalling molecule. *Cell Death Dis.* **2**, e213 (2011).

81. Zhang, Y. *et al.* Mitochondrial redox sensing by the kinase ATM maintains cellular antioxidant capacity. *Sci. Signal.* **11**, (2018).

82. Gorrini, C., Harris, I. S. & Mak, T. W. Modulation of oxidative stress as an anticancer strategy. *Nat. Rev. Drug Discov.* **12**, 931–47 (2013).

Chapter 2

Evaluation of mitochondrial and cytosolic NADPH dynamics in response to mitochondrial oxidative stress

This chapter is adapted from

***Sun Jin Moon**, Wentao Dong, Greg Stephanopoulos and Hadley Sikes, Oxidative pentose phosphate pathway and glucose anaplerosis support maintenance of mitochondrial NADPH pool under mitochondrial oxidative stress, Bioengineering & Translational Medicine, 2020, 5 e10184 (2020).*

2.1. Abstract

A major role of mitochondrial NADPH pool is to maintain mitochondrial antioxidant system by protecting cells against excessive generation of mitochondrial H_2O_2. Due to technical challenges, it has been unknown to what extent the mitochondrial oxidative stress influences cytosolic and mitochondrial NADPH levels. Here, I systemically modulate production rates of H_2O_2 in mitochondria using D-amino acid oxidase that is localized to mitochondria, and monitor the dynamics of NADPH levels using iNap sensors. Time-course measurement reveals distinct dynamic patterns of cytosolic and mitochondrial NADPH levels. Mitochondrial NADPH decreases upon excessive generation of mitochondrial H_2O_2, whereas the cytosolic NADPH is unaltered.

2.2. Introduction

Mitochondria emerge as a major source of reactive oxygen species (ROS), and excessive production of ROS has been linked to various diseases including neurodegeneration, inflammation, aging, diabetes, and cancers via induction of lipid peroxidation, protein oxidation, and DNA damage [1–7]. Of various types of ROS, hydrogen peroxide (H_2O_2) acts as a signaling molecule that can initiate expression of survivor genes such as antioxidant response elements (e.g., Nrf2), induce DNA repair mechanisms (e.g., p53 and ATM), or activate programmed cell death pathways (e.g., NF-κB) [4,8,9]. As accumulation of H_2O_2 can induce toxicity, cells maintain a defensive system to clear H_2O_2 via redox reactions [2,10,11].

In the antioxidant network, NADPH plays a critical role by serving as a reductant during removal of H_2O_2 to maintain redox homeostasis. It donates two electrons to reduce oxidized

cysteine residues of thioredoxin via thioredoxin reductase, or glutathione via glutathione reductase[12–15]. Thioredoxin with reduced cysteine residues reacts with peroxiredoxins, which have been known to be the major scavenger of H_2O_2 based on their abundance and fast second order rate coefficient compared to glutathione peroxidase reaction at low levels of intracellular H_2O_2[16,17]. In mitochondria, peroxiredoxin 3 is known to scavenge 90% of H_2O_2, suggesting peroxiredoxin-thioredoxin-NADPH as the major clearance pathway for mitochondrial H_2O_2[16]. In parallel, glutathione reacts with glutaredoxin which serves as a reductase for oxidized proteins, and with glutathione peroxidase during direct reactions with H_2O_2 [18,19].

Oxidative stress, a condition caused by an inadequate clearance or excessive production of H_2O_2, has been reported to decrease the total NADPH pool, NADPH/$NADP^+$ ratio, and modulate NADP-dependent metabolic fluxes [12,13,20]. For instance, oxidative stress in fibroblast cells led to a shift of glycolytic flux toward the oxidative pentose phosphate pathway to regenerate NADPH [20–23]. In isolated cardiac myocytes under a pathological workload, the direction of mitochondrial nicotinamide transhydrogenase reaction was reversed, lowering the total NADPH pool and increasing the production of mitochondrial ROS [24]. Similarly, the availability of NADPH in mitochondria along with NADPH-producing enzymes such as isocitrate dehydrogenase 2 (IDH2) and nicotinamide nucleotide transhydrogenase (NNT) was shown to control the antioxidant network for clearance of H_2O_2 [25].

To our knowledge, little has been known about the causal relationship between oxidative stress derived within mitochondria and mitochondrial or cytosolic NADPH pools. Previously, the total NADPH level or its ratio to $NADP^+$ has been reported to decrease by exogenous oxidative stress introduced extracellularly or to the exterior of isolated mitochondria, but no direct evidence of compartmentalized NADPH dynamics by mitochondria specific oxidative stress in

living cells. Gas or liquid chromatography coupled to mass spectrometry and enzymatic cycling assays provide great sensitivity and specificity for measurement of NADPH, but these analytical tools are based on measurements of the average of cell lysates, making it difficult to preserve spatial and temporal information of NADPH in living cells at single cell resolution [26,27].

Co-expressing compartment-specific NADPH sensors and D-amino acid oxidase (DAAO) which is used as H_2O_2 generator, I evaluate mitochondrial and cytosolic NADPH dynamics upon localized H_2O_2stress. iNap sensors are genetically-encoded probes for NADPH and provided a wide dynamic range with a ratiometric fluorescent readout, which can be simply recorded using a fluorescence microscope at single-cell resolution [28]. For mitochondrial NADPH experiments, we express the sensors using mitochondria using localization tags. Fluorescence ratio is defined as a ratio between fluorescence emissions at 515 nm excited at 415 nm and 488 nm ($R = \frac{F_{em:515,ex:415}}{F_{em:515\ nm,ex:488}}$). Due to the influence of pH fluctuations to iNap fluorescence at 488 nm, the fluorescence ratio of iNap can be normalized to that of iNapC, a control iNap sensor engineered to lose its binding affinity to NADPH. As cytoplasmic pH is shown to be stable during oxidative stress [28], we use the fluorescence ratio (R) for cytoplasmic iNap experiments. For mitochondrial iNap experiments, we use a normalized form of fluorescence ratio, defined as fluorescence readout ($R' = \frac{R_{iNap-mito}}{R_{iNapC-mito}}$). For kinetic experiments, fluorescence ratio or readout is normalized to initial values. For modulation of mitochondrial H_2O_2 level, we express D-amino acid oxidase (DAAO) with a mitochondrial localization sequence. Upon addition of varying concentrations of D-alanine, reactions with oxygen produce H_2O_2 as a byproduct [29].

2.3. Materials and Methods

2.3.1. Cloning and transformation of iNap variants into mammalian vectors

A total of five iNap sensor variants have been successfully cloned into mammalian expression vectors. iNap33 is a cytosolic sensor with dissociation constant (Kd) of 3.6μM. In detection of NADPH in mammalian cells, it is ideal to prepare a sensor whose dissociation constant is closely matched with the physiological level of NADPH. It is because a small change of NADPH level can lead to a significant response change if the physiological level of NADPH is near the Kd as it has the steepest slope in a signal response (y-axis) and dose response (x-axis) graph. A high Kd will give a low signal-to-ratio fluorescence and a too low Kd will saturate the fluorescence.

Currently, exact cytosolic or mitochondrial NADPH levels has not been reported. However, previous studies indicate a total NADPH level is presumably in a micromolar range. Thus, I prepare two iNap sensors, iNap1 and iNap3, each having a Kd of 2.0μM and 25.2μM based on the literature [28,30]. After cloning the iNap3 sensor, I make point mutations around the binding pocket to lower the Kd by following the literature and using a point mutation kit from the New England Biolabs. In addition, I also prepare iNapC which has an infinite dissociation constant. The control is necessary because the iNap sensor is based on the circularly permuted yellow fluorescent protein, whose fluorescence response is affected by the change of pH. Thus, it is important to have the iNap control in parallel to account for the pH effect in other iNap sensors. For mitochondrial iNap sensors, iNap3-mito and iNapC-mito are constructed by linking mitochondrial localization sequences to original constructs.

In specific, iNap fragments are cloned into pLJM1-EGFP vector by replacing the enhanced green fluorescent protein (EGFP) to five variants of iNap sensors using BamHI and NheI restriction sites. pLJM1-EGFP contains a CMV promotor making it a constitutive

expression system. This vector is also widely used in the lentivirus production as a transfer plasmid. Thus, I choose this vector as a transient expression vector as well as a lentivirus transfer vector. Later, the lentivirus will be made by following a third generation lentiviral system. Briefly, a pLJM1-iNap transfer plasmid, a packaging vector of psPAX2, and an envelope vector of pMD2.G, are co-expressed in Hek293FT cells and the lentivirus is harvested after 48 hours. After cloning of iNap sensors into pLJM1 vectors, the plasmid is transformed into DH5α *E. coli* and stored in the -80C for further use.

Table *2.1.* Five iNap sensors were cloned to a pLJM1 vector and transformed into a *DH5α E. coli*

iNap sensors	Target location	Dissociation constant (μM)	Vector	Restriction sites used
iNap33	Cytosol	3.6		
iNap3	Cytosol	25.2		
iNapC	Cytosol	∞	pLJM1	NheI, BamHI
iNap3-mito	Mitochondria	2		
iNapC-mito	Mitochondria	∞		

2.3.2. Generation of cell lines that stably express iNap and iNap-mito sensors

HEK293 FT cells were seeded at 7.5×10^5 cells per 35mm well in 6 well plates (Corning, VWR 29442-042) for two days until 70 – 90% confluency. pLJM-1 vectors encoding appropriate sensors were co-transfected with the packaging plasmids pMD2.G and Pax2 vectors at a 3: 1: 2 ratio for a total of 5 μg plasmids and 10 μg of Lipofectamine 2000 in OptiMEM medium overnight. Next morning, the media was replaced with 1mL of Dulbecco's modified Eagle's medium (DMEM; Lonza) supplemented with 10% 10% fetal bovine serum (FBS; ATCC) and the media was collected every 24 hour for two days. The collected media was centrifuges at 500 g for five minutes and the supernatant was collected and stored at -80C freezer. After virus containing supernatant was prepared, Hela cells were seeded at 3.5×10^5 cells per 35 mm well in 6 well plates for two days until 70-90% confluency. 1 mL of virus-containing supernatant was added to wells containing Hela cells with 6 μg/mL of polybrene. After three days of infection, cells from each well were expanded to 10 cm dish with 6 μg/mL puromycin selection media for about seven days until 70-90% confluency.

2.3.3. Transient transfection of mito- D-amino oxidase (mito-DAAO)

Hela cells stably expressing appropriate iNap sensors were seeded at 1.75×10^5cells per 35 mm well in 6 well plates or 35 mm single well dish. After two days, the media was replaced to 1mL of OptiMEM medium and transiently transfected with the pLJM1-mito-DAAO plasmid or pLJM1-FLAG-mito-DAAO using the Lipofectamine 2000 in OptiMEM medium with a total DNA concentration of 2ug.

2.3.4. Immunofluorescent analysis of Hela cells transiently transfected with mito-DAAO-FLAG.

Hela cells, expressing mito-DAAO-FLAG in 6-well plates at a cell density of approximately 35,000 cells per well, were fixed with 4% paraformaldehyde and permeabilized with 0.1% Triton X-100 in PBS for 30 minutes at room temperature and blocked with an Odyssey Blocking buffer (Li-Cor) in PBS with a 1:1 ratio for 30 minutes. Cells were stained with AlexaFluor 488 conjugated FLAG-tag, monoclonal antibody (Product # MA1-142-A488) at a dilution of 1:100 for an hour at room temperature. The sequence of Flag-tag is DYKDDDDK and it can be appended to any recombinant gene so that the protein of interest it encodes can be easily labeled within the cell to check for expression and localization. Nuclei were stained with the DAPI. Images were captured on an Olympus IX-81 microscope with a CCD camera at 20X magnification.

2.3.5. Cellular imaging using fluorescence microscopy

The fluorescence emission signal was recorded using an inverted IX81 wide field fluorescence microscope (Olympus) with a 20x objective lens and Prior Lumen 2000 lamp. The Chroma 415/30 nm and a Semrock 488/6 nm excitation filters were used and a Semrock 525/ 40 nm filter was used for the emission filter. The exposure time was 300 ms and 10% lamp intensity was used. An in-built multi-dimensional setup was used for automated time-course measurement. Images were captured every 20 seconds, 1 or 3 minutes and exported to either ImageJ or MATLAB 2016a for post image processing.

2.3.6. Image analysis of iNap sensors

Backgrounds of short (415nm) and long (488nm) wavelength images were subtracted using a rolling ball algorithm from ImageJ. Long-wavelength images were converted to 32 bit and a threshold of one was applied to minimize artifact. The pixels values of the 415 nm filters were divided those of the 488 nm. Individual cells, neither too bright not too dim, were randomly selected and the mean fluorescence intensity of region of interest was calculated. All the fluorescence emission ratios were recorded as the mean $\pm$ SEM. The images were created using the image processing algorithm in MATLAB 2016a with pseudo colors.

2.4. Results

2.4.1. Expression of DAAO and iNap in mitochondria enables mitochondria-specific production of H_2O_2 and measurement of NADPH

We designed a system capable of producing H_2O_2 and measuring NADPH simultaneously **(Figure 2.1)**. First, a plasmid that encoded D-amino acid oxidase enzyme (DAAO) was constructed with a mitochondrial localization sequence at the N terminus and FLAG tag at the C terminus. The localization was confirmed via immunofluorescence staining with anti-Flag antibody, Mitotracker, and DAPI in fixed Hela cells that transiently expressed the mito-DAAO construct **(Figure 2.2A)**.

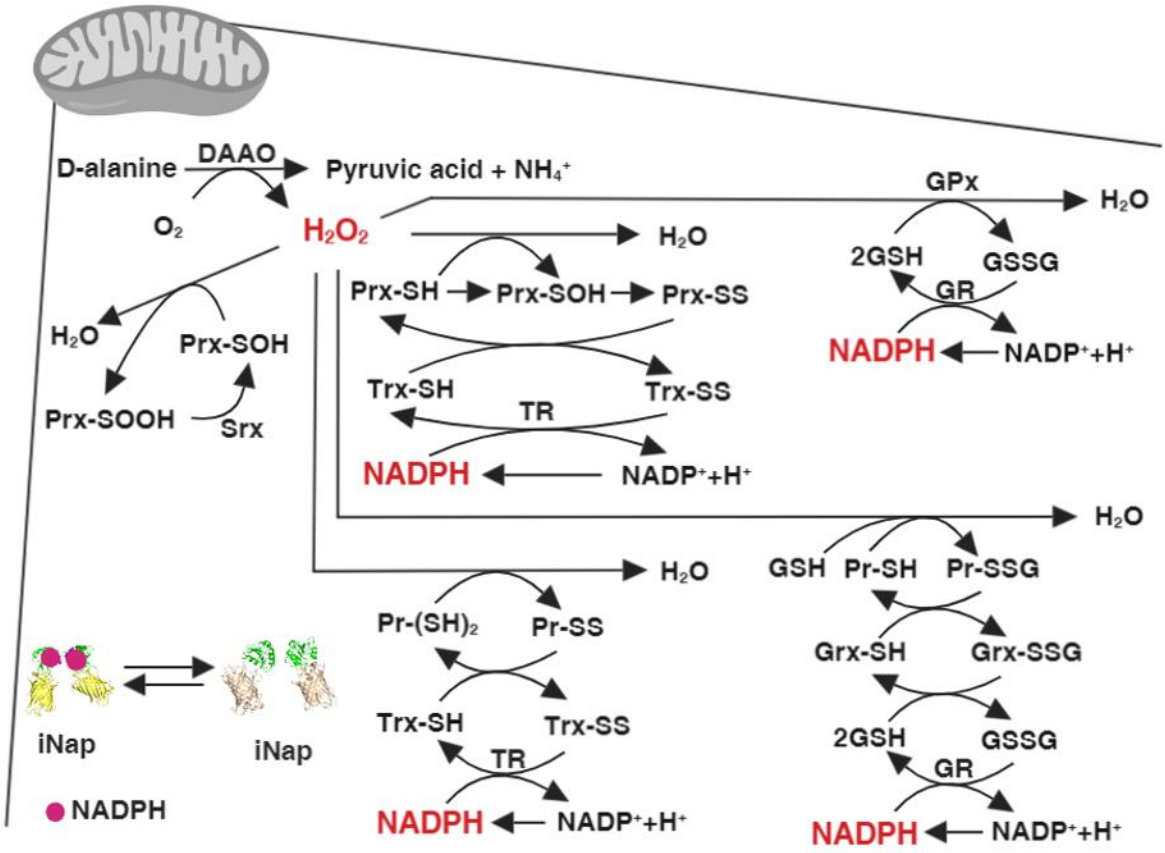

Figure 2.1. Schematics representing a mechanistic connection between hydrogen peroxide and NADPH via a network of mitochondrial redox reactions. H_2O_2 was generated via mito-DAAO and mitochondrial NADPH was measured using mito-iNap sensor.

Next, enzymatic activity was tested using a horseradish peroxidase based Amplex UltraRed assay in response to varying concentrations of D-alanine added to lysed Hela cells with mito-DAAO (**Figure 2.2B)**. Using the Michaelis-Menten kinetic relation and the previously determined turnover rate of DAAO enzyme, we calculated DAAO concentration in mitochondria to be approximately 0.6 µM per cell, assuming the radius of a Hela cell is 10 µm and the mitochondrial volume comprises 10% of the total volume [31]. A maximum peroxide generation rate, v_{max}, was estimated to be 2.0×10^{-4} M/s per cell, and the K_m to be 10.4 mM. Lastly, we confirmed the phenotypic influence of DAAO-mediated H_2O_2 generation by counting the number of live cells after 24 hours of stimulation with D-alanine. The Hela/mito-DAAO cells

were treated with D-alanine concentration from 0 to 25 mM. Doses below 5 mM D-alanine did not inhibit cell growth. Perturbation with D-alanine to Hela cells devoid of DAAO system did not induce toxicity, consistent with the previous reports (Figure S8) [29,32]. The findings shown in **Figure 2.2C** were consistent with previous results that a high dose of D-alanine such as 25 mM killed cells through an apoptotic pathway[29].

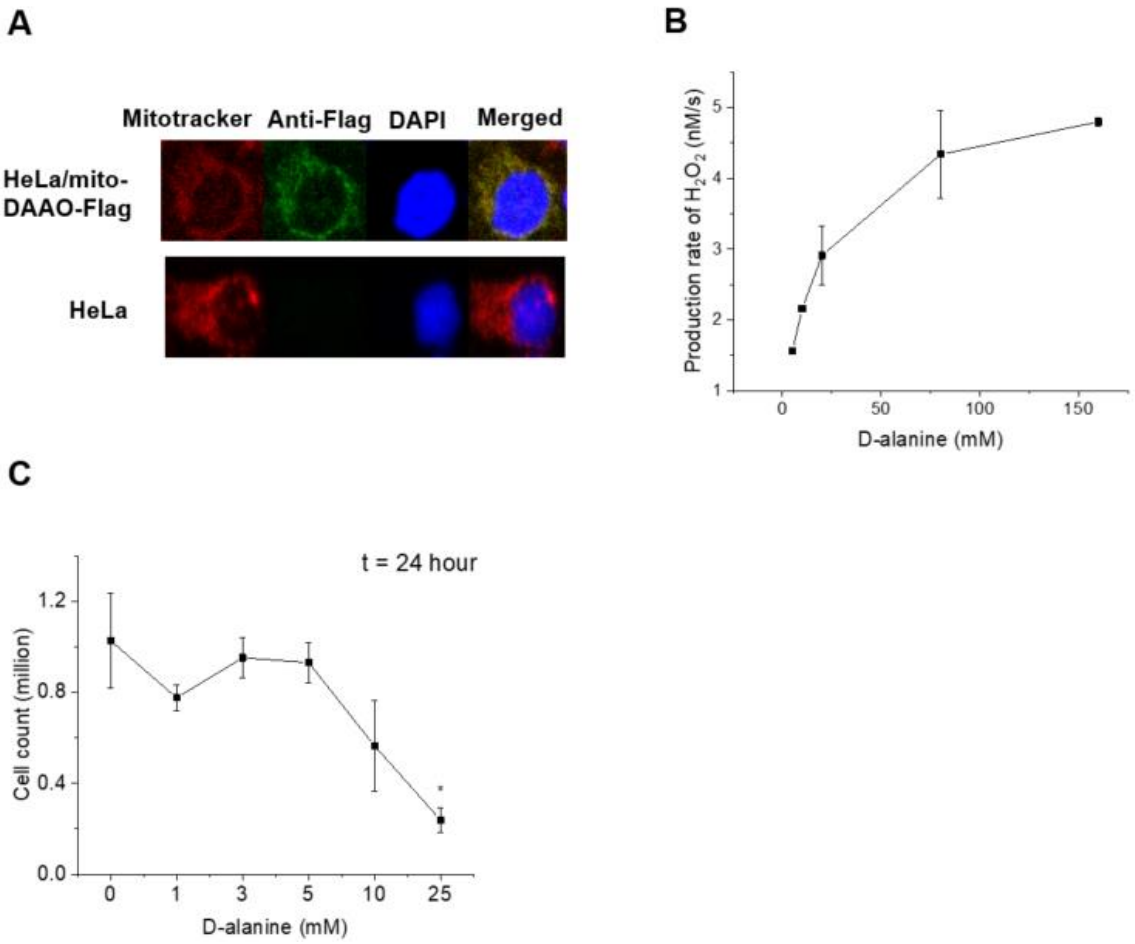

Figure 2.2. Validation of mito-DAAO targeted to mitochondria and its generation of H_2O_2 upon D-alanine addition. **(A)** Hela cells were transiently transfected with a mito-DAAO-FLAG and its localization to mitochondria was confirmed. Staining: Mitotracker (red), anti-FLAG (green), DAPI (blue). **(B)** The enzymatic activity of DAAO was measured via a horseradish peroxidase based Amplex UltraRed assay. Fluorescence intensity was measured after incubation of HeLa cell lysates with D-alanine for an hour. Fluorescence readings were converted to hydrogen peroxide concentrations using a standard curve

constructed using known concentrations of hydrogen peroxide. Data represent two independent experiments ± SD. **(C)** Cell numbers were counted after 24 hours of incubation of D-alanine with Hela/mito-DAAO cells with error bars representing SEM of three independent experiments.

Next, we tested the functionality of the mitochondrial iNap sensor before implementation of experiments with DAAO system. First, we introduced an artificial oxidative stress by stimulating cells with 500 μM diamide, which was previously shown to minimally influence the fluorescence of iNap control sensor [28]. We recorded an excitation spectrum with the emission wavelength centered at 515nm, confirming a decrease of the ratio of 515nm emission upon excitation with light centered at 415 nm and 488 nm as previously described **(Figure 2.3A)** [28]. Afterwards, we obtained the maximum fluorescence ratio of the iNap-mito sensor. We stimulated Hela/iNap-mito cells with 400 μM of NADPH with 0.05 mg/mL digitonin, and measured the change of fluorescence ratio every 20 seconds. The effective fluorescence ratio was achieved by normalizing the fluorescence ratio of the iNap-mito sensor to that of iNapC-mito, which was designed to function as a control sensor that responds to pH **(Figure 2.3B)** [28]. Once the functionality of mito-DAAO and iNap-mito were validated, we constructed HeLa cell lines that stably expressed iNap sensors, either cytosolic or mitochondrial iNap variants, and transiently expressed mito-DAAO to modulate mitochondrial H_2O_2 production rates.

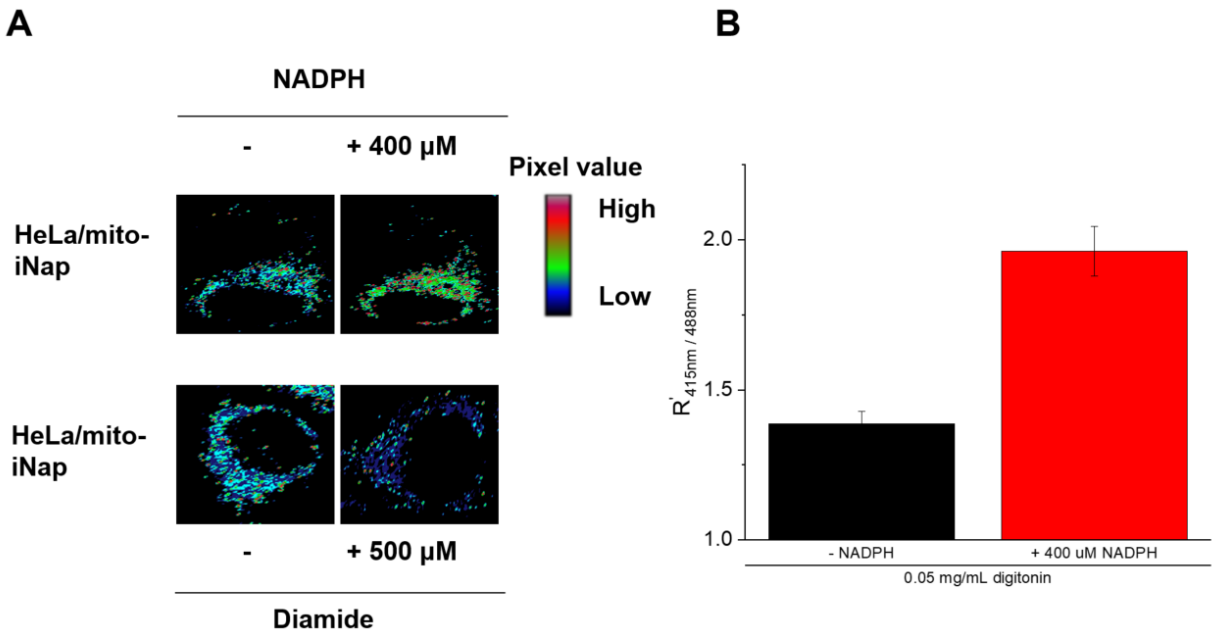

Figure 2.3. Validation of a mito-iNap sensor functioning in mitochondria. **(A)** Pseudo-colored images represent the change of fluorescence intensity of Hela/mito-iNap cells in the presence or absence of NADPH, or diamide. For incubation of NADPH, 0.05 mg/mL digitonin was used to permeabilize the mitochondrial membrane. **(B)** Fluorescence readout ($R' = \frac{R_{iNap-mito}}{R_{iNapC-mito}}$) was quantified before and after addition of 400 µM NADPH in digitonin treated Hela cells expressing iNap sensors. Data represents the mean of fluorescence ratio of individual cells from three independent experiments ± SEM. (n = 22 and 16 cells)

2.4.2. Generation of mitochondrial H_2O_2 decreases mitochondrial NADPH and not cytosolic NADPH level

To determine a threshold of D-alanine concentration that would generate H_2O_2 in mitochondria and perturb the NADPH pool, we stimulated cells by adding 0, 1, 5, 10, 15, 25, 50 mM of D-alanine and recorded the change of fluorescence readout (R′) of iNap-mito **(Figure 2.4A-D)**.

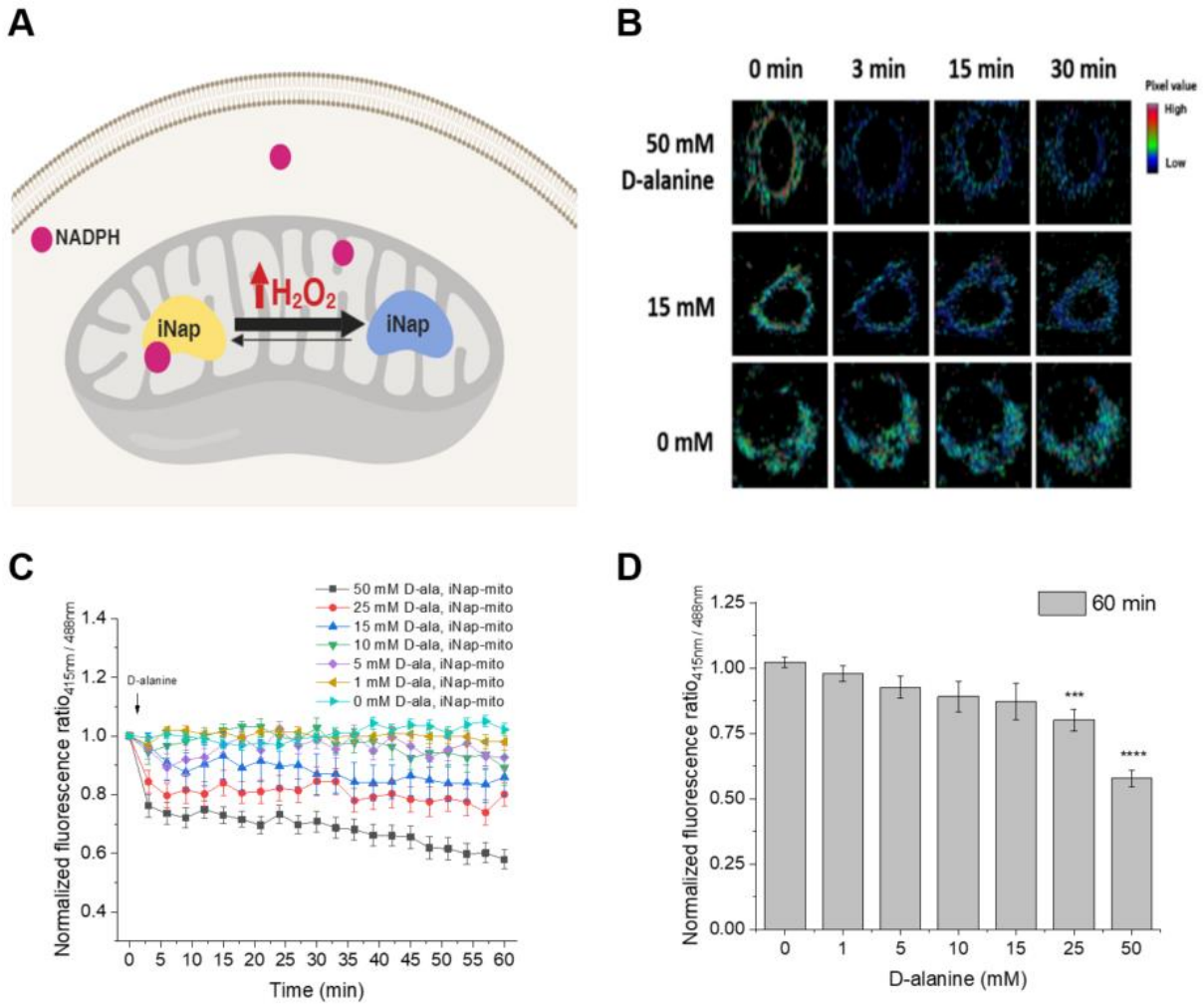

Figure 2.4. Mitochondrial H_2O_2 decreased mitochondrial NADPH levels. (A) Schematic of cytosolic H_2O_2 generation by DAAO expressed in cytosol and NADPH measured by the cytosolic iNap sensor. (B) Normalized R from iNap-cyto was monitored after stimulating cells with 6 different concentrations of D-alanine. Values were recorded at every 3 minutes for an hour and represent mean of individual cells from at least two independent experiments ± SEM. (n = 10, 14, 14, 9, 9, 9 cells from experiments with 50 to 0

mM D-alanine). (C) Normalized R from iNap-cyto was measured at 60 minutes. A two-tailed student's *t*-test was used for statistical analysis with p-values < 0.05 considered statistically significant ($* P < 0.05$, $*** P < 0.001$,$**** P < 0.0001$).

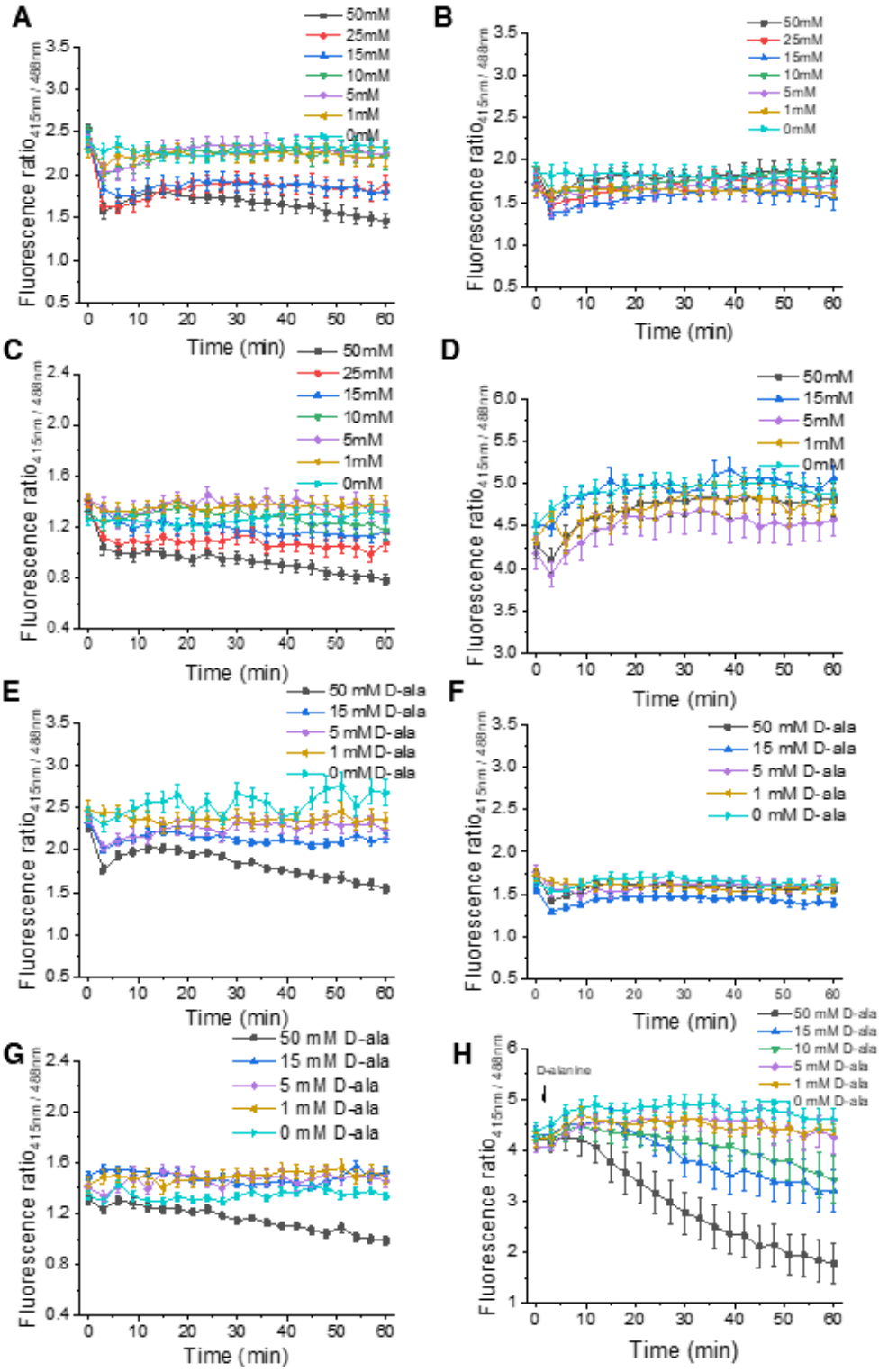

Figure 2.5. Raw fluorescence ratios of iNap sensors upon generation of hydrogen peroxide via DAAO-mito by stimulating cells with varying concentration of D-alanine. Raw fluorescence ratios of iNap sensors upon generation of hydrogen peroxide via DAAO-mito by stimulating cells with varying

concentration of D-alanine. (A) Fluorescence ratio of iNap-mito, (B) iNapC-mito, (C) ratio of iNap-mito to iNapC-mito, and (D) iNap-cyto. (E) Raw fluorescence ratio of iNap sensors upon generation of H_2O_2 via DAAO: Fluorescence ratio of iNap-mito, (F) iNapC-mito, (G) ratio of iNap-mito to iNapC-mito, and (H) iNap-cyto.

The fluorescence ratios (R) were recorded every 3 minute for 60 minutes. To account for the pH effect that could be introduced during the perturbation and generate an artificial fluorescence signal by the intrinsic property of circularly permuted yellow fluorescent protein, we performed parallel experiments with the pH sensor and normalized the fluorescence ratio of the iNap-mito to that of iNapC-mito (**Figure 2.5A-C).** Upon addition of D-alanine below 25 mM, we observed the normalized fluorescence readout remained within 13% of that of the control sensor throughout the time span **(Figure 2.4D)**. Above 25 mM, the fluorescence readout of the sensor decreased by 15 % within 3 minutes and decreased by approximately 20% after 60 minutes. Upon addition of 50 mM of D-alanine, the decrease of fluorescence readout was larger as it declined by 22% within 3 minutes and steadily decreased up to 40 % in 60 minutes.

We previously demonstrated that an excessive generation of H_2O_2 via mito-DAAO system could increase oxidation states of peroxiredoxin as well as glutathionylation of proteins under high concentration of D-alanine, and suggested a threshold concentration of D-alanine that triggered cellular toxicity to be between 15 mM and 25 mM for short perturbation times in Hela-DAAO system [29,33]. Similarly, our data demonstrated that 25 mM D-alanine was the threshold concentration that allowed a significant decrease of NADPH pools in mitochondria. Additionally, we assessed whether the absence of carbon source such as glucose or glutamine could influence the mitochondrial NADPH pool during high production of mitochondrialH_2O_2. In the absence of glucose, the normalized R' from iNap-mito decreased by nearly 50 % compared to the samples that were treated with 25 mM D-alanine with glucose **(Figure 2.6A)**. In

the presence of glutamine, the fluorescence readout was not statistically different, suggesting glucose metabolism as the primary source for maintenance of mitochondrial NADPH pool in 30 minutes.

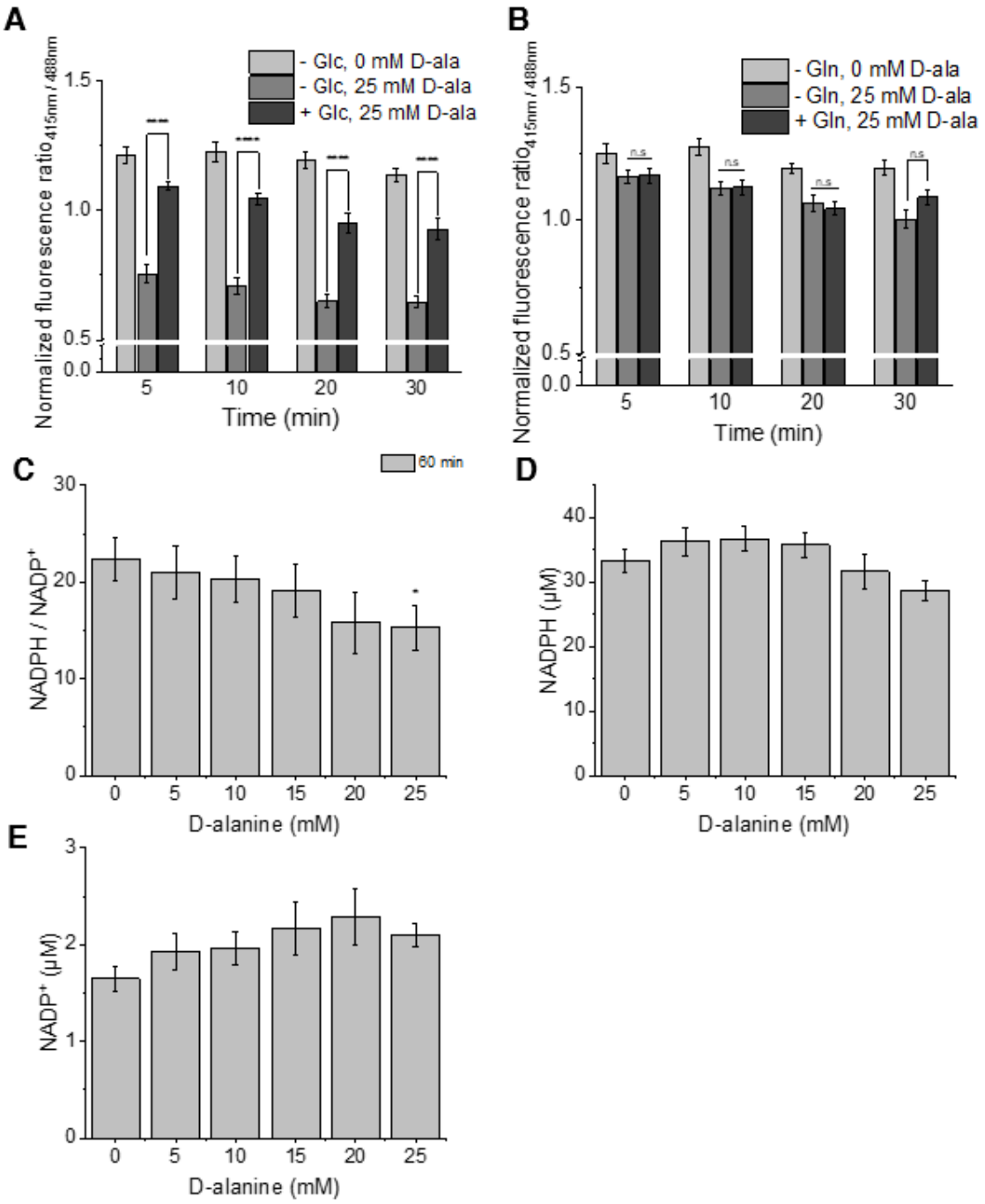

Figure 2.6. The fluorescence ratio of iNap sensors were recorded upon generation of mitochondrial hydrogen peroxide in media with absence or presence of glucose or glutamine. 3.5×10^5 Cells were plated into 6 well plates for two days before the transient tracnsfection with DAAO-mito. The fluorescence ratio was recorded every minute in media with or without (A) glucose, and (B) glutamine. (C) The whole cellular NADPH/NADP ratio, (D) NADPH, and (E) $NADP^+$ were measured using the luminescence-based enzymatic assay by Promega. Cells were cultured in 6-well plates as described in

methods with intracellular NADPH and $NADP^+$ concentration estimated assuming volume of Hela cells were 4.188 pL and the number of cells in each well of 96-well plates was 21,000 [38]. Values were determined following manufacturer's protocol. Mean and error bars represent five biological replicates with three technical replicates each. A two-tailed student's *t*-test was used for statistical analysis with p-values < 0.05 considered statistically significant ($* \text{P} < 0.05$, $*** \text{P} < 0.001$,$**** \text{P} < 0.0001$).

Next, we explored whether the generation of mitochondria H_2O_2influenced the cytosolic NADPH pool. We generated mitochondrial H_2O_2via mito-DAAO and recorded the fluorescence ratio of the cytosolic iNap sensor (**Figure 2.7A-C**). We expected that the fluorescence ratio of the cytosolic sensor would be maintained under low perturbation and change only at high perturbation. As predicted, addition of D-alanine below 15 mM did not alter the fluorescence readout compared to that of the control. Interestingly, even at 50 mM of D-alanine concentration, the fluorescence readout remained robust (**Figure 2.7C)**. This experimental data suggested that NADPH was impermeable to mitochondrial membrane as previously reported [34], and the cytosolic NADPH pool would not be depleted even under high production of mitochondrial H_2O_2. Additionally, we measured whether the DAAO-mediated H_2O_2 production decreased the cellular NADPH pool using the luminescence-based Promega NADP/NADPH-Glo assay, and observed that the cellular NADPH/$NADP^+$ decreased by up to 32 % upon generation of mitochondrial H_2O_2 **(Figure 2.6C-E)**.

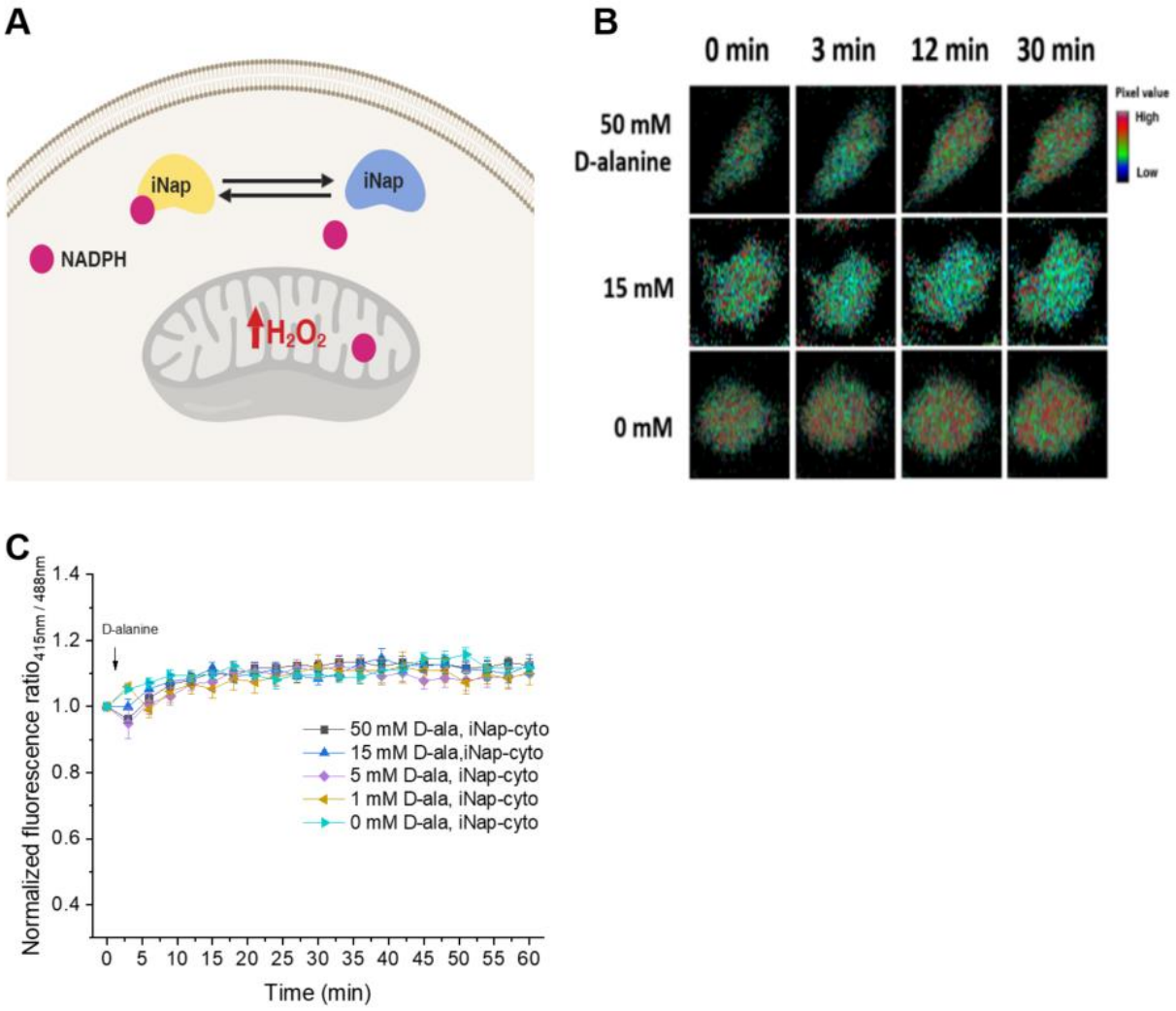

Figure 2.7. Cytosolic NADPH levels were maintained under varying mitochondrial $\mathbf{H_2O_2}$ generation. (A) Schematics representing a system with H_2O_2 generator in mitochondria and iNap-cyto. (B) Time-dependent change of a ratiometric fluorescence signal of cytosolic iNap sensor in response to D-alanine treatment. (C) Normalized fluorescence ratio (R) was recorded with D-alanine ranging from 0 to 50 mM. Values represent mean of individual cells from at least two independent experiments $\pm$ SEM. (n = 21, 11, 7, 8, 23 cells from experiments with 50 to 0 mM D-alanine. A two-tailed student's *t*-test was used for statistical analysis with p-values < 0.05 considered statistically significant ($* \ P < 0.05$, $*** \ P < 0.001$,$*** \ P < 0.0001$).

2.4.3. Production of cytosolic H_2O_2 decreases cytosolic NADPH first followed by mitochondrial NADPH pool

As the fluorescence ratio of the cytosolic sensor was maintained under mitochondrial production of H_2O_2, we investigated whether the production of excessive H_2O_2 in the cytoplasm would in turn affect the mitochondrial NADPH pool. In this converse experiment, we generated cytosolic H_2O_2 via DAAO-cyto by adding 0 to 50 mM of D-alanine, and monitored the R or R' of iNap-cyto and iNap-mito in parallel (**Figure 2.8A and D**). When cells were challenged with D-alanine below 5 mM concentration, the fluorescence ratio of the iNap-cyto remained stable compared to that of control (**Figure 2.8B**). As the concentration increased above 10 mM of D-alanine, the fluorescence ratio started to decrease over 60 minutes, with 50 mM D-alanine lowering the fluorescence signal approximately 60 % after 60 minutes (**Figure 2.8B and C**).

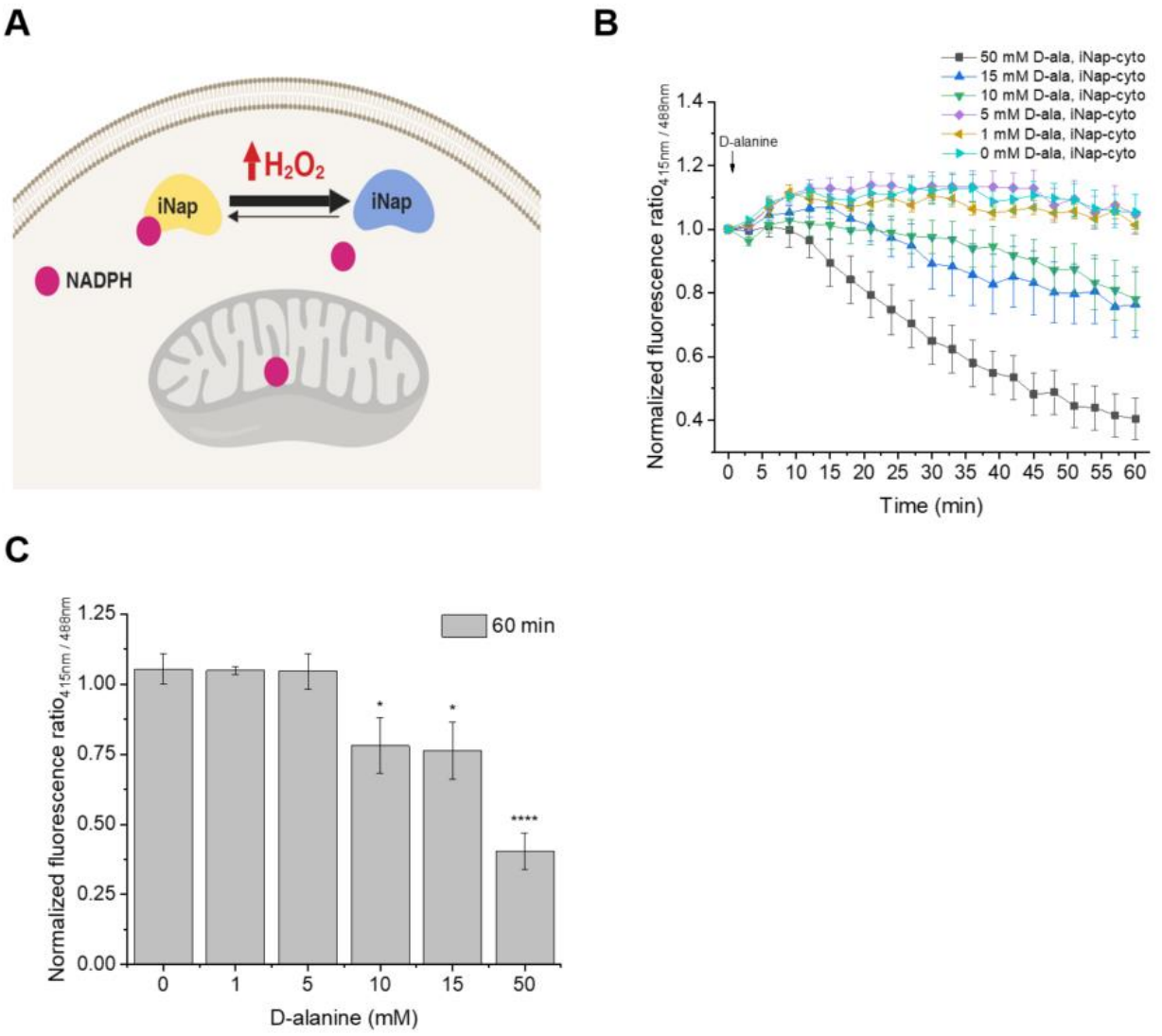

Figure 2.8. Production of cytosolic $\mathbf{H_2O_2}$ decreased cytosolic NADPH first followed by mitochondrial NADPH pool. (A) Schematic of cytosolic H_2O_2 generation by DAAO expressed in cytosol and NADPH measured by the cytosolic iNap sensor. (B) Normalized R from iNap-cyto was monitored after stimulating cells with 6 different concentrations of D-alanine. Values were recorded at every 3 minutes for an hour and represent mean of individual cells from at least two independent experiments ± SEM. (n = 10, 14, 14, 9, 9, 9 cells from experiments with 50 to 0 mM D-alanine). (C) Normalized R from iNap-cyto was measured at 60 minutes. A two-tailed student's *t*-test was used for statistical analysis with p-values $<$ 0.05 considered statistically significant ($* \ P < 0.05$, $*** \ P < 0.001$,$**** \ P < 0.0001$).

The rate of decrease was higher with increasing dose above 10 mM. Unlike immediate decreases of mitochondrial NADPH pool as observed by iNap-mito, iNap-cyto revealed that the reduction of signal was delayed after 6 minutes under 50 mM D-alanine perturbation. In parallel, we monitored the change of fluorescence readout of iNap-mito under production of cytosolic H_2O_2 (**Figure 2.9Aand B**). Interestingly, unlike the response of cytosolic iNap where the normalized fluorescence ratio remained robust throughout different mitochondrial perturbations, the normalized fluorescence readout of the iNap-mito remained relatively constant throughout the cytosolic perturbation, except for a 50 mM D-alanine perturbation (**Figure 2.9B)**.

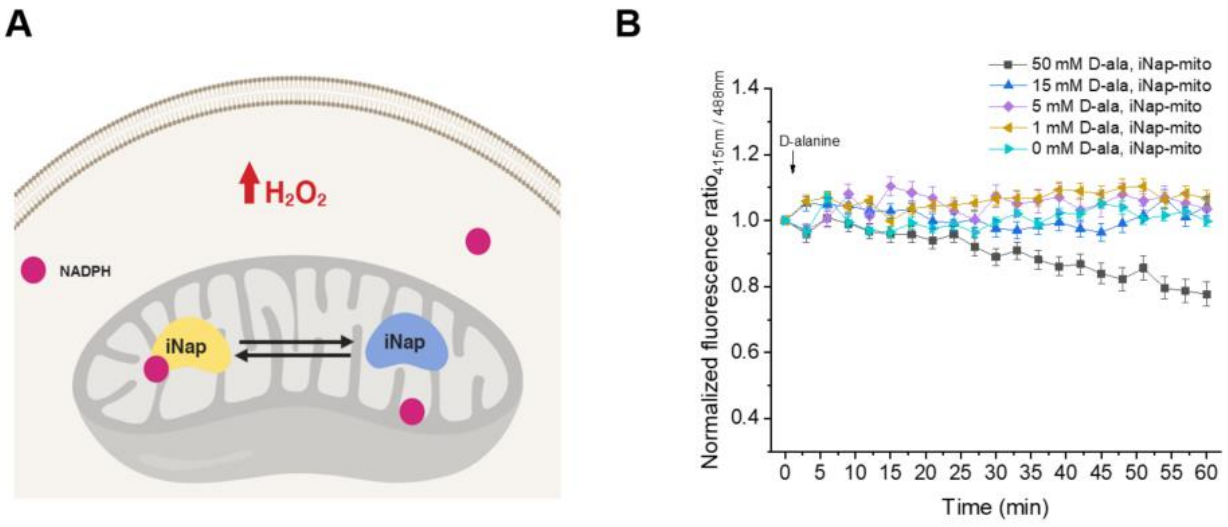

Figure 2.9. (**A**) Schematic depicting the generation of cytosolic H_2 O_2 by DAAO expressed in cytosol and the mitochondrial NADPH pools measured by iNap-mito. (**B**) Normalized R' from iNap-mito was monitored after stimulating cells with a range of D-alanine concentrations. Values were recorded every 3 minutes for an hour and represent mean of individual cells from at least two independent experiments± SEM. (n = 39, 42, 12, 28, 17 cells from experiments with 50 to 0 mM D-alanine).

2.5. Discussion

Here, we explored the distribution and dynamics of compartmental NADPH pools while systemically modulating generation rates of H_2O_2 in mitochondria. Previous work to assess mitochondrial NADPH metabolism was undertaken with deuterium-labeled tracers and an expression of a reporter system of 2-HG. These tracers were useful in examining directionality of pathways that are present in both the cytoplasm and mitochondria, but a direct measurement of compartmentalized NADPH pools and evaluation of NADPH dynamics in living cells was still lacking.

Imaging experiments revealed that the mitochondrial NADPH pool was sensitive to both mitochondrial and cytosolic oxidative stress whereas the cytosolic NADPH pool was minimally perturbed by the mitochondrial oxidative stress. Unlike the cytosolic NADPH pool that remained robust under mitochondrial oxidative stress, we observed the mitochondrial NADPH pool started to decrease under cytosolic oxidative stress. This could be due to diffusion of H_2O_2 via aquaporin or depolarization of mitochondrial membrane, causing a decrease of mitochondrial NADPH pools upon excessive production of cytosolic H_2O_2. Additionally, mitochondria lacked G6PD and 6PGD enzymes, which rapidly regenerate cytosolic NADPH via an allosteric regulation mechanism and were known to be major contributors of cytosolic NADPH pool. Thus, the regeneration of mitochondrial NADPH could be slower than the cytosolic production rate, resulting in a greater impact of compartment-specific oxidative stress to the mitochondrial NADPH pool. Our work was based on Hela cells and this approach could be applicable to other cancer cell lines. The extent of NADPH buffering capacity and its influence on metabolic processes upon oxidative stress on different cancer cell lines remains to be investigated.

2.6. References

1. Esposito, L. A., Melov, S., Panov, A., Cottrell, B. A. & Wallace, D. C. Mitochondrial disease in mouse results in increased oxidative stress. *Proc. Natl. Acad. Sci.* **96**, 4820–4825 (1999).

2. Kang, J. & Pervaiz, S. Mitochondria: Redox Metabolism and Dysfunction. *Biochem. Res. Int.* **2012**, 1–14 (2012).

3. Shadel, G. S. & Horvath, T. L. Mitochondrial ROS Signaling in Organismal Homeostasis. *Cell* **163**, 560–569 (2015).

4. Kohen, R. & Nyska, A. Oxidation of Biological Systems: Oxidative Stress Phenomena, Antioxidants, Redox Reactions, and Methods for Their Quantification. *Toxicol. Pathol.* **30**, 470 ou pag cap. 150–180 (2002).

5. Wallace, D. C. A mitochondrial paradigm of metabolic and degenerative diseases, aging, and cancer: a dawn for evolutionary medicine. *Annu. Rev. Genet.* **39**, 359–407 (2005).

6. Reuter, S., Gupta, S. C., Chaturvedi, M. M. & Aggarwal, B. B. Oxidative stress, inflammation, and cancer: How are they linked? *Free Radic. Biol. Med.* **49**, 1603–1616 (2010).

7. Gilgun-Sherki, Y., Melamed, E. & Offen, D. Oxidative stress induced-neurodegenerative diseases: The need for antioxidants that penetrate the blood brain barrier. *Neuropharmacology* **40**, 959–975 (2001).

8. Marnett, L. J. Oxyradicals and DNA damage. *Carcinogenesis* **21**, 361–370 (2000).

9. Paul D. Ray, Bo-Wen Huang, Y. T. Reactive oxygen species (ROS) homeostasis and redox regulation in cellular signaling. *Cell. Signal.* **24**, 981–990 (2012).

10. Lennicke, C., Rahn, J., Lichtenfels, R., Wessjohann, L. A. & Seliger, B. Hydrogen peroxide - Production, fate and role in redox signaling of tumor cells. *Cell Commun. Signal.* **13**, 1–19 (2015).

11. Gough, D. R. & Cotter, T. G. Hydrogen peroxide: a Jekyll and Hyde signalling molecule. *Cell Death Dis.* **2**, e213 (2011).

12. Ying, W. NAD^+/NADH and $NADP^+$/NADPH in Cellular Functions and Cell Death: Regulation and Biological Consequences. *Antioxid. Redox Signal.* **10**, 179–206 (2008).

13. Pollak, N., Dölle, C. & Ziegler, M. The power to reduce: pyridine nucleotides – small molecules with a multitude of functions. *Biochem. J.* **402**, 205–218 (2007).

14. Losman, J. A. & Kaelin, W. G. What a difference a hydroxyl makes: Mutant IDH, (R)-2-hydroxyglutarate, and cancer. *Genes Dev.* **27**, 836–852 (2013).

15. Cairns, R. A. & Mak, T. W. Oncogenic isocitrate dehydrogenase mutations: Mechanisms, models, and clinical opportunities. *Cancer Discov.* **3**, 730–741 (2013).

16. Cox, A. G., Winterbourn, C. C. & Hampton, M. B. Mitochondrial peroxiredoxin involvement in antioxidant defence and redox signalling. *Biochem. J.* **425**, 313–325 (2010).

17. Langford, T. F., Huang, B. K., Lim, J. B., Moon, S. J. & Sikes, H. D. Monitoring the action of redox-directed cancer therapeutics using a human peroxiredoxin-2-based probe. *Nat. Commun.* **9**, 1–12 (2018).

18. Lundberg, M., Fernandes, A. P., Kumar, S. & Holmgren, A. Cellular and plasma levels of human glutaredoxin 1 and 2 detected by sensitive ELISA systems. *Biochem. Biophys. Res. Commun.* **319**, 801–809 (2004).

19. Winterbourn, C. C. & Metodiewa, D. Reactivity of biologically important thiol compounds with superoxide and hydrogen peroxide. *Free Radic. Biol. Med.* **27**, 322–328 (1999).

20. Kuehne, A. *et al.* Acute Activation of Oxidative Pentose Phosphate Pathway as First-Line Response to Oxidative Stress in Human Skin Cells. *Mol. Cell* **59**, 359–371 (2015).

21. Heiden, M. G. Vander & Deberardinis, R. J. Review Understanding the Intersections between Metabolism and Cancer Biology. *Cell* **168**, 657–669 (2017).

22. Dong, W., Keibler, M. A. & Stephanopoulos, G. Review of metabolic pathways activated in cancer cells as determined through isotopic labeling and network analysis. *Metab. Eng.* **43**, 113–124 (2017).

23. Fan, J. *et al.* Quantitative flux analysis reveals folate-dependent NADPH production. *Nature* **510**, 298–302 (2014).

24. Nickel, A. G. *et al.* Reversal of mitochondrial transhydrogenase causes oxidative stress in heart failure. *Cell Metab.* **22**, 472–484 (2015).

25. Dey, S., Sidor, A. & O'Rourke, B. Compartment-specific control of reactive oxygen species scavenging by antioxidant pathway enzymes. *J. Biol. Chem.* **291**, 11185–11197 (2016).

26. Veech, R. L., Eggleston, L. V & Krebs, H. a. The redox state of free nicotinamide-adenine dinucleotide phosphate in the cytoplasm of rat liver. *Biochem. J.* **115**, 609–619 (1969).

27. Lu, W., Wang, L., Chen, L., Hui, S. & Rabinowitz, J. D. Extraction and quantitation of NAD(P)(H). *Antioxid. Redox Signal.* **00**, ars.2017.7014 (2017).

28. Tao, R. *et al.* Genetically encoded fluorescent sensors reveal dynamic regulation of NADPH metabolism. *Nat. Methods* **14**, 720–728 (2017).

29. Stein, K. T., Moon, S. J. & Sikes, H. D. Mitochondrial H_2O_2 generation using a tunable chemogenetic tool to perturb redox homeostasis in human cells and induce cell death. *ACS Synth. Biol.* **7**, acssynbio.8b00174 (2018).

30. Lu, W., Wang, L., Chen, L., Hui, S. & Rabinowitz, J. D. Extraction and Quantitation of Nicotinamide Adenine Dinucleotide Redox Cofactors. *Antioxidants Redox Signal.* **28**, 167–179 (2018).

31. Posakony, J., England, J. & Attardi, G. Mitochondrial growth and division during the cell cycle in Hela cells. **74**, 468–491 (1977).

32. Haskew-Layton, R. E. *et al.* Controlled enzymatic production of astrocytic hydrogen peroxide protects neurons from oxidative stress via an Nrf2-independent pathway. *Proc. Natl. Acad. Sci.* **107**, 17385–17390 (2010).

33. Huang, B. K., Stein, K. T. & Sikes, H. D. Modulating and Measuring Intracellular H_2O_2 Using Genetically Encoded Tools to Study Its Toxicity to Human Cells. *ACS Synth. Biol.* **5**, 1389–1395 (2016).

34. Nikiforov, A., Dölle, C., Niere, M. & Ziegler, M. Pathways and subcellular compartmentation of NAD biosynthesis in human cells: From entry of extracellular precursors to mitochondrial NAD generation. *J. Biol. Chem.* **286**, 21767–21778 (2011).

Chapter 3

Assessment of NADPH generation pathways using ^{13}C-glucose isotopic tracers under mitochondrial oxidative stress

This chapter is adapted from:

***Sun Jin Moon**, Wentao Dong, Greg Stephanopoulos and Hadley Sikes, Oxidative pentose phosphate pathway and glucose anaplerosis support maintenance of mitochondrial NADPH pool under mitochondrial oxidative stress, Bioengineering & Translational Medicine, 2020, 5 e10184 (2020).*

*Wentao Dong, **Sun Jin Moon**, Joanne K Kelleher, Gregory Stephanopoulos, Dissecting Mammalian Cell Metabolism through 13C- and 2H-Isotope Tracing: Interpretations at the Molecular and Systems Levels, Ind. Eng. Chem. Res. 59, 6, 2593–2610 (2020).*

Sun Jin Moon contributed to NADPH generation pathway section

3.1. Abstract

Cellular oxidative stress was known to activate the pentose phosphate to regenerate NADPH. However, it was unclear how cells maintained mitochondrial and cytosolic NADPH under mitochondrial oxidative stress. In the previous chapter, I demonstrated the dynamics of mitochondrial and cytosolic NADPH levels when cells were challenged with mitochondrial oxidative stress. In this chapter, I used ^{13}C-glucose isotopic tracers to assess NADPH generation pathways, particularly focusing on TCA cycle metabolites labeling patterns and pentose phosphate pathway and. First, I reviewed isotopic tracers that were available to measure NADPH generation pathway activities and interpreted the labeling data based on atomic transitions of isotopes. Based on these studies, I investigated the TCA cycle metabolic patterns and pentose phosphate pathways under mitochondrial oxidative stress.

3.2. Introduction

Over the past decades, stable isotopes such as ^{13}C, ^{2}H, ^{15}N and $^{17/18}$O have been developed and widely used in studying metabolism[1,2]. For instance, ^{13}C-isotopic tracers have been used to investigate central carbon metabolism that include glycolysis, TCA cycle, and pentose phosphate pathway. On the other hand, ^{2}H has been used to probe the hydride transfer related metabolic pathways which is particularly useful in examination of NAD(P)H generation pathways. ^{15}N has been incorporated in nitrogen metabolism which is typically related to amino acids metabolism. Lastly, $^{17/18}$O has been used for oxygen metabolism. Altogether, application of these tracers provide dynamic pictures of metabolic networks instead of a simple static view.

Isotopic tracers can be simply utilized to validate certain substrates are patriated in specific metabolic pathways. For instance, cells that catabolize [U-^{13}C]glucose show a labeled ribose 5 phosphate (R5P) which indicate that glucose can be used to make R5P, which is in the pentose phosphate pathway and an important precursor for nucleotide synthesis. A more advanced application involves dissecting the labeling patterns of the catabolized metabolites and compare the labeling patterns, or mass isotopomer distribution (MID). For instance, when cells catabolize [U-^{13}C]glucose, the oxaloacetate (OAA) may have M+2 or M+3 labeled states. With a prior knowledge that pyruvate can be reduced through pyruvate carboxylase (PC), M+3 oxaloacetate shows the usage of PC reaction. This can be compared with M+2 OAA, which is generated through TCA cycle. Therefore, by showing a relative ratio between M+2 and M+3, one can determine the relative usage of pyruvate to carboxylation reaction or catabolic reaction.

For assessment of NADPH generation pathways, deuterium labeled tracers has been most effective. It is because NADPH dependent redox reactions involve a transfer of hydride atoms (H-). Therefore, probing the hydride transfer will provide a direct evidence of NADPH reaction activity. However, one needs to consider the kinetic effects occurring by the deuterium[3]. Additionally, costs of deuterium tracers are high, limiting its accessibility to common biology labs. To overcome this limitation, ^{13}C tracers can also be used. Although heavy carbons are not transferred in NADPH dehydrogenase reactions, these tracers are still capable of providing some of NADPH generation pathway activities. For instance, [1,2-$^{13}C_2$]glucose provides relative metabolic pathway activities between glycolysis and oxPPP. Heavy carbons lose as CO_2 in the oxPPP, allowing one to detect the pathway differences. For [U-$^{13}C_6$]glucose, it provides labeling patterns of TCA cycle metabolites. Many of these metabolites are essentially substrates

of NADPH generating reactions. Therefore, change of labeling patterns may indirectly indicate NADPH generation capacity.

Here, I evaluate whether activities of NADPH generation pathways are altered in response to changes in NADPH pools caused by increasing mitochondrial H_2O_2. Using [U-$^{13}C_6$]glucose and [1,2-$^{13}C_2$]glucose, I examine the labeling patterns of TCA cycle metabolites and the activity of the pentose phosphate pathway (PPP). Investigation of TCA cycle metabolite labeling patterns are important, because in mitochondria, TCA cycle metabolites such as citrate and malate can be used to regenerate NADPH via IDH2 and malic enzymes (ME3), respectively. Additionally, nicotinamide nucleotide transhydrogenase (NNT) is also located in the mitochondrial membrane, maintaining mitochondrial NADPH/$NADP^+$ by converting $NADP^+$ to NADPH at the expense of NADH [4]. The PPP, occurring in cytoplasm, is known as the major site of NADPH production via glucose 6-phosphate dehydrogenase (G6PD) and 6-phosphogluoconate dehydrogenase (6GPD), and increased activity of the PPP has been identified as a key characteristic of cancer metabolism [5,6].

3.2.1. ^{2}H- tracers for probing NADPH metabolic pathways

Deuterium (^{2}H) isotopic tracers have been widely used for measurement of the activities of NAD(P)H production pathways, fatty acid, and protein synthesis in mammalian cells (Fan et al., 2014; Grassian et al., 2014; Jang et al., 2018; Lewis et al., 2014; Liu et al., 2016; Zhang et al., 2017). As pyridine nucleotides such as NAD(H) or NADP(H) serve as electron carriers by transferring electron in the form of hydride ion (H^-), deuterium isotopic tracers have become

particularly useful in tacking the flow of electrons involved in redox reactions, particularly NAD(P) dependent dehydrogenase reactions (**Figure 3.1**) [11,12].

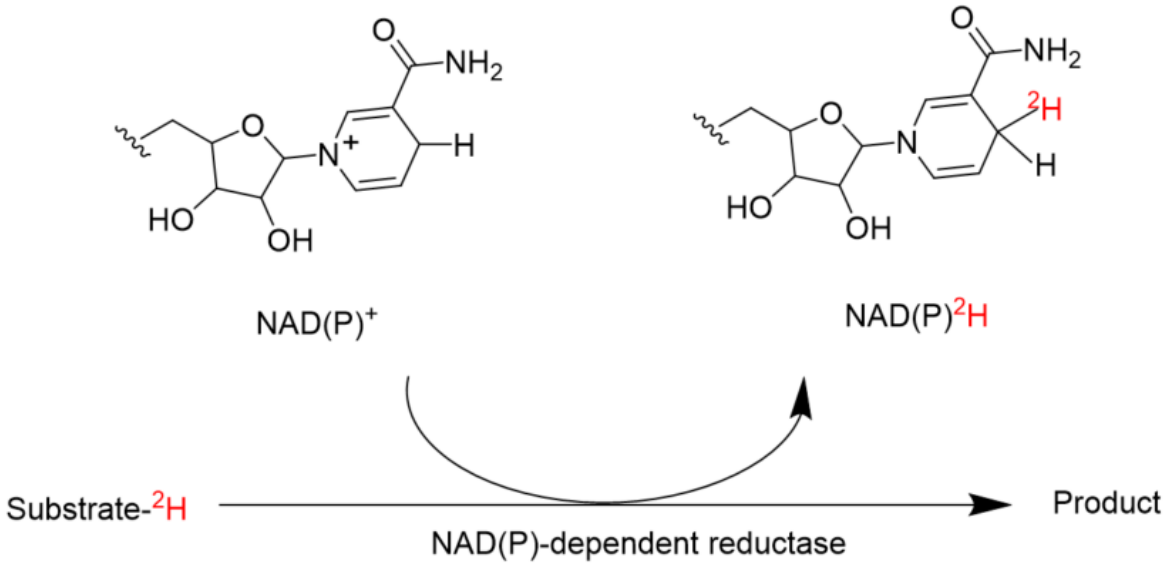

Figure 3.1. Deuterium isotopic tracers for measurement of pathway activities of NAD(P)H generation, fatty acid, and protein synthesis. Deuterium, labeled hydride ion, is transferred to NAD(P) via NAD(P) dependent reductases, making a deuterium labeled NAD(P)H. Redox reactions occur in the fourth position of the nicotinamide group, where the hydride ion acts as a nucleophile. Oxidized form of NADPH serves as an hydride acceptor while the reduced form serves as a donor.

^{2}H-glucose tracers have been used to measure pathway activities involved in generation of NADPH in oxidative pentose phosphate pathway [10]. For instance, 1-^{2}H-glucose tracer can monitor the extent of NADPH generation via the G6PD reaction step (Figure 9b) [5]. As G6P is converted to 6PG, the ^{2}H of 1-^{2}H-glucose is transferred to NADP+, yielding NADP^{2}H. The deuterium labeled NADPH can be subsequently measured using the LC/MS with mass-to-charge ratio shifting from 744 to 745 [5]. In addition, 3-^{2}H-glucose tracer is used to measure the activity of 6PGD, the third reaction step in the oxPPP that generates both NADPH and carbon dioxide (**Figure 3.2**) [3]. The kinetic isotope effects of these ^{2}H glucose tracers were shown minimal and

the labeling of deuterium to NADPH has been shown fast with half-time ($t_{1/2}$) approximately 5 minutes, making it feasible to observe changes in pathway activities in short time scale [3,5]. As a result, these two tracers are useful in assessing the contribution of the oxidative pentose phosphate pathway for production of NADPH in mammalian cells.

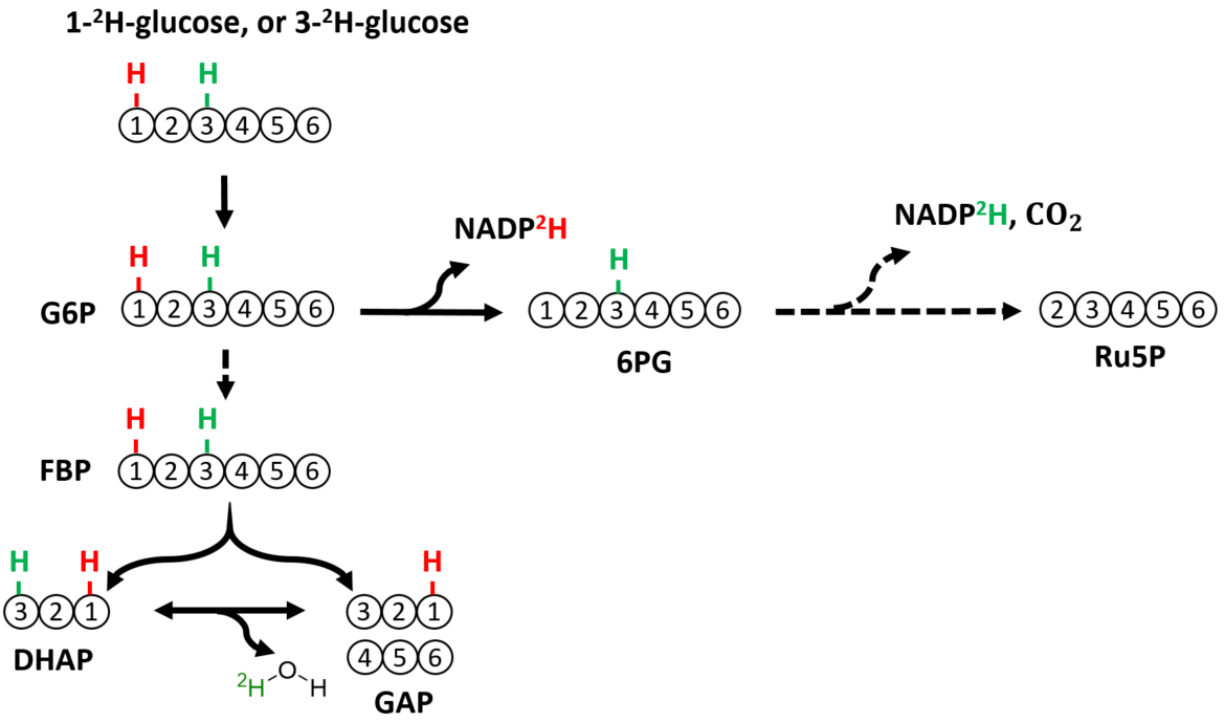

Figure 3.2. [1-^{2}H]glucose and [3-^{2}H]glucose are used to label NADPH in the oxidative PP pathway and the upper part of glycolysis. Hydrogen in red indicates deuterium placed in the first carbon of glucose. Hydrogen in green represents deuterium replaced in the third carbon of glucose. Deuterium positioned at the third carbon in DHAP can be lost at the TPI reaction step.

When ^{2}H is labeled to the 4th position of glucose, or 4-^{2}H-glucose, significant labeling has been observed to central carbon metabolites such as lactate, malate, and glycerol-3-phosphate (Glyc-3P), through reactions that use NADH as a cofactor (**Figure 3.3**) [3]. Thus, 4-^{2}H-glucose has been designed as a tracer for NADH-related metabolism.

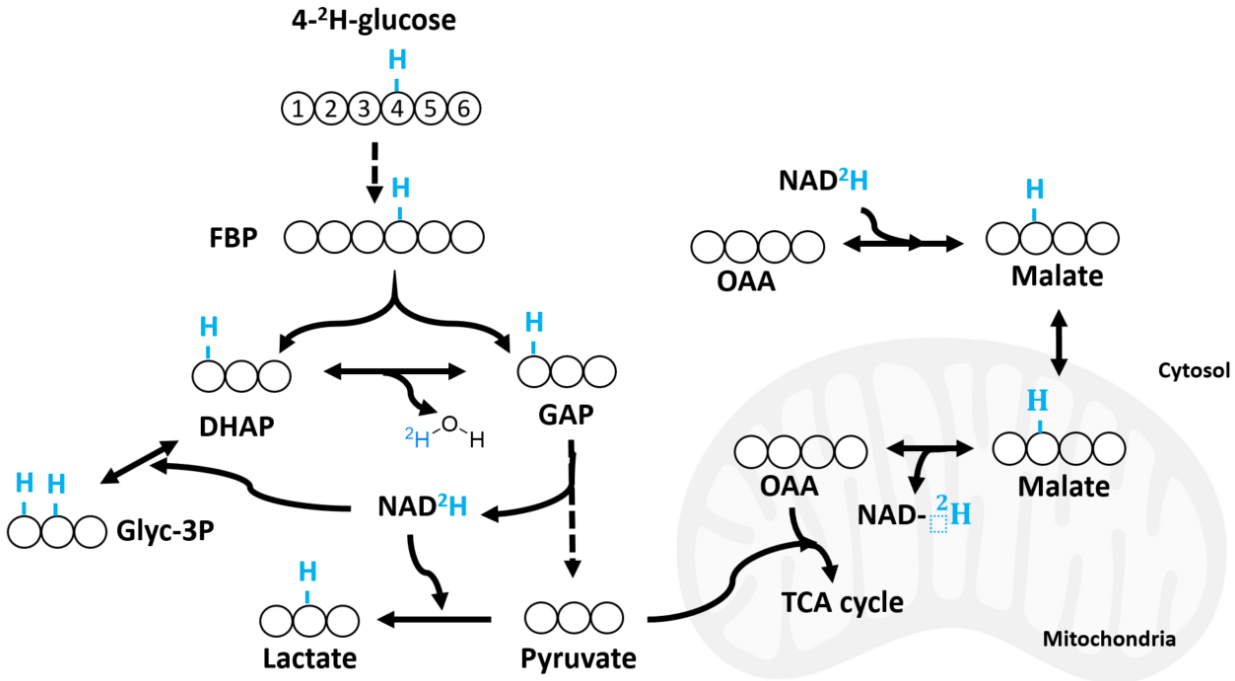

Figure 3.3. [4-^{2}H]glucose is used to label NADH. Deuterium labeled NADH, generated by GAPDH, is incorporated into glycolytic metabolites such as lactate, malate and Glyc-3P via NAD-dependent reductases such as LDH and MDH.

Along with the ^{2}H glucose tracers, 3,3-$^{2}H_2$-serine, 2,3,3-$^{2}H_3$-serine and or 2,2-$^{2}H_2$-glycine tracers have been incorporated to investigate the metabolism through serine hydroxymethyltransferase (SHMT) and methylenetetrahydrofolate dehydrogenase (MTHFD) (**Figure 3.4**) [3]. ^{2}H of these tracers can be transferred to either cytosolic or mitochondrial NAD(P)H, characterizing the directionality of serine/glycine metabolism in two compartments along with a 2-HG reporter system [3].

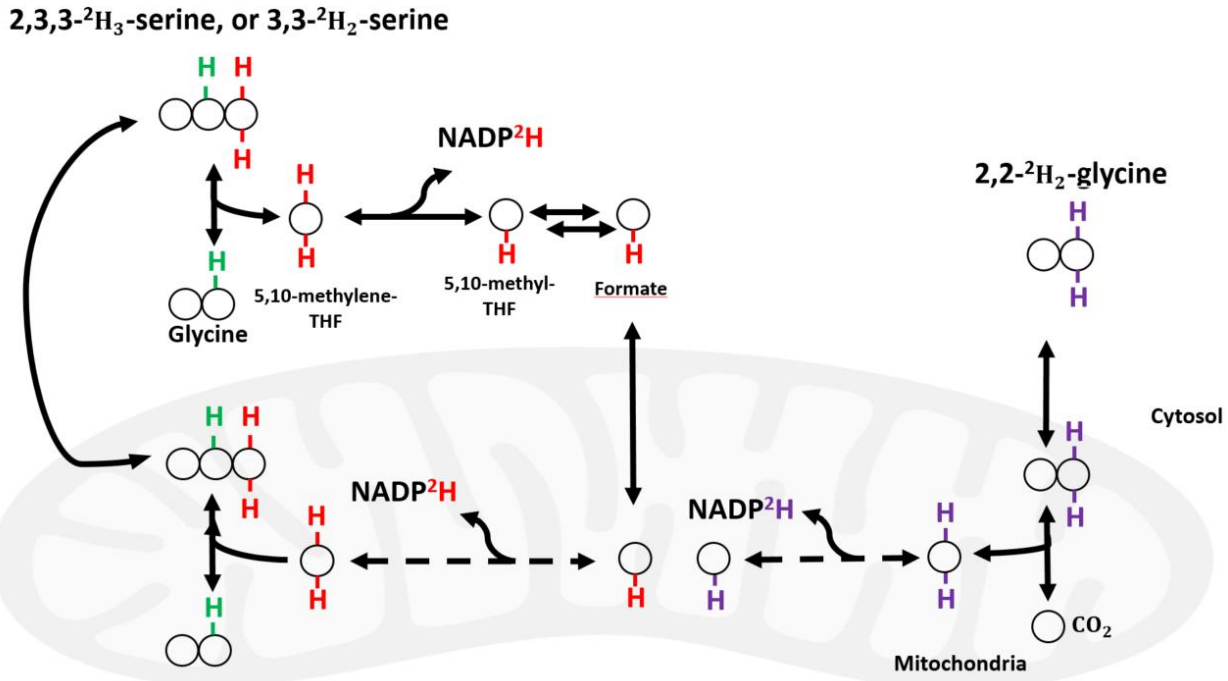

Figure 3.4. [2,3,3-^{2}H]serine, [3,3-^{2}H]serine, and [2,2-^{2}H]glycine are used to label NADPH in cytosol and mitochondria. 2,3,3-^{2}H-serine is converted to one deuterium labeled glycine along with two deuterium labeled 5,10-methyl-THF via SHMT. The one carbon unit subsequently undergoes a series of reactions to a formate, in which deuterium is transferred to NADPH via MTFHD. 2-2-^{2}H –glycine is cleaved to carbon dioxide and two deuterium labeled 5,10-methyl-THF, whose deuterium is transferred to NADPH via MTFHD.

2,2,3,3-^{2}H$_4$-dimethyl succinate has recently been designed for evaluation of malic enzyme (ME) dependent NADPH production pathway in adipocytes (**Figure 3.5**) [7]. As fatty acid synthesis requires an ample supply of reducing equivalents such as NADPH, the labeling patterns of fatty acid such as palmitate can be also examined using 2,2,3,3-^{2}H$_4$-dimethyl succinate.

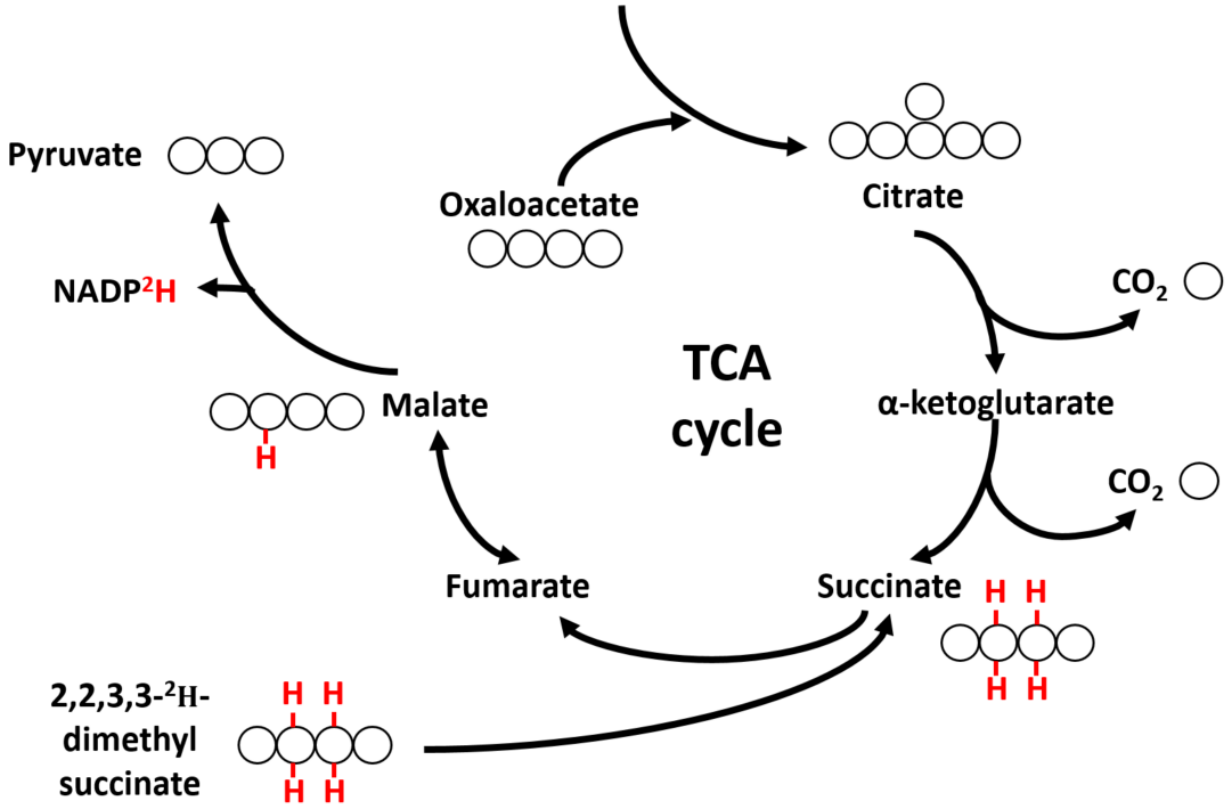

Figure 3.5. [2,2,3,3-^{2}H]4-dimethyl succinate for NADPH via malic enzyme.

Additionally, deuterium oxide ($^{2}H_2O$) has been utilized for examination of de novo fatty acid synthesis and of protein synthesis (**Figure 3.6**). Lee at al. measured the extent of deuterium incorporated in synthesis of fatty acids of nervous and liver tissues by feeding rats with $^{2}H_2O$, and found $t_{1/2}$ of newly synthesized lipids from nervous tissues to be 5 to 28 days, which turned out slower than that of liver ($t_{1/2}$ <4 days) [13]. Recently, Zhang et al. revealed that hydrogen of fatty acids could be directly transferred from solvent ($^{2}H_2O$) along with NADPH [9]. In regards to the measurements of protein synthesis *in vivo*, Busch et al. utilized $^{2}H_2O$ and examined MIDs of newly made proteins such as alanine or leucine, whose hydrogen was labeled by ^{2}H transfer from $^{2}H_2O$.

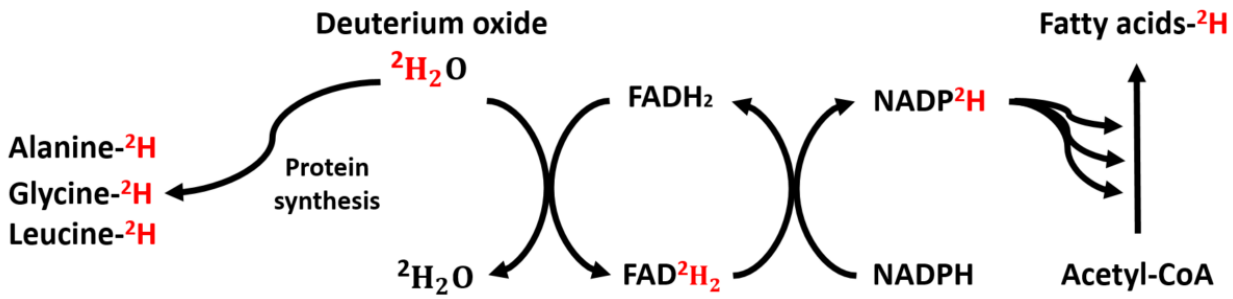

Figure 3.6. Deuterium oxide (^2H_2O) is used to examine relative pathway strengths of de novo fatty acid and protein synthesis. Hydride from ^2H_2O is transferred to NADPH through hydride shuttling of FADH2. Deuterium labeled NADPH is incorporated into the fatty acid synthesis pathways. Similarly, newly synthesized proteins such as alanine, glycine, and leucine, incorporated deuterium from ^2H_2O tracers.

3.2.2. ^{13}C- and ^{14}C isotopic for probing NADPH pathways

^{13}C- and ^{14}C based tracers are more stable than ^2H- based tracers and less prone to oxidation during extraction steps, as well as potential complication by carbon scrambling via reactions in non-oxidative pentose pathway is negligible[5,7]. For measurement of oxidative pentose phosphate pathway, [1-^{14}C]glucose has been used to measure the oxidative pentose phosphate pathway. [1-^{14}C]glucose will lose labeled carbon via oxPPP. Another tracer is [1,2-^{13}C]glucose tracer. As the tracer is catabolized through the oxPPP, M+1 lactate will be generated, whereas M+2 lactate will be produced if the tracer is catabolized through glycolysis. Therefore, by takin a ratio between M+1 and M+2 lactates, the relative pathway activities can be estimated.

[U-^{13}C]serine and [3-^{14}C]serine have been also used to estimate the folate metabolic pathways, in which NADPH can be generated in cytosol or mitochondria through methylenetetrahydrofolate dehydrogenase 1 (MTHFD1) or MTHFD2 reactions. Lastly, [U-^{13}C]glucose tracers are also used to probe the central carbon metabolic pathway activities. When the tracer is fully catabolized through TCA cycle, the TCA cycle metabolites will have M+2

labeling patterns. Cycling of TCA will generate M+4 metabolites after one cycle. If the tracer is catabolized through pyruvate carboxylation, metabolites will be labeled with M+3.

3.3. Materials and Methods

3.3.1. Cell culturing and isotope labeling experiments.

For isotopic tracer labeling experiments, 1.75×10^5 cells were seeded onto 6 well plates with 2 mL of DMEM (Lonzo, 12001-568) containing 10% dialyzed FBS (ATCC 30-2020) and 6 μg/mL puromycin (Sigma), and cultured for two days. The cells were transiently transfected with 2 μg of DAAO-mito and 4 μL of Lipofectamine 2000 following the manufacturer's protocol. For isotopic labeling experiments, glucose-free RPMI (Thermofisher, 11879020) was supplemented to a total 11.1 mM of 100% composition [1,2-$^{13}C_2$]glucose (Cambridge Isotope Labs) or [U-$^{13}C_6$]glucose (Cambridge Isotope Labs). After replacement of the culture media to the RPMI media with isotopic tracers, the plates were placed in humidified CO_2 incubator at 37 ºC for 2 hours before performing experiments.

3.3.2. Metabolite extractions and GC/MS analysis.

Extraction and analysis methods were followed as previously described [14]. At 70 – 80% confluency, media was aspirated and intracellular metabolites were quenched with -20 °C methanol. Internal standards were added and cells were scraped from the well and resuspended in the centrifuge tube. -20 °C chloroform was added, centrifuged at a max speed in 4 °C. The polar phase and nonpolar phase solvents were obtained in separate tube, and the polar phase solvents were dried until completely evaporated. The polar metabolites were derivatized by

addition of Methoxyamine in pyridine (MOX) at 40 °C for 1.5 hour and *tert*-butyldimethylchlorosilane (TBDMS) was subsequently added and dried at 60 °C for 1 hour. The derivatized samples were injected on the GC/MS. GC/MS analysis was complete using an Agilent 6890 GC connected with a 30-m DB-35MS capillary column with an Agilent 5975B MS operation under electron impact ionization at 70 eV. 1 μL of the sample was injected at 270 °C using helium as the carrier gas at a flow rate of 1 mL per min. The GC oven temperature was fixed at 100 °C for 3 minute and increased to 300 °C at 3.5 per min. The detector was set in scanning mode and the mass-to-charge ratio was measured in range of 100 – 1000 m/z.

3.4. Results

3.4.1. Mitochondrial oxidative stress activates glucose anaplerosis

We used a [U-$^{13}C_6$]glucose tracer to determine whether the excessive production of mitochondrial H_2O_2 led to a faster glucose oxidation rate and label TCA cycle metabolites labeling **(Figure 3.7)**. As the [U-$^{13}C_6$]glucose tracer was catabolized to pyruvate, the M+3 pyruvate was converted to either M+2 acetyl-CoA via pyruvate dehydrogenase complex (PDH) or M+3 oxaloacetate via pyruvate carboxylase (PC). Through PDH reaction, the M+2 acetyl-CoA entered the TCA cycle and two carbons of the TCA cycle metabolites were subsequently labeled as ^{13}C (**Figure 3.8A)** [1,15]. At high production rate of mitochondrial H_2O_2, we expected the glucose oxidation rate to increase so as to replenish TCA metabolites and support NADPH regeneration. Upon addition of 5 mM of D-alanine, the fractional change of M+2 metabolites was less than 10 %. However, stimulation with 25 mM of D-alanine increased the fraction of

M+2 metabolites by nearly 50 % compared to that of non-treated cells, suggesting a relative elevation of glucose oxidation via PDH reaction.

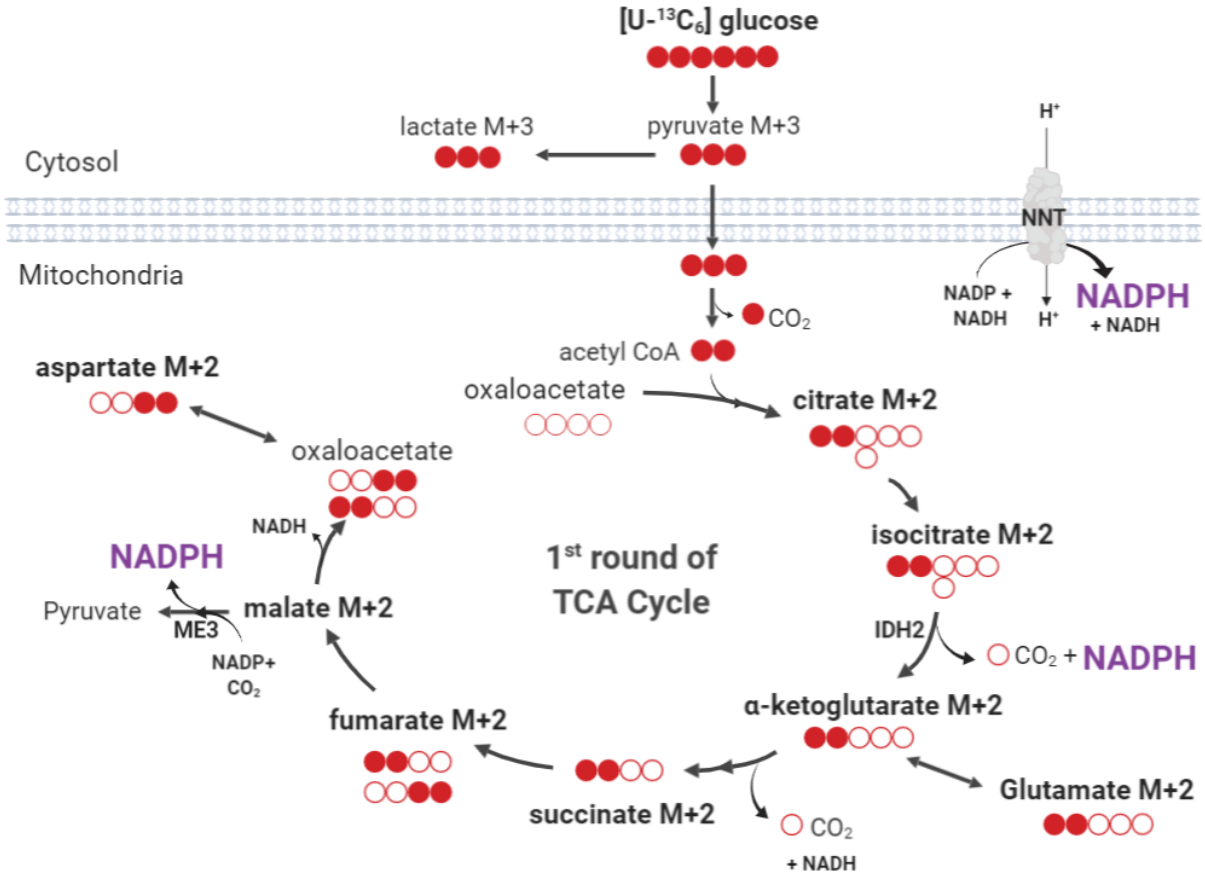

Figure 3.7. Carbon transition map demonstrating oxidation of $\mathbf{[U\text{-}^{13}C_6]glucose}$ tracer and the labeling pattern of TCA metabolites.

Similar to the labeling profiles of M+2 TCA metabolites, the addition of 25 mM of D-alanine increased the fraction of M+3 malate and fumarate (**Figure 3.8B)**. The increase of M+3 TCA metabolites was attributed to second and higher rounds of TCA cycling or to utilization of PC reaction (**Figure 3.9A-D)**. Heavily labeled mass isotopomers, such as M+5 citrate, M+5 α-ketoglutarate and M+4 succinate, represented the labeling pattern of the third and higher rounds of the TCA cycle. In a two-hour time scale, perturbed cells did not reach metabolic steady state and the fractions of M+4 or M+5 metabolites were shown less than 3% compared to the non-

treated cells whose fraction reached to 10 -15% after 24 hours (**Figure 3.9E-J)**. As a result, the increased fraction of M+2 and M+3 metabolites suggested that mitochondrial reactions derived from the TCA cycle metabolites could be used as the main source of mitochondrial NADPH pools.

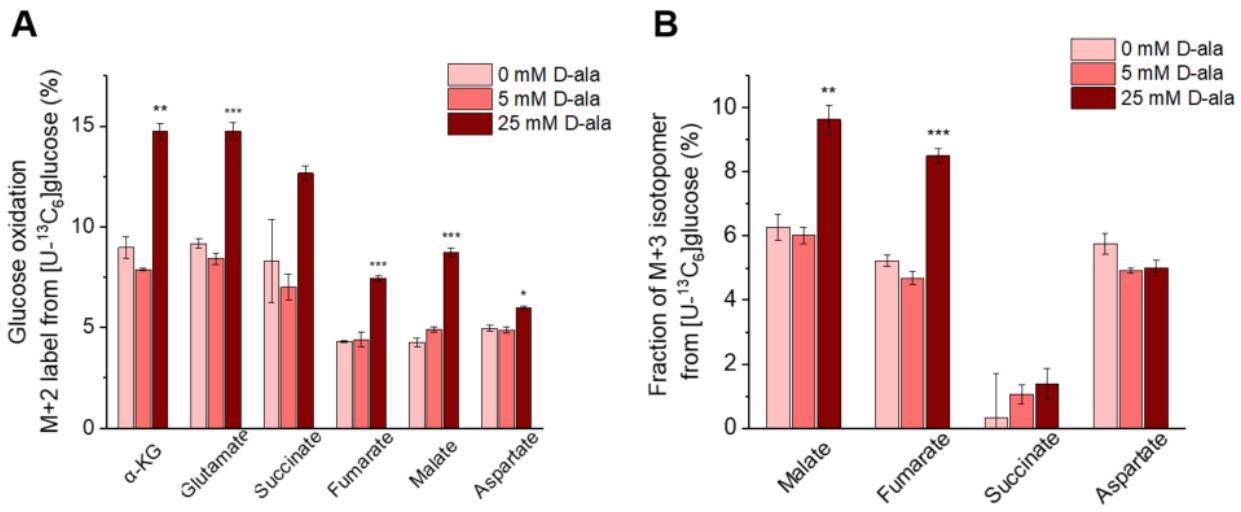

Figure 3.8. Increased mitochondrial oxidative stress induced glucose anaplerosis, increasing the labeling fractions of TCA cycle metabolites. (A) M+2 and (B) M+3 labeling patterns of the TCA cycle metabolites are depicted under different concentrations of D-alanine added to Hela cells that expressed mito-DAAO for 2 hr.

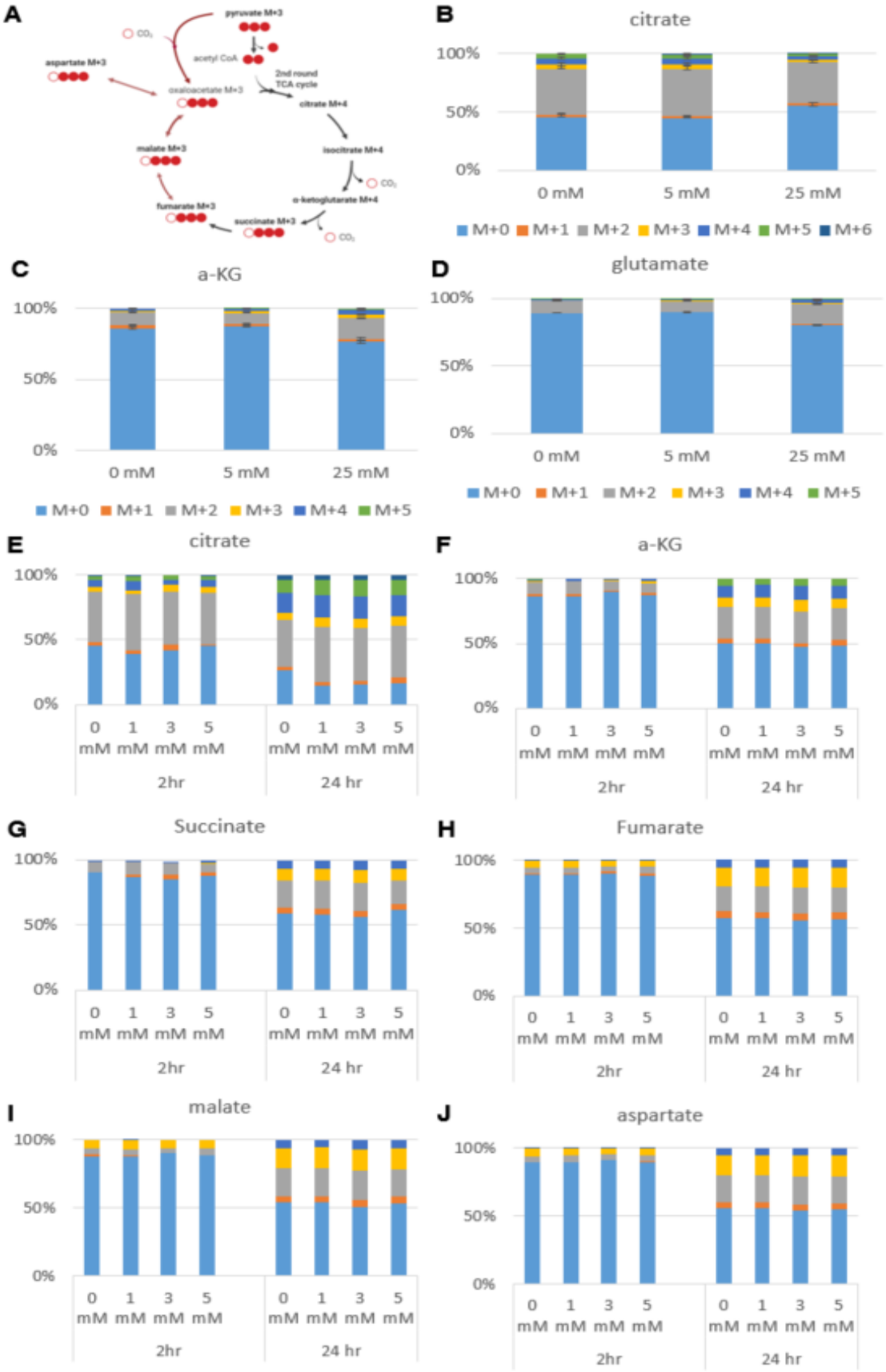
A
pyruvate M+3
acetyl CoA
aspartate M+3
oxaloacetate M+3
2nd round TCA cycle
citrate M+4
isocitrate M+4
α-ketoglutarate M+4
succinate M+3
fumarate M+3
malate M+3
B
citrate
100%
50%
0%
0 mM
5 mM
25 mM
M+0 M+1 M+2 M+3 M+4 M+5 M+6
C
a-KG
100%
50%
0%
0 mM
5 mM
25 mM
M+0 M+1 M+2 M+3 M+4 M+5
D
glutamate
100%
50%
0%
0 mM
5 mM
25 mM
M+0 M+1 M+2 M+3 M+4 M+5
E
citrate
100%
50%
0%
0 mM
1 mM
3 mM
5 mM
2hr
24 hr
F
a-KG
100%
50%
0%
0 mM
1 mM
3 mM
5 mM
2hr
24 hr
G
Succinate
100%
50%
0%
0 mM
1 mM
3 mM
5 mM
2hr
24 hr
H
Fumarate
100%
50%
0%
0 mM
1 mM
3 mM
5 mM
2hr
24 hr
I
malate
100%
50%
0%
0 mM
1 mM
3 mM
5 mM
2hr
24 hr
J
aspartate
100%
50%
0%
0 mM
1 mM
3 mM
5 mM
2hr
24 hr

Figure 3.9. (A) Schematics representing the utilization of pyruvate to oxaloacetate via pyruvate carboxylase from [U-$^{13}C_6$]glucose. When the 2nd TCA cycle undergoes from the first cycle of TCA, the M+4 metabolites would be observed. Citrate could be made as M+5 if the M+3 oxaloacetate is combined with M+2 acetyl-CoA. **(B)** The mass isotopomer distribution (MID) of citrate is depicted. The M+0 fraction is increase up to 10 % under 25 mM D-alanine perturbation, suggesting an effect of dilution introduced by non-labeled pyruvates from the degradation of DAAO. M+2 and M+3 citrate decreased from 39% to 35% and from 3% to 2 % due to the effect of dilution, respectively. In a two hour time-scale, the heavy labeling patterns were not achieved. **(C)** The MID of a-KG represents that M+4 labeling fraction was increased from 1 to 4 %. **(D)** The MID of glutamate demonstrated the same labeling pattern, suggesting these two metabolites were quickly equilibrated. Mass isotopomer distributions (MIDs) of the TCA cycle metabolites after 2 and 24 hours of incubation with 0, 1, 3 and 5 mM D-alanine in media containing [U-$^{13}C_6$]glucose. MIDs were determined based on **(E)** citrate **(F)** a-KG **(G)** succinate **(H)** fumarate **(I)** malate **(J)** aspartate.

DAAO system generated pyruvate as a byproduct and may interfere with central carbon metabolism. Upon the addition of 25 mM of D-alanine, the total citrate pool increased and the fraction of M+2 citrate was lower than that in the control cells. This could be due to the dilution effect of non-labeled citrate introduced by the DAAO-system and thus the fraction of M+2 citrate could be underestimated as evidenced by the increase of the fraction of M+0 citrate (**Figure 3.9B)**. However, under low production of H_2O_2 with D-alanine concentrations below 5 mM, the mass istopomer distribution pattern was similar across TCA cycle metabolites (**Figure 3.9E-J)**. The non-labeled pyruvate produced by DAAO could be catabolized to M+0 acetyl-CoA and participate in the TCA cycle by reacting with M+2 aspartate from the end of a first round of TCA cycle. In this case, M+1 isotopomers of α-KG, succinate, and fumarate would be expected to appear (**Figure 3.10)**. If DAAO produced a substantial amount of non-labeled pyruvate that subsequently fueled the TCA cycle, the fraction of M+1 isotopomers would be expected to increase with higher perturbation, because M+2 pyruvate derived from [U-$^{13}C_6$]glucose could not theoretically generate M+1 TCA cycle metabolites, assuming PDH as the major route of the

anaplerotic pathways and correcting contributions of naturally occurring isotopomers. However, the fraction of M+1 of all TCA cycle metabolites did not elevate throughout the perturbation, remained less than 3%, and were not statistically different from the control. Thus, these evidences suggest that DAAO-mediated pyruvate would minimally interfere the central carbon metabolism under low perturbation.

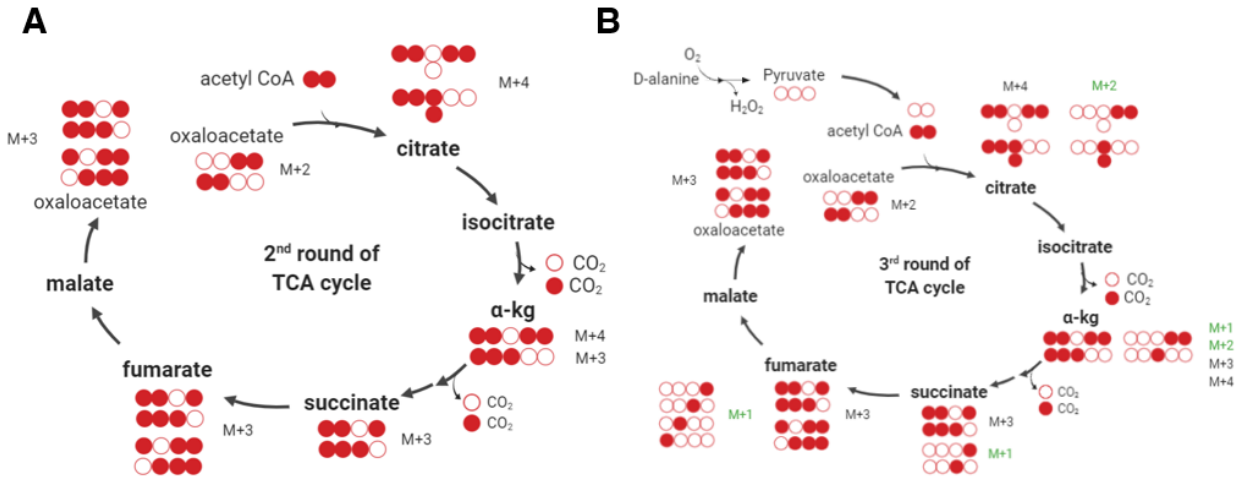

Figure 3.10. (A) Schematics representing the 2nd round of TCA cycle. As M+2 labeled oxaloacetate enters the 2nd round of TCA cycle, succinate, fumarate, and oxaloacetate can be M+3 at the end of the 2nd round of TCA cycle. **(B)** Schematics representing the 3rd round of TCA cycle with non-labeled pyruvate that can be introduced by the DAAO system. The green labeled mass isotopomer represented an artificial labeling pattern introduced by the non-labeled pyruvate. The black label represents the theoretical labeling pattern by [U-$^{13}C_6$]glucose. With the non-labeled acetyl-CoA, remaining TCA cycle metabolites were either M+1 or M+2 instead of M+3 or higher.

3.4.2. Mitochondrial oxidative stress activates pentose phosphate pathway

We further investigated whether the mitochondria-derived oxidative stress trigger NADPH generation pathways in cytosol. To address this question, we used a [1,2-$^{13}C_2$]glucose tracer and analyzed the relative pathway strength between glycolysis and the oxPP pathway [15–17]. When the [1,2-$^{13}C_2$]glucose tracer was converted to pyruvate through glycolysis, none or two carbons of pyruvate were labeled as ^{13}C. On the other hand, as the [1,2-$^{13}C_2$]glucose was catabolized

through the PP pathway, the first ^{13}C-labeled carbon was lost at the 6-phosphogluconate dehydrogenase reaction step along the 6GPD pathway, and thus only one was labeled, assuming the carbon shuffling and reductive pathway activity was minimal (**Figure 3.11)** [15]. As the pyruvate pool rapidly equilibrated with that of lactate, we used lactate labeling data as a surrogate of that of pyruvate. Since the M+0 lactate was a product from either glycolysis or the PP pathway, we calculated the fraction of M+1 or M+2 only. The fraction of M+1 lactate represented the utilization of the PP pathway, whereas that of M+2 lactate indicated the usage of glycolysis.

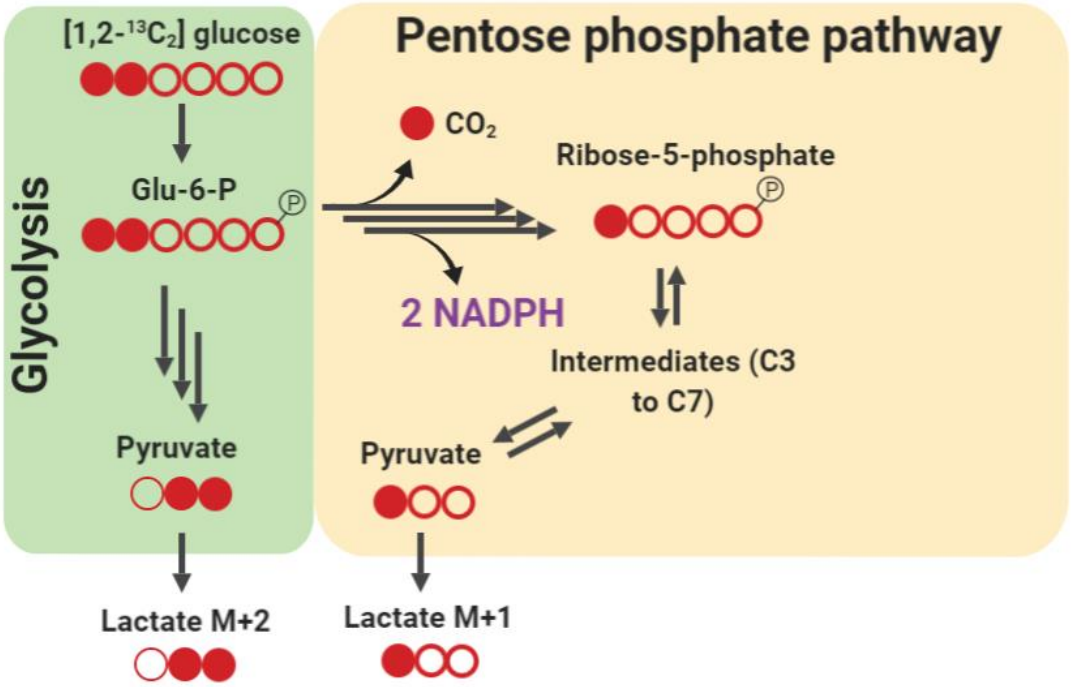

Figure 3.11. Schematic of the labeling pattern from $[1,2\text{-}^{13}C_2]$glucose isotope tracer for measurement of a relative pathway strength between glycolysis and the pentose phosphate pathway.

We hypothesized that flux though the PP pathway could increase when cells were challenged with excessive mitochondrial H_2O_2 generation rate. When a production rate of H_2O_2 in mitochondria increased beyond a certain threshold, H_2O_2 could diffuse out of mitochondria

via aquaporin channels and the depolarization of mitochondria has been observed in longer time scales (t > 2hr), leading to diffusion of H_2O_2 to the cytosol[18,19]. As a result, cytosolic NADPH could decrease, increasing the $NADP^+$ level and activating glucose 6-phosphate dehydrogenase [20]. Alternatively, excessive generation of H_2O_2 in mitochondria could increase the $NADP^+$ level in mitochondria and be transported to cytosol via indirect shuttles and activate the oxPP pathway [3,21]. Interestingly, even at mild perturbation such as 5 mM D-alanine, the fraction of M+1 lactate was increased by 4 % compared to that of control within 30 minutes, 9 % in 1 hour, and 7 % in 2 hours **(Figure 3.12A)**. For the treatment of 25 mM D-alanine, the fraction was increased by approximately 14 % in 30 minutes, 18 % in 1 hour, and 19 % in 2 hours. As a positive control, we supplemented 25 mM of D-alanine to Hela cells that expressed the cytosolic DAAO and measured the fractions of M+1 and M+2 lactate. The cytosolic perturbation elevated the fraction of M+1 lactate higher than that in mitochondria. The fraction of M+1 lactate was increased by 20% in 30 minutes, 29% in 1 hour and 24% in 2 hours. As the fraction of M+1 lactate increased in proportional to the D-alanine concentration, the M+2 lactate fraction decreased with increasing D-alanine concentration. (**Figure 3.12B)**. As a result, the increased ratio between the fractions of M+1 and M+2 lactate indicated a shift of some glycolytic flux to PP pathway during mitochondrial or cytosolic oxidative stress.

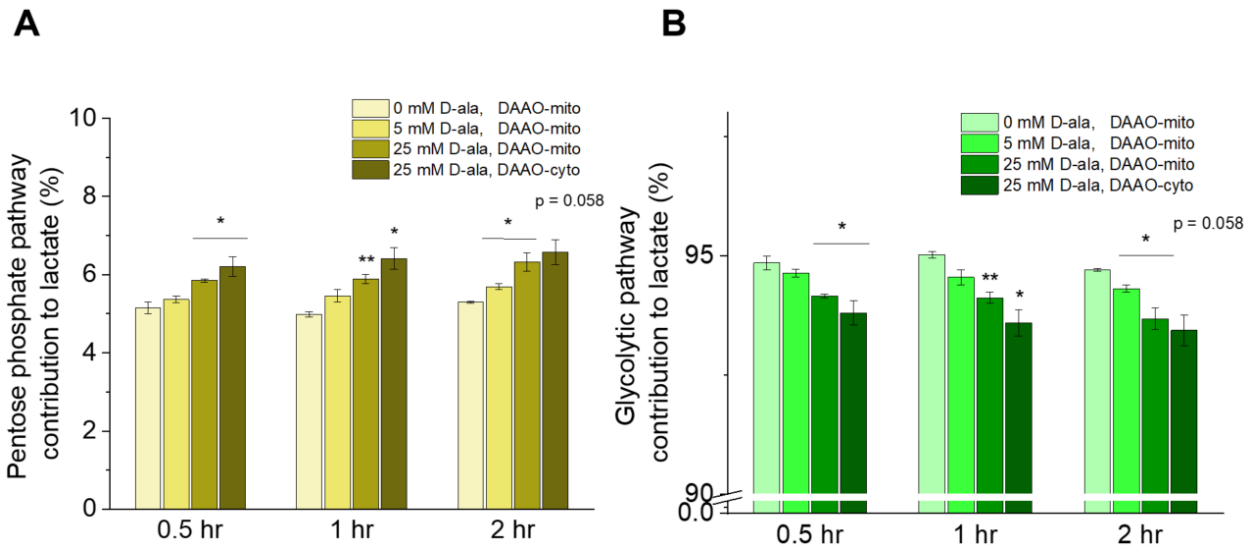

Figure 3.12. Mitochondrial oxidative stress increased fluxes through pentose phosphate pathway. (A) Relative strength of pentose phosphate pathway was represented by the fraction of M+1 of the sum of M+1 and M+2 lactate. (B) Glycolytic pathway activity was indicated by the fraction of M+2 lactate.

3.5. Discussion

^{13}C Glucose isotopic tracers demonstrated the activation of oxPP pathway and enrichment of TCA cycle metabolites during mitochondrial oxidative stress. As the oxPP pathway was considered a route for regeneration of cytosolic NADPH, we first expected the PP pathway would not be activated by a decrease of the NADPH pool in mitochondria. However, We observed the oxPP pathway activity was increased upon a relatively small decrease of mitochondrial NADPH, indicating that oxPP pathway may contribute to maintenance of NADPH pools under mitochondrial oxidative stress through The NADPH transport via metabolite shuttle systems such as malate/pyruvate, citrate/αKG or serine/glycine conversion[3,21–23]. Evaluation of shuttle systems involved in transport of NADPH between cytosol and mitochondria could provide insight on how NADPH can be redistributed between mitochondria and cytosol upon

oxidative stress. Furthermore, upon mitochondrial oxidative stress, the mitochondrial NADPH pool was reported to be maintained by activation of serine metabolism as knockdown of serine hydroxymethyltransferase (SHMT2) decreased cellular NADPH/$NADP^+$ and impaired tumor growth in MYC-dependent cells [24]. Investigation of the extent of serine metabolism in maintaining compartmentalized NADPH provided additional axes of NADPH homeostasis from nutrients other than glucose and glutamine.

Additionally, it was reported that an increase of mitochondrial $NADP^+$ caused an increase of mitochondrial NAD^+ [25], indicating an interchange between $NADP^+$ and NAD^+ in mitochondria facilitated transfers of the cofactors between the cytosol and mitochondria through shuttle systems. The activation of the oxPP pathway was immediate (< 30 minutes) under relatively low production rate of mitochondrial H_2O_2. On the other hand, we observed increased labeling patterns of TCA cycle metabolites under high production rates of mitochondrial H_2O_2, or so-called mitochondrial oxidative stress. TCA cycle metabolites such as malate, isocitrate, or NADH cofactor were used for regeneration of NADPH in mitochondria via ME3, IDH2, or NNT, respectively. NNT was suggested to play a major role in maintenance of mitochondrial NADPH as knockdown of NNT caused a disturbed NAD(P)H/$NADP^+$ balance [4]. Future imaging experiments with NADH/NAD^+ sensors such as Peredox, SoNar, and Apollo in both mitochondria and cytoplasm could elicit insight on whether NNT enzyme plays a major role in the generation of mitochondrial NADPH [26–28]. Alternatively, by utilizing serine tracers with mutant isocitrate enzymes, the activity of folate metabolism could be visualized under conditions of enhanced production of mitochondrial H_2O_2[3].

3.6. References

1. Dong, W., Keibler, M. A. & Stephanopoulos, G. Review of metabolic pathways activated in cancer cells as determined through isotopic labeling and network analysis. *Metab. Eng.* **43**, 113–124 (2017).

2. Dong, W., Moon, S. J., Kelleher, J. K. & Stephanopoulos, G. Dissecting Mammalian Cell Metabolism through 13C- A nd 2H-Isotope Tracing: Interpretations at the Molecular and Systems Levels. *Ind. Eng. Chem. Res.* **59**, 2593–2610 (2020).

3. Lewis, C. A. *et al.* Tracing Compartmentalized NADPH Metabolism in the Cytosol and Mitochondria of Mammalian Cells. *Mol. Cell* **55**, 253–263 (2014).

4. Gameiro, P. A., Laviolette, L. A., Kelleher, J. K., Iliopoulos, O. & Stephanopoulos, G. Cofactor balance by nicotinamide nucleotide transhydrogenase (NNT) coordinates reductive carboxylation and glucose catabolism in the tricarboxylic acid (TCA) cycle. *J. Biol. Chem.* **288**, 12967–12977 (2013).

5. Fan, J. *et al.* Quantitative flux analysis reveals folate-dependent NADPH production. *Nature* **510**, 298–302 (2014).

6. Patra, K. C. & Hay, N. The pentose phosphate pathway and cancer. *Trends Biochem. Sci.* **39**, 347–354 (2014).

7. Liu, L. *et al.* Malic enzyme tracers reveal hypoxia-induced switch in adipocyte NADPH pathway usage. *Nat. Chem. Biol.* **12**, 345–352 (2016).

8. Grassian, A. R. *et al.* IDH1 mutations alter citric acid cycle metabolism and increase dependence on oxidative mitochondrial metabolism. *Cancer Res.* **74**, 3317–3331 (2014).

9. Zhang, Z., Chen, L., Liu, L., Su, X. & Rabinowitz, J. D. Chemical Basis for Deuterium Labeling of Fat and NADPH. *J. Am. Chem. Soc.* **139**, 14368–14371 (2017).

10. Jang, C., Chen, L. & Rabinowitz, J. D. Leading Edge Primer Metabolomics and Isotope Tracing. *Cell* **173**, 822–837 (2018).

11. Katz, J. & Rognstad, R. Futile cycling in glucose metabolism. *Trends Biochem. Sci.* **3**, 171–174 (1978).

12. Hermes, J. D., Roeske, C. A., O'Leary, M. H. & Cleland, W. W. Use of Multiple Isotope Effects To Determine Enzyme Mechanisms and Intrinsic Isotope Effects. Malic Enzyme and Glucose-6-

phosphate Dehydrogenase. *Biochemistry* **21**, 5106–5114 (1982).

13. Lee, W. N. *et al.* In vivo measurement of fatty acids and cholesterol synthesis using D2O and mass isotopomer analysis. *Am. J. Physiol. Metab.* **266**, E699–E708 (1994).

14. Metallo, C. M. *et al.* Reductive glutamine metabolism by IDH1 mediates lipogenesis under hypoxia. *Nature* **481**, 380–384 (2012).

15. Dong, W., Moon, S. J., Kelleher, J. K. & Stephanopoulos, G. Dissecting Mammalian Cell Metabolism through 13 C- and 2 H - Isotope Tracing: Interpretations at the Molecular and Systems Levels. (2019) doi:10.1021/acs.iecr.9b05154.

16. Ahn, W. S. *et al.* Glyceraldehyde 3-phosphate dehydrogenase modulates nonoxidative pentose phosphate pathway to provide anabolic precursors in hypoxic tumor cells. *AIChE J.* **64**, 4289–4296 (2018).

17. Jang, C., Chen, L. & Rabinowitz, J. D. Metabolomics and Isotope Tracing. *Cell* **173**, 822–837 (2018).

18. Cox, A. G., Winterbourn, C. C. & Hampton, M. B. Mitochondrial peroxiredoxin involvement in antioxidant defence and redox signalling. *Biochem. J.* **425**, 313–325 (2010).

19. Stein, K. T., Moon, S. J. & Sikes, H. D. Mitochondrial H_2O_2 generation using a tunable chemogenetic tool to perturb redox homeostasis in human cells and induce cell death. *ACS Synth. Biol.* **7**, acssynbio.8b00174 (2018).

20. Au, S. W. N., Gover, S., Lam, V. M. S. & Adams, M. J. Human glucose-6-phosphate dehydrogenase: The crystal structure reveals a structural NADP+ molecule and provides insights into enzyme deficiency. *Structure* **8**, 293–303 (2000).

21. MacDonald, M. J. Feasibility of a mitochondrial pyruvate malate shuttle in pancreatic islets. Further implication of cytosolic NADPH in insulin secretion. *Journal of Biological Chemistry* vol. 270 20051–20058 (1995).

22. Sazanov, L. A. & Jackson, J. B. Proton-translocating transhydrogenase and NAD- and NADP-linked isocitrate dehydrogenases operate in a substrate cycle which contributes to fine regulation of the tricarboxylic acid cycle activity in mitochondria. *FEBS Lett.* **344**, 109–116 (1994).

23. Jiang, P., Du, W., Mancuso, A., Wellen, K. E. & Yang, X. Reciprocal regulation of p53 and malic enzymes modulates metabolism and senescence. *Nature* **493**, 689–693 (2013).

24. Ye, J. *et al.* Serine catabolism regulates mitochondrial redox control during hypoxia. *Cancer Discov.* **4**, 1406–1417 (2014).

25. Cracan, V., Titov, D. V., Shen, H., Grabarek, Z. & Mootha, V. K. A genetically encoded tool for manipulation of NADP+/NADPH in living cells. *Nat. Chem. Biol.* **13**, 1088–1095 (2017).

26. Cameron, W. D. *et al.* Apollo-NADP+: A spectrally tunable family of genetically encoded sensors for NADP+. *Nat. Methods* **13**, 352–358 (2016).

27. Hung, Y. P., Albeck, J. G., Tantama, M. & Yellen, G. Imaging Cytosolic NADH-NAD+ Redox State with a Genetically Encoded Fluorescent Biosensor. *Cell Metab.* **14**, 545–554 (2011).

28. Zhao, Y. *et al.* SoNar, a Highly Responsive NAD+/NADH Sensor, Allows High-Throughput Metabolic Screening of Anti-tumor Agents. *Cell Metab.* **21**, 777–789 (2015).

Chapter 4

Estimation of the mitochondrial NADPH/$NADP^+$ using a kinetic model of mitochondrial antioxidant network

This chapter is adapted from:

Sun Jin Moon, *Wentao Dong, Greg Stephanopoulos and Hadley Sikes, Oxidative pentose phosphate pathway and glucose anaplerosis support maintenance of mitochondrial NADPH pool under mitochondrial oxidative stress, Bioengineering & Translational Medicine, 2020, 5 e10184 (2020).*

Kassi T Stein, ***Sun Jin Moon****, Athena N Nguyen, Hadley D Sikes, Kinetic modeling of H2O2 dynamics in the mitochondria of HeLa cells, PLOS Computational Biology, 16 e1008202 (2020).*

Sun Jin Moon contributed to a successful revision process, specifically providing Monte Carlo random sampling simulations on mitochondrial H_2O_2 metabolic network.

4.1. Abstract

Measurement of mitochondrial NADPH/$NADP^+$ ratio was experimentally challenging. To overcome this limitation, I used a kinetic modeling of mitochondrial antioxidant network to extract concentration of NADPH and NADPH/$NADP^+$ ratio. Based on the least squares methods for parameter fitting, I estimated the concentration of mitochondrial NADPH and NADPH/$NADP^+$ ratio at the basal and mitochondrial oxidative stress conditions. Additionally, the model predicted an activation of cytosolic NADPH transport was necessary to maintain mitochondrial NADPH under mitochondrial stress.

4.2. Introduction

Based on a reaction network of mitochondrial H_2O_2 scavenging system, I performed computer simulation that examined the extent of change of mitochondrial NADPH/ $NADP^+$ under mitochondrial oxidative stress. Previous redox models were designed to evaluate cytosolic H_2O_2 scavenging network and determined H_2O_2 diffusion rates across the extracellular membrane and kinetic parameters of an antioxidant reaction network[1–4]. However, these models were based on the values of cytosolic kinetic parameters and the generation rate of NADPH was designated to the G6PD enzyme, which was expressed solely in cytosol [5]. Mitochondrial NADPH could be regenerated via reactions catalyzed by isoforms of NADP-dependent enzymes such as ME3, IDH2, glutamate dehydrogenase 1 (GLUD1), methylenetetrahydrofolate 2 (MTHFD2), aldehyde dehydrogenase, and NNT [6]. Thus, we developed a model while updating initial concentrations of redox species in mitochondria and kinetic parameter values compiled in a bioinformatics database[7,8]. This reaction network designated for mitochondrion provides kinetic information of

redox species and insights on a phenomenon that cannot be easily captured with experiments only.

4.3. Materials and Methods

4.3.1. Overview of kinetic model

The purpose of this model was to quantify the mitochondrial NADPH and NADPH/$NADP^+$ under varying production rates of H_2O_2 using a system of ordinary differential equations (ODEs). The source of input data included the fraction of sensor readout described in the later section and the well-established literature values for kinetic constants and initial concentrations. First, we created a system of ordinary differential equations for redox species, the kinetic model first reported by Adimora et al [1]. With the model as a framework, we updated values of rate constants and initial concentration of redox species found in mitochondria. In regards to the regeneration rate for NADPH in mitochondria, we set a first order kinetic equation that represents major enzymatic reactions for NADPH production such as IDH2, ME3, NAD^+transhydrogenases (NNT), and methylene tetrahydrofolate dehydeogenase 2 (MTHFD2) [9,10].

We included the transport and degradation rates of glutathione, removing the glutathione synthesis rate as it was exclusively formed in the cytoplasm [80, 82]. The thioredoxin influx and degradation rates were removed as their rates were indicated to be three orders magnitude lower than other redox reactions, thereby its sensitivity to the system low[1]. The generation rate of mitochondrial H_2O_2 at the basal level was determined from references, which reported values that were within the same order of magnitude [12–14]. The generation rate of was D-alanine we

introduced would only be catabolized by the D-amino acid oxidase we expressed in mitochondria and not by other enzymatic reactions based on the fact that HeLa and most other human cells lack naturally occurring D-amino acid oxidase [15,16]. Thus, we set cytosolic D-alanine to be constant. Because of this assumption and for simplification of mathematical model, we can set only one D-alanine transport rate that separates D-alanine in media and D-alanine in mitochondria. Lastly, we included a stress-dependent NADPH flux that was defined as a function of the total mitochondrial H_2O_2 flux.

The initial concentrations of oxidized redox species in mitochondria were calculated based on the steady state approximation with the molar balance equations as described before [2]. Unless noted, we assumed rate constants of redox reactions in mitochondria are within the same order of magnitude of those in cytosol and thus used accordingly as listed in table 1 in Appendix A. For the initial concentration of mitochondrial NADPH concentration, we converted the fluorescence ratio of the sensor to NADPH concentration based on the digitonin based calibration experiments as described previously [17]. The average concentration of NADPH in mitochondria was determined to be 41.8 μM based on the fluorescence images of 243 single cells.

4.3.2. Quantification of NADPH level

We quantified the mitochondrial NADPH level by calculating the fraction of sensor readout (Y^{exp}) and equating it to the fraction of sensor-NADPH complex (Y^{model}), which are expressed as follows:

$$Y^{exp} = \frac{R' - R'_{min}}{R'_{max} - R'_{min}}, Y^{model} = \frac{NADPH}{K_d + NADPH}$$

R' is an effective fluorescence signal obtained by $\frac{R_{415nm/488nm}|_{iNap-mito}}{R_{415nm/488nm}|_{iNapC-mito}}$ [17]. R'_{max} was obtained by permeabilizing Hela cells expressing mito-iNaps with an optimized concentration of 0.05 mg/mL of digitonin and incubating with 400 μM NADPH. To minimize artifact effects such as leakage of sensor, we have used the control NADPH sensor with no binding affinity to NADPH in parallel and normalized the sensor readout to that of control sensor [17]. To control the permeabilization of mitochondrial NADPH, we varied the concentration of digitonin from 0 to 1 mg/mL in presence or absence of NADPH in context of our experiments. As NADPH sensor was localized to mitochondria, NADPH sensor fluorescence signal did not change unless we introduced a threshold digitonin concentration. We observed the rise of signal was dependent on time-scale as lower concentration (0.05 mg/mL) allowed increase of signal at later time-points while higher concentration (0.1 mg/mL) allowed permeabilization effect in earlier time-point such that we observed a sharp increase of signal followed by steep decrease of signal potentially due to the leakage of sensors.

R'_{min} was determined by addition of 100 mM D-alanine to Hela cells expressing DAAO and mito-iNaps. Due to the presence of antioxidant network present in cells, the R'_{min} could be underestimated. Thus, we compared the quantified NADPH concentration to that of reference [17], where the estimation of intracellular NADPH level from different variants of iNap sensors was consistent with *in-vitro* evaluation, and our estimates of free NADPH value fell within 5% of that determined in the reference. For Y^{model}, NADPH represents concentration of mitochondrial NADPH and K_d is the dissociation constant of the iNap3 or 33 sensors, which are either 25.2 or 3.6 μM taken from the literature [17]. Y^{model} was derived based on the equation of binding interaction between the ligand and the sensor with one to one stoichiometry.

4.3.3. Objective function for parameter evaluation

With time-course measurement of NADPH level in terms of concentration, we fitted model parameters by minimizing an objective function that calculates the sum of squared difference between predicted and observed values as follows:

$$Z(\theta) = \sum_{i=1}^{N_{exp}} \sum_{k=1}^{N_k} w_i(t_k)[y_i^{pred}(t_k;\theta) - y_i^{obs}(t_k)]^2$$

, where y^{obs} is the experimentally observed NADPH concentration, $w_i(t_k)$ is the $1/\sigma_i(t_k)^2$, σ is the standard error of mean, N_k is the number of data points taken for duration of 60 minutes with time interval of 3 minutes, and N_{exp} is the number of experiments with five different conditions.

4.3.4. Sensitivity analysis

Using the finite approximation methods, we implemented a sensitivity analysis to the NADPH level by every parameters in the reaction model [18]. The equation of sensitivity analysis is as follows:

$$s_i = \frac{\partial C_{NADPH}}{\partial \theta_i} = \frac{C_{NADPH}(\theta_i + \Delta\theta_i, t) - C_{NADPH}(\theta_i, t)}{\Delta\theta_i}$$

, where s_i represents the sensitivity to the θ_i model parameters and C_{NADPH} is the concentration of NADPH. Parameters were varied by 10% and the time was evaluated at 3 minutes. As the parameter values vary by orders of magnitude, we normalized the sensitivity to $C_{NADPH}(t)$ and θ_i. The final sensitivity equation is as follows:

$$\overline{s_i} = \frac{\partial C_{NADPH}/C_{NADPH}}{\partial \theta_i/\theta_i}$$

All the normalized sensitivities were evaluated at corresponding D-alanine perturbations and the top 5 most sensitizing parameters were reported (**Table 4.3**).

4.4. Results

4.4.1. Mathematical model estimates mitochondrial NADPH/NADP$^+$ to drop by 67-fold under mitochondrial oxidative stress

With the dynamic experimental data obtained from the iNap sensors and the analysis of central carbon metabolism upon perturbation, we formulated a mathematical model to quantify the concentration of mitochondrial NADPH and NADPH/NADP$^+$ upon varying production rates of H_2O_2. Based on the system of ordinary differential equations for redox species [1], we modified the model by updating kinetic vales of redox species for mitochondria and added new reaction terms such as (a) a permeability coefficient of D-alanine, *P*, (b) a generation rate of hydrogen peroxide by DAAO, k_{gen,H_2O_2}, (c) a regeneration rate of NADPH, $k_{gen,NADPH}$, and (d) a stress-dependent NADPH flux coefficient, α (**Figure 4.1 and Table 4.1**).

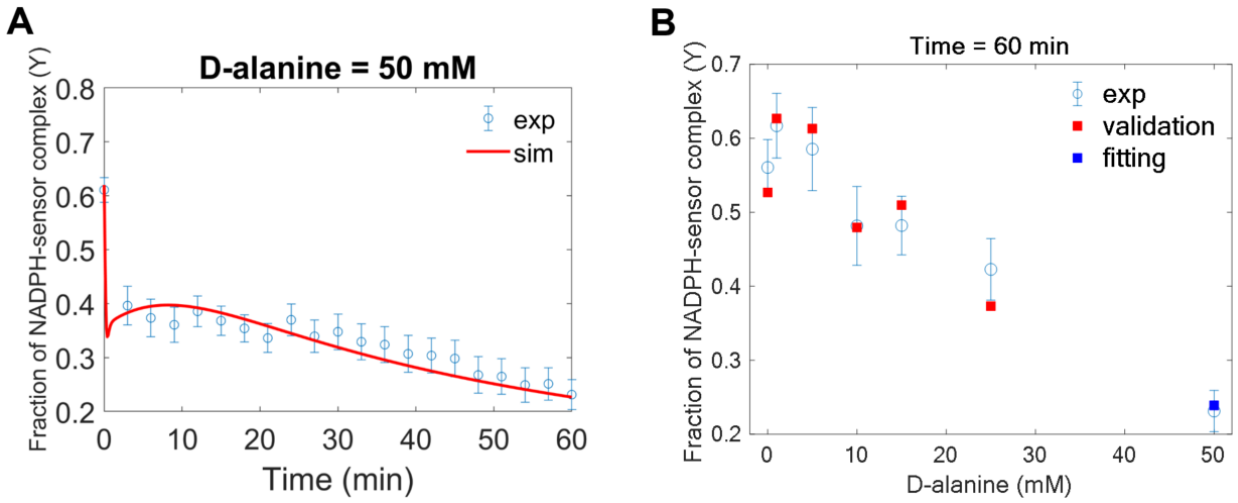

Figure 4.1. Model simulation and validation with the best fitted parameters. (**A**) Unknown parameters were fitted to the experimental data of 50 mM D-alanine to determine values consistent with the experimental data over 60 minutes. (**B**) To assess the validity of these parameter values over a range of conditions, the fitted parameter values determined using the one condition in (A) were used to predict the binding fraction between NADPH and sensor (Y^{model}) with different initial concentrations of D-alanine and compared to the experimentally obtained value (Y^{exp}) at t = 60 minutes. The blue square is the fitted condition, where the model and experiment must coincide. The red squares are not fit to the experimental data points.

Table 4.1, Parameters for the mitochondrial redox reactions.

	Reaction	*Parameter*	*Reference*
r_1:	Intracellular H_2O_2 generation	$k_{gen,intra H_2O_2} = 4.0 \times 10^{-6} M/s$	[49,50]
r_2^*:	$P \times \frac{A_m}{V_{cell}} \times ([\text{D-alanine}]_{ex}) \times V_{well}$	$P = 6.92 \times 10^{-10}\ cm/s$	Fitted
r_3^*:	$P \times A \times ([\text{D-alanine}]_{in}) \times$ cell number		
r_3:	$k_{gen,H_2O_2}([\text{D-alanine}]_{in})$	$k_{gen,H_2O_2} = 8.83 \times 10^{-2} s^{-1}$	Fitted
r_4:	$k_{gen,NADPH}([NADP^+])$	$k_{gen,NADPH} = 1.59\ s^{-1}$	Fitted
r_5:	$k_{import,GSH}$	$k_{import,GSH} = 4.8 \times 10^{-7} M/s$	[82]
r_6:	$k_{degradation,GSH}$	$k_{degradation,GSH} = 3.2 \times 10^{-8} M/s$	[82]
v_{11}:	$k_{11}([GSSG])([NADPH])$	$k_{11} = 3.2 \times 10^6\ M^{-1}s^{-1}$	[51]
v_{12}:	$k_{12}([GrxSSG])([GSH])$	$k_{12} = 3.7 \times 10^4\ M^{-1}s^{-1}$	[52]
v_{13}:	$k_{13}([GrxSH])([PrSSG])$	$k_{13} = 1.2 \times 10^4\ M^{-1}s^{-1}$	[53]
v_{14}:	$k_{14}([PrSOH])([GSH])$	$k_{14} = 1.2 \times 10^5\ M^{-1}s^{-1}$	[54,55]

v_{15}:	$k_{15}([PrSH])([H_2O_2])$	$k_{15} = 1 \times 10^2\ M^{-1}s^{-1}$	[36]
v_{16}:	$k_{16}([GSH])$	$k_{16} = 7.4 \times 10^{-5}\ s^{-1}$	[34]
v_{21}:	$k_{21}([TrxSS])([NADPH])$	$k_{21} = 2 \times 10^7\ M^{-1}s^{-1}$	[16]
v_{22}:	$k_{22}([PrxSS])([TrxSH])$	$k_{22} = 2.2 \times 10^5\ M^{-1}s^{-1}$	[56]
v_{23}:	$k_{23}([H_2O_2])([PrxSH2])$	$k_{23} = 2 \times 10^7\ M^{-1}s^{-1}$	[16]
v_{24}:	$k_{24}([H_2O_2])([PrxSOH])$	$k_{24} = 1.4 \times 10^4\ M^{-1}s^{-1}$	[36]
v_{25}:	$k_{25}([PrxSOOH])$	$k_{25} = 3 \times 10^{-3}\ s^{-1}$	[57]
v_{26}:	$k_{26}([PrxSOH])$	$k_{26} = 20\ s^{-1}$	[58]
v_{31}:	$k_{31}([TrxSH])([PrSS])$	$k_{31} = 1 \times 10^2\ M^{-1}s^{-1}$	[36]
v_{32}:	$k_{32}([H_2O_2])([PrSH2])$	$k_{32} = 1 \times 10^2\ M^{-1}s^{-1}$	[36]
v_{41}:	$k_{41}([H_2O_2])([GPxRd])$	$k_{41} = 6 \times 10^7\ M^{-1}s^{-1}$	[59]
v_{42}:	$k_{42}([GSH])([GPxOx])$	$k_{42} = 4 \times 10^4\ M^{-1}s^{-1}$	[59]
v_{43}:	$k_{43}([GPxSSG])([GSH])$	$k_{43} = 1 \times 10^7\ M^{-1}s^{-1}$	[59]
v_{51}:	$k_{51}([H_2O_2])([Prx5SH2])$	$k_{51} = 3 \times 10^5\ M^{-1}s^{-1}$	[83]
v_{52}:	$k_{52}([Prx5SOH])$	$k_{52} = 14.7\ s^{-1}$	[83]
v_{53}:	$k_{53}([Prx5SS])([TrxSH])$	$k_{53} = 2 \times 10^6\ M^{-1}s^{-1}$	[83]
v_{61}:	$k_{61}([H_2O_2])([GPx4Rd])$	$k_{61} = 4.8 \times 10^4\ M^{-1}s^{-1}$	[84]
v_{62}:	$k_{62}([GSH])([GPx4Ox])$	$k_{62} = 2 \times 10^4\ M^{-1}s^{-1}$	[84]
v_{71}:	Srx import	$k_{71} = 1.23 \times 10^{-5}\ M/s$	[85]
r_6	$\alpha \times v_{H_2O_2}^{tot}$ $v_{H_2O_2}^{tot} = r_1 + r_3 - v_{15} - v_{23} - v_{24} - v_{32} - v_{41}$	$\alpha = 80.9$	Fitted

* $A_m = 1.26 \times 10^{-9}\ m^2$, r_2^* and r_3^* are units of mol per s; cell = 7×10^5; volWell = $2 \times 10^{-6}\ m^3$; volCell = $4.19 \times 10^{-15}\ m^3$

Reasoning that NADPH could be transferred between cytosol and mitochondria via indirect metabolite shuttle systems above a certain threshold hydrogen peroxide generation rate in mitochondria[19,20], we introduced the stress-dependent NADPH flux, which was defined as a $\alpha \times v_{H_2O_2}^{total}$. As the mitochondrial NADPH pool was decreased by high production rates of mitochondrial H_2O_2 flux, we expected an additional NADPH flux introduced in mitochondria to maintain the mitochondrial NADPH level.

We used a weighted least-square minimization method based on time-dependent experimental data ($Y^{exp} = \frac{R' - R'_{min}}{R'_{max} - R'_{min}}$) and model data ($Y^{model} = \frac{NADPH}{K_d + NADPH}$), which is derived from the binding kinetic equation between the sensor and NADPH. The initial concentration of redox species involved in this system were calculated as previously described (**Table 4.2)** [2]. The model data, including Y^{model}, was obtained by solving the system of ordinary differential equations with 1000 different sets of randomly-chosen initial parameter values along with the basal NADPH concentration obtained from experiment and initial concentration of redox species found in literature (**Table 4.2 and Figure 4.2A-B)**. For the experimental data, we used 21 data points obtained from the experiment with 50 mM D-alanine stimulation as it represented the extreme condition *per se* mitochondrial oxidative stress (**Figure 4.1)**. Once optimized parameter values were determined, we assessed whether these values could simulate experimental data that were collected under six other conditions, each of which contained 21 time-dependent data points (**Figure 4.3, Figure 4.2C)**. Model-predicted NADPH concentration and subsequently Y^{model} was compared to Y^{exp}, demonstrating the robustness of the model as the values resided mostly within the mean$\pm$SEM range of experimental data at each time point.

Table 4.2. Initial concentrations of the mitochondrial redox model for Hela cells.

Species	Initial concentration (M)	Reference
$[\text{D-alanine}]_{ex}$	0 to 50×10^{-3}	Assigned
$[\text{D-alanine}]_{en}$	0	Assigned
$[H_2O_2]$	3.33×10^{-9}	Calculated
$[\text{Prx-}(SH)_2]$	6×10^{-5}	[16]
[Prx-SS]	2.36×10^{-7}	Calculated

$[\text{Trx-(SH)}_2]$	7.7×10^{-6}	[60]
[Trx-SS]	7.54×10^{-8}	[60]
[GSSG]	1.78×10^{-6}	[34]
[GSH]	5×10^{-3}	[34]
[Grx-SSG]	1.8×10^{-18}	Calculated
[Grx-SH]	1×10^{-6}	[36]
[Pr-SSG]	2.78×10^{-14}	Calculated
[Pr-SH]	1×10^{-9}	[36]
[Pr-SOH]	5.56×10^{-19}	Calculated
[Pr-SS]	4.72×10^{-7}	Calculated
$[\text{Pr-(SH)}_2]$	1.09×10^{-3}	[34]
[GPx-Ox]	1.5×10^{-11}	Calculated
[GPx-SH]	1.5×10^{-8}	[16]
[GPx-SSG]	6.00×10^{-14}	Calculated
[Prx-SOH]	2×10^{-7}	Calculated
[Prx-SOOH]	2.67×10^{-9}	Calculated
$[\text{NADP}^+]$	4.18×10^{-6}	Assigned
[NADPH]	4.18×10^{-5}	Calculated
$[\text{Prx5-(SH)}_2]$	1.4×10^{-5}	[60]
[Prx5-SOH]	9.43×10^{-10}	Calculated
[Prx5-SS]	9.00×10^{-10}	Calculated
[GPx4-SH]	2.30×10^{-7}	[60]
[GPx4-Ox]	3.60×10^{-13}	Calculated
[GPx4-SSG]	7.29×10^{-16}	Calculated
[Srx]	8.78×10^{-9}	[60]

The model predicted the overall generation rate constant of mitochondrial NADPH, $k_{gen,NADPH}$, as $1.59\ s^{-1}$ $(1/s)$, and the steady-state NADPH flux at the basal condition was

estimated to be 4.05 $\mu M/s$. This value was within the same order of magnitude of the overall NADPH flux estimated from the FBA model in previous studies [21,22]. The stress-dependent NADPH flux coefficient (α) was found to be 80.9. In the absence of α, the model prediction failed to predict the experimental data under higher perturbation **(Figure 4.2D).** The addition of D-alanine increased the mitochondrial H_2O_2 level within the nM range with 15 mM D-ala increasing the H_2O_2 level up to 7.5 times higher than the initial concentration of 3.3 nM **(Figure 4.3A, Figure 4.2E-H).** Simultaneously, the NADPH level decreased inversely by the increase of H_2O_2 with 15 mM D-alanine lowering NADPH pool approximately 34% (**Figure 4.3B)**. When the model was simulated with 50 mM D-alanine, the NADPH level dropped sharply within 0.5 minutes, increased again for approximately 27% within the next 8 minutes, and decreased again to a final concentration of 7.9 μM.

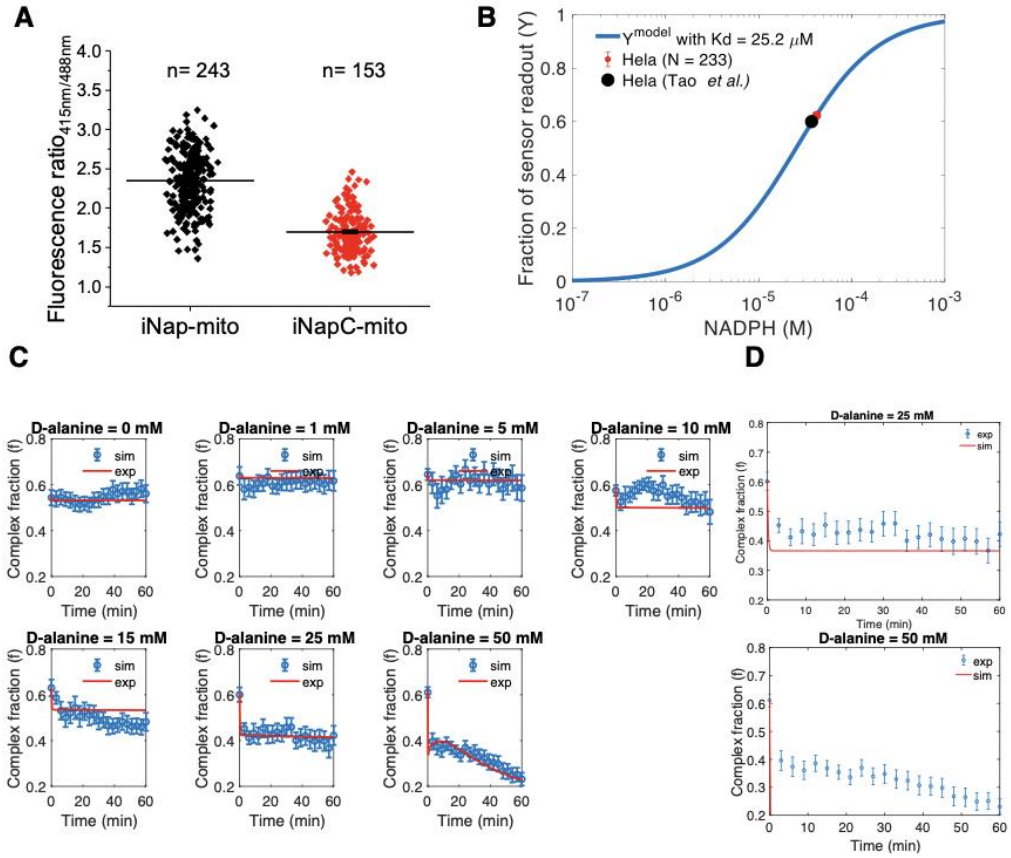
A
n= 243
n= 153
Fluorescence ratio415nm/488nm
iNap-mito
iNapC-mito
B
Ymodel with Kd = 25.2 μM
Hela (N = 233)
Hela (Tao et al.)
Fraction of sensor readout (Y)
NADPH (M)
C
D
D-alanine = 0 mM
D-alanine = 1 mM
D-alanine = 5 mM
D-alanine = 10 mM
D-alanine = 15 mM
D-alanine = 25 mM
D-alanine = 50 mM
sim
exp
Complex fraction (f)
Time (min)

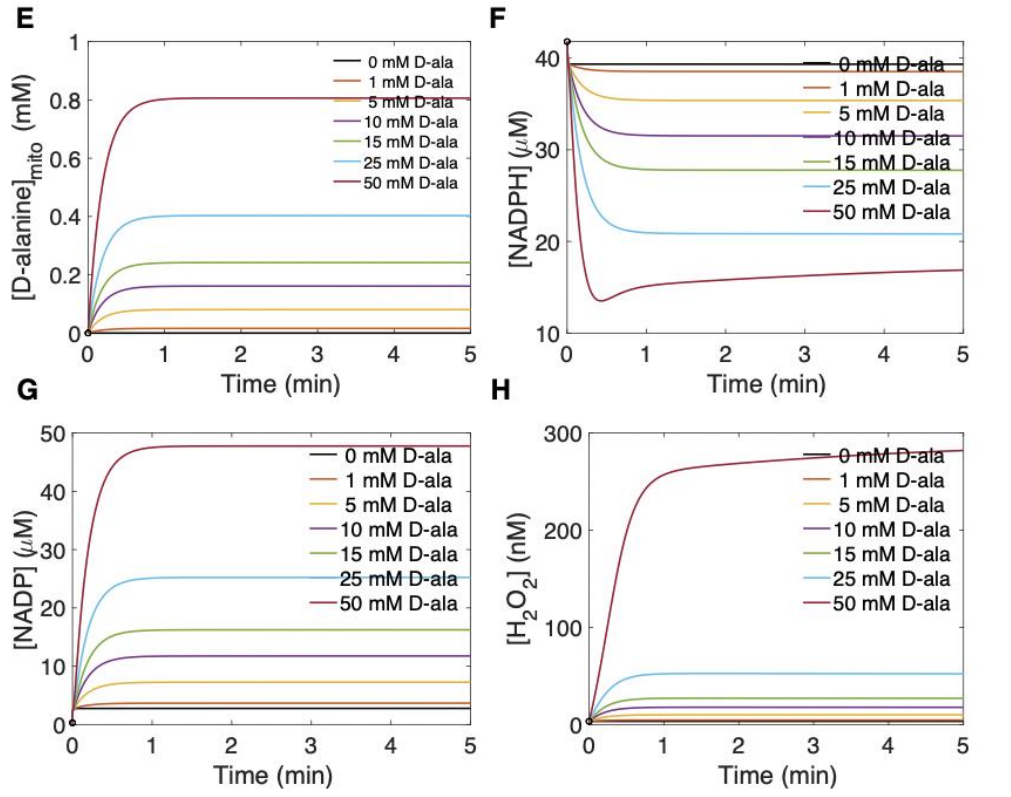
E
F
G
H
0 mM D-ala
1 mM D-ala
5 mM D-ala
10 mM D-ala
15 mM D-ala
25 mM D-ala
50 mM D-ala
[D-alanine]mito (mM)
[NADPH] (μM)
[NADP] (μM)
[H2O2] (nM)
Time (min)

Figure 4.2. (A) A scatter plot represented fluorescence signals from iNap-mito and iNapC-mito with its mean and S.E.M. The mean of iNap-mito is 2.35 and that of iNapC-mito is 1.71. The normalized average signal is 1.38, which is equal to 62% of sensor being in a bound state with the NADPH after calibrating with the maximum and minimum signals. **(B)** The fraction was converted to concentration by equating Y^{model} and Y^{exp}. Based on Tao paper, the NADPH level was determined 37 μM and its sensor occupancy were approximately 60% in this model. **(C)** The presence and absence of stress-dependent NADPH flux term**.** The model with fitted parameter values was run with different initial inputs and compared to the experimental data. The rate of NADPH included the $\alpha \times v_{H_2O_2}^{tot}$ term, which prevented a collapse of readout under 25 and 50 mM of D-alanine input. **(D)** The model was simulated with the stress-dependent NADPH flux term at 25 and 50 mM D-alanine conditions. The complex fraction (Y) decreased immediately within one minute. The error bar of experimental data represented the S.E.M. **(E)** The model simulation with the fitted parameter values. The model was run with different concentration of D-alanine and the concentration of intracellular D-alanine in mitochondria were predicted over the course of 5 minutes. **(F)** The model simulation for NADPH over the first 5 minutes. A rise of concentration under 50 mM D-alanine condition was due to the increased stress-dependent NADPH flux, preventing a continuous drop of NADPH level. **(G)** NADP level was tracked over 5 minutes. **(H)** The intracellular H_2O_2 level was traced over 5 minutes.

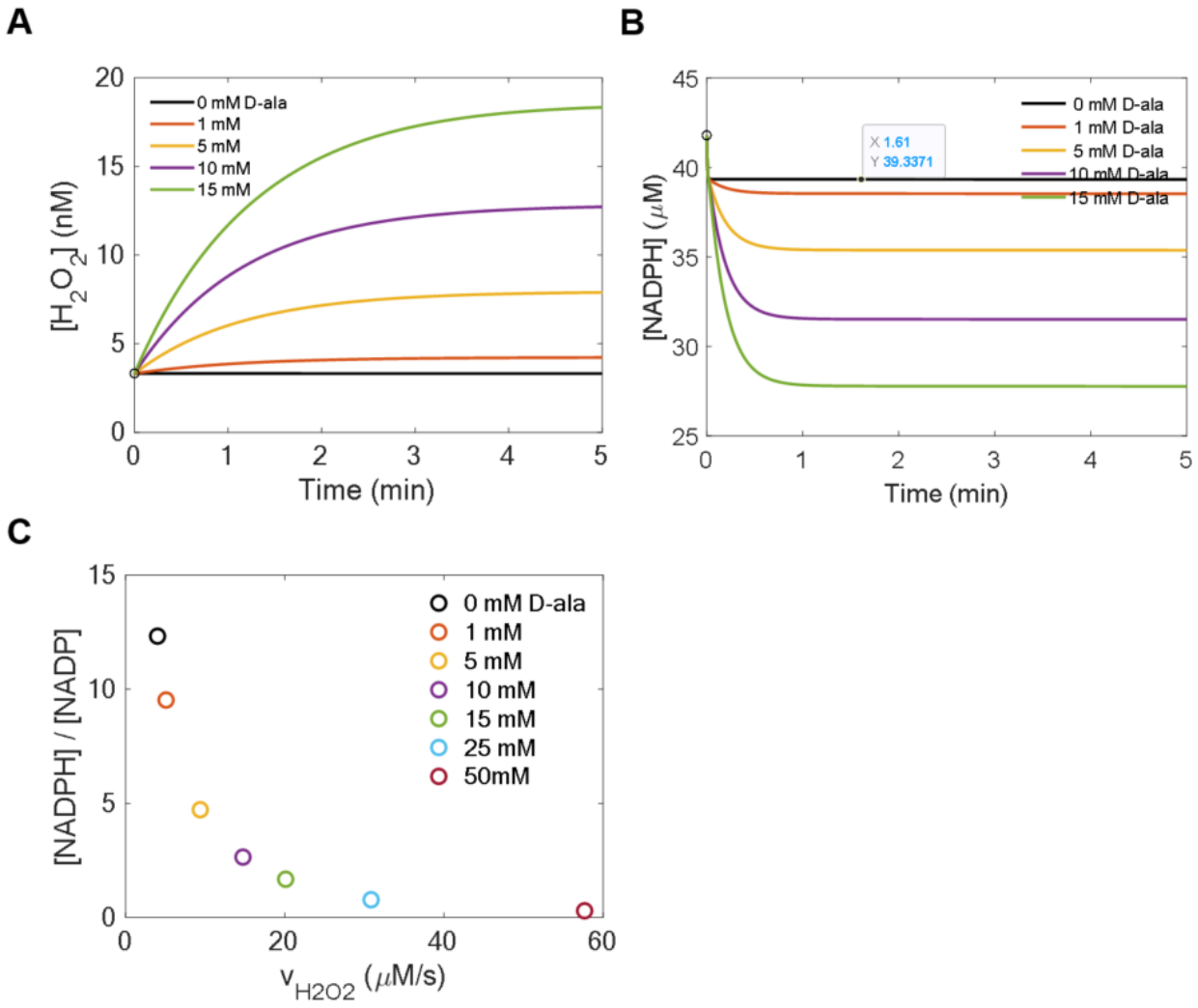

Figure 4.3. Computational model predicted mitochondrial NADPH/NADP$^+$ ratio upon varying generation rates of $\mathbf{H_2O_2}$ in mitochondria. Upon different concentrations of D-alanine used as input value, the model predicted (A) the intracellular H_2O_2 concentration in mitochondria, (B) NADPH, and (C) NADPH/NADP$^+$.

Sensitivity analysis further supported the increased role of stress-dependent NADPH flux when the production rate of H_2O_2 was high (**Table 4.3**). The sensitivity of α to NADPH level was about three orders of magnitude lower than that of NADPH generation rate parameter below 15 mM D-alanine perturbation, but it became within the same order of magnitude under 50 mM D-alanine condition. Throughout the perturbation, the sensitivity of the NADPH generation rate

parameter was the largest. At relatively lower perturbation (D-alanine < 15mM), the sensitivity of H_2O_2 generation rate parameters ranked within top 5 along with the transport of D-alanine. At higher perturbation (D-alanine >25 mM), rate parameters such as TrxSS-NADPH and H_2O_2-Prx reactions become significant in controlling mitochondrial NADPH pools. Other fitted parameters included the permeability coefficient of D-alanine, which was determined to be $6.92 \times 10^{-10}\ cm/s$ and the generation rate coefficient of H_2O_2 by mito-DAAO, which was evaluated to be $8.83 \times 10^{-2}\ s^{-1}$ (**Table 4.1)**.

Table 4.3. Results of the sensitivity analysis for NADPH at time = 3 min. The top 5 most sensitive parameters were represented at 0, 1, 5, 10, 15, 25, and 50 mM D-alanine perturbation. The stress-dependent transport coefficient became more sensitive as the perturbation increased.

#	***0 mM***		***1 mM***		***5 mM***		***10 mM***	
1	$k_{gen,H_2O_2,intra}$	0.12086	$k_{gen,NADPH}$	0.09241	$k_{gen,NADPH}$	0.17438	$k_{gen,NADPH}$	0.46751
2	$k_{gen,NADPH}$	0.11166	$k_{gen,H_2O_2,intra}$	0.08011	$k_{Dala,trans}$	0.10629	$k_{Dala,trans}$	0.35775
3	k_{16}	0.00085	$k_{Dala,trans}$	0.02020	$k_{gen,H_2O_2,intra}$	0.08428	$k_{gen,H_2O_2,intra}$	0.13767
4	k_{41}	0.00062	$k_{gen,H_2O_2,DAAO}$	0.00364	$k_{gen,H_2O_2,DAAO}$	0.01874	$k_{gen,H_2O_2,DAAO}$	0.06384
5	k_{23}	0.00047	k_{16}	0.00056	α	0.00101	k_{11}	0.00404

#	***15 mM***		***25 mM***		***50 mM***	
1	$k_{gen,NADPH}$	0.55124	$k_{gen,NADPH}$	0.66726	$k_{gen,NADPH}$	1.57764
2	$k_{Dala,trans}$	0.48497	k_{21}	0.45893	k_{41}	1.30468
3	$k_{gen,H_2O_2,intra}$	0.12243	k_{41}	0.28549	α	1.17850
4	$k_{gen,H_2O_2,DAAO}$	0.08272	α	0.25236	k_{21}	0.43024
5	α	0.0049	k_{42}	0.01961	k_{42}	0.08844

k rate constants are of $k_{11}([GSSG])([NADPH])$; $k_{16}(GSH)$; $k_{21}([TrxSS])([NADPH])$; $k_{23}([H_2O_2])([PrxSH2])$; $k_{41}([H_2O_2])([GPxRd])$; $k_{42}([GSH])([GPxOx])$.

Furthermore, the mitochondrial NADPH/NADP$^+$ ratio decreased by 67-fold when the generation of mitochondrial H_2O_2 increased by 19 times higher compared to basal rate (**Figure 4.3C)**. The NADPH/ NADP$^+$ ratio plays critical roles as multiple NADP dependent enzymes are reversible and a subtle change of ratio can alter the directionality of reactions, thereby switching the cellular metabolism [23,24]. Our model estimated the steady-state mitochondrial NADPH/ NADP$^+$ ratio at basal condition (0 mM D-alanine) to be 13.4 (**Table 4.4)**. This value is approximately 100-fold lower than the whole NADPH/NADP ratio of live cells examined from classic literature, which reports that the ratio can reach as high as 1000 under starved condition using a near equilibrium approximation [25]. Under different initial concentrations of D-alanine, the NADPH/ NADP$^+$ ratio decreased inversely proportional to the total generation rate of H_2O_2 with 50 mM D-alanine stimulation dropping the ratio down to 0.17, about two orders of magnitude lower than the basal ratio.

Table 4.4. Model prediction on the extent of NADPH/NADP$^+$ under varying production rates of mitochondrial H_2O_2. Instantaneous generation rate of H_2O_2 by DAAO-mito system and the total generation rate was determined based on the simulation results with best-fitted parameter values from experimental results. The ratio was calculated at t = 60 minutes.

D-alanine (mM)	$v_{gen,H_2O_2}^{D\text{-}ala}(\mu M/s)$	$v_{gen,H_2O_2}^{total}(\mu M/s)$	$\frac{NADPH}{NADP^+}$
0	0	4	13.4
1	1.4	5.4	10.1
5	7.1	11.1	4.8
10	14.1	18.1	2.6
15	21.2	25.2	1.7

25	35.3	39.3	0.8
50	70.7	74.7	0.2

4.4.2. Mathematical model predicts an activation of indirect NADPH shuttle system to maintain mitochondrial NADPH pools.

Additionally, we also observed an activation of NADPH influx rate upon higher perturbation **(Figure 4.4)**. For model simulation, a lack of influx rate failed to fit the model to the experimental data upon higher mitochondrial oxidative stress.

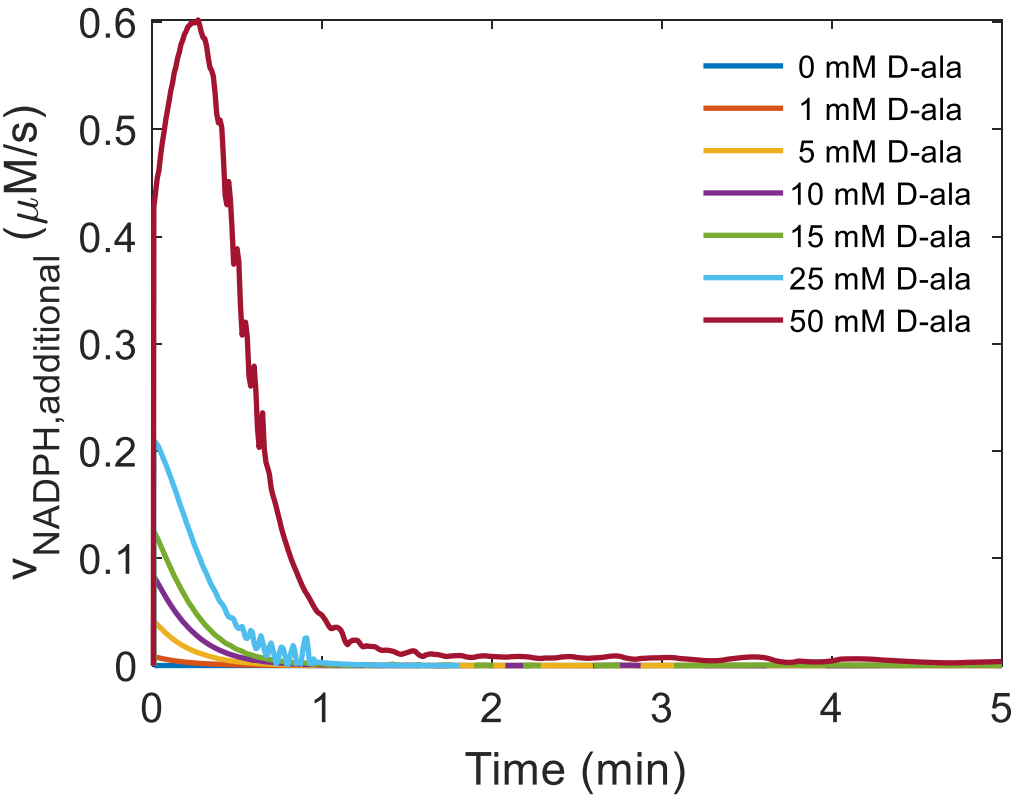

Figure 4.4. Activation of NADPH influx rate to mitochondria upon mitochondrial oxidative stress. Upon 50 mM D-alanine addition simulation, which is similar to mitochondrial oxidative stress, NADPH influx increased most.

4.5. Discussion

The main objectives of our mathematical model was to evaluate the mitochondrial NADPH concentration and NADPH/$NADP^+$ because this information was challenging to obtain solely from experimental data. As many NADPH dependent dehydrogenases in central carbon metabolism were reversible, the NADPH/$NADP^+$ ratio could alter the directionality of reaction pathways depending on the ratio. Additionally, higher fluxes of reactive oxygen species such as H_2O_2 could transiently trigger signaling processes through redox relay via protein oxidation or induction of transcriptional factors such as Nrf2, where NADPH was involved in this regulatory network via electron donors to support the antioxidant pathways[26–28].

Several genome-scale flux balance analysis (FBA) models were recently adopted to predict NADPH flux at steady-state and assessed metabolic reactions that contributed NADPH pools with constraints obtained from experimental results such as metabolite intake and uptake rates or proteome bioinformatics data [6,21]. Although these models demonstrated feasibility of identifying metabolic reactions that contributed most to NADPH pool such as folate cycle pathway, PP pathway or IDH reaction, the model was limited by the steady-state assumption and difficulty of quantifying concentration of species involved in the model. The NADPH/$NADP^+$ ratio and free pool sizes were known to vary depending on subcellular organelles, nutritional or stress conditions [24,25]. The FBA or metabolic flux analysis (MFA) could not estimate the change of NADPH pool size or its ratio as a function of time.

The kinetic model employed in our study provides time-dependent changes of NADPH concentration and subsequently mitochondrial NADPH/$NADP^+$, which was be easily determined by experiments or FBA or MFA models. Based on the model simulation, we estimated the

mitochondrial NADPH/$NADP^+$ could decrease by nearly 10-fold when mitochondrial H_2O_2 flux increased 6.3 times greater than the basal rate. This condition could be an artificial threshold line as we observed a statistically significant decrease of mitochondrial NADPH pool from the imagining experiments. Classic literature calculated the NADPH/$NADP^+$ under different diet conditions of rat liver assuming near-equilibrium states of cytosolic malic or isocitrate dehydrogenase enzymes, and indicated that the cytosolic ratio could increase up to 8.8 times higher under starved condition [25]. When the generation rate of mitochondrial H_2O_2 increased by nearly 15 times higher, the model predicted the ratio could drop to 67-fold. Additionally, the increased sensitivity of the stress-dependent NADPH flux coefficient (α) under stronger perturbations suggested an importance of additional NADPH production required to maintain mitochondrial NADPH pool. This finding suggested an increased role of NADPH transport from cytosol to mitochondria via metabolite shuttle systems. Whether cells would prefer specific shuttle systems remain to be determined.

4.6. References

1. Adimora, N. J., Jones, D. P. & Kemp, M. L. A Model of Redox Kinetics Implicates the Thiol Proteome in Cellular Hydrogen Peroxide Responses. *Antioxid. Redox Signal.* **13**, 731–743 (2010).

2. Lim, J. B., Huang, B. K., Deen, W. M. & Sikes, H. D. Analysis of the lifetime and spatial localization of hydrogen peroxide generated in the cytosol using a reduced kinetic model. *Free Radic. Biol. Med.* **89**, 47–53 (2015).

3. Huang, B. K. & Sikes, H. D. Quantifying intracellular hydrogen peroxide perturbations in terms of concentration. *Redox Biol.* **2C**, 955–962 (2014).

4. Antunes, F. & Brito, P. M. Quantitative biology of hydrogen peroxide signaling. *Redox Biol.* **13**, 1–7 (2017).

5. Letizia Canepa, A. M. gerraris. M. M. and G. F. G. Bound and unbound pyridine dinucleotides in normal and glucose-6-phosphate dehydrogenase-deficient erythrocytes. *Biochim. Biophys. Acta.* **1074**, 101–104 (1991).

6. Lewis, J. E. *et al.* Genome-scale modeling of NADPH-driven β-lapachone sensitization in head and neck squamous cell carcinoma. *Antioxid. Redox Signal.* **29**, ars.2017.7048 (2017).

7. Goto, M. K. and S. KEGG: Kyoto Encyclopedia of Genes and Genomes. *Nucleic Acids Res.* **28**, 27–30 (2000).

8. Cox, A. G., Winterbourn, C. C. & Hampton, M. B. Mitochondrial peroxiredoxin involvement in antioxidant defence and redox signalling. *Biochem. J.* **425**, 313–325 (2010).

9. McKenna, M. C. *et al.* Mitochondrial malic enzyme activity is much higher in mitochondria from cortical synaptic terminals compared with mitochondria from primary cultures of cortical neurons or cerebellar granule cells. *Neurochem. Int.* **36**, 451–459 (2000).

10. Jo, S. H. *et al.* Control of Mitochondrial Redox Balance and Cellular Defense against Oxidative Damage by Mitochondrial NADP+-dependent Isocitrate Dehydrogenase. *J. Biol. Chem.* **276**, 16168–16176 (2001).

11. Ribas, V., García-Ruiz, C. & Fernández-Checa, J. C. Glutathione and mitochondria. *Front. Pharmacol.* **5 JUL**, 1–19 (2014).

12. Wagner, B. A., Venkataraman, S. & Buettner, G. R. The rate of oxygen utilization by cells. *Free Radic. Biol. Med.* **51**, 700–712 (2011).

13. Treberg, J. R., Munro, D., Banh, S., Zacharias, P. & Sotiri, E. Differentiating between apparent and actual rates of H2O2 metabolism by isolated rat muscle mitochondria to test a simple model of mitochondria as regulators of H2O2 concentration. *Redox Biol.* **5**, 216–224 (2015).

14. Brand, M. D. Mitochondrial generation of superoxide and hydrogen peroxide as the source of mitochondrial redox signaling. *Free Radic. Biol. Med.* **100**, 14–31 (2016).

15. Haskew-Layton, R. E. *et al.* Controlled enzymatic production of astrocytic hydrogen peroxide protects neurons from oxidative stress via an Nrf2-independent pathway. *Proc. Natl. Acad. Sci.* **107**, 17385–17390 (2010).

16. Halvey, P. J. *et al.* Selective oxidative stress in cell nuclei by nuclear-targeted D-amino acid oxidase. *Antioxidants Redox Signal.* **9**, 807–816 (2007).

17. Tao, R. *et al.* Genetically encoded fluorescent sensors reveal dynamic regulation of NADPH metabolism. *Nat. Methods* **14**, 720–728 (2017).

18. Yue, H. *et al.* Insights into the behaviour of systems biology models from dynamic sensitivity and identifiability analysis: A case study of an NF-κB signalling pathway. *Mol. Biosyst.* **2**, 640–649 (2006).

19. MacDonald, M. J. Feasibility of a mitochondrial pyruvate malate shuttle in pancreatic islets. Further implication of cytosolic NADPH in insulin secretion. *Journal of Biological Chemistry* vol. 270 20051–20058 (1995).

20. Lewis, C. A. *et al.* Tracing Compartmentalized NADPH Metabolism in the Cytosol and Mitochondria of Mammalian Cells. *Mol. Cell* **55**, 253–263 (2014).

21. Fan, J. *et al.* Quantitative flux analysis reveals folate-dependent NADPH production. *Nature* **510**, 298–302 (2014).

22. Liu, L. *et al.* Malic enzyme tracers reveal hypoxia-induced switch in adipocyte NADPH pathway usage. *Nat. Chem. Biol.* **12**, 345–352 (2016).

23. Ying, W. NAD^+/NADH and $NADP^+$/NADPH in Cellular Functions and Cell Death: Regulation and Biological Consequences. *Antioxid. Redox Signal.* **10**, 179–206 (2008).

24. Goodman, R. P., Calvo, S. E. & Mootha, V. K. Spatiotemporal compartmentalization of hepatic NADH and NADPH metabolism. *J. Biol. Chem.* **293**, 7508–7516 (2018).

25. Veech, R. L., Eggleston, L. V & Krebs, H. a. The redox state of free nicotinamide-adenine

dinucleotide phosphate in the cytoplasm of rat liver. *Biochem. J.* **115**, 609–619 (1969).

26. Schieber, M. & Chandel, N. S. ROS function in redox signaling and oxidative stress. *Curr. Biol.* **24**, R453–R462 (2014).

27. Pollak, N., Niere, M. & Ziegler, M. NAD kinase levels control the NADPH concentration in human cells. *J. Biol. Chem.* **282**, 33562–33571 (2007).

28. Keleku-Lukwete, N., Suzuki, M. & Yamamoto, M. An Overview of the Advantages of KEAP1-NRF2 System Activation During Inflammatory Disease Treatment. *Antioxid. Redox Signal.* **29**, 1746–1755 (2017).

Chapter 5

Influence of nutrients to cytosolic and mitochondrial NADPH dynamics

5.1. Abstract

Cancer cells were capable of acquiring specific nutrients from an often nutrient-poor environment and metabolize these nutrients to meet the demands of unregulated and rapid growth. Major substrates of cellular NADPH were known to be glucose, glutamine, and serine. However, it was unclear how cells coordinated available nutrient sources to maintain compartment-specific NADPH pool. Here, I measured the changes of cytosolic and mitochondrial NADPH leves under varying nutrient conditions.

5.2. Introduction

Nutrient availability influences metabolic phenotypes [1]. Warburg suggest highly proliferating cells such as cancer cells use glucose to produce lactate via glycolysis despite the presence of oxygen[2]. This phenomenon, called aerobic glycolysis, is a core of cancer metabolism in which cancer cells increase glucose consumption in comparison to non-proliferating normal cells[3]. Recent cancer metabolism studies have focused more on defining fuels that contribute to different metabolic phenotypes of cancer cells, and whether exploiting these differences can lead to effective cancer therapeutics. Besides glucose and glutamine, a variety of other nutrients and metabolic pathways have recently been evaluated to find their metabolic functions[4]. These include cancer cells utilizing serine, lactate, fatty acids, branched amino acids, and glycine as a fuel to meet the metabolic demands of diverse cancer cells. Not only these nutrients are catabolized to provide essential building blocks for macromolecular synthesis, but also many of these nutrients undergo reduction and oxidation reactions, influencing cellular redox states[5].

Reduction reactions require NADPH as an electron donor, whereas oxidation reactions require NAD^+ as an electron acceptor. NADPH needs to be constantly regenerated from $NADP^+$ to maintain reducing environment and support biosynthetic processes, whereas NAD^+ regeneration is required to support glycolysis and TCA cycle functions[6]. Additionally, many of metabolic enzymes use NAD(P)H as cofactors and are reversible. The change of redox states influence metabolic enzyme directions and subsequently metabolic pathways. Further, NADPH is impermeable to intracellular membrane, suggesting NADPH redox states are different in subcellular organelles[7]. Therefore, it is essential to assess the influence of nutrient availability and metabolic pathways to compartmentalized NADPHH redox states.

Glucose, glutamine, and serine have been considered as major substrates for regenerating cellular NADPH redox states[8,9]. For instance, glucose metabolism involves in regenerating NADPH in both cytosol and mitochondria. Through pentose phosphate (PP) pathway, one mole of glucose can generate up to 2 to 12 molecule of cytosolic NADPH[2]. Glucose can be further metabolized through TCA cycle, making isocitrate. Through isocitrate dehydrogenase (IDH2) reaction one mole of NADPH can be regenerated in mitochondria. Malate, another intermediate of TCA cycle, can be transported out to cytosol and make NADPH through malic enzyme, while making pyruvate[10].

Another principal nutrient source for cell growth in mammalian cells is glutamine. Glutamine not only provide carbon sources that fuel TCA cycle but also nitrogen for amino acid synthesis[11]. Glutamine can be catabolized to glutamate, which can be deaminated through glutamate dehydrogenase, making one mole of NADPH. Glutamate can also be converted to α-KG though glutamate-aspartate transaminase (GOT), followed by malate dehydrogenase and malic enzyme reactions making one mole of NADPH in cytosol[12].

Lastly, extracellular serine has been reported to be a source of cytosolic or mitochondrial NADPH regeneration through folate-dependent one carbon metabolism[8]. Depending on the direction of one carbon metabolism cycle, one mole of serine can produce one mole of NADPH in cytosol via Methylenetetrahydrofolate Dehydrogenase (MTHFD1) or in mitochondria via the isoform of MTHFD enzyme[13]. Recent study reveal a high concentration of folate in media mediates production of NADPH in mitochondria, whereas at physiologically relevant concentration NADPH is regenerated in cytosol[14]. The extent of generation rate in cytosol or mitochondria also depends on different cancer cells.

Here, I examine cytosolic and mitochondrial NADPH levels in a variety of cancer cells that are grown in different nutrient conditions. I specifically modulate glucose, glutamine, and serine concentration in media as they are regarded as important substrates for maintenance of compartmentalized NADPH redox states. Under varying nutrient conditions, I measure cytosolic and mitochondrial NADPH levels using iNap sensors, followed by growth rates under respective experimental conditions. Next, I relate the compartmentalized NADPH redox states to other redox parameter values, intracellular metabolites level, and growth rates.

5.3. Materials and Methods

5.3.1. Generation of cells lines that stably express iNap sensors

Details of the stable cell line development were reported in Chapter 2. In brief, I collected lentivirus that contains plasmids of iNap, iNap-mito, iNap-ctr, and iNap-mito-ctr sensors. Then, I seeded Hela, A549, MDA-MB-231, and HCT-116 cells in 35 mm well of 6 well plates. When cells reach 70 – 90% confluency, I added lentiviral solution to the media with 6 μg/ml of

polybrene. After 3 days of infection, cells from each well were expanded to 10 cm dish with 6 μg/ml puromycin selection media for about 7 days until 70–90% confluency.

5.3.2. Imaging analysis with CellProfiler

CellProfiler, a high-throughput cell image analysis software, was used to identify cells from images and quantify pixel values of the identified objects[15]. In brief, we modulated the image processing, illumination correction, object identification, and measurement modules. For background subtraction, we applied EnhanceOrSuppressFeatures module to enhance objects from background. Then, we applied threshold using Otsu thresholding method with threshold smoothing scale and correction factors. Afterwards, we used IdentifyPrimaryObjects module to automatically identify cells while setting typical diameter objects in pixel units. Once the objects were selected, we applied MeasureObjectIntensity module to calculate the mean intensity of the identified objects. The results were further exported as an excel file and MATLAB was used to process the output data.

5.3.3. Quantification of NADPH level

Methods for sensor calibration and quantification of NADPH level were described in detail in chapter 4. In brief, we calibrated the iNap sensor by suturing the sensor output, which is a fluorescence ratio between F_{415nm}/F_{488nm} with 4 mM NADPH while treating cells with digitonin. To deplete the sensor signal, we treated cells with 1 mM of digitonin. After obtaining both maximum and minimum sensor output, we converted the output to NADPH using a Hill's equation.

5.4. Results

5.4.1. Monitoring cytosolic NADPH dynamics in single cells using iNap sensors and CellProfiler

We designed a system to quantify cytosolic and mitochondrial NADPH dynamics in large numbers of samples. The system mainly consisted of three steps: generation of cell lines that constitutively expressed NADPH sensors to either cytosol or mitochondria, monitoring of single-cell NADPH dynamics over time, and analysis of compartmentalized NADPH dynamics of large numbers of single-cell data (**Figure 5.1**). As a tool to measure cytosolic and mitochondrial NADPH, we used iNap sensors, which are genetically encoded and can be expressed in subcellular organelles such as mitochondria[16]. In general, a fluorescence ratio between 415 and 488 nm was represented as a sensor readout, with the increase of ratio indicating an increase of NADPH levels. However, since iNap sensor was sensitive to pH change at 488 nm emission wavelength and mitochondrial pH fluctuates depending on metabolic demands, we accounted the pH effect by normalizing the fluorescence ratio of iNap to that of iNap-control sensor, which had no binding affinity to NADPH but only pH. We defined NADPH index, which was a pH-corrected iNap fluorescence ratio, and used this output as a proxy to NADPH level.

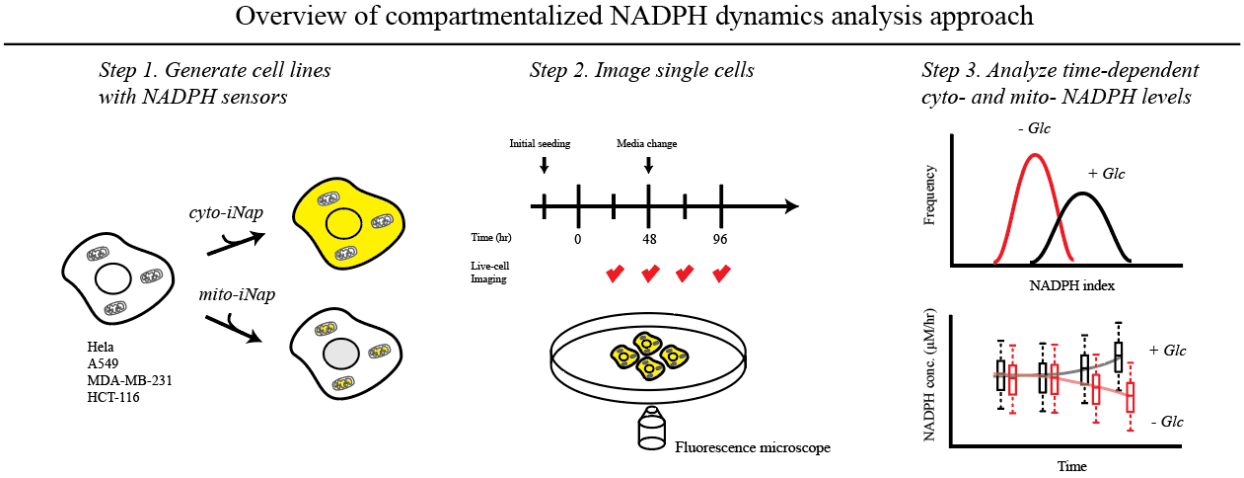

Figure 5.1. Schematics representing a system to assess cytosolic and mitochondrial NADPH dynamics.

$$\text{NADPH index} = \frac{\text{Fluorescence ratio}_{\text{iNap}}}{\text{Fluorescence ratio}_{\text{iNap-ctr}}}$$

For an imaging analysis platform, we used a CellProfiler software[17] and optimized a pipeline that allowed automated background subtraction, identification of cells, and measurement of a fluorescence ratio of iNap sensors for large number of samples. To validate the CellProfiler based imaging analysis and quantification of cytosolic and mitochondrial NADPH, we used Hela cell lines that stably expressed either iNap, iNap-ctr, mito-iNap, or mito-iNap-ctr[18]. We cultured the cell lines either regular DMEM + 10 % FBS condition or under glucose deprived conditions for 96 hours. We confirmed that single cells expressing iNap sensors were identified as individual objects after three classes Otsu thresholding method (**Figure 5.2**).

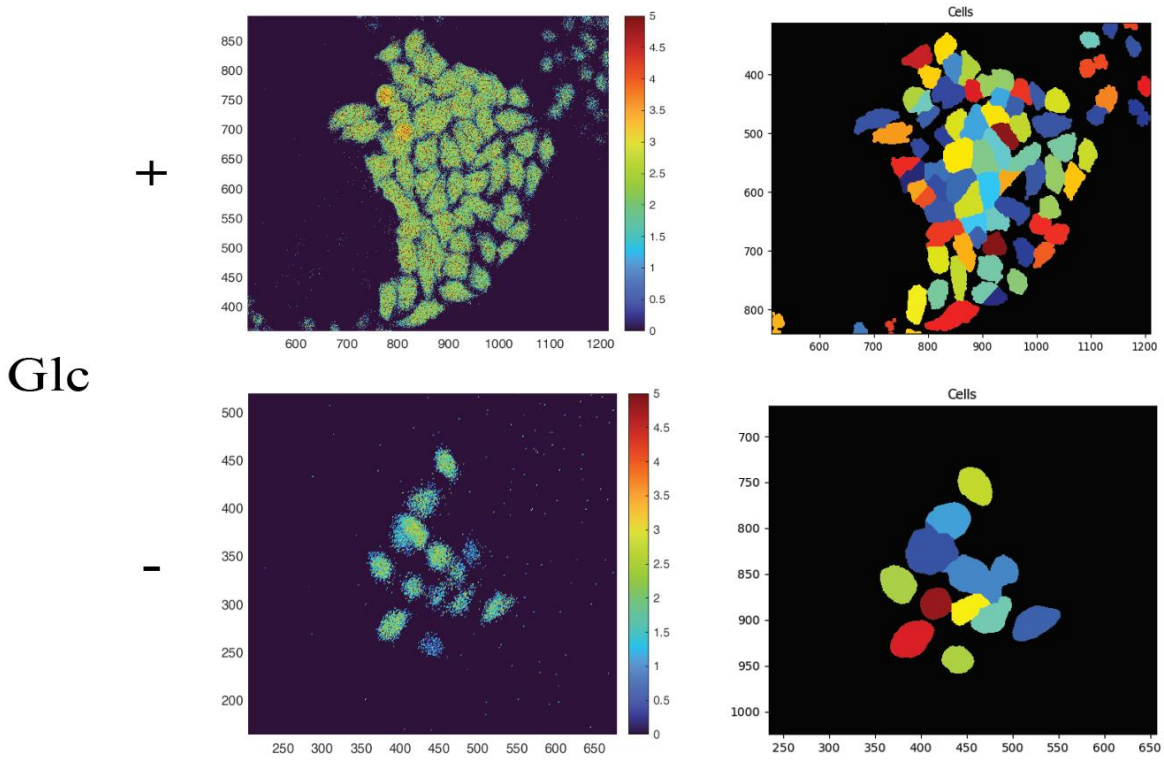

Figure 5.2. CellProfiler image analysis identifies Hela cells expressing iNap sensors. Hela-iNap were grown either regular DMEM with 10% FBS media or glucose deprived media. Images were taken after 96 hours.

Single cells' corresponding fluorescence intensities at 415 and 488 nm were measured subsequently. The mean fluorescence ratio of iNap of cells growing under DMEM + 10 % FBS was 2.84 and a total number of cells captured in one technical image was 183. On the other hand, the mean fluorescence ratio of iNap under glucose-deprived condition decreased to 1.89 for a total of 38 cells (**Figure 5.3**). We also confirmed that CellProfiler based imaging acquisition and analysis of iNap fluorescence ratio was consistent with the ImageJ based imaging analysis (**Figure 5.4**).

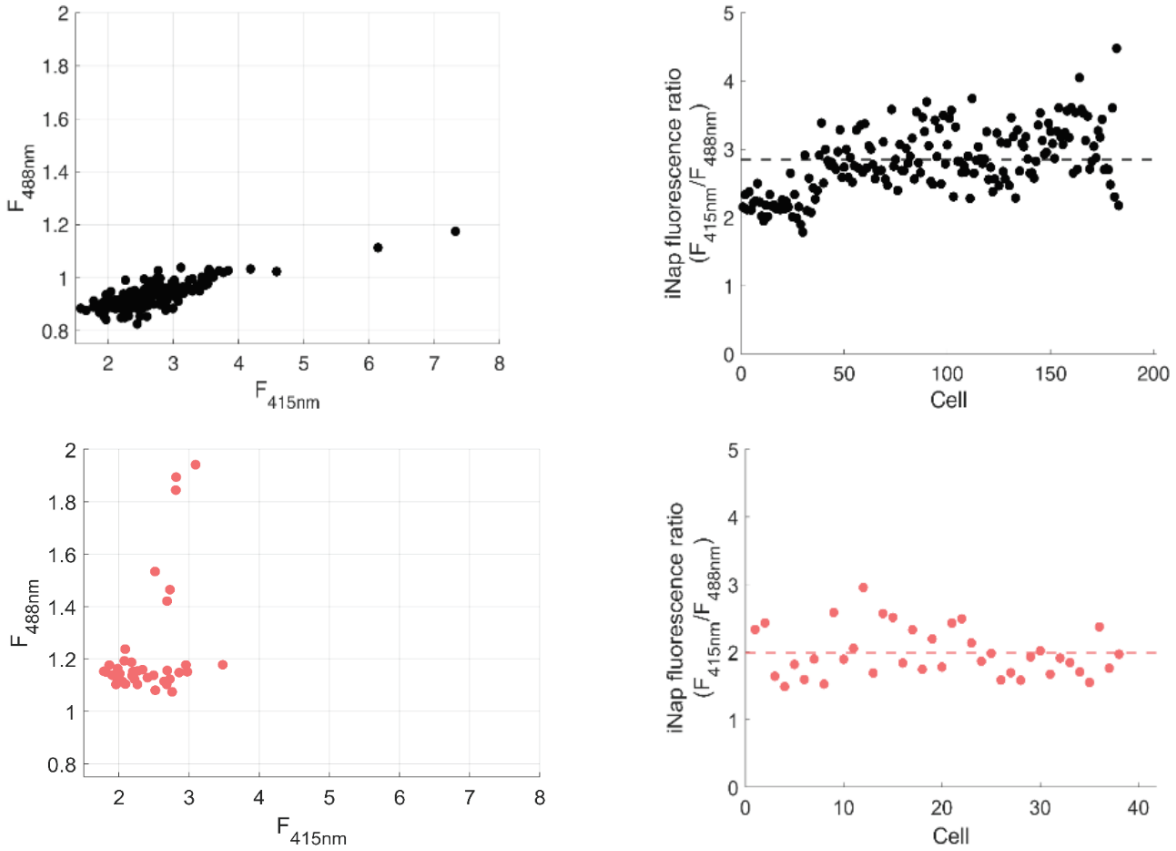

Figure 5.3. Quantification of fluorescence intensities emitted from cpYFP of iNap sensor when Hela-iNap cells were excited at 415 nm and 488 nm. Top row represents either intensities at single excitation value or ratios obtained from Hela-iNap grown in regular growth media, whereas the bottom row represents Hela-iNap cells grown in glucose deprived condition. The right column represents that iNap fluorescence ratio against each of Hela-iNap cells.

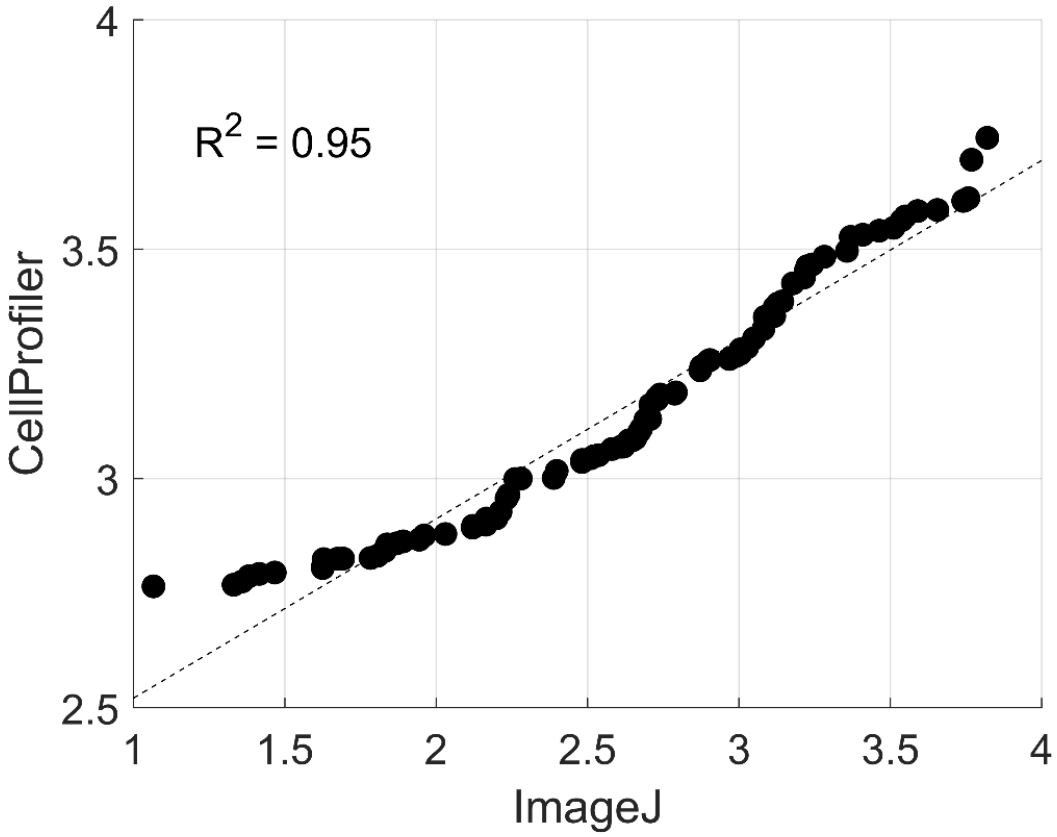

Figure 5.4. iNap fluorescence ratio were obtained based on CellProfiler and ImageJ image analysis software, confirming both software provides similar values that are linearly correlated.

For each experiment, we repeated imaging experiments for at least five technical replicates and three biological replicates, revealing that the mean ratio of iNap fluorescence decreased by 23% under glucose deprived condition (**Figure 5.5A**). To calculate NADPH index, we measured the fluorescence ratio of iNap-ctr and used it as a normalization factor to the iNap fluorescence ratio (**Figure 5.5B and C**).

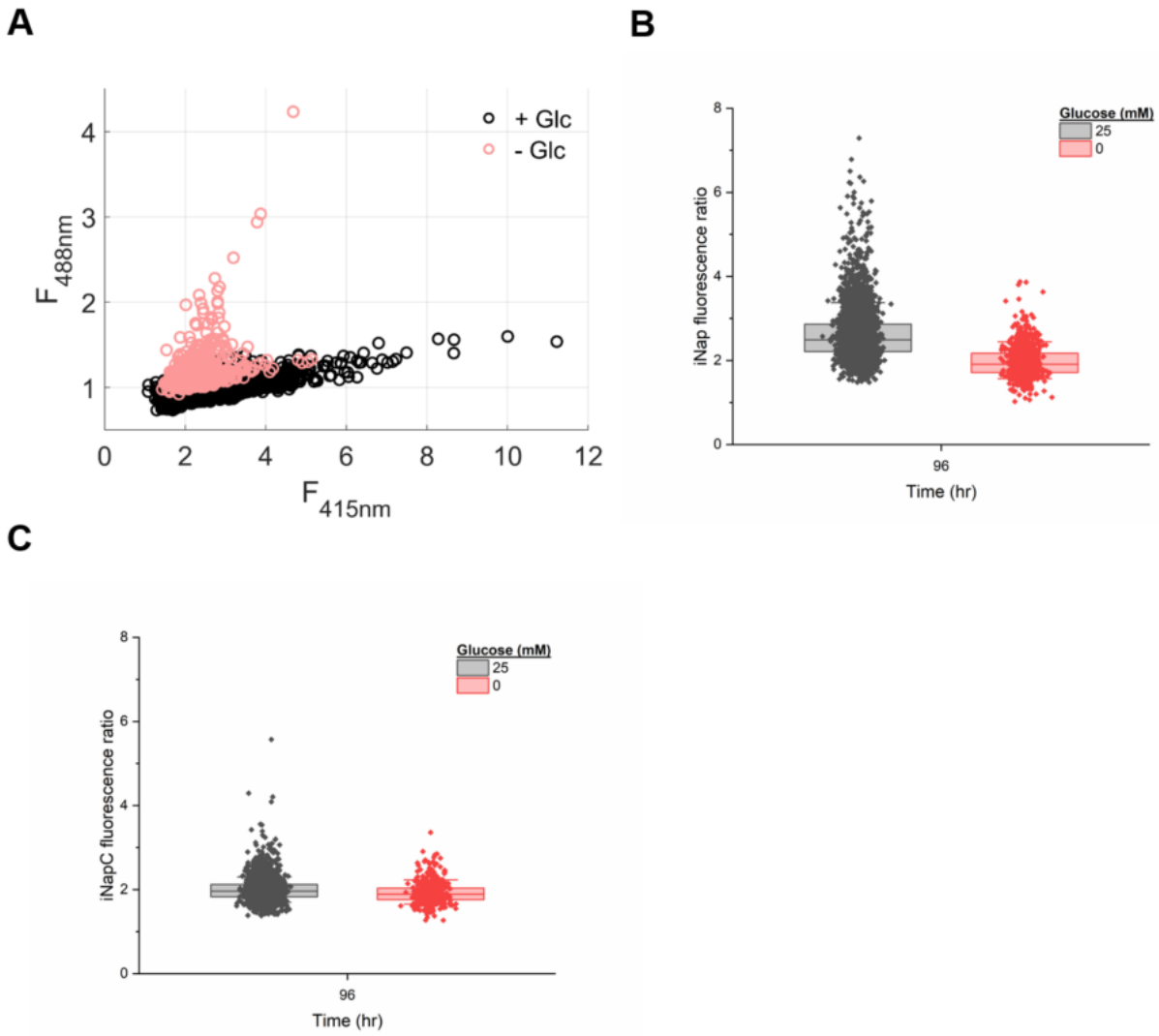

Figure 5.5. iNap and iNap-ctr fluorescence ratio are quantified. (A) The fluorescence emission values at 515 nm under excitation at 415 nm and 488 nm were plotted under media with or without glucose. **(B)** iNap fluorescence ratio, which is $F_{415\ nm}/F_{488\ nm}$ were calculated under two different conditions. **(C)** iNap-ctr fluorescence ratio was calculated under two different conditions.

The median cytosolic NADPH index decreased by 20 % under glucose deprived condition. Hela cells growing under DMEM + 10 % FBS revealed the median of cytosolic NADPH index to be 1.25 for a total of 3460 cells. On the other hand, the median for glucose deprived condition was 0.99 based on 751 cells (**Figure 5.6**). Coefficient of variation (CV) analysis on the three biological replicates revealed there was no significant difference between these two conditions (**Figure 5.7**).

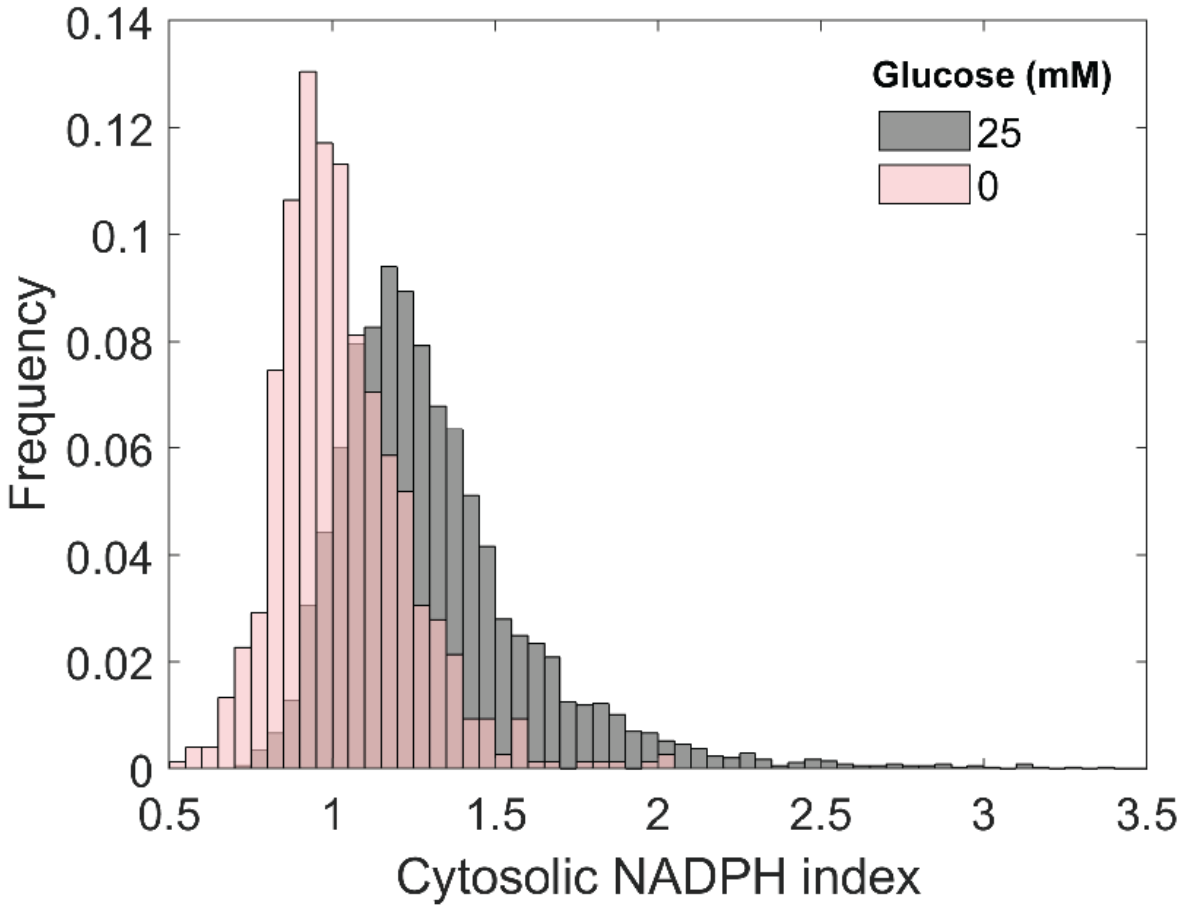

Figure 5.6. Histogram representing cyto-NADPH index**.** Hela-iNap cells were grown under media with or without glucose. The NADPH index is calculated by dividing the iNap fluorescence ratio to iNap-ctr fluorescence ratio. The NADPH index accounts of the possible pH effects that may influence iNap fluorescence ratio.

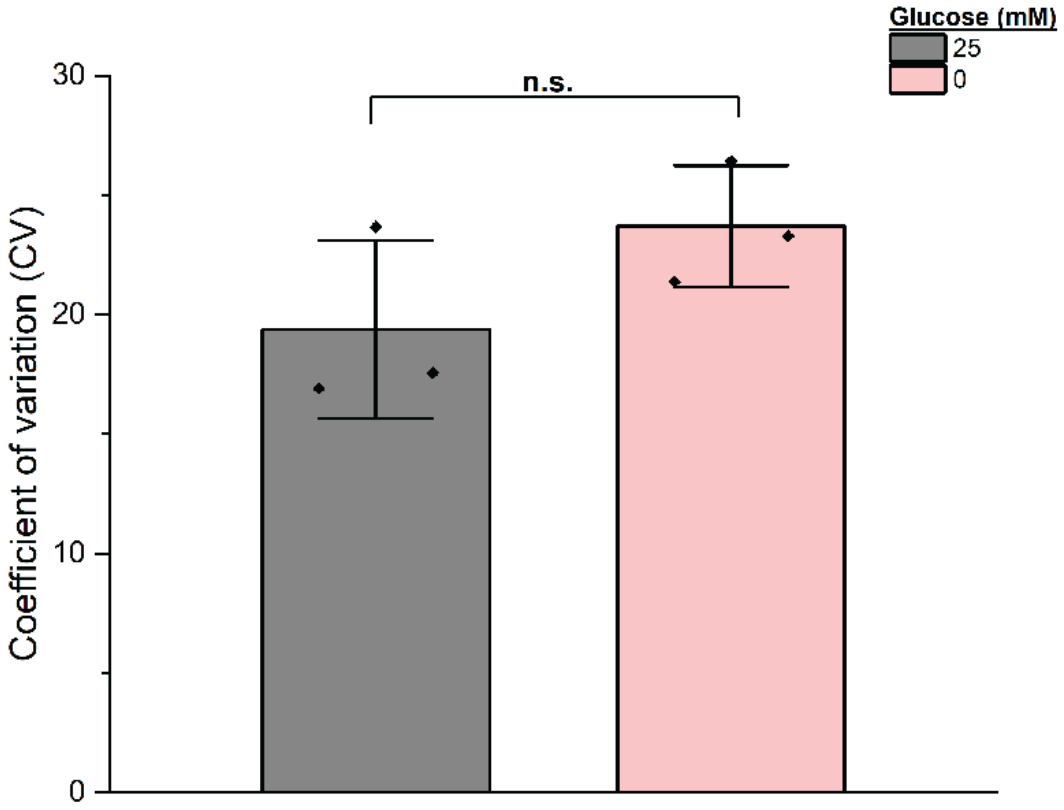

Figure 5.7. Coefficient of variation of NADPH index at 96 hours**.** The mean NADPH index was obtained from three biological replicates under glucose containing or deplete conditions.

We further converted NADPH index to concentration after calibrating the sensor with a previously reported method[16,18]. In brief, we measured both maximum and minimum NADPH index by either saturating the NADPH index with 4 mM NADPH after treating cells with optimized concentration of digitonin, or depleting NADPH by using oxidizing reagent such as diamide (**Figure 5.8**A). These measurements allowed to estimate a fraction of NADPH bound to the sensor and subsequently can be converted to the concentration (**Figure 5.8B**). After the calibration of sensor, we converted the NADPH index to concentration (**Figure 5.8C**). At 48 hours, the median concentration of cytosolic NADPH decreased from 2.09 to 1.9 µM under glucose-deprived condition, which was about 9.1% decrease of concentration. At 96 hours, the median concentration decreased from 2.55 to 1.6 µM, which was about 37.3% decrease.

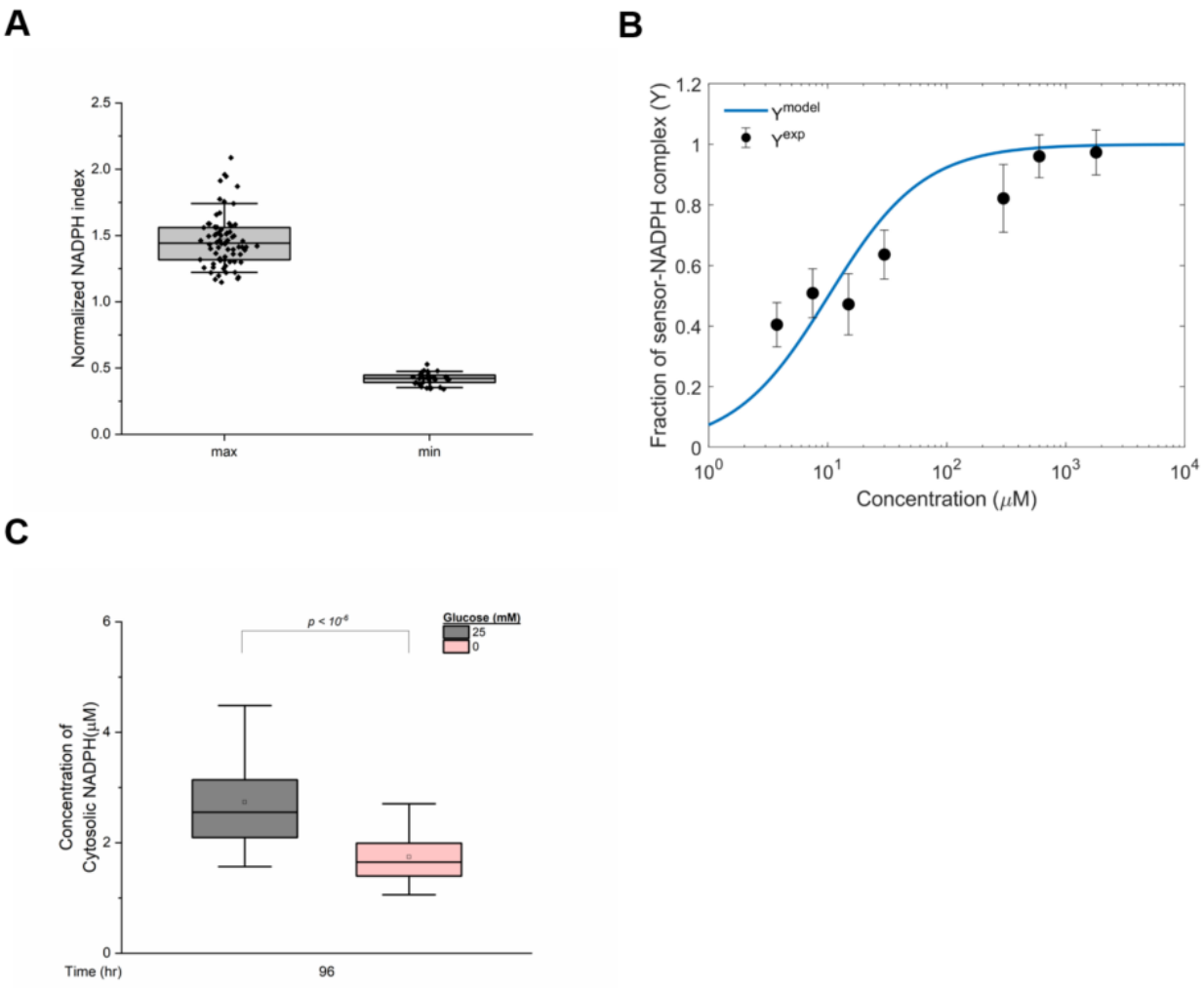

Figure 5.8. Conversion of NADPH index to concentration**. (A)** The maximum and minimum cytosolic NADPH index were calculated. The mean value of normalized NADPH index represented 46 % increase for maximum value and 59% decrease for the minimum value. The maximum value of NADPH index is 1.68 and the minimum value if 0.42. **(B)** The fraction of sensor-NADPH complex ($Y^{exp} = \frac{R'-R'_{min}}{R'_{max}-R'_{min}}$) is plotted against different NADPH concentration added to the media. The line represents a theoretical value, which can be calculated by $Y^{model} = \frac{NADPH}{K_d+NADPH}$. **(C)** The conversion of NADPH index to concentration at 96 hours. The input data is from Figure 1.6.

5.4.2. Monitoring mitochondrial NADPH dynamics using CellProfiler

Next, we assessed Hela cell lines that stably expressed mito-iNap sensors applying the same pipeline used for cytosolic NADPH analysis. First, we selected a sample image to adjust

parameter settings that identify cells expressing mitochondrial NADPH sensors under glucose present or deprived conditions (**Figure 5.9**). Under a regular media condition, 124 cells were identified and the mean fluorescence ratio was 2.56, whereas a total of 14 cells were identified under glucose-limited condition and the mean fluorescence ratio was 2.43 (**Figure 5.10**). Overall, the mean fluorescence ratio of mito-iNap decreased by 26 % from 2.65 to 1.98 (**Figure 5.11**).

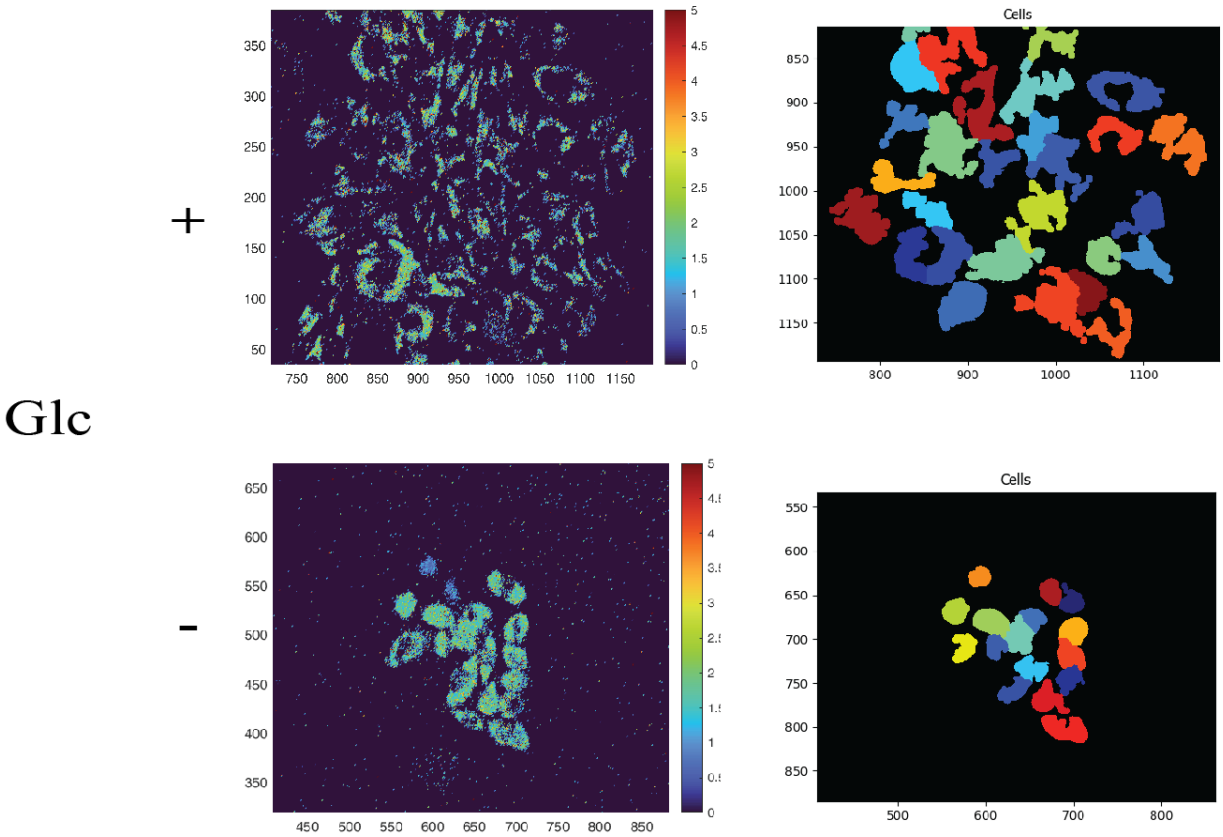

Figure 5.9. CellProfiler image analysis identifies Hela cells expressing mito-iNap sensors. Hela-mito-iNap were grown either regular DMEM with 10% FBS media or glucose deprived media. Images were taken after 96 hours.

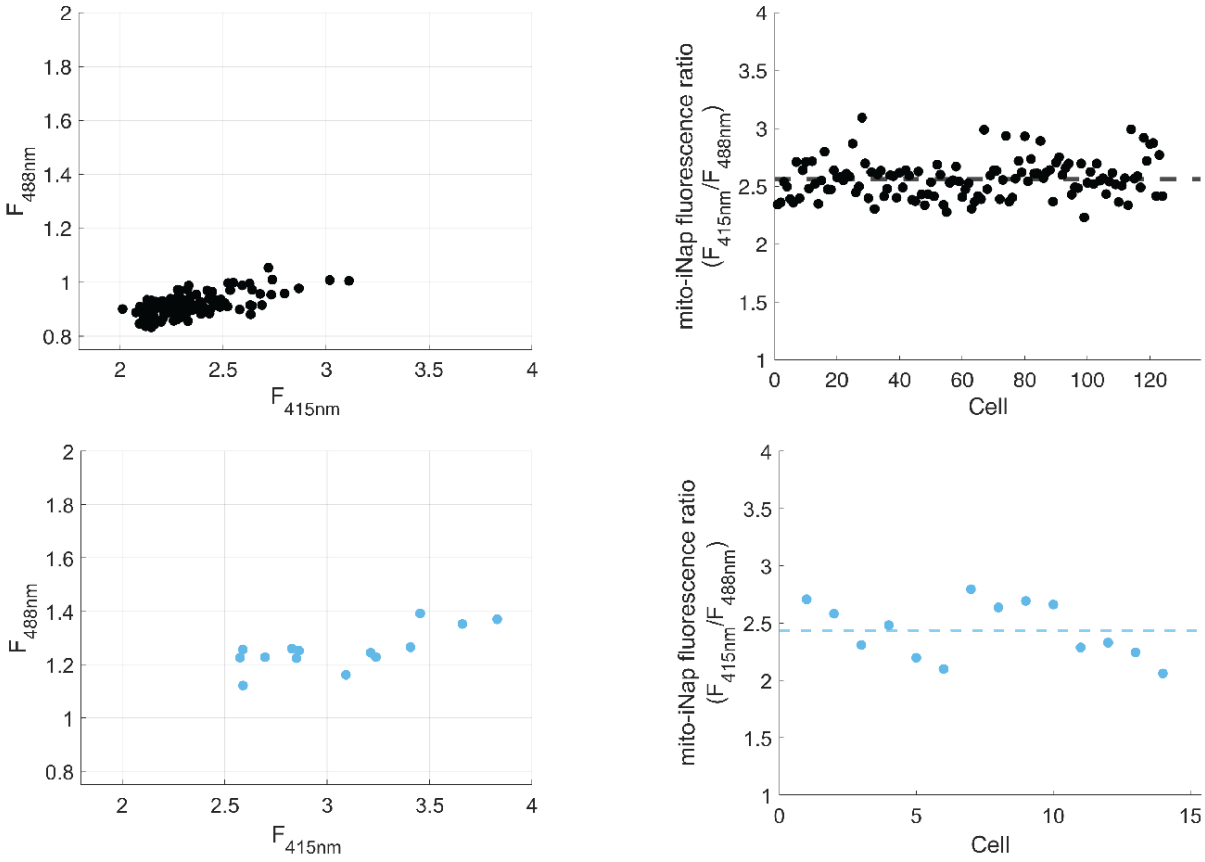

Figure 5.10. Quantification of fluorescence intensities at 415 and 488 nm and the corresponding ratio from mito-iNap sensors. Top row represents the fluorescence intensities obtained from Hela-mito-iNap cells grown in regular growth media, whereas the bottom row represents Hela-mito-iNap cells grown in glucose deprived condition. The right column represents that mito-iNap fluorescence ratios, with black dots representing a control and the blue representing the glucose deprived condition.

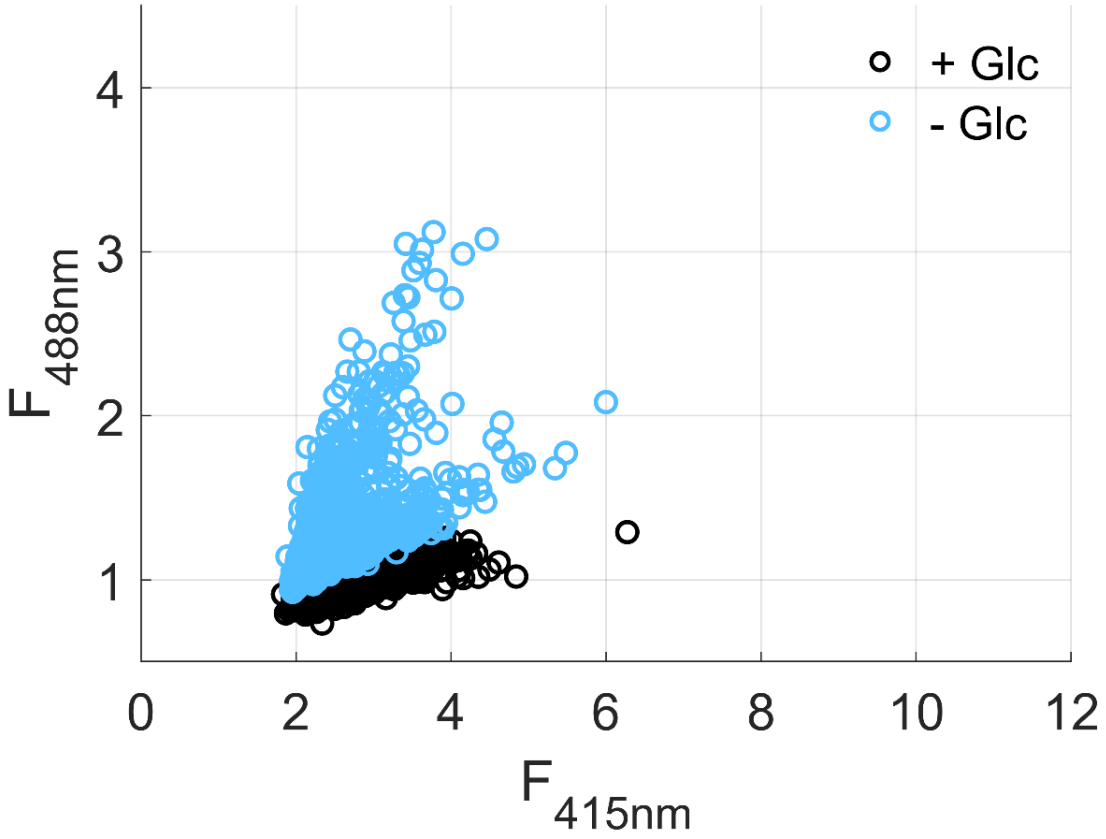

Figure 5.11. Mito-iNap fluorescence intensities upon excitation of 415 nm and 488 nm. Hela-mito-iNap cells were grown in media with or without glucose for 96 hours. The fluorescence emission was set at 515 nm and the two excitation wavelengths were set at 415 and 488 nm.

For mitochondrial NADPH index, the median index under glucose deprived condition decreased by 13.8 % compared to the control. The median for control was 1.23 based on 1561 cells and that of glucose deprived condition was 1.06 based on 917 cells (**Figure 5.12**). CV analysis revealed the variation of mitochondrial NADPH from individual cells was greater under glucose deprived conditions (**Figure 5.13**).

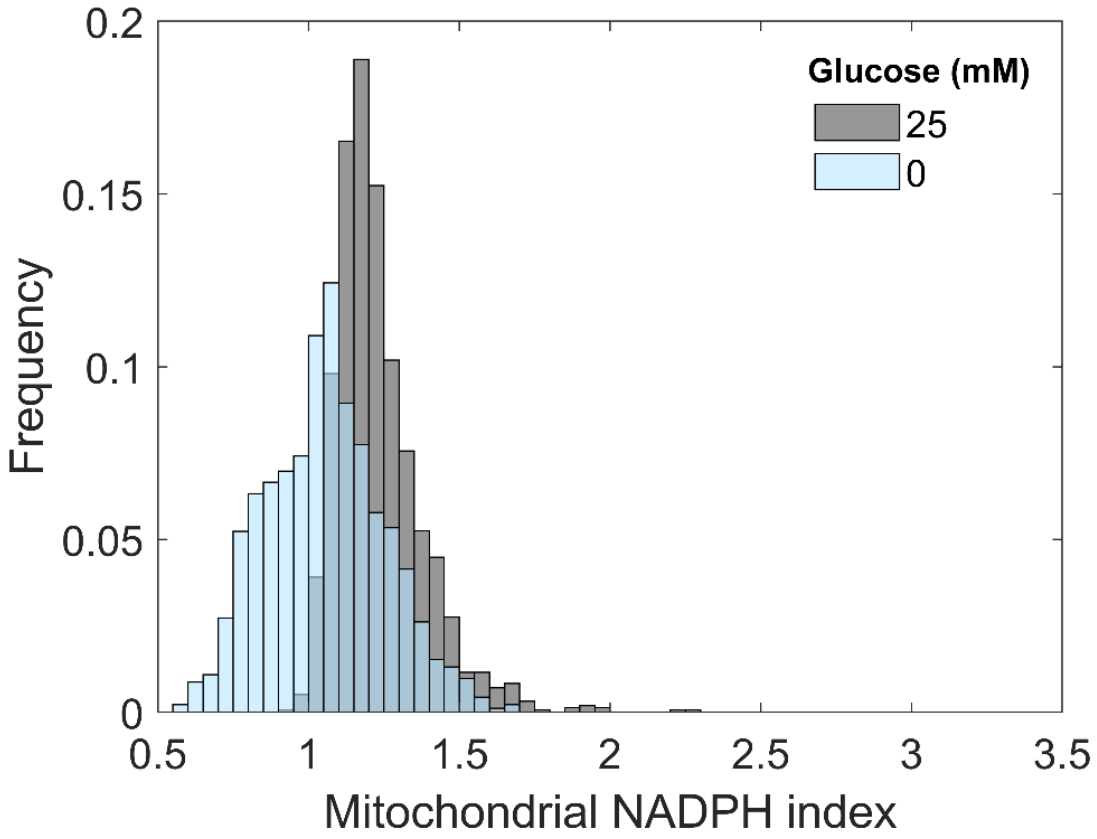

Figure 5.12. Histogram representing mito-NADPH index. Hela-mito-iNap cells were grown under media with or without glucose. The mito-NADPH index is calculated by dividing the mito-iNap fluorescence ratio to mito-iNap-ctr fluorescence ratio. The mito-NADPH index accounts of the possible pH effects that may influence mito-iNap fluorescence ratio.

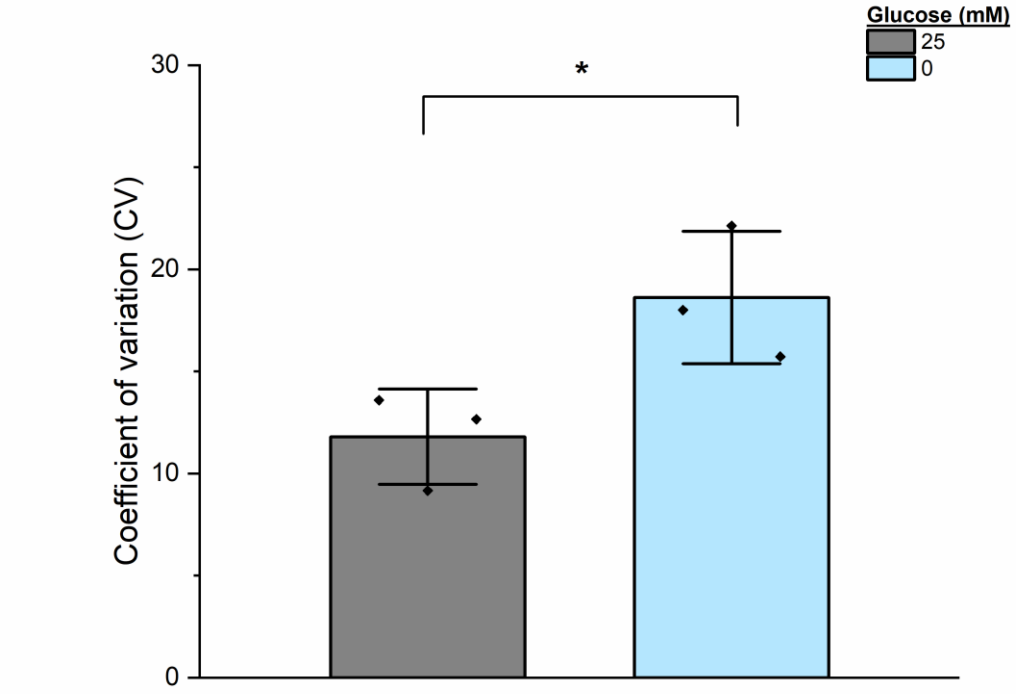

Figure 5.13. Coefficient of variation of mito-NADPH index at 96 hours**.** The mean mito-NADPH index was obtained from three biological replicates under glucose containing or deplete conditions.

Similar to the cytosolic NADPH calculation, we converted the mitochondrial NADPH index to concentration using the previously measured calibrated parameter values. We used previously measured maximum and minimum parameter values, which are 1.96 and 0.43 respectively[18]. Additionally, we used 3.6 µM for K_d. Detailed calibration methods can be found in chapter 4. The mean concentration of mitochondrial NADPH is 31.2 µM and it decreases to 27.1 µM in glucose deprived condition. The basal concentration was lower than 42 µM, which was calculated in our previous report. It may be due to a new media that was reconstituted with powders generated from different vendors (**Figure 5.14**).

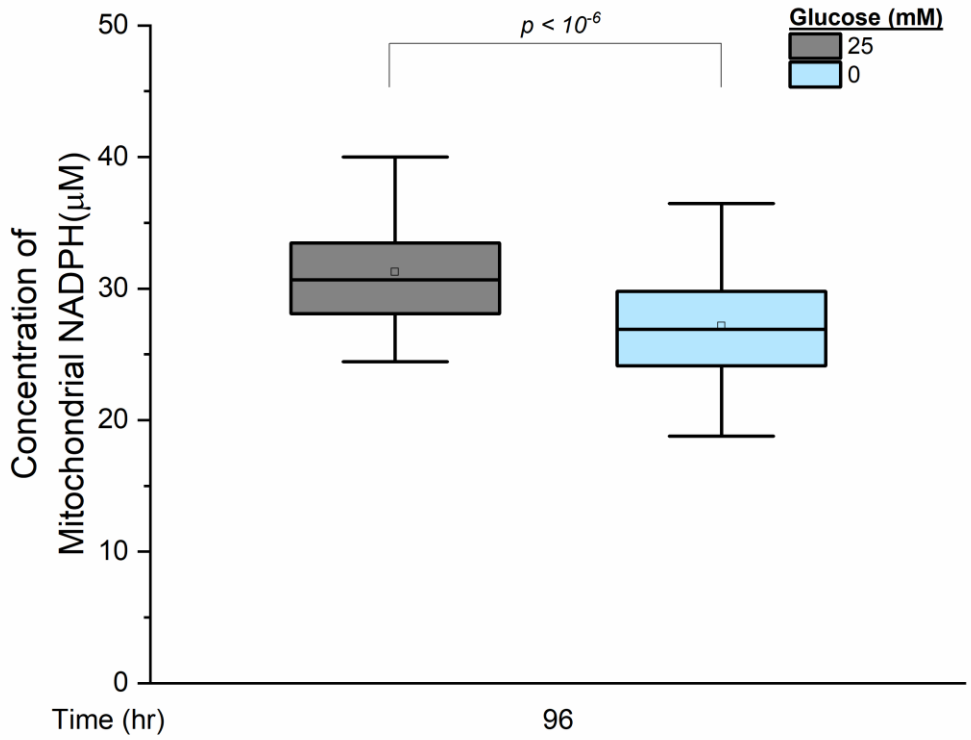

Figure 5.14. Concentration of mitochondrial NADPH.

Lastly, the average rate of change of cytosolic and mitochondrial NADPH is calculated based on the values obtained at 48 and 96 hour time points for presence or absence of glucose conditions (**Figure 5.15**). The median cytosolic NADPH rate for glucose present condition is 6.8 nM/hr and it became -7.7 nM/hr for glucose deprived condition conditions (**Figure 5.15C**). The median mitochondrial NADPH is 31.7 nM/hr whereas it become -5.9 nM/hr for glucose deprived condition (**Figure 5.15D**).

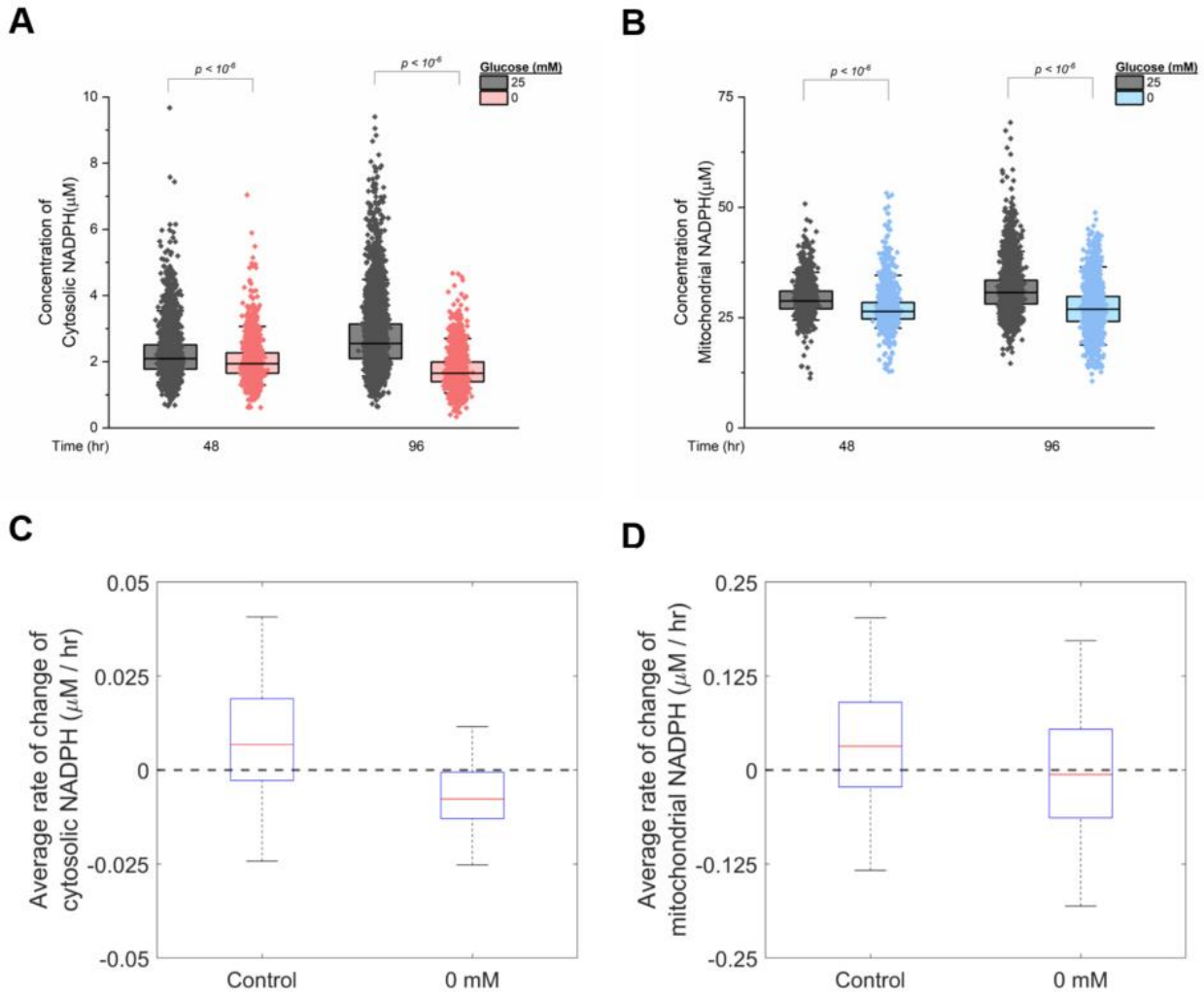

Figure 5.15. Cytosolic and mitochondrial NADPH concentration at 48 and 96 hours and the average rate of change of NADPH levels between the two time points. (A) The cytosolic and (B) mitochondrial NADPH concentration at 48 and 96 hours. The average rate of change of (A) cytosolic and (B) mitochondrial NADPH.

5.4.3. Lack of glucose or low glucose availability decreases both cytosolic and mitochondrial NADPH levels

For mammalian cells, glucose is considered a key carbon source that can be partially used for production of cytosolic NADPH via oxidative pentose phosphate pathway, isocitrate dehydrogenase, and malic enzymes[5,7]. As glucose is readily consumed by cancer cells, glucose

can be limited under certain tumor microenvironment[19]. To test how extracellular glucose concentration influences cytosolic and mitochondrial NADPH levels, I modulate glucose condition in media and monitor compartmentalized NADPH levels every day for four days **(Figure 5.16)**. Within two hours, the lack of glucose or 1 mM glucose concentration elevated the median cytosolic NADPH index up to 4.3 %. After 24 hours, the extent of increase was reduced. Cytosolic NADPH index decreased by 3 % for 6 mM glucose condition, increased by 1 % for 1 mM, and 2 % for 0 mM glucose conditions. After 48 hours, the median cytosolic NADPH index started to decrease proportionally. Cytosolic NADPH index decreased by 4.7% in absence of glucose after 48 hours. After 72 hours, the median cytosolic NADPH index decreased by 3, 15, and 22 % for 6, 1, 0 mM glucose conditions. Lastly, after 96 hours, the difference becomes greater as cytosolic NADPH index decreases by 10, 22, and 24% for 6, 1, 0 mM glucose conditions **(Figure 5.16A).**

Similarly, we monitored the change of mitochondrial NADPH index over 96 hour under varying glucose concentrations **(Figure 5.16B).** After 2 hours, we observed the mitochondrial NADPH index decreased by 5 and 3 % for 6 and 1 mM conditions. After 24 hours, we observed the mitochondrial NADPH index increased by 1, 4.5, and 2.5% for 6, 1, and 0 mM glucose conditions. Similar to cytosolic NADPH index, the median cytosolic NADPH index started to decrease proportionally after 48 hours. Absence of glucose lowered the mito-NADPH index by approximately 7 %. After 72 hours, the median mito-NADPH index decreased by approximately 10% in glucose deprived condition. Lastly, the median mitochondrial NADPH index decreased by -11.6, -10.3, and -10 % for 6, 1, and 0 mM glucose conditions compared to 25 mM glucose condition. When the cyto- and mito- NADPH indices were compared to those of control at

specific time points and plotted against each other, we did not observe a strong linear change between these two values (**Figure 5.17**).

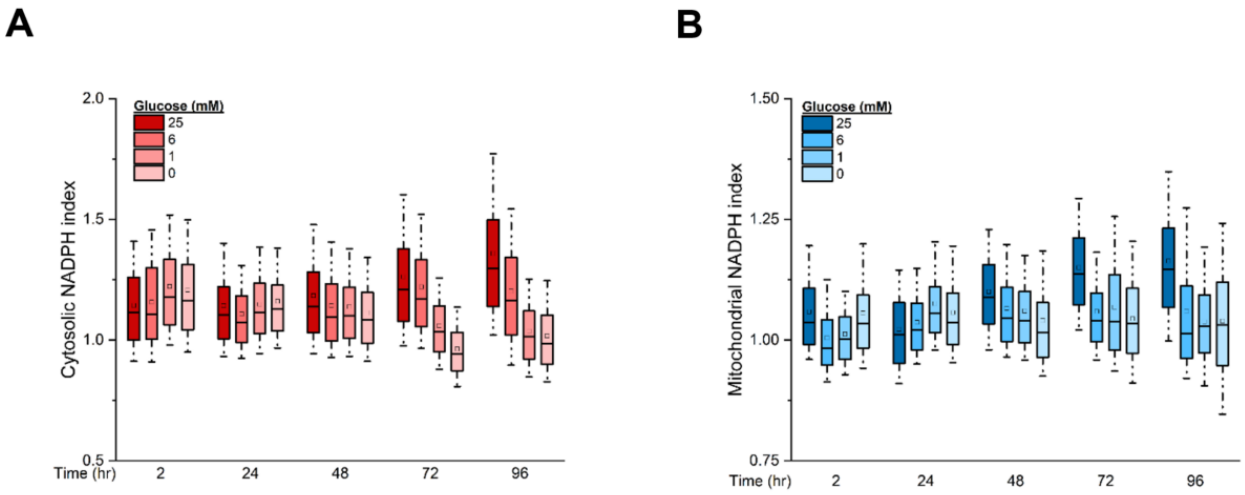

Figure 5.16. Cytosolic and mitochondrial NADPH indices under different concentrations of glucose in media. (A) Cytosolic NADPH index was measured under varying glucose concentration from 2 to 96 hours. (B) A relative change of cytosolic NADPH index was calculated by dividing the difference between the indices at 48 and 96 hours to the index at 48 hour. Boxes represents 10^{th}, 25^{th} , 50^{th} , 75^{th}, and 90^{th} percentiles.

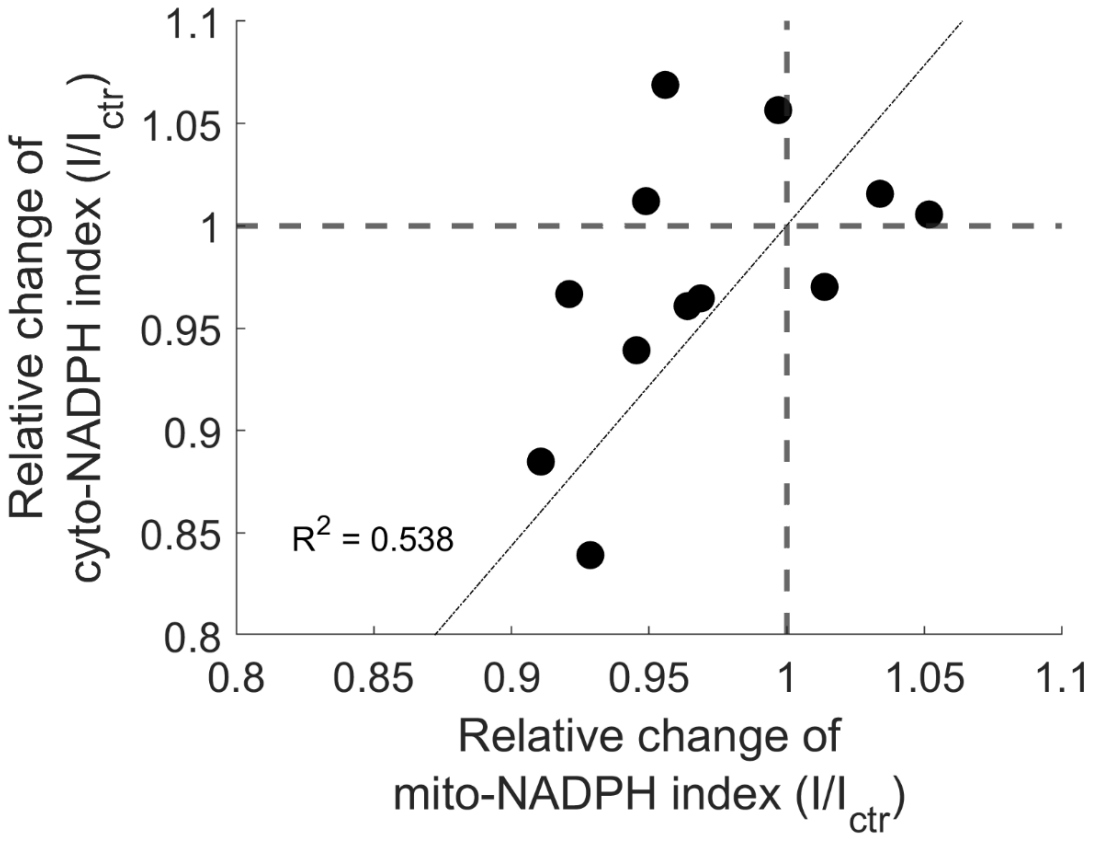

Figure 5.17. Relationship between the relative changes of cyto- and mito- NADPH indices across different time points.

Next, we calculated the relative change of cyto-NADPH index between 48 and 96 hours to determine how the cyto-NADPH indices changes over time at specific condition (**Figure 5.18).** When cells were growing under regular 25 mM glucose growth media condition, cytosolic NADPH increased by 9.4 % over 48 hours, but it decreased by approximately -2% for 6 mM glucose condition, and approximately 11% for either 1 or 0 mM glucose conditions (**Figure 5.18A).** We also calculated the relative change of mito-NADPH index between 48 and 96 hours. The relative changes of mito-NADPH index relative to 48 hours for each experimental condition were 4, -8, -7, and -6% for 25, 6, 1, and 0 mM glucose conditions (**Figure 5.18B)**.

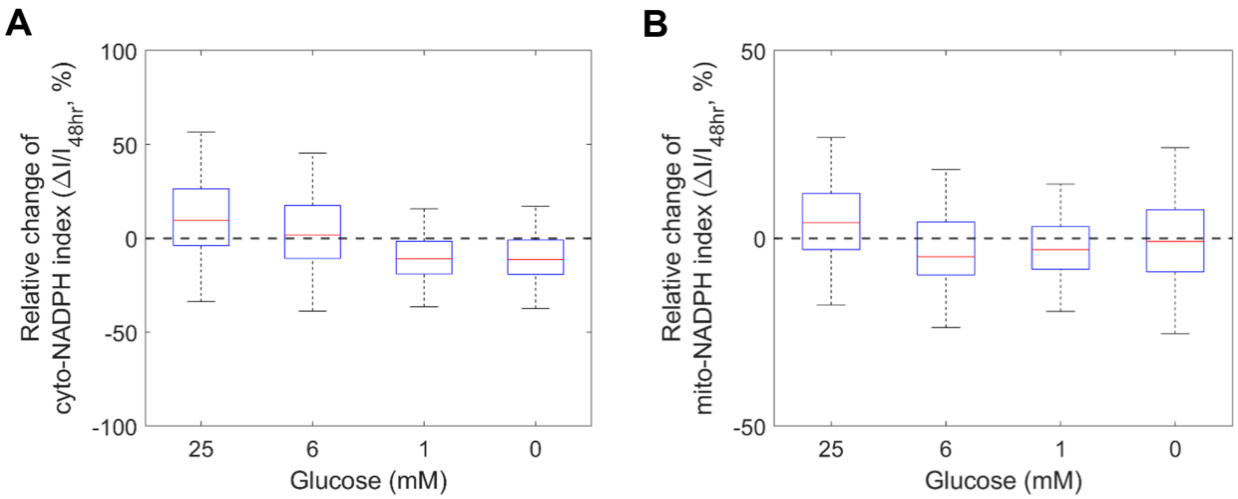

Figure 5.18. Relative changes of cytosolic NADPH index were calculated by dividing the difference between the indices at 48 and 96 hours to the index at 48 hour. (A) A relative change of cytosolic NADPH index was calculated by dividing the difference between the indices at 48 and 96 hours to the index at 48 hour. (B) Boxes represent 25th , 50th , 75th and 1.5 times the interquartile range away from the bottom or top of the box and are generated by a default boxplot function in MATLAB.

5.4.4. Absence of glutamine lowers both cytosolic and mitochondrial NADPH levels more than the absence of serine

Serine and glutamine are non-essential amino acids that are consumed by some cancer cells and partially used to support regeneration of NADPH in cytosol or mitochondria[8,12]. We measured the cytosolic and mitochondrial NADPH indices in absence of serine or glutamine (**Figure 5.19**). In absence of serine, the cytosolic NADPH decreased by 6 % after 24 hours, 5 % after 48 hours, and minimally perturbed after 72 hours and decreased by 5 % after 96 hours (**Figure 5.19A**). On the other hand, the mitochondrial NADPH did not change after 24 hours, decreased by 2 % after 48 hours, 6 % after 72 hours, and 7 % after 96 hours (**Figure 5.19B**). For glutamine, cytosolic NADPH index decreased proportionally over time. It decreased by 3, 9, 14, and 21 % after 24, 48, 72, and 96 hours (**Figure 5.19C**). Mitochondrial NADPH also decreased proportionally but less extent compared to the cytosolic NADPH index. It decreased by 2, 8, 10, 13 % after 24, 48,

72, and 96 hours (**Figure 5.19D**). When the relative changes of cyto- and mito- NADPH indices were compared, no linear relationship was observed under serine deprived condition (**Figure 5.20A)** but there was a linear correlation observed for glutamine deprived condition (**Figure 5.20B).**

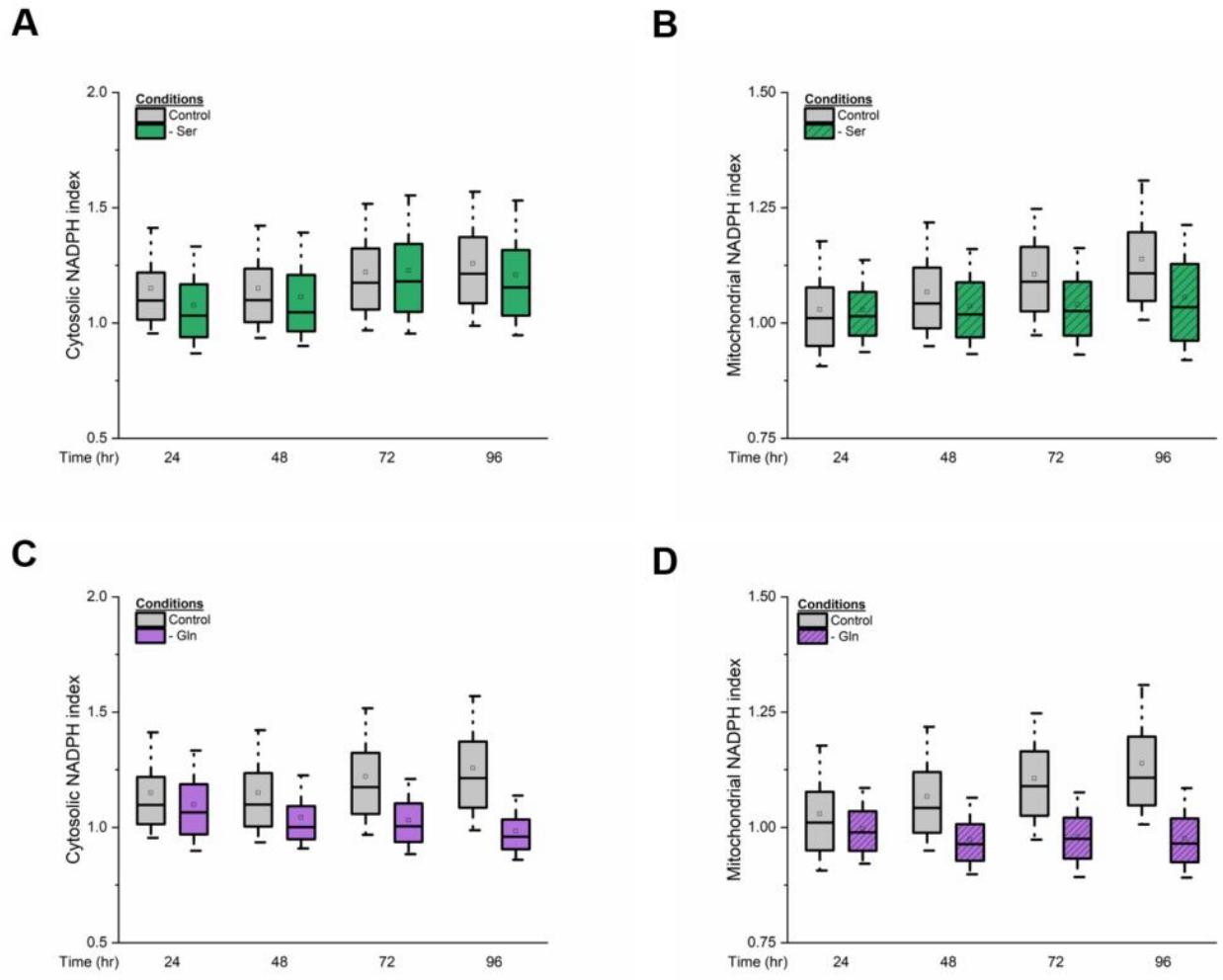

Figure 5.19. Cytosolic and mitochondrial NADPH indices upon depletion of serine or glutamine. (A) Cytosolic and (B) mitochondrial NADPH indices of cells grown in serine depleted conditions over 96 hours. Under glutamine deprived condition, (C) cytosolic and (D) mitochondrial NADPH indices were measured.

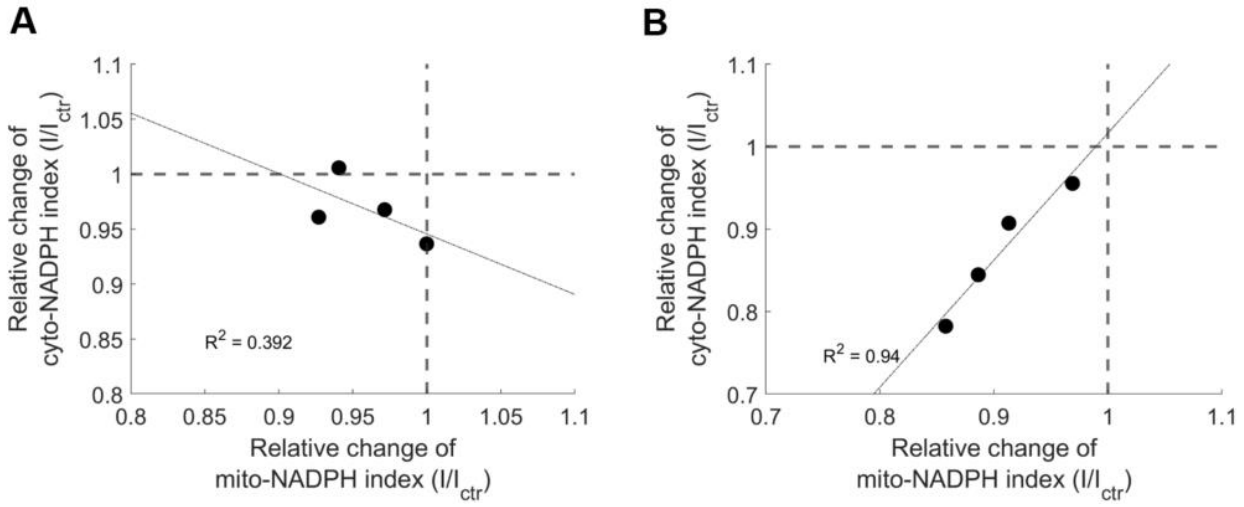

Figure 5.20. Relationship between the relative changes of cyto- and mito- NADPH indices at 24, 48, 72, and 96 hours. Relative change was calculated by dividing the index under (A) serine or (B) glutamine deprived condition to the control.

Next, we compared the change of cyto- and mito- NADPH indices relative to different time points, while fixing the concentration. For instance, by calculating the difference between the cyto-NADPH indices between 48 and 96 hours normalized to the index at 48 hour, the relative change of NADPH index over time was measured (**Figure 5.21**). For cytosolic NADPH index, the median relative changes were 9, -6, and -20 % for control, no serine, and no glutamine conditions (**Figure 5.21A**). For mitochondrial NADPH index, the median relative change was 4, -8, and -14 % for control, no serine, and no glutamine condition (**Figure 5.21B**).

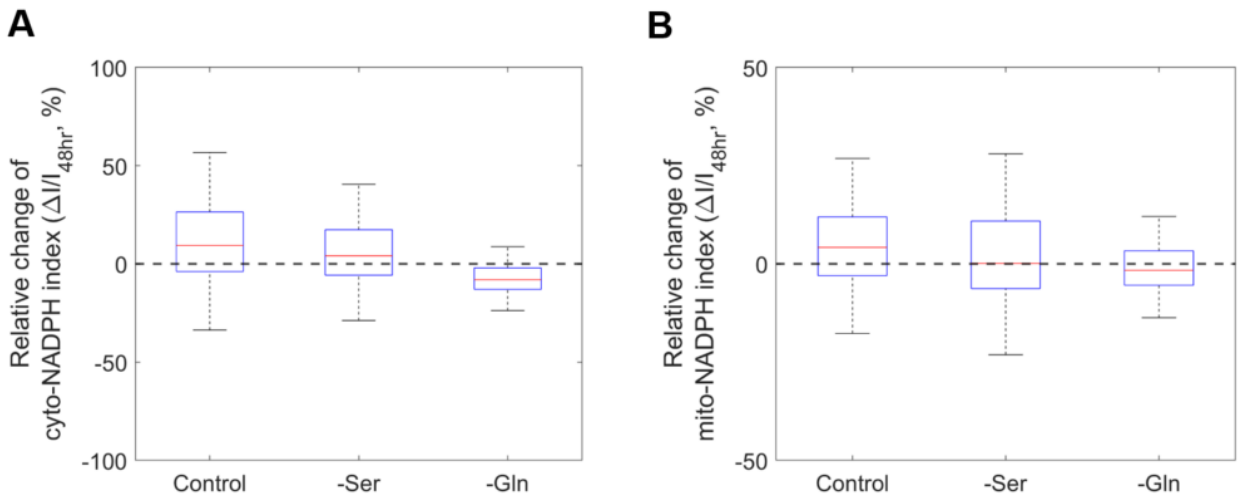

Figure 5.21. Relative changes of cytosolic NADPH index were calculated by dividing the difference between the indices at 48 and 96 hours to the index at 48 hour. (A) A relative change of cytosolic NADPH index was calculated under serine or glutamine deprived conditions. (B) A relative change of mitochondrial NADPH index was calculated under serine or glutamine deprived conditions.

Lastly, we plotted all the relative change of cyto-NADPH index against those of mito-NADPH index across different conditions to determine whether there is a linear or polynomial relationships. The mean coordinates of these data points are 1.5 and 0.5 %. The standard deviation are 7.6 and 10.3 %, indicating that the cytosolic NADPH levels are changing greater than the mitochondrial NADPH levels.

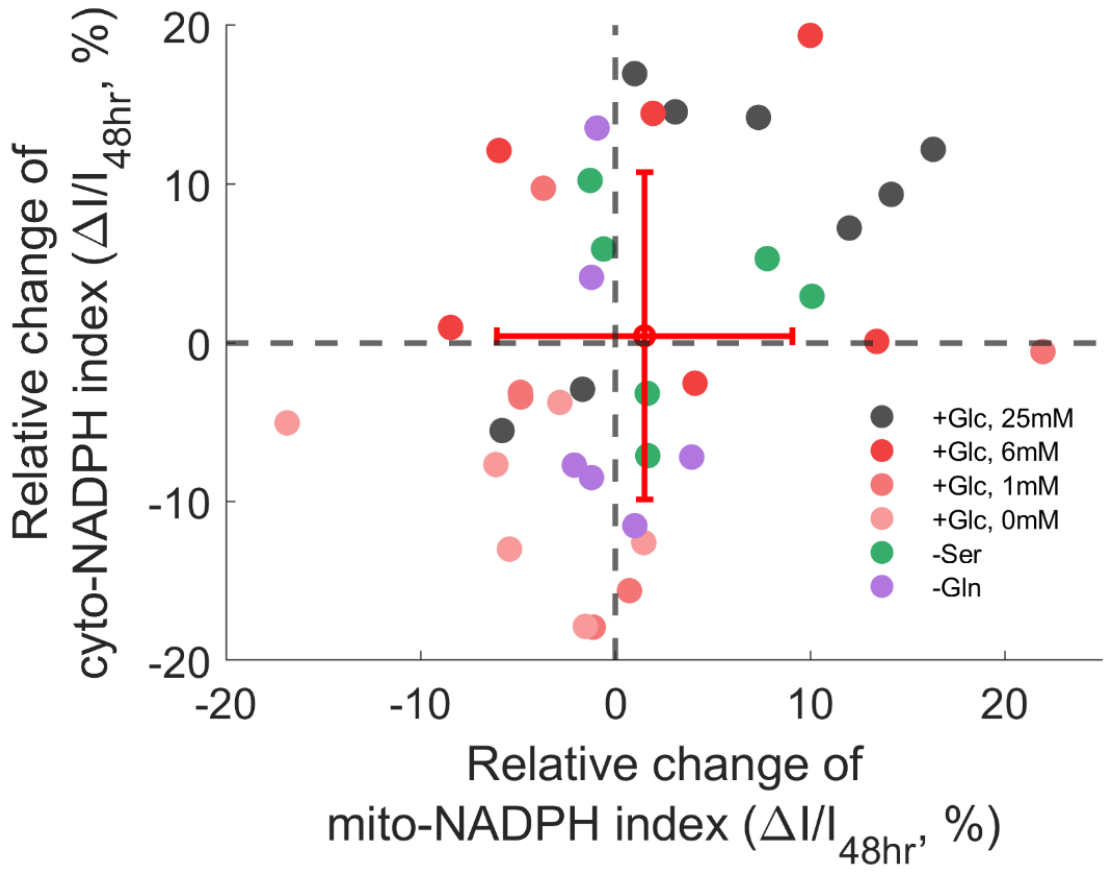

Figure 5.22. A scatter plot representing the relative change of cyto- and mito- NADPH indices under varying nutrient conditions.

5.4.5. Cytosolic and mitochondrial NADPH levels change differently under nutrient stress across cancer cells

To test whether the change of cytosolic and mitochondrial NADPH indices follows a similar trend across other cell types under varying nutrient conditions, we stably expressed the iNap sensors and measured the change of compartmentalized NADPH indices in cell lines, including A549 (non-Small Cell Lung Cancer), HCT-116 (colorectal Cancer), and MDA-MB-231 (breast Cancer). After 72 hours, we observed lowering glucose concentration decreased the cytosolic NADPH index across other cell lines except A549 (**Figure 5.23A**). Under serine deprived

condition, all cell lines showed a decrease of cytosolic NADPH index. Absence of glutamine also lowered cytosolic NADPH except HCT-116 cells. After 96 hours, we observed that nutrient stress lowered cytosolic NADPH index for A549 and MDA-MB-231 cell lines but increased the index for HCT-116 cells (**Figure 5.23B**). Interestingly, absence of serine increased the cytosolic NADPH index by approximately 45% for HCT-116 cell line.

For mitochondrial NADPH index, A549 cell line showed a decrease of mitochondrial NADPH index in absence of glucose, serine, or glutamine after 72 hours (**Figure 5.23C)**. For HCT-116 and MDA-MB-231 cell lines, we observed an increase of mitochondrial NADPH index under nutrient stress. However, after 96 hours, we observed the nutrient stress lowered mitochondrial NADPH index across the cell lines except the HCT-116, which showed an increase of mitochondrial index by 6, 22, and 24% for glucose, serine, and glutamine deprived conditions (**Figure 5.23D**).

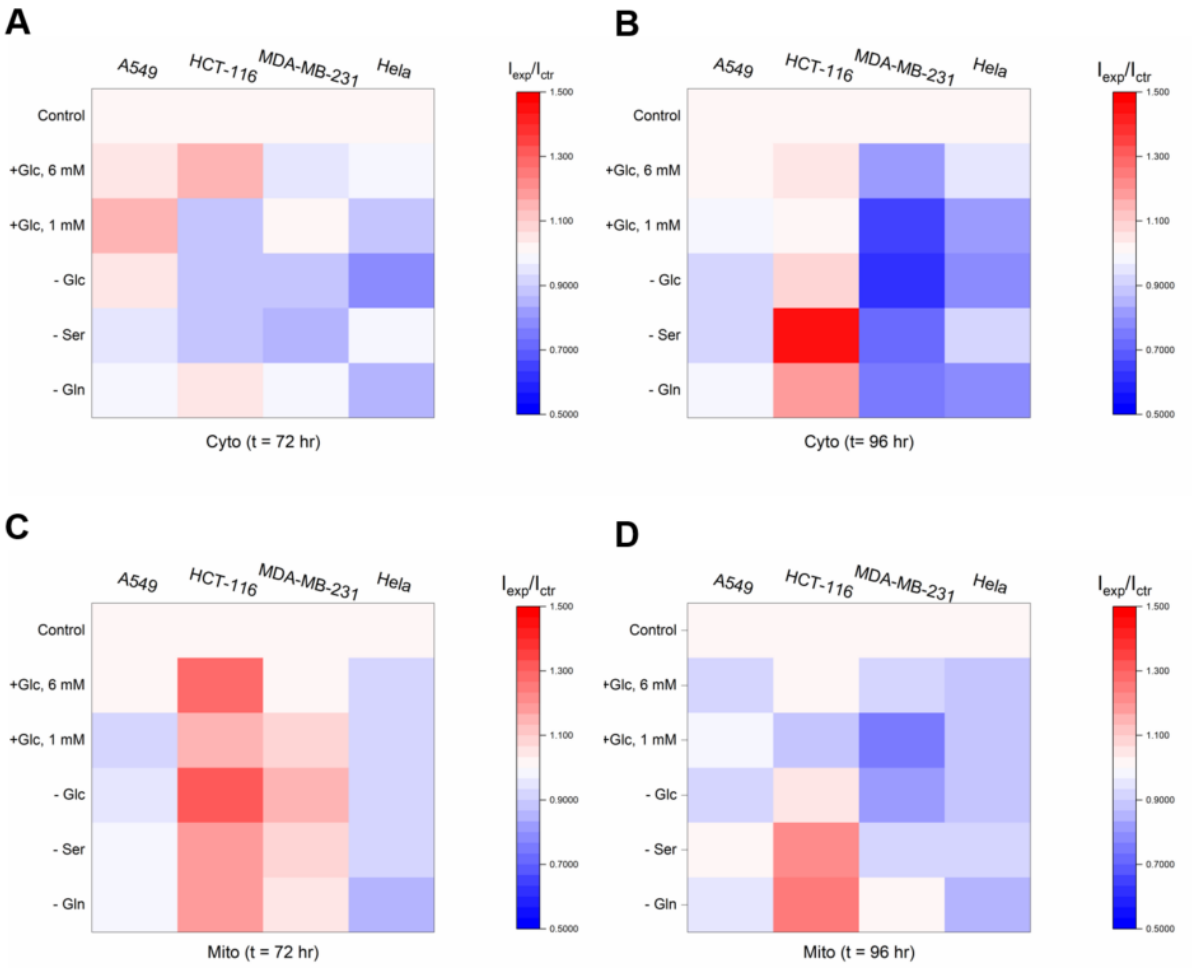

Figure 5.23. Heat maps representing relative change of NADPH indices at 72 and 96 hours across different cell lines under varying nutrient conditions. Relative change of cytosolic NADPH index was measured by normalizing the NADPH index under varying conditions to that of control for different cell lines at (A) 72 and (B) 96 hours. Relative change of mitochondrial NADPH index was measured by normalizing the NADPH index under varying conditions to that of control for different cell lines at (C) 72 and (D) 96 hours.

In addition to the estimation of the relative change of cytosolic and mitochondrial NADPH indices to that of control at specific time point, we also calculated the percent change of cytosolic and mitochondrial NADPH indices ($\frac{I_{96hr}-I_{48hr}}{I_{48hr}}$) to those at earlier time point (**Figure 5.24**). We observed different patterns across the cell lines. Throughout the perturbation, A549 showed the least variability of cytosolic NADPH index change upon varying nutrient conditions.

Despite the presence of glucose, the cyto-NADPH decreased by -10 % compared to that of 48 hours. In absence of glucose or serine, the median cytosolic NADPH decreased most by approximately 17 % (**Figure 5.24A**). On the other hand, for HCT-116 cells, we observed that absence of serine, and glutamine increased the cytosolic NADPH indices by 33 % and 8 % compared to the indices at 48 hours (**Figure 5.24B**). The relative change of cyto-NADPH index for control and absence of glucose was approximately -8 and -2 % respectively. For MDA-MB-231 cell, the trend was similar to that of A549 cell line, but the magnitude of the change was greater. In absence of glucose, serine, and glutamine, the NADPH indices decreased by approximately 37, 27, and 23 %, respectively. In presence of glucose, the cyto-NADPH increased by nearly 3 % (**Figure 5.24C**).

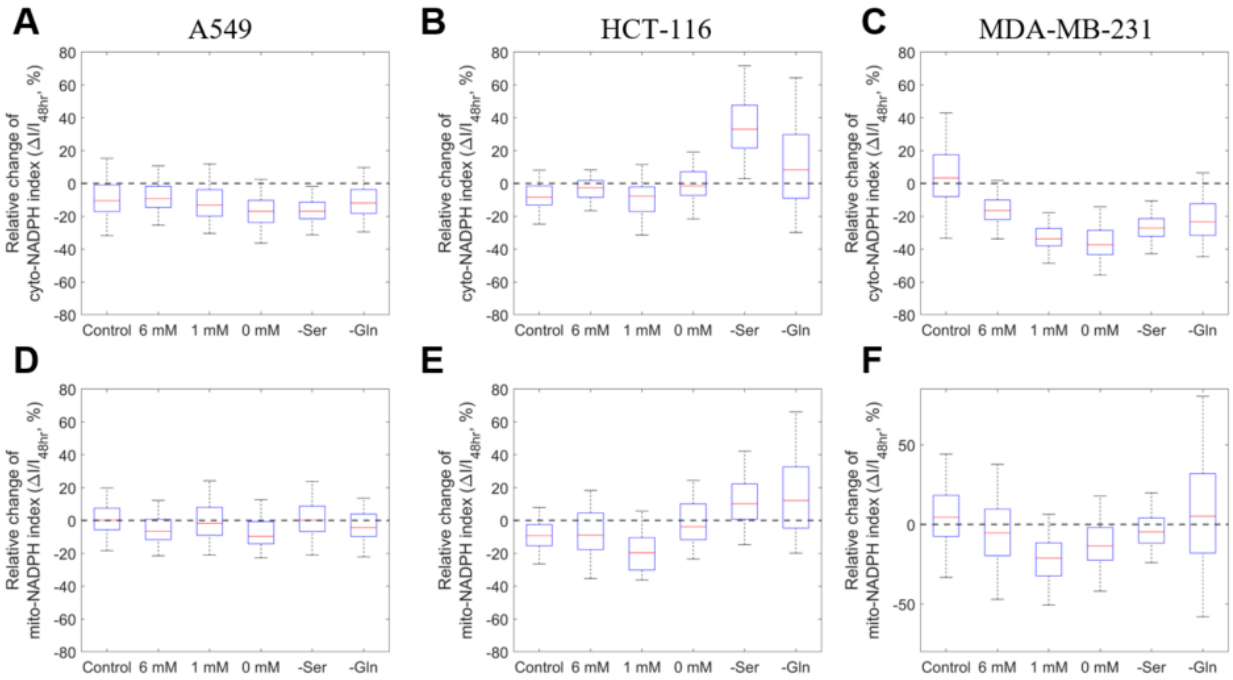

Figure 5.24. Relative changes of cyto- and mito- NADPH indices reveal different trends for cancer cells under varying nutrient conditions. The relative change was calculated by normalizing the difference between NADPH indices at 48 and 96 hours to the index at 48 hour per experimental condition. (A) Box plots representing relative changes of cytosolic NADPH indices per experimental conditions across three

different cell lines, including A549, HCT-116, and MDA-MB-231. (B) Box plots representing relative changes of mitochondrial NADPH indices per experimental conditions across three different cell lines, including A549, HCT-116, and MDA-MB-231.

The mitochondrial NADPH index showed similar trends observed in the cytosolic NADPH index change but with lower magnitude. For A549, the absence of glucose impacted the mitochondrial NADPH index most by lowering the index to nearly 10 %. A difference of NADPH indices between the control and absence of glucose conditions was similar to that of cytosolic NADPH index difference. In absence of glutamine, the mitochondrial NADPH index decreased by 4 % compared to that of 48 hours, and the difference of NADPH index between control and absence of glutamine condition was similar to that of cytosolic NADPH index difference. However, in absence of serine, the mitochondrial NADPH index was maintained compared to the value at 48 hours (**Figure 5.24D**).

For HCT-116 cell line, we also observed the change of mitochondrial NADPH index increased by 10 and 12 % in absence of serine, and glutamine conditions. The relative change of mito-NADPH index for control and absence of glucose was approximately -9 and -4 % respectively. These changes were similar to that of cytosolic NADPH indices (**Figure 5.24E**).

Lastly, for MDA-MB-231, the relative change for control was approximately 10 %. However, under glucose deprived condition, the NADPH index decreased by 9 % compared to the mito-NADPH index measured at 48 hours. In absence of serine or glutamine, the mito-NADPH index change was 0.7 and 11 %. Unlike the cytosolic NADPH index which decreased by more than 20 % when cells were grown either in absence or glutamine, the mitochondrial NADPH index remained for absence of serine and increased for glutamine absent condition (**Figure 5.24F**). Interestingly, mitochondrial NADPH index decreased most under 1 mM glucose conditions for both HCT-116 and MDA-MB-231 cell lines.

Next, we plotted relative change of cyto-NADPH index to that of mito-NADPH index to determine whether there exists linear or other relationships. For A549, we observed the change of both indices were in the negative regime under varying nutrient conditions and the mean relative change of cyto- and mito- NADPH indices were -9.3 and -1.9 %. The corresponding standard deviation were 4.7 for cytosolic and 5.4 for mitochondrial NADPH indices (**Figure 5.25A)**. Unlike A549, HCT-116 cell lines showed mean values of 11.6 % for cytosolic and 2.8 % for mitochondrial NADPH indices with standard deviations of 12 for both indices (**Figure 5.25B)**. For MDA-MB-231, the mean values were -21.7 for cytosolic and -2 % for mitochondrial NADPH indices with standard deviations of 12.3 and 10.7, respectively (**Figure 5.25C)**.

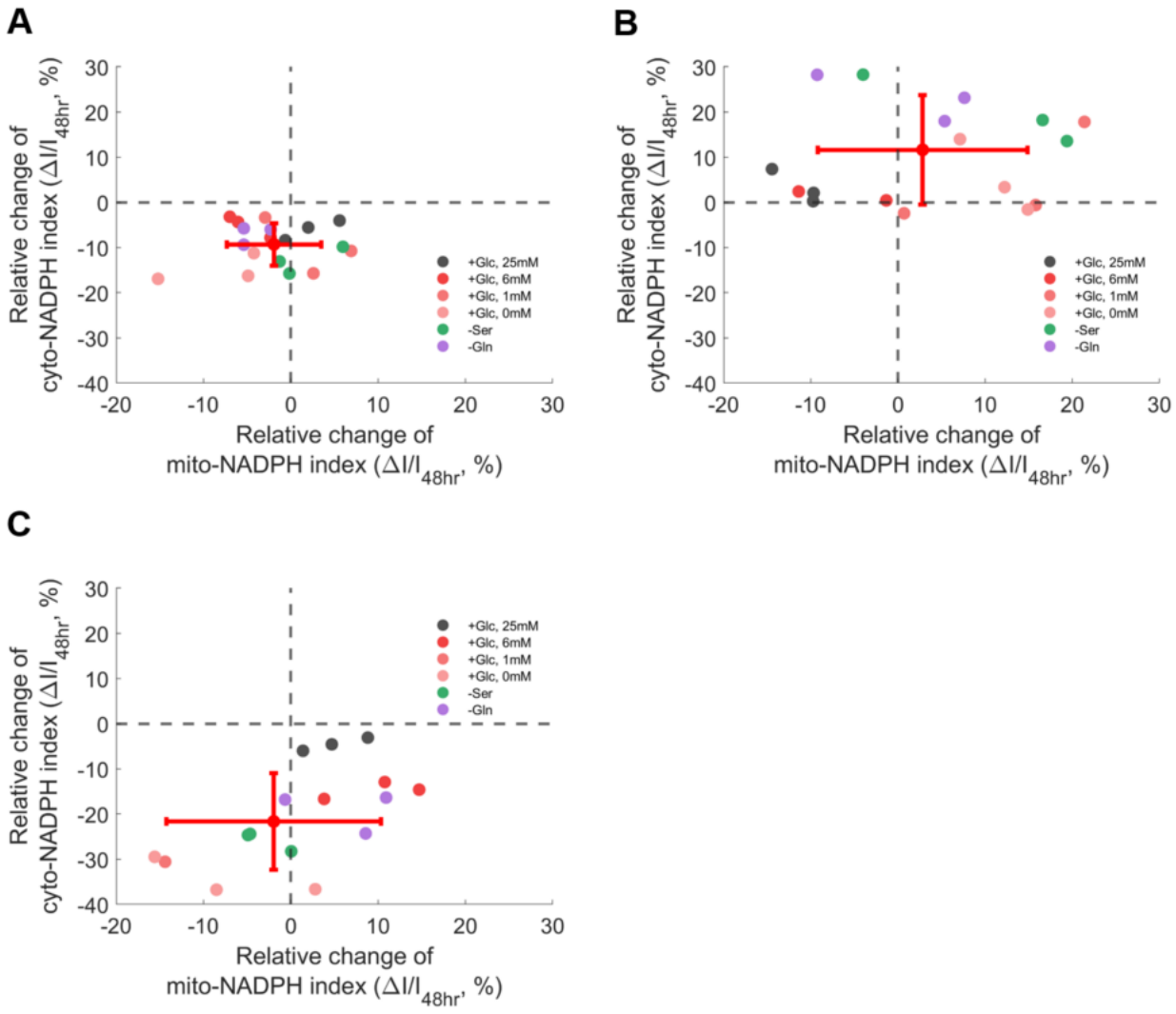

Figure 5.25. Scatter plots representing the relative change of cyto- and mito- NADPH indices under varying nutrient conditions. Relative change of cyto- and mito- NADPH indices were calculated by dividing the difference between NADPH indices at 48 and 96 hours to the corresponding index at 48 hours under specific nutrient conditions. Each dot represents one biological replicates. The red dot represents mean cyto- and mito- NADPH indices. Error bar represents a standard deviation. Scatter plots are of (A) A549, (B) HCT-116, and (C) MDA-MB-231.

5.4.6. Heterogeneity among A549, HCT-116, MDA-MB-231, and HELA

In the previous section, we monitored cytosolic and mitochondrial NADPH indices changed differently depending on nutrient conditions. To under whether the mRNA expression levels of

NADPH generating enzymes are different among the cell lines, I implemented bioinformatics survey to find out that the gene expression levels of NADPH generating enzymes were indeed different among the cancer cell lines (**Figure 5.26**). It was interesting to note that HCT-116 cells expressed low NNT enzymes and ME3, but upregulated MTHFD2 gene, which was related to serine derived 1C metabolism. This indicated that HCT-116 cells might rely more on serine derived 1C metabolism to fuel mitochondrial NADPH regeneration than ME3, NNT, or IDH2 enzymes. However, it was rather counter intuitive that HCT-116 cells revealed increased cytosolic and mitochondrial NADPH indices in absence of serine.

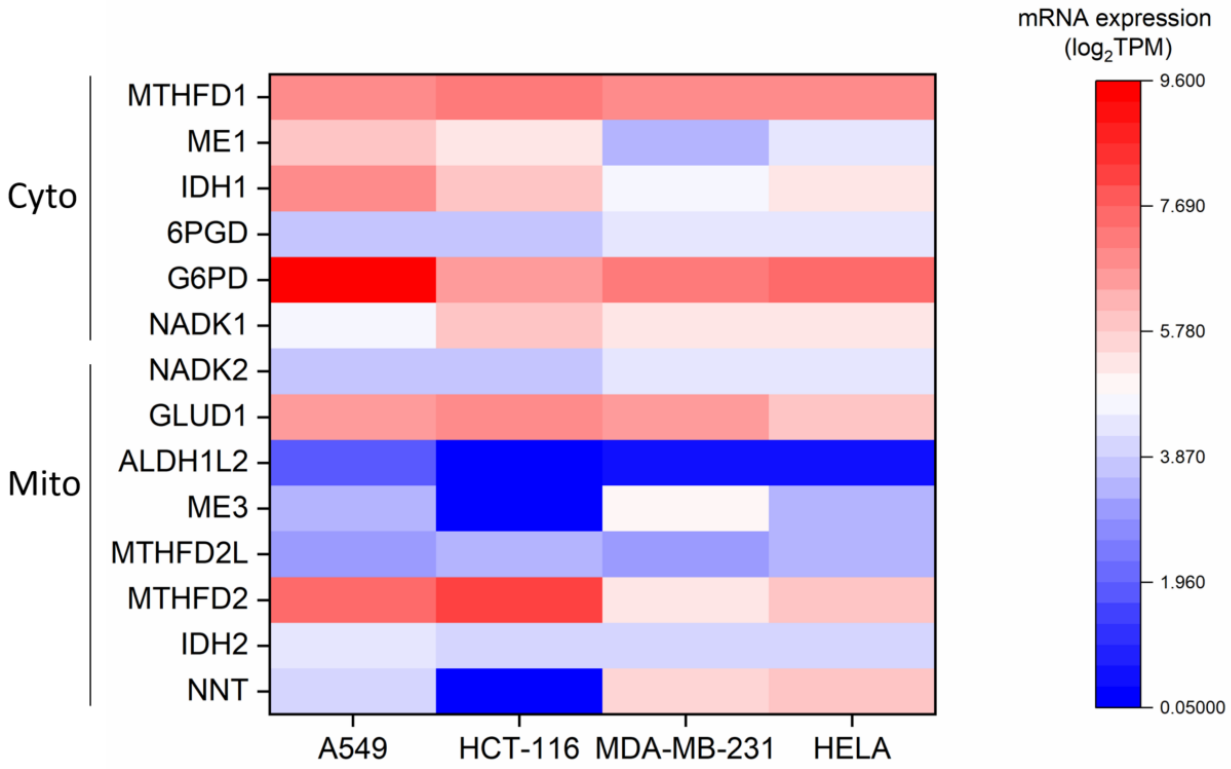

Figure 5.26. mRNA expression levels based on Cancer Cell Line Encyclopedia database.

Perhaps, HCT-116 cells upregulated genes in serine synthesis pathway to replenish both cytosolic and mitochondrial NADPH levels when there was no extracellular serine available. Thus, we evaluated the serine pathway gene expression levels as well as the serine derived 1C

metabolic pathways (**Figure 5.27**). Indeed, compared to MDA-MB-231 cells which showed lower expression level of PHGDH, HCT-116 cells upregulated PHGDH enzyme by nearly 13 fold. Additionally, compared to MDA-MB-231 cells which showed the most decrease of both cytosolic and mitochondrial NADPH indices by the absence of serine, HCT-116 cells showed increase of both cytosolic and mitochondrial NADPH indices and they also showed greater expression levels of serine pathway as well as serine-derived 1C pathways.

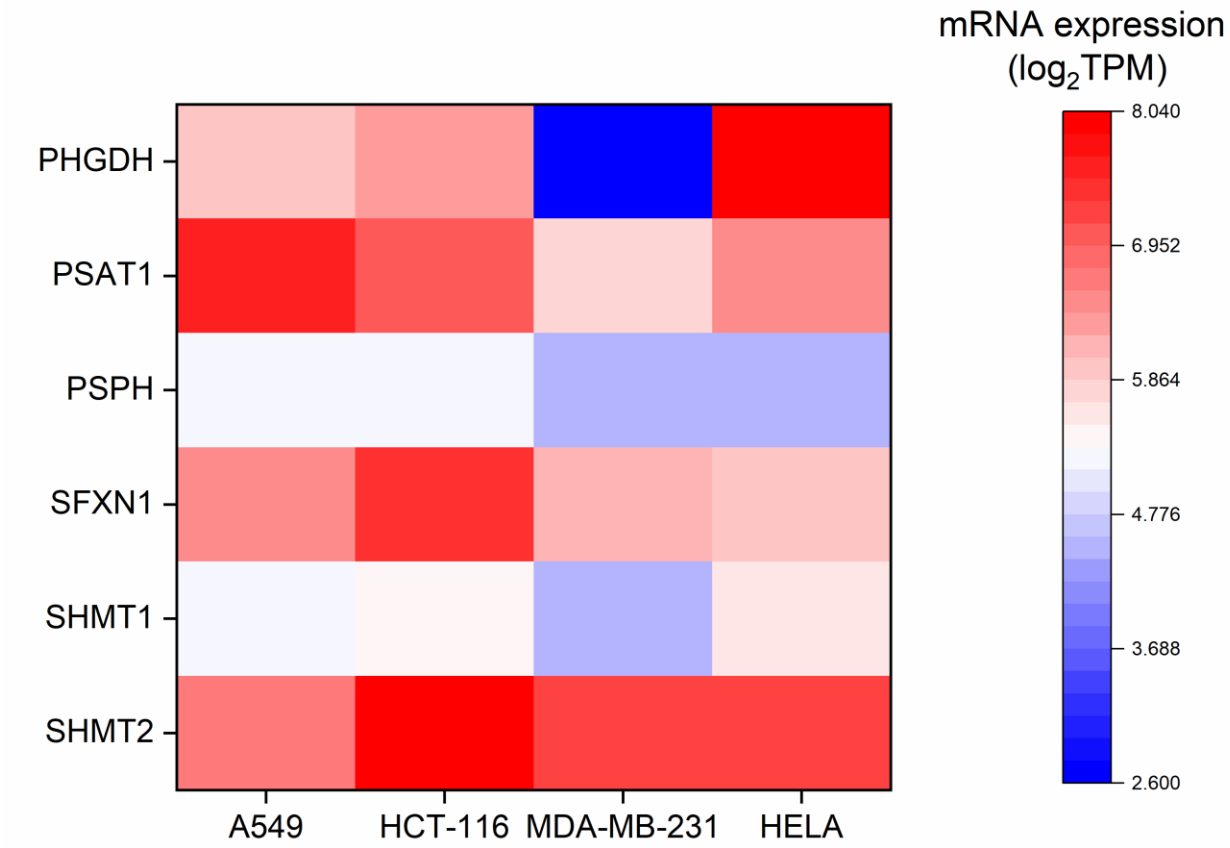

Figure 5.27. mRNA expression levels of serine synthesis pathway and a part of serine-1C pathway. PHGDH, PSAT1, and PSPH are the enzymes required for de novo serine synthesis pathway. The SFXN1 is a serine transporter to mitochondria. Serine hydroxymethyltransferase are to generate glycine and 5, 10-methylene-tetrahydrofolate and the serine-1C cycle allows generation of primarily mitochondrial NADPH.

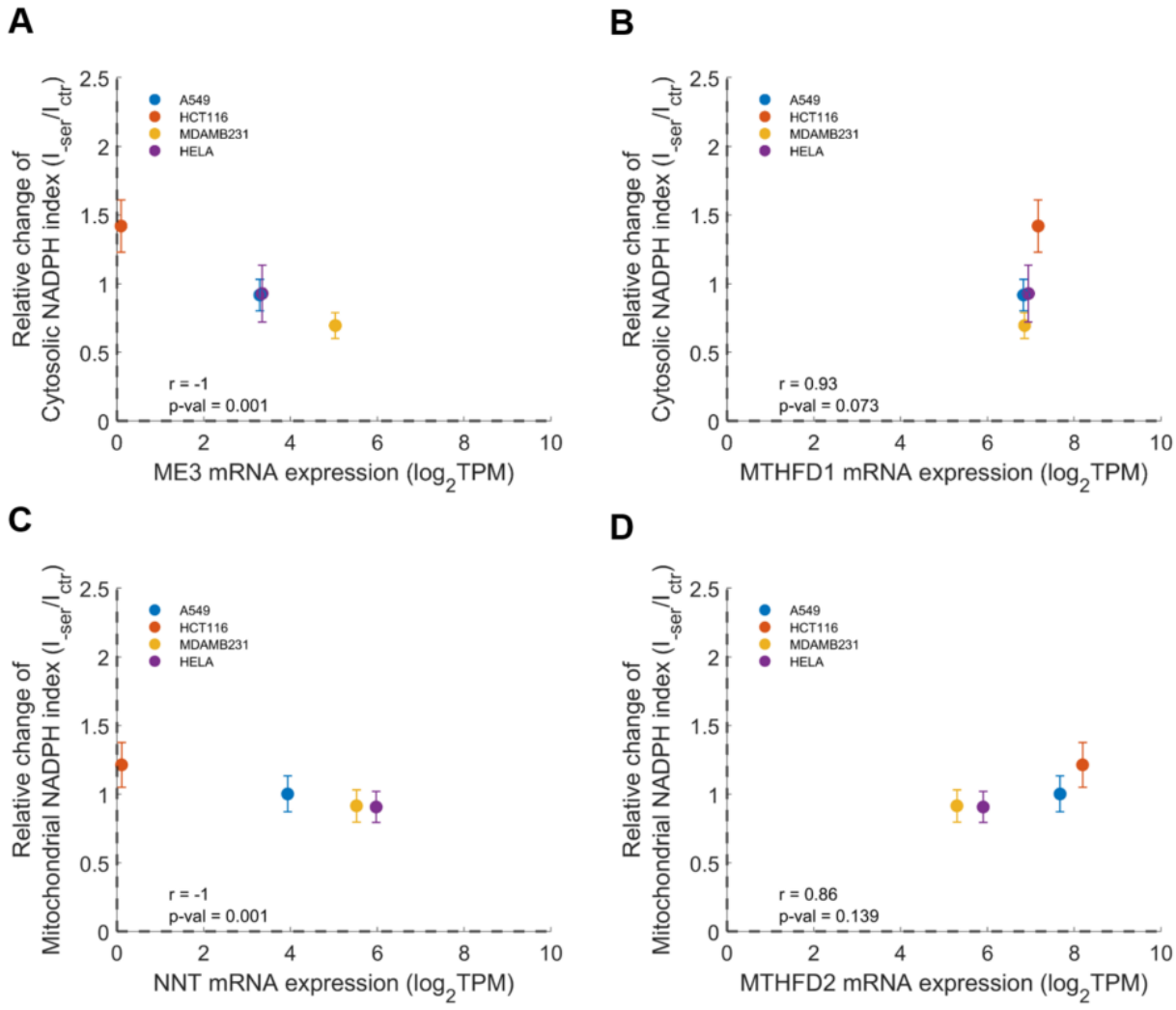

Figure 5.28. Correlation between mRNA expression levels and the relative change of cytosolic or mitochondrial NADPH indices under serine deprived conditions. Of NADPH generating enzymes, enzymes whose expression levels are highly correlated with relative change of cytosolic or mitochondrial NADPH indices are selected. (A) Malic enzyme 3 expression levels has a high negative correlation to the change of cytosolic NADPH index. (B) MTHFD1 is positively correlated with the change of cytosolic NADPH. (C) NNT expression level has a negative correlation to the mitochondrial NADPH change. (D) MTHFD2 expression level has a high correlation to change of mitochondrial NADPH index.

We also compared NADPH generating enzymes' expression levels to the change of cytosolic and mitochondrial NADPH indices (**Figure 5.28**). Interestingly, it turned out that the cytosolic NADPH index change was negatively correlated with the ME3 and positively

correlated with MTHFD1 enzyme (**Figure 5.28A and B)**. For mitochondrial NADPH index change, NNT expression levels were negatively correlated with mitochondrial NADPH index and MTHFD2 expression levels were positively correlated with the mitochondrial NADPH index (**Figure 5.28C and D**). Based on these correlation analysis with gene expression levels of serine pathway, serine mediated NADPH production might play an important roles in maintaining both cytosolic and mitochondrial NADPH pools under serine deprived condition.

For A549 cells, it upregulated G6PD enzyme most among the cell lines tested. It increased the expression level by nearly 4 fold compared to Hela cells, by 8 fold compared to HCT-116 cells, and by 6 fold compared to MDA-MB-231 cells. This might indicate the A549 cells may utilize pentose phosphate pathway to a greater extent than the other cell lines, and thus when there are no glutamine or serine available, A549 was still able to maintain NADPH levels in both cytosol and mitochondria. The phenomenon was different from the serine deprived condition in which serine synthesis allowed maintenance of cytosolic and mitochondrial NADPH pools. Interestingly, for NNT, A549 and HCT-116 cells had lower expression levels compared to MDA-MB-231 and HELA cells.

For the effect of glutamine, glutamine was previously reported to replenish the cytosolic NADPH levels through amino acid transferases, or TCA cycle, and malic enzyme derived NADPH production in cytosol[12,20]. Additionally, glutamine derived TCA cycle activity generated NADH, which could be utilized for NADPH production in mitochondria via NNT enzyme[21]. Therefore, those cell lines that had lower expression levels of either NNT or ME1 might be vulnerable to the absence of glutamine. Indeed, MDA-MB-2321 and HELA cells had lower expression levels of NNT genes compared to HCT-116 cells and they showed greater effect when glutamine was absent. However, MDA-MB-231 and HELA cells had higher expression

level of NNT enzyme. It was still interesting to see that HCT-116 cells increased higher cytosolic and mitochondrial NADPH indices when there was no glutamine. Another possibility was that HCT-116 cells had higher expression level of glutamine synthase, compared to A549 or MDA-MB-231 cells but not Hela. The log2 values is 7. Its expression level was about 6 fold more than A549, 1.33 fold compared to MDA-MB-231, and 0.72 compared to Hela. Another possibility was that when HCT-116 cells are under nutrient stress, it might activate the AMPK pathway more than other cell lines and accumulate both cytosolic and mitochondrial NADPH levels.

Interestingly, the GLUD1 gene expression levels were highly correlated with the mitochondrial NADPH indices changes. Similar to the serine deprived condition, in which mitochondrial NADPH indices had a high correlation with MTHFD2 gene, the mitochondrial NADPH index also ironically increased with higher GLUD1 gene expression in absence of glutamine. One explanation was that αKG may be converted to glutamate via transaminase more in glutamine deprived condition and increase the generation of mitochondrial NADPH under glutamine deprived condition (**Figure 5.29**).

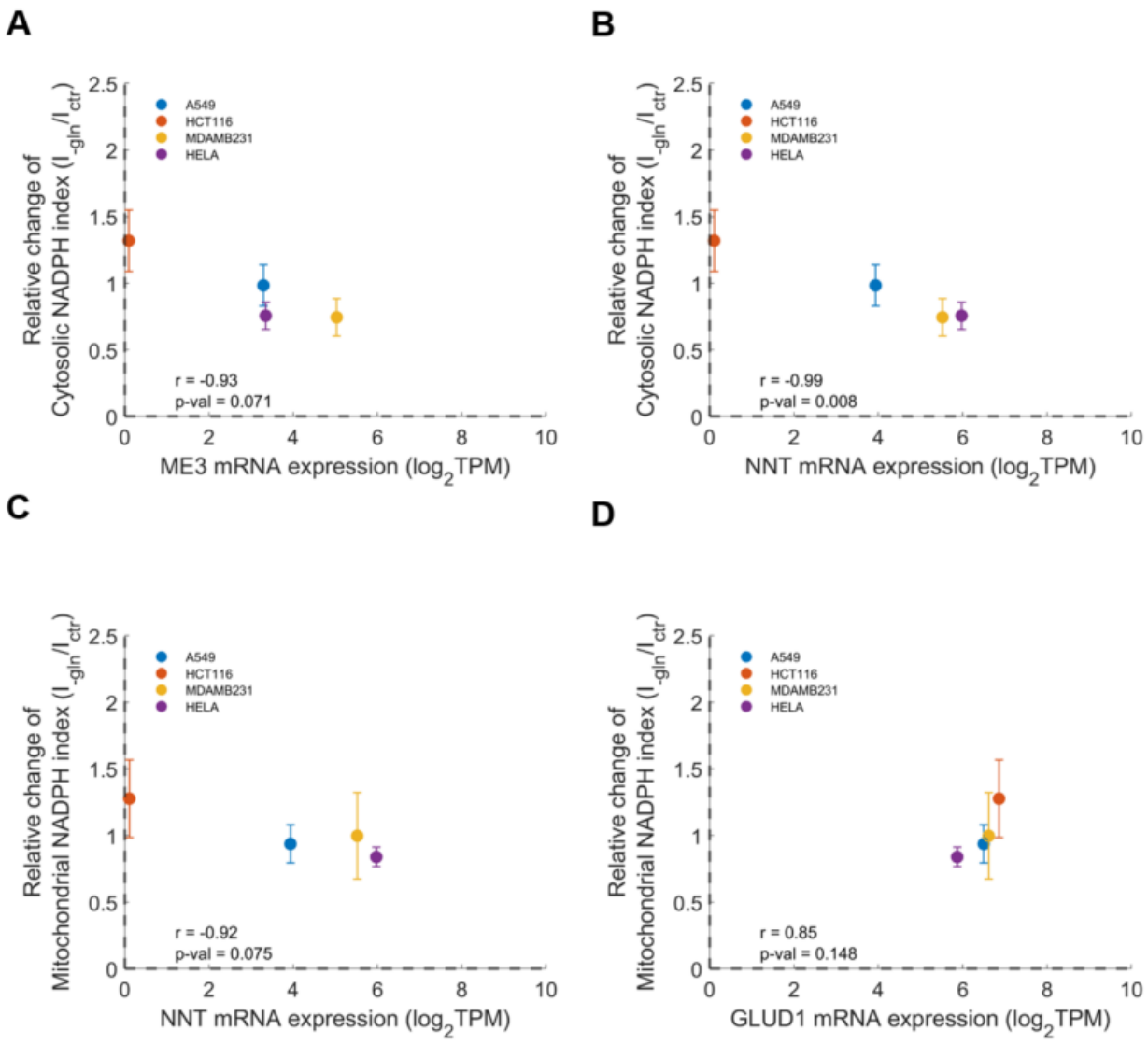

Figure 5.29. Correlation between mRNA expression levels and the relative change of cytosolic or mitochondrial NADPH indices under glutamine deprived conditions. Of NADPH generating enzymes, enzymes whose expression levels are highly correlated with relative change of cytosolic or mitochondrial NADPH indices are selected. (A) Malic enzyme 3 expression levels has a high negative correlation to the change of cytosolic NADPH index. (B) NNT is also negatively correlated with the change of cytosolic NADPH. (C) NNT expression level has a negative correlation to the mitochondrial NADPH change. (D) GLUD1 expression level has a high correlation to change of mitochondrial NADPH index.

Lastly, we also correlated the cytosolic and mitochondrial NADPH indices to NADPH generating enzyme expression levels (**Figure 5.30**). For cytosolic NADPH, high correlated genes

include NNT genes and 6PGD enzymes. It make sense that oxidative pentose phosphate pathway is the major source of cytosolic NADPH. Thus, high expressions may correlate with the higher NADPH production (**Figure 5.30A and B).** For mitochondrial NADPH, the high correlation was also observed with ME3 and NNT genes. Perhaps, mitochondrial NADPH generation via ME3 can be significant. Additionally, higher expression of NNT genes are highly correlated with cytosolic NADPH levels. Perhaps, NNT enzymatic activities and expression levels can be an indicative of cytosolic and mitochondrial NADPH redox states.

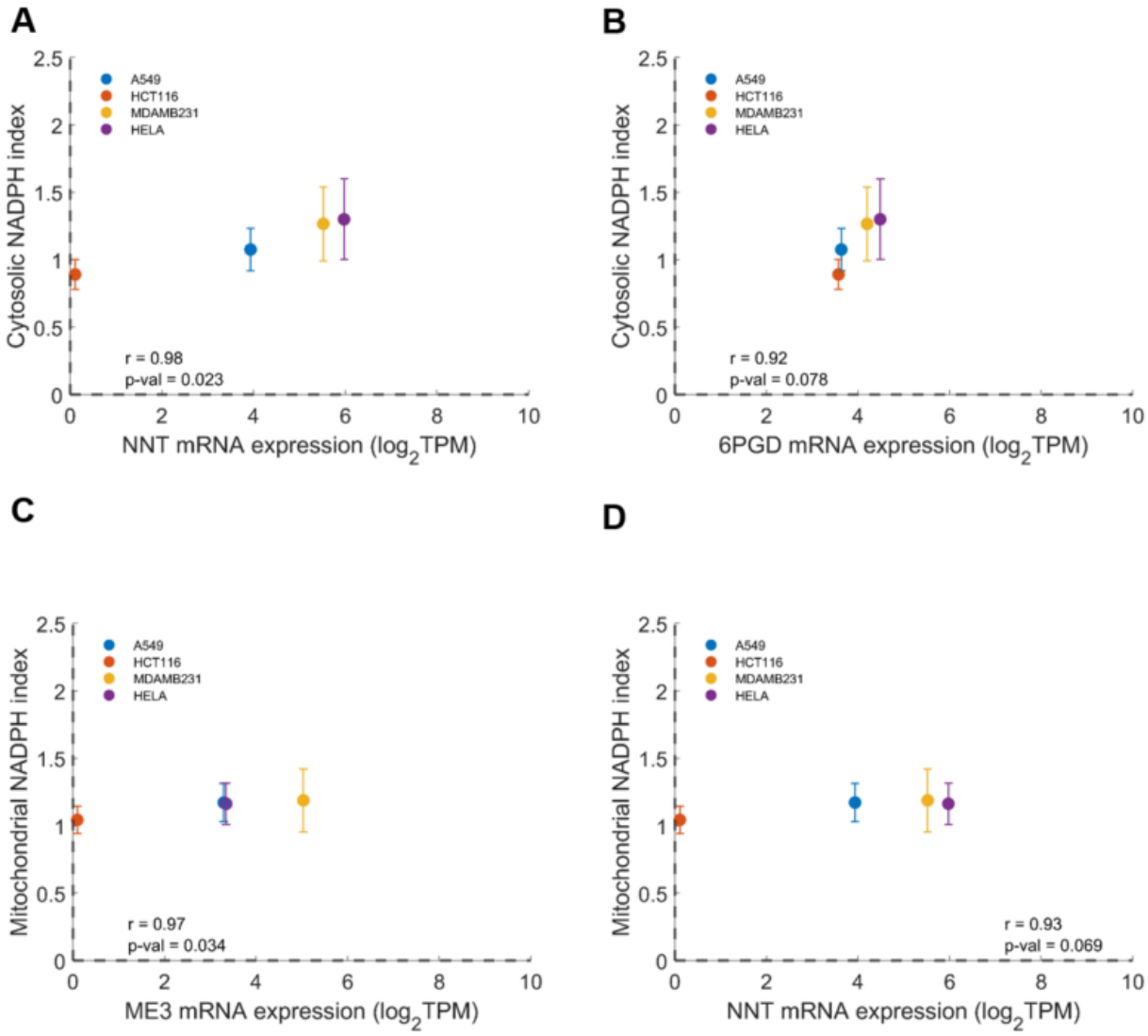

Figure 5.30. Correlation between mRNA expression levels and cytosolic and mitochondrial NADPH indices after 96 hours. Of NADPH generating enzymes, enzymes whose expression levels are highly correlated with relative change of cytosolic or mitochondrial NADPH indices are selected. (A) NNT expression levels reveal a high positive correlation to the NADPH index. (B) 6PGD expression levels are highly correlated with the change of cytosolic NADPH. (C) ME3 expression level has a high correlation to the mitochondrial NADPH index. (D) NNT expression level has a high correlation to change of mitochondrial NADPH index.

5.5. Discussion

Nutrient availability and metabolic processes influenced cancer phenotypes[1]. Of various nutrient sources, glucose was a major carbon substrate readily consumed by cancer cells, not only ATPs but also other intermediates that were necessary for biosynthetic processes and proliferation [3,4]. Indeed, many cancer cells upregulated glycolytic enzymes, including glucose transporter 1 (GLUT1), a major isoform of glucose transporter and the Km value of approximately 3 mM[22]. Due to such reliance on glucose, extracellular glucose was indeed limited in certain tumor microenvironment and some cancers became more sensitive to glucose availability[19].

Here, I evaluated the influence of glucose and other amino acids to cytosolic and mitochondrial NADPH levels and dynamics. To measure cytosolic and mitochondrial NADPH levels, I generated cell lines that stably express cytosolic and mitochondrial NADPH sensors. Further, I applied advanced imaging analysis software to effectively measure compartmentalized NADPH levels for large number of samples in high-throughput manner. This imaging analysis system enabled measurement of cytosolic and mitochondrial NADPH indices in high throughput fashion. Cytosolic and mitochondrial NADPH indices, which were proxy to NADPH concentration, decreased as initial glucose concentration decreased. Indeed, at least in pancreatic beta cells from mouse, addition of glucose stimulated cellular NADPH levels, indicating a presence of glucose modulated NADPH levels[23].

Additionally, other cancer cell lines also showed lack of glucose decreased both cytosolic and mitochondrial NADPH levels. However, HCT-116 cells maintained NADPH levels in cytosol even in absence of glucose, whereas MDA-MB-231 cells were sensitive to glucose availability as the decrease of both cytosolic and mitochondrial NADPH was greatest. It was previously shown that MDA-MB-231 cells were highly dependent on glucose[24], and we also

used publicly available mRNA expression data to find that MDA-MB-231 cells were indeed highly expressing the glucose transporters of the cell lines we have tested here. Higher expression of glucose transporter indicated that these cell lines were more dependent on glucose metabolism and thus removal of glucose might impact glucose metabolic pathways, which included generation of NADPH. Indeed, we observed that MDA-MB-231 cells revealed a greater extent of decrease of both cytosolic and mitochondrial NADPH indices upon depletion of glucose.

Other than glucose, absence of glutamine also decreased both cytosolic NADPH levels across cell lines except HCT-116 cells. Glutamine was essential substrate by serving as nitrogen source for amino acid synthesis and glutathione, but also could be utilized for NADPH production in mitochondria through GLUD1[25]. GLUD1 was localized to mitochondria and absence of glutamine might impact mitochondrial NADPH production, but cytosolic NADPH decreased more than the mitochondrial NADPH levels. As mitochondrial and cytosolic NADPH were constantly shuttled between two compartments, decrease of mitochondrial NADPH might influence cytosolic NADPH as a result. Another possible explanation was that glutamine could be still catabolized to substrates such as a-KG and malate and these could be used for production of cytosolic NADPH via malic and isocitrate enzymes[12]. Therefore, absence of glutamine impacted cytosolic NADPH production.

Lastly, absence of serine also perturbed both cytosolic and mitochondrial NADPH levels. Serine and one carbon metabolism could be used to generate NADPH mostly in mitochondria *in vitro*, or with physiologically relevant level of folic acids *in vivo* [13,14,26]. In our sensor experiments, absence of serine did not decrease mitochondrial NADPH as much as the cytosolic NADPH. This suggested that either glucose or glutamine could still maintain mitochondrial

NADPH even in absence of serine. However, absence of serine perturbed cytosolic NADPH levels for A549 and MDA-MB-231 cells, but not HCT-116 and Hela cells. These difference suggested cell-line specific sensitivities to serine and one-carbon metabolism to NADPH homeostasis.

HCT-116 cells were interesting as it exhibited low NADPH levels in cytosol compared to other cell lines. Because of low levels of cytosolic NADPH, a small increase might contribute to large percent change of cytosolic NADPH level when we calculated a relative change. Additionally, in absence of glucose, serine, or glutamine, NADPH levels in both cytosol and mitochondria increased over time relative to control. Publicly available mRNA expression data also revealed that HCT-116 cells highly expressed genes related to one carbon metabolism, particularly the MTHFD1,2, and SHMT2 genes, which were used for regeneration of NADPH in cytosol and mitochondria. HCT-116 cell lines also exhibited high levels of gene expression for the serine synthesis pathway. These might suggest that even in absence of serine, HCT-116 cells were still capable of make serine and partially use if for production of NADPH in mitochondria. For cytosolic NADPH, HCT-116 cells might have greater capacity in coordinating metabolic network than other cancer cell lines and allowed increase of cytosolic and mitochondria NADPH in absence of glutamine and serine.

5.6. References

1. Vander Heiden, M. G. & DeBerardinis, R. J. Understanding the Intersections between Metabolism and Cancer Biology. *Cell* **168**, 657–669 (2017).

2. Heiden, M. G. Vander *et al.* Understanding the Warburg Effect : Cell Proliferation. *Science (80-.).* **324**, 1029 (2009).

3. Pavlova, N. N., Zhu, J. & Thompson, C. B. The hallmarks of cancer metabolism: Still emerging. *Cell Metab.* **34**, 355–377 (2022).

4. De Berardinis, R. J. & Chandel, N. S. Fundamentals of cancer metabolism. *Sci. Adv.* **2**, (2016).

5. Hosios, A. M. & Matthew, G. V. H. The redox requirements of proliferating mammalian cells. *J. Biol. Chem.* **293**, 7490–7498 (2018).

6. Goodman, R. P. *et al.* Hepatic NADH reductive stress underlies common variation in metabolic traits. *Nature* **583**, 122–126 (2020).

7. Ying, W. NAD $^{+}$ /NADH and NADP $^{+}$ /NADPH in Cellular Functions and Cell Death: Regulation and Biological Consequences. *Antioxid. Redox Signal.* **10**, 179–206 (2008).

8. Fan, J. *et al.* Quantitative flux analysis reveals folate-dependent NADPH production. *Nature* **510**, 298–302 (2014).

9. Chen, L. *et al.* NADPH production by the oxidative pentose-phosphate pathway supports folate metabolism. *Nat. Metab.* **1**, 404–415 (2019).

10. MacDonald, M. J. Feasibility of a mitochondrial pyruvate malate shuttle in pancreatic islets. Further implication of cytosolic NADPH in insulin secretion. *Journal of Biological Chemistry* vol. 270 20051–20058 (1995).

11. Pavlova, N. N. & Thompson, C. B. The Emerging Hallmarks of Cancer Metabolism. *Cell Metabolism* (2016) doi:10.1016/j.cmet.2015.12.006.

12. Son, J. *et al.* Glutamine supports pancreatic cancer growth through a KRAS-regulated metabolic pathway. *Nature* **496**, 101–105 (2013).

13. Lewis, C. A. *et al.* Tracing Compartmentalized NADPH Metabolism in the Cytosol and Mitochondria of Mammalian Cells. *Mol. Cell* **55**, 253–263 (2014).

14. Lee, W. D. *et al.* Tumor Reliance on Cytosolic versus Mitochondrial One-Carbon Flux Depends

on Folate Availability. *Cell Metab.* **33**, 190-198.e6 (2021).

15. Carpenter, A. E. *et al.* CellProfiler: Image analysis software for identifying and quantifying cell phenotypes. *Genome Biol.* **7**, (2006).

16. Tao, R. *et al.* Genetically encoded fluorescent sensors reveal dynamic regulation of NADPH metabolism. *Nat. Methods* **14**, 720–728 (2017).

17. Caicedo, J. C. *et al.* Data-analysis strategies for image-based cell profiling. *Nat. Methods* **14**, 849–863 (2017).

18. Moon, S. J., Dong, W., Stephanopoulos, G. N. & Sikes, H. D. Oxidative pentose phosphate pathway and glucose anaplerosis support maintenance of mitochondrial NADPH pool under mitochondrial oxidative stress. *Bioeng. Transl. Med.* 1–18 (2020) doi:10.1002/btm2.10184.

19. Birsoy, K. *et al.* Metabolic determinants of cancer cell sensitivity to glucose limitation and biguanides. *Nature* **508**, 108–112 (2014).

20. DeBerardinis, R. J. *et al.* Beyond aerobic glycolysis: Transformed cells can engage in glutamine metabolism that exceeds the requirement for protein and nucleotide synthesis. *Proc. Natl. Acad. Sci. U. S. A.* **104**, 19345–19350 (2007).

21. Mullen, A. R. *et al.* Oxidation of alpha-ketoglutarate is required for reductive carboxylation in cancer cells with mitochondrial defects. *Cell Rep.* **7**, 1679–1690 (2014).

22. Yun, J. *et al.* Vitamin C selectively kills KRAS and BRAFmutant colorectal cancer cells by targeting GAPDH. *Science (80-.).* **350**, (2015).

23. Santos, L. R. B. *et al.* NNT reverse mode of operation mediates glucose control of mitochondrial NADPH and glutathione redox state in mouse pancreatic β-cells. *Mol. Metab.* **6**, 535–547 (2017).

24. Zordoky, B. N. M., Bark, D., Soltys, C. L., Sung, M. M. & Dyck, J. R. B. The anti-proliferative effect of metformin in triple-negative MDA-MB-231 breast cancer cells is highly dependent on glucose concentration: Implications for cancer therapy and prevention. *Biochim. Biophys. Acta - Gen. Subj.* **1840**, 1943–1957 (2014).

25. Martinez-Outschoorn, U. E., Peiris-Pagés, M., Pestell, R. G., Sotgia, F. & Lisanti, M. P. Cancer metabolism: A therapeutic perspective. *Nat. Rev. Clin. Oncol.* **14**, 11–31 (2017).

26. Ducker, G. S. *et al.* Reversal of Cytosolic One-Carbon Flux Compensates for Loss of the Mitochondrial Folate Pathway. *Cell Metab.* **23**, 1140–1153 (2016).

Chapter 6

Role of citrate transporter for NADPH homeostasis

6.1. Abstract

NADPH is impermeable to inner mitochondrial membrane. Thus, NADPH pools and its ratio to $NADPH^+$ are known to be different in cytosol and mitochondria. NADPH shuttle systems have been shown to transfer reducing equivalents of NADPH from cytosol to mitochondria, or vice versa. However, it is difficult to measure the direction of NADPH shuttles in living cells. Here, I use both computational and experimental approach to uncover how citrate- αKG shuttle system mediates cytosolic and mitochondrial NADPH dynamics. First, I use a computational simulation to determine SLC25A1, a gene that encodes citrate transporter, is important for maintenance of NADPH homeostasis among SLC25 gene family. Then, I perform live-cell imaging experiments to determine dynamics of cytosolic and mitochondrial NADPH upon inhibition of this transporter and mitochondrial oxidative stress.

6.2. Introduction

Eukaryotic metabolism is characterized by compartmentalization[1]. Several isoenzymes use different cofactors, or exist in different compartments. NADPH is an ultimate reducing equivalents, supporting reductive biosynthesis and combatting against oxidative stress. However, due to a phosphate group, NADPH is considered impermeable to the inner mitochondrial membrane[2]. Therefore, NADPH levels and its ratio to $NADP^+$ are considered to be different between cytosol and mitochondria. Yet, the reducing equivalents can be indirectly shuttled from the cytosol to mitochondria, or vice versa, through several metabolite shuttle systems.

In humans, there are 53 mitochondrial carriers[3]. Of those, there are several metabolite shuttles that can transport NADPH from cytosol to mitochondria, or vice versa. First is the citrate

and αKG shuttle systems. SLC25A1 gene encodes citrate transporter, which is an anti-transporter for citrate and malate[4]. It has been shown that citrate transporter is important for biological function as citrate can be lysed to oxaloacetate and acetyl-CoA, which can be used for lipid synthesis pathway. Mutation of citrate transporter has been associated with autosomal recessive neurometabolic disorder by disrupting lipid, dolichol, ubiquinone and sterol synthesis[5]. For Nonalcoholic fatty liver disease (NAFLD), inhibition of citrate transporter ameliorated glucose intolerance and reverted steatosis for preclinical models[6]. For cancers, the citrate transporter mediated therapy resistance in non-small lung cancers cells[7].

Citrate-αKG shuttle systems are based on the transport of citrate and αKG between cytosol and mitochondria. As citrate is transported out to cytosol, it can be converted to isocitrate via aconitase, followed by isocitrate dehydrogenase reaction to make αKG, while generating NADPH and CO_2. Then, αKG can be transported into mitochondria through the αKG carrier, which is encoded by SLC25A11 gene. αKG in mitochondria can be further oxidized through the TCA cycle, but it can also be reduced to isocitrate dehydrogenase through isocitrate dehydrogenase reaction in mitochondria. This isocitrate can be converted to citrate. This completes the citrate-αKG shuttle system.

Under physiologically relevant conditions, citrate-αKG shuttle system is shown to work in a direction of transporting citrate out to cytosol as citrate is a key precursor for lipid synthesis[8]. However, cells growing detached from the extracellular matrix are associated with increase production of reactive oxygen species and the shuttle system reversed its direction such that citrate is transported into mitochondria, while indirectly transferring NADPH from cytosol to mitochondria[9]. Indeed, it is shown that when citrate transporter is inhibited for cells growing in monolayer, citrate is accumulated in mitochondria, whereas citrate is accumulated in cytosol

for spheroids[7]. Acetylated citrate transporter increase kinetic rates by transporting citrate to cytosol faster in macrophages[10]. More recently, mitochondrial carrier, including citrate transporter, contain reactive cysteine residues that are vulnerable to modification and change of reaction kinetics[11].

Another metabolite shuttle system for NADPH is pyruvate-malate system[12]. It is first proposed and shown that malate generated through TCA cycle or pyruvate carboxylation and malate dehydrogenase is transported out to cytosol via dicarboxylate carrier. In cytosol, malate is converted to pyruvate, while generating NADPH and CO_2 in cytosol. The pyruvate enters into mitochondria and the cycle repeats[13]. Pancreatic cells, liver, and kidney exhibited high expression levels of pyruvate carboxylase and malate-pyruvate cycling in pancreatic beta cells was implicated to generate large quantity of NADPH and implicated in insulin secretion[13,14]. Cancer cells with high pyruvate carboxylase activity may use pyruvate-malate shuttle system in greater extent than the pentose phosphate pathway to replenish cytosolic NADPH. Oxaloacetate from the pyruvate via pyruvate carboxylase can go directly convert to pyruvate and replenish NADPH in the mitochondria. It can be quite reasonable as the carbon may not need to go through this TCA cycle to generate malate.

Additionally, adipocytes are shown to produce NADPH through malic enzyme in cytosol under normoxic condition[15]. Additionally, some cancer cells require pyruvate carboxylase for glutamine independent growth[16]. Dicarboxylate carrier (DIC) is important for transporting malate from mitochondria to cytosol. Knockdown of DIC inhibits A549 growth by shifting glycolysis to oxidative phosphorylation through glutamine catabolism[17]. Additionally, DIC is not only transporting malate, but also facilitates transport of malonate, succinate in exchange of phosphate, sulfate, sulfite, or glutathione[18,19].

Many other combinations of mitochondrial carriers exist to transfer reducing equivalents from cytosol to mitochondria, or vice versa, in the form of NADH or NADPH[3]. Many of metabolic enzymes that are related to metabolite shuttle systems particularly share the same metabolites that use either NAD(P)H, allowing the change of both NADH and NADPH redox states in cytosol and mitochondria[20].

The goal of this chapter is to explore which of the mitochondrial carrier and subsequently metabolite shuttle systems are important for indirect NADPH shuttle. To achieve this goal, I first employ a genome-scale metabolic model for human metabolic network with constraints to determine that SLC25A1, a gene that encodes citrate transporter, is a key metabolite shuttle system for NADPH from SLC25 gene family. Then, I perform live-cell imaging experiments to determine the direction of this shuttle system at basal and oxidative stress by inhibiting the citrate transporter and/or induce oxidative stress pharmacologically.

6.3. Materials and Methods

6.3.1. Essentiality and co-essentiality analysis

The purpose of essentiality analysis in this work was to determine which of SLC25 gene family influence cell growth most. Essential genes were identified through a genome-wide CRISPR screening[21]. CRISPR score (CS) was defined as the mean log2 fold-change in sgRNAs levels that target a specific gene. As a specific gene knockout impairs cell growth, cells died and the sgRNA counts after 14 population doubling time will be lower than the initial sgRNA. Thus, by calculating the fold-change of sgRNA abundances, one could determine the influence of specific gene knockouts to cell proliferation. The cut-off line that determined the essentiality was rather

subjective, but a score lower than -0.5 was considered be essential in general. Broad Institute generated CRISPR-Cas9 Knockout-out screens based on 18,333 genes on 689 cell lines. The CRISPR score data was deposited and freely available now.

Co-essentiality analysis was an expansion of gene essentiality analysis, in which two sets of CS of genes were plotted against each other and the correlation analysis is performed[22]. Genes that shared a same pathway or similar functions showed similar patterns of essentiality and revealed high correlation. In this work, we downloaded the essentiality file, performed co-essentiality across the SLC25 genes. After performing the gene essentiality analysis, I selected the top 10 genes that show least CS score. Then, of those genes, I performed co-essentiality analysis to determine whether each of the selected genes have other unknown genes or sets of genes that may share functions related to NADPH metabolism. Additionally, I selected the top 50 genes of highly correlated genes and used Panther gene enrichment analysis to determine in which biological processes the selected SLC25 gene was most highly related[23].

6.3.2. Curated genome-scale metabolic model for human metabolism

The goal of using genome-scale metabolic model was to perform gene knockout simulation on SLC25 genes and determine which of genes perturb NADPH metabolic pathways most. We used the genome-scale metabolic model for humans (GEM-human) developed by Nielsen lab[24]. This model curated the most recent human metabolic models such as Rcon3D and upgraded in a way that it facilitated metabolic analysis for cell lines and tissue specific models by integrating other omics data. In this work, I first downloaded the Human-GEM and curated the model by constraining the nutrient uptake rates and additionally applying the transcriptomics data obtained from the Human Protein Atlas data. Through the transcriptomics incorporation, I reduced the

model size from 8378 by 13082 to 5378 by 7472. After the model curation, I performed flux balance analysis using COBRA toolbox by setting an objective function of maximum cell growth, followed by the maximum NADPH generation rates in cytosol and mitochondria while setting the minimum flux through the growth is one half of the optimized flux. With the objectives established, we implemented SLC25 gene knockout simulations and determined the rates of NADPH generating enzymes as well as the net NADPH generation rates.

6.3.3. Time-lapse imaging for cytosolic and mitochondrial NADPH dynamics

As previously described in Chapter 2, the fluorescence emission signal was recorded using an inverted IX81 wide field fluorescence microscope (Olympus) with a 20x objective lens and Prior Lumen 2000 lamp. The Chroma 415/30 nm and a Semrock 488/6 nm excitation filters were used and a Semrock 525/ 40 nm filter was used for the emission filter. The exposure time was 300 ms and 10% lamp intensity was used. An in-built multi-dimensional setup was used for automated time-course measurement. Images were captured every minute and exported to either ImageJ or MATLAB 2016a for post image processing.

6.4. Results

6.4.1. Essentiality and co-essentiality analysis on SLC25 genes identify key SLC25 genes required for cell growth and their biological functions

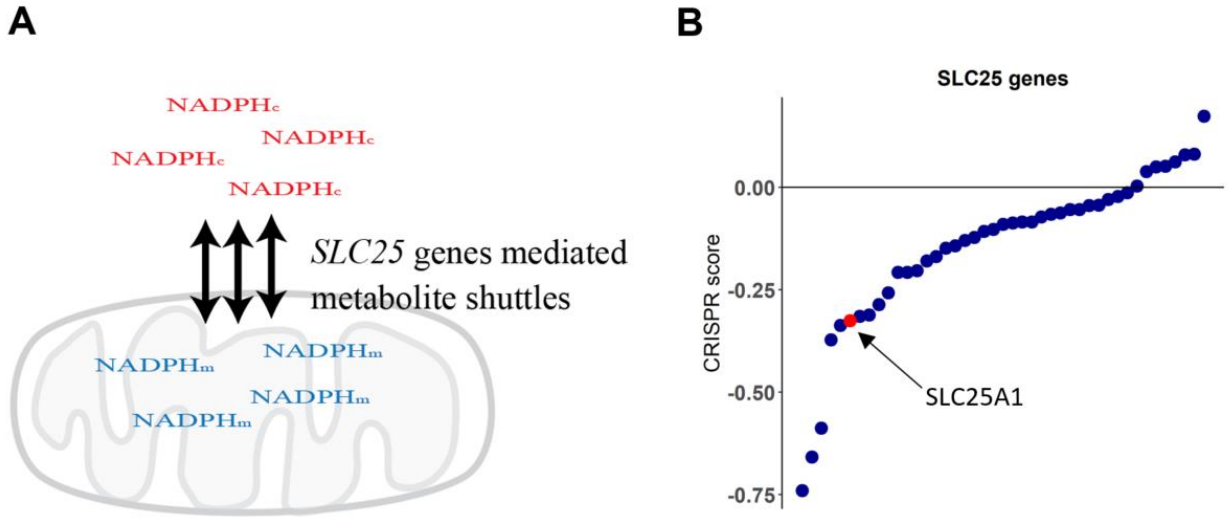

Figure 6.1. SLC25 genes transport metabolites across inner mitochondrial membranes, transferring NADPH reducing equivalents during the process. (A) Schematics representing SLC25 genes that facilitate metabolite shuttles for NADPH reducing equivalents. (B) CRISPR scores on SLC25 genes reveals an extent of gene knockout to cell growth.

NADPH was known to be transferred between cytosol and mitochondria via indirect metabolite shuttle systems such as malate-pyruvate, isocitrate-αKG, citrate-malate-pyruvate, glutamate-malate, etc (**Figure 6.1**)[3]. To understand which of SLC25 genes played an important role in shuttling NADPH reducing equivalents and for cell survival, we implemented gene essentiality and co-essentiality analysis. First, based on the Achilles Gene Effect database from Broad Institute, we implemented essentiality analysis on 43 known SLC25 family to estimate which of SLC25 genes are essential for cell growth. Lower CRISPR score (CS) implicate a knockout of specific gene impairs cell growth more. We determined the median CS of individual SLC25 genes across 739 cell lines and found approximately 81% of the tested SLC25 genes showed negative CS score, meaning knockout of these genes inhibited cell growth (**Figure 6.1**).

SLC25A11 gene that encoded αKG transporter ranked in top 23 and its CS was near 0. The Top 10 SLC25 genes with lowest CS score included transporters that carried small molecules such as phosphate, S-adenosyl methionine, succinate, citrate, malate, glutamate, and other metabolites (**Table 6.1**).

Table 6.1. Top 10 SLC25 genes with lowest CS score from Achilles Gene Effect database

Gene name	CS Score	Aliases	Substrates
SLC25A3	-0.74	Phosphate carrier	Phosphate
SLC25A26	-0.66	S-adenosyl methionine carrier	S-adenosyl methionine, S-adenosyl homocysteine
SLC25A10	-0.59	Dicarboxylates carrier	Succinate, malate, phosphate, sulphate, thiosulphate
SLC25A28	-0.37	mitoferrin-2	Unknown
SLC25A22	-0.34	Glutamate carrier 1	Glutamate
SLC25A25	-0.33	ATP-MG/Pi carrier	ATP-Mg, Pi, ADP, ATP
SLC25A1	-0.31	Citrate carrier	Citrate, isocitrate, malate
SLC25A19	-0.31	Thiamine-pyrophosphate carrier	thiamine-pyrophosphate, thiamine-monophosphate, (deoxy)nucleotides
SLC25A48	-0.29	unknown	Unknown
SLC25A18	-0.26	Glutamate carrier 2	Glutamate

Then, we performed a co-essentiality analysis on top 10 selected genes to determine in which biological process each of SLC25 gene is involved. After implementing co-essentiality analysis for 18336 genes with each of SLC25 gene in the top 10 list, we pulled out the top 100

genes that showed high correlation with the target gene and implemented for biological process enrichment analysis using the PANTHER classification[23]. Of the top 10 genes selected, only five of the SLC25 gene family showed linked GO biological processes. The results were consistent with the previous findings[3]. For instance, SLC25A3 was a phosphate carrier, and its main function was to provide phosphate group to ADP and make ATP during oxidative phosphorylation step. The essentiality and co-essentiality analyses captured both of these functions. Similarly, SLC25A26 imports S-adenosylmethionine (SAM) and provides methyl group for methylation of DNA, RNA, proteins including complex I, coenzyme Q, iron-sulfur cluster biosynthesis, and was important for maintaining mitochondrial energy metabolism[4,25]. In regards to NADPH reducing equivalent transport, only SLC25A1 gene appeared in both essentiality and co-essentiality analysis. Other genes were as essential to SLC25A1 gene but their linked biological functions were not statistically significant (**Table 6.2**). SLC25A11 genes that encoded αKG transporter did not statistically significant biological processes based on GO enrichment analysis.

Table 6.2. Pathway enrichment analysis for selected SLC25 genes with co-essential hits

Gene name	GO biological process	Raw p-value	FDR
SLC25A3	mitochondrial electron transport	6.6E-37	6.9E-34
SLC25A26	glutaminyl-tRNAGln biosynthesis	2.4E-06	4.7E-04
SLC25A10	No statistically significant results		
SLC25A28	protein insertion into mitochondrial inner membrane	1.3E-06	6.6E-03

SLC25A22	No statistically significant results		
SLC25A25	No statistically significant results		
SLC25A1	mitochondrial acetyl-CoA biosynthetic process from pyruvate	8.0E-08	2.2E-05
SLC25A19	valyl-tRNA aminoacylation	1.5E-04	2.0E-02
SLC25A48	No statistically significant results		
SLC25A18	No statistically significant results		

6.4.2. Genome-scale metabolic model reveals a knockout of SLC25A1 impairs NADPH homeostasis

In addition to the essentiality and co-essentiality analysis, we performed knockout simulation on SLC25 genes to predict which of genes will perturb NADPH homeostasis and NADPH dependent reactions, if deleted. We first curated a default genome-scale metabolic model for Hela metabolism provided by Nielsen group by constraining nutrient uptake rates and incorporating transcriptomics data. Based on the curated model, we implemented flux balance analysis with random sampling methods that account for 14,850 inputs for single gene knockout simulations for SLC25 genes (**Figure 6.2**). The median net NADPH generation rate for wild type was 0.01 mmol g-DCW^{-1} hr^{-1}. Upon knockout of the SLC25A1 gene, which encoded citrate transporter, the net NADPH generation decreased by nearly 56 %. The knockout of SLC25A26 gene, which encoded S-adenosyl methionine carrier also decreased the rate by nearly 13 %. On the other hand, knockout of other SLC25 genes increased the net NADPH generation rates. Knockout of SLC25A3 and SLC25A11 genes increased the net NADPH generation rates by

nearly 2 fold. The SLC25A10 knockout simulation showed a wide variation as it transfers a wide range of metabolites.

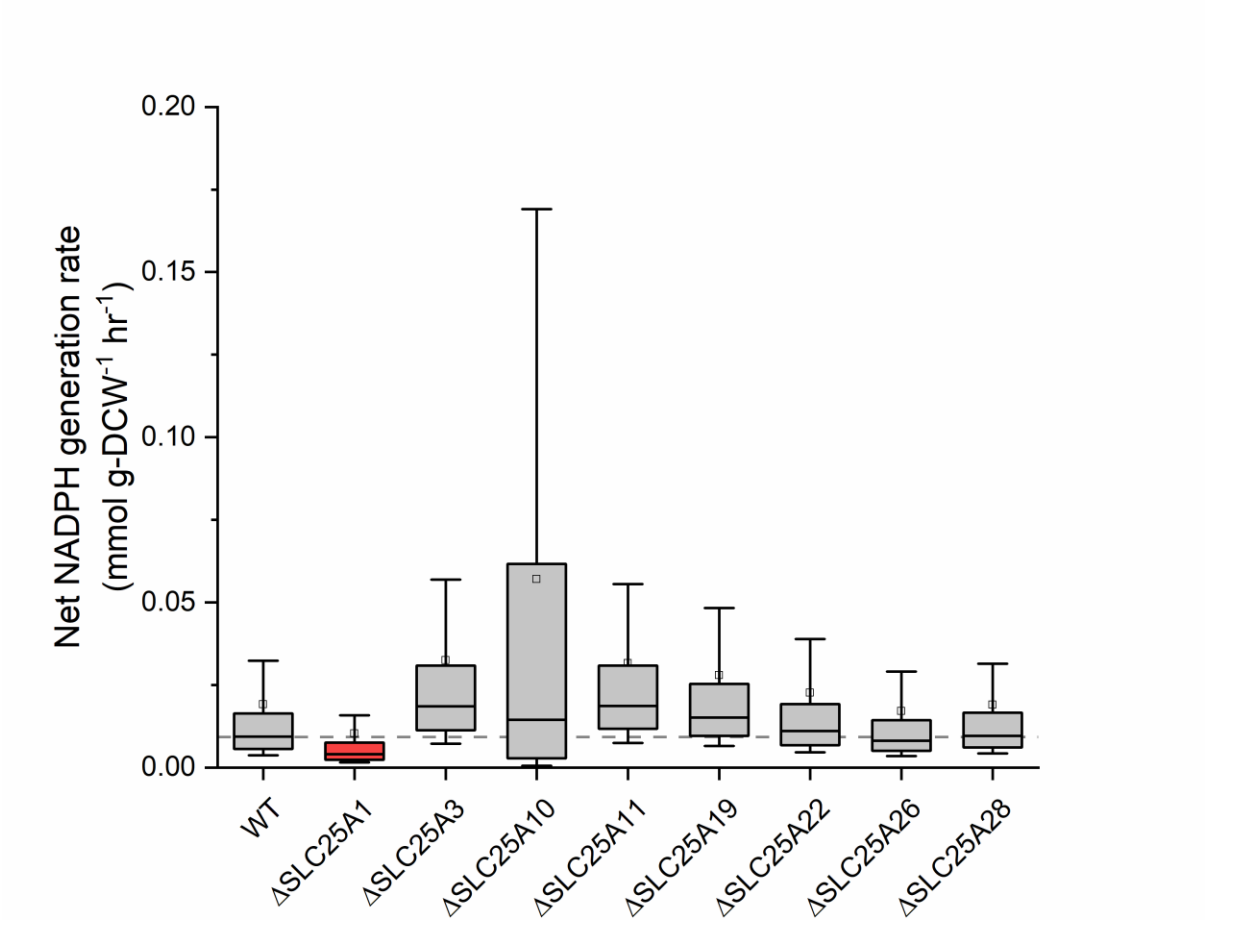

Figure 6.2. Flux balance analysis on a curated genome-scale metabolic model for Hela cells reveals distributions of a net NADPH generation rate on SLC25 gene knockout simulations.

Additionally, we evaluated the NADPH generating rates within the metabolic network upon knockout of SLC25 genes. Knock out of SLC25A1 genes decreased pentose phosphate pathway flux most by reducing the flux nearly 34 %. Additionally, IDH1 and MTFD1 rates also decreased by 34% and 78%. While the IDH1 reaction decreased, the IDH2 reaction increased by 3.3 fold. On the other hand, knock-out of other SLC25 genes that were selected from the essentiality and co-essentiality analysis did not show much impact on NADPH dependent

metabolic enzymes, except SLC25A10 and SLC25A11 and SLC25A22 genes. SLC25A10 was dicarboxylate transporter and related to malate transporter. Indeed, the analysis showed that knockout of SLC25A10 completely reduced the flux through malic enzyme but also altered the direction of MTHFD1 to generate NADPH in cytosol, while maintaining the same flux. Direction of IDH2 reaction also changed in a way of consuming NADPH in mitochondria. SLC25A11 was a αKG transporter. Knockout simulation of SLC25A11 gene showed the direction of IDH2 changed in a way of consuming NADPH in mitochondria and increasing the flux by nearly 6 fold. The MTFD1 reaction flux decreased by 33 %. Knockout simulation of glutamate carrier, which was encoded by SLC25A22, decreases flux through IDH1, IDH2, and pentose phosphate pathway by 2 % and increased the rate of ME1 by 80 % (**Figure 6.3**).

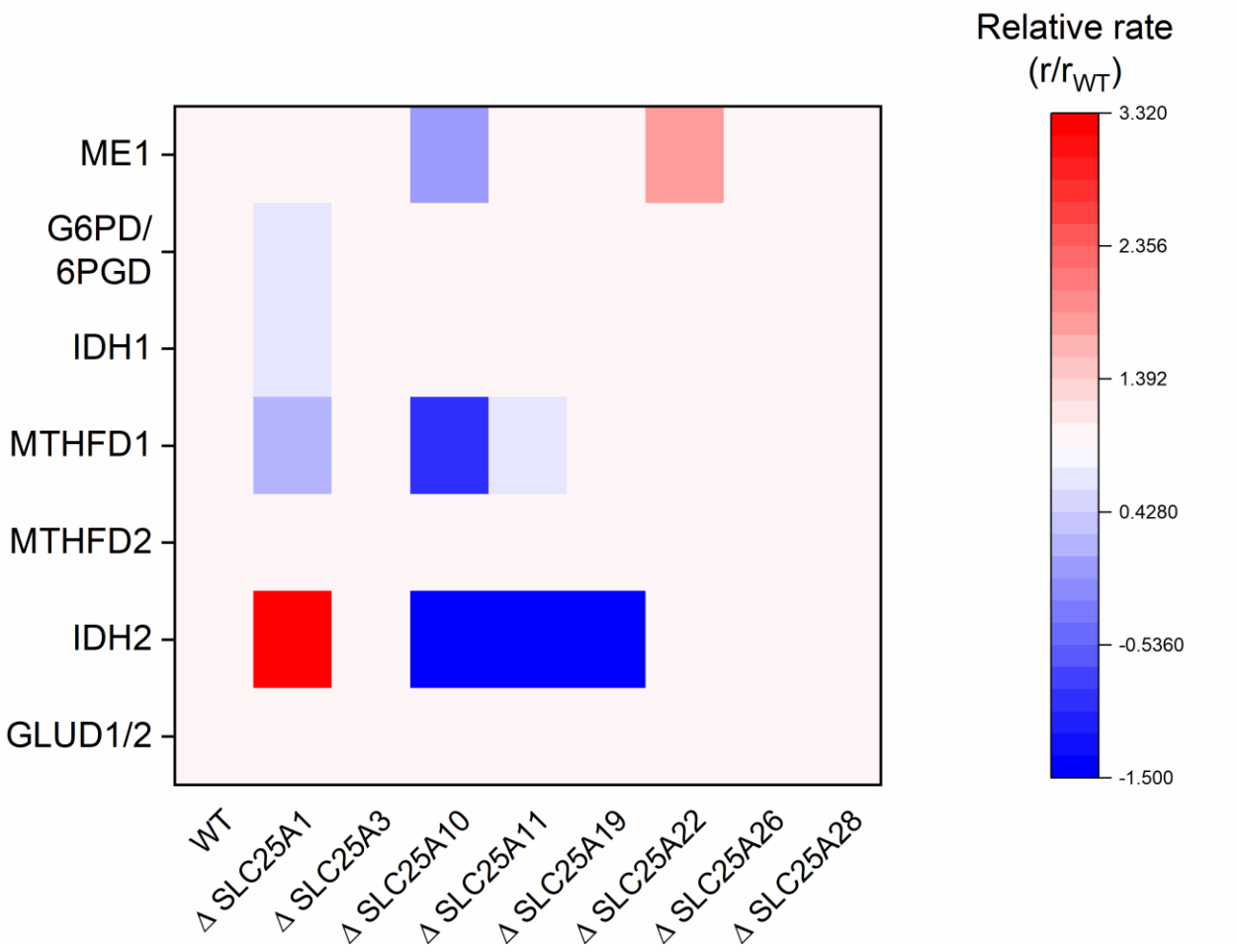

Figure 6.3. A heat map representing a knockout simulation of SLC25 genes and its influence on NADPH generating enzymatic reaction rates.

6.4.3. Inhibition of citrate transporter decreases cytosolic NADPH pools.

To determine a direction of citrate αKG NADPH shuttle system, we implemented time-lapse imaging experiment while perturbing the shuttle system through inhibition of citrate transport (**Figure 6.4**). If the shuttle system worked in a clockwise direction, we hypothesized an acute inhibition of citrate transporter accumulated citrate in mitochondria and increased flux through TCA cycle, leading to an increased NADH and NADPH generation through IDH2, ME3, and NNT enzymatic reactions. As cytosolic NADPH could be maintained through other NADPH

generating enzymes, we reasoned that cytosolic NADPH would not change greatly or may decrease slightly.

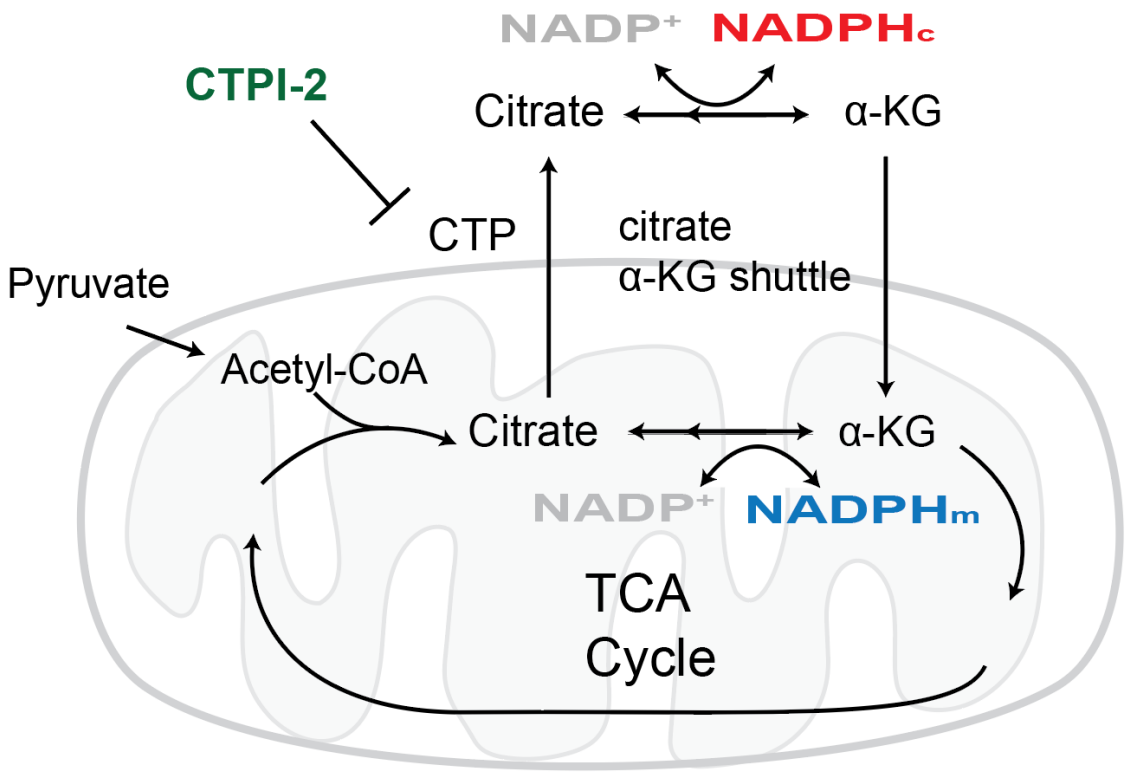

Figure 6.4. Schematics representing a citrate αKG NADPH shuttle system.

As citrate transporter was inhibited, we observed a declining trend of cytosolic NADPH index as it decreased by 6% compared to the initial value and by 10 % compared to the control condition after 15 minutes of inhibition. On the other hand, the mitochondrial NADPH showed increasing trend upon inhibition. The mitochondrial NADPH index increased by 13% compared to the initial value and by 17% compared to the control after 15 minutes (**Figure 6.5**).

Since the NADPH index was more of qualitative term as it did not indicate a value such as concentration or rate, we converted the signal to concentration after calibration of the sensor as previously described. After converting the index to concentration and by taking the rate of 15

minute time span, we determined the rate of change of NADPH. For cytosolic NADPH, the baseline rate was approximately 1.5 nM/min, whereas the inhibition of citrate transporter decreased the rate to -17.7 nM/min. For mitochondrial NADPH, the baseline rate was approximately 125 nM/min, whereas the inhibition increased the rate to 305 nM/min. Based on the rates, the cytosolic NADPH rate decreased by 11.8 fold whereas the mitochondrial NADPH rate increased by 2.4 fold.

Upon inhibition of citrate transporter, we observed the cytosolic NADPH rate decreased whereas the mitochondrial NADPH rate increased. These opposite directionality indicated that the citrate transporter mediated transporter operated in a clockwise direction. With inhibition, the cytosolic NADPH transport via citrate transporter was blocked such that NADPH was not shuttled out to cytosol and thus transient reduction in cytosolic NADPH. On the other hand, the mitochondrial NADPH transiently accumulated with inhibition. From the literature, the inhibition of citrate transporter allowed accumulation of citrate in mitochondria, which could subsequently fuel the TCA cycle and subsequent metabolites could allow transient increase of mitochondrial NADPH via reactions such as IDH2, NNT, and ME3.

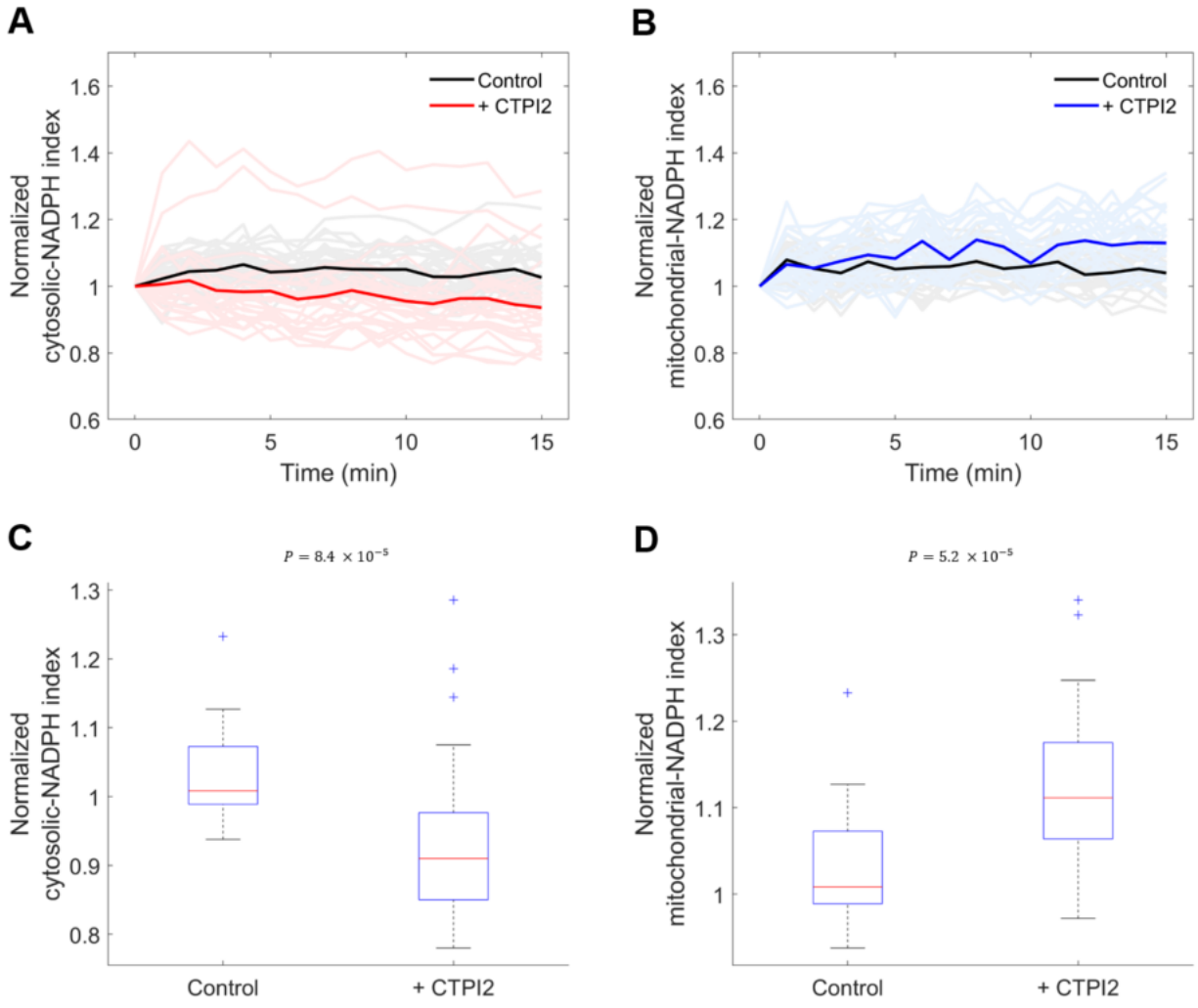

Figure 6.5. Cytosolic and mitochondrial NADPH dynamics upon inhibition of citrate transporter. Kinetics of (A) cytosolic and (B) mitochondrial NADPH indices normalized to the initial index at t = 0 min. Box plots represent a distribution of normalized (C) cytosolic and (B) mitochondrial NADPH indices at t = 15 minutes.

Next, we tested the same experiments with other cell lines and whether the patterns are consistent through the cell lines. The cytosolic NADPH levels decreased throughout different cell lines, but the mitochondrial NADPH levels did not change for these cell lines. In specific, the cytosolic NADPH index decreased by nearly 8, 7, 6 % across A549, HCT-116, and MDA-MB-231 cell lines (**Figure 6.6**). On the other hand, for mitochondrial NADPH index, only Hela cells exhibited increase of mitochondrial NADPH index, whereas other cell lines remained near

constant (**Figure 6.7**). The consistent decrease of cytosolic NADPH levels upon citrate transporter inhibition might be due to lack of citrate available for IDH1 reactions. However, addition of citrate did not increase cytosolic NADPH levels upon inhibition of citrate transporter and even lower the mitochondrial NADPH levels (**Figure 6.8**). This indicated that citrate transporter may perturb NADPH generation pathways due to lack of citrate available in the cytosol but the inhibitor itself perturbs other biological functions that influence cytosolic NADPH pools.

Lastly, we measured the cytosolic and mitochondrial NADPH indices after 24 hours of treatment of citrate transporter inhibitor. Treatment of citrate transporter inhibitor decreased both cytosolic and mitochondrial NADPH indices. For 400 μM of CTPI-2, both cytosolic and mitochondrial NADPH indices decreased by 15 and 13 % respectively. For 800 μM of CTPI-2 treatment, cytosolic and mitochondrial NADPH indices decreased by 60 and 47 % (**Figure 6.9A**). In regards to cell growth, approximately 60 % of cells survived in 400 μM of CTPI-2 treatment, whereas nearly all cells did not survive under 800 μM of CTPI-2 treatment (**Figure 6.9B)**.

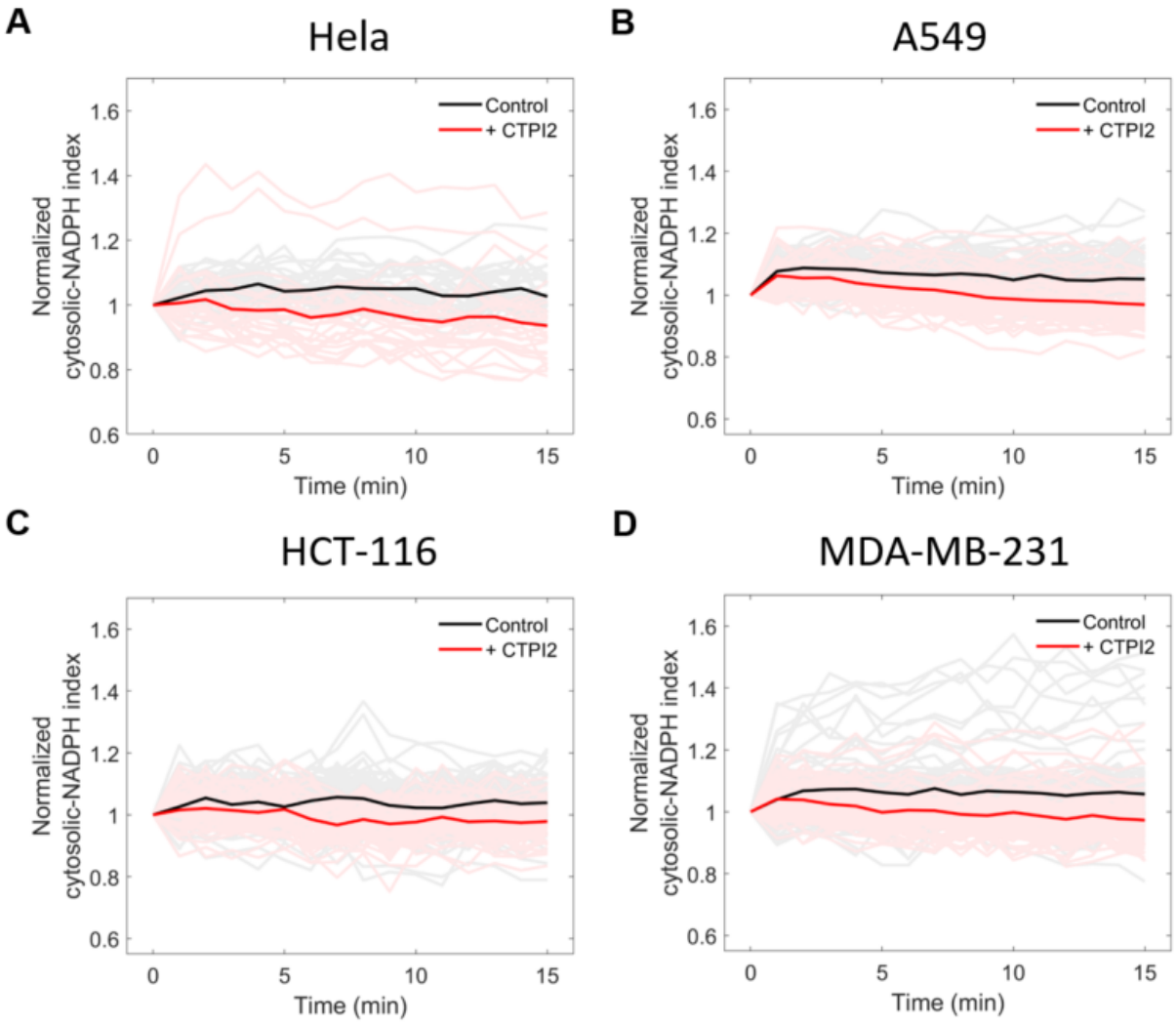

Figure 6.6. Cytosolic NADPH dynamics upon inhibition of citrate transporter for other cell lines. Normalized cytosolic NADPH indices of (A) Hela, (B) A549, (C) HCT-116, and (D) MDA-MB-231 cell lines.

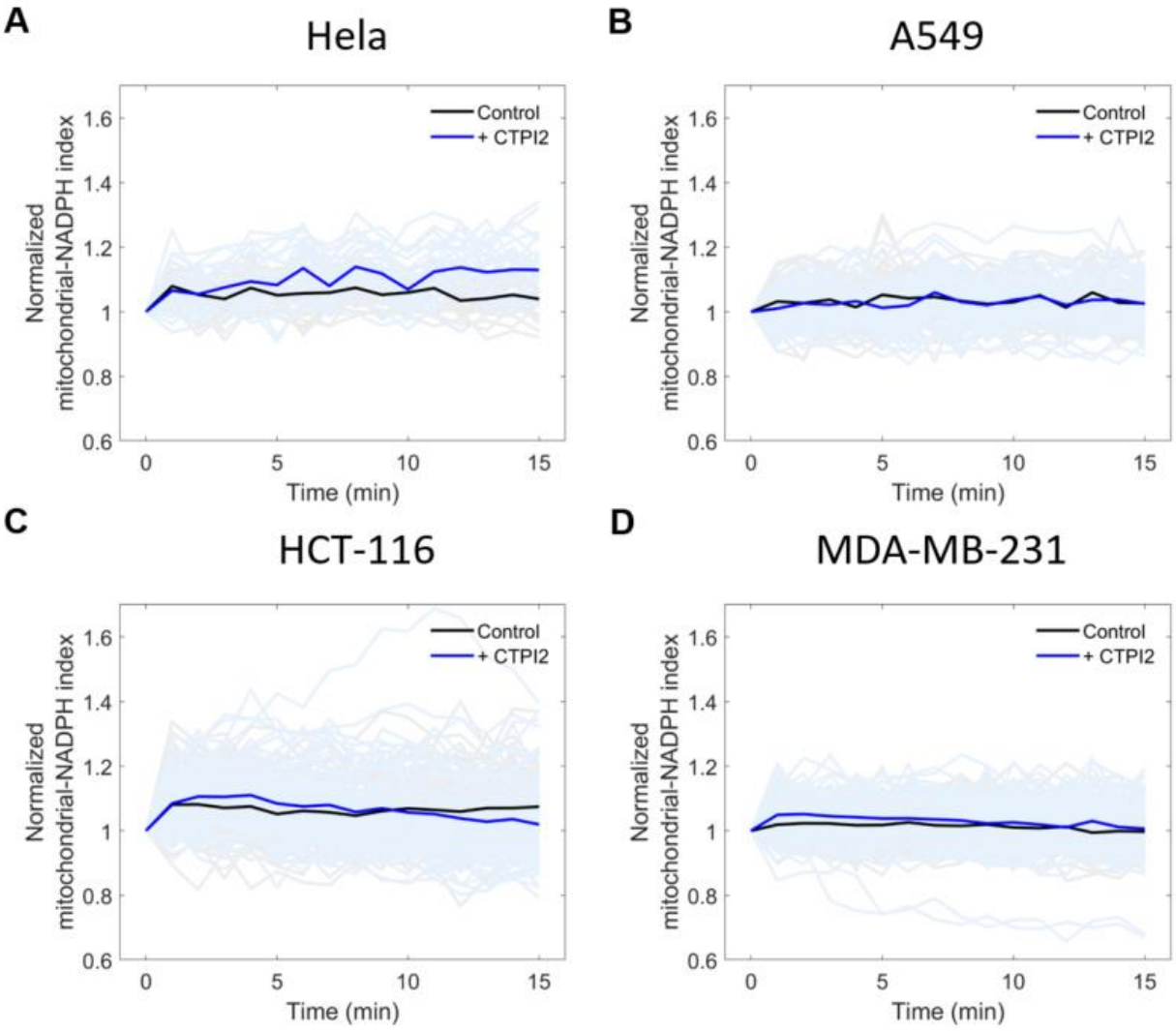

Figure 6.7. Mitochondrial NADPH dynamics upon inhibition of citrate transporter for other cell lines. Normalized cytosolic NADPH indices of (A) Hela, (B) A549, (C) HCT-116, and (D) MDA-MB-231 cell lines.

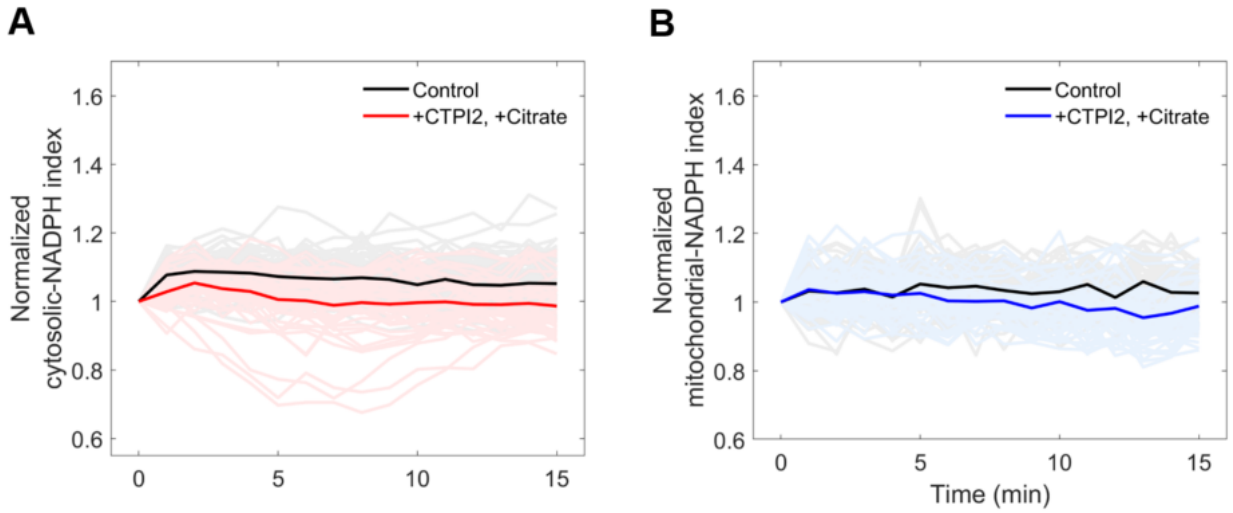

Figure 6.8. Cytosolic and mitochondrial NADPH dynamics upon inhibition of citrate transporter with citrate.

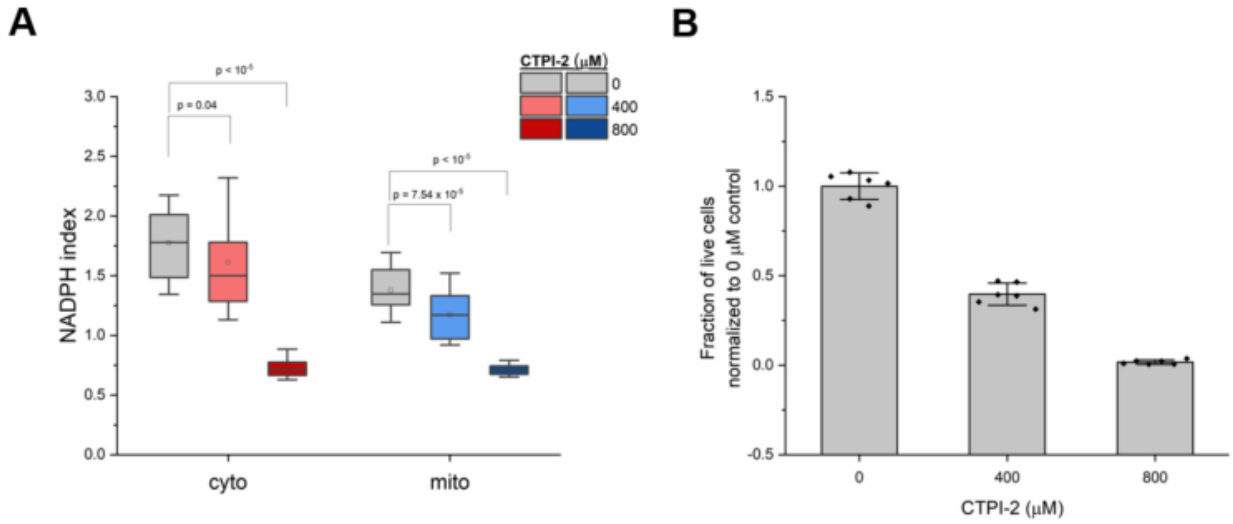

Figure 6.9. Cytosolic and mitochondrial NADPH indices after 24 hours upon treatment of CTPI-2. (A) The cytosolic and mitochondrial NADPH indices after 24 hours. (B) Influence of CTPI-2 to cell growth after 24 hours.

6.4.4. Inhibition of electron transport chain complex III increases mitochondrial NADPH levels

We hypothesized that the direction of citrate αKG NADPH shuttle system reverses in a way to shuttle NADPH from cytosol to mitochondria. As a method to generate mitochondrial stress, we used antimycin-A, which is an inhibitor of electron transport chain complex III. Antimycin-A is known to generate mitochondrial $O^{\cdot -}$ and H_2O_2, but it was also shown to increase mitochondrial NADH (**Figure 6.10**) [26,27]. When we treated cells with antimycin-A, we observed that mitochondrial NADPH levels did not change for Hela cells in 15 minutes, but for other cell lines mitochondrial NADPH levels increased (**Figure 6.11**). For Hela, the mitochondrial NADPH index increased by 1 % and statistically no significant compared to the control. For A549 cells, the mitochondrial NADPH index increased by nearly 5 % more than the control after 15 minutes. After 8 minutes, the mito-NADPH increased by nearly 12 %. For HCT-116 cells, the mito-NADPH index decreased by 2 % after 16 minutes. However, after 5 minutes, the index increased by nearly 11 % compared to the control at the peak. For MDA-MB-231 cells, the mito-NADPH index increased by 12 % compared to the control after 16 minutes (**Figure 6.12**).

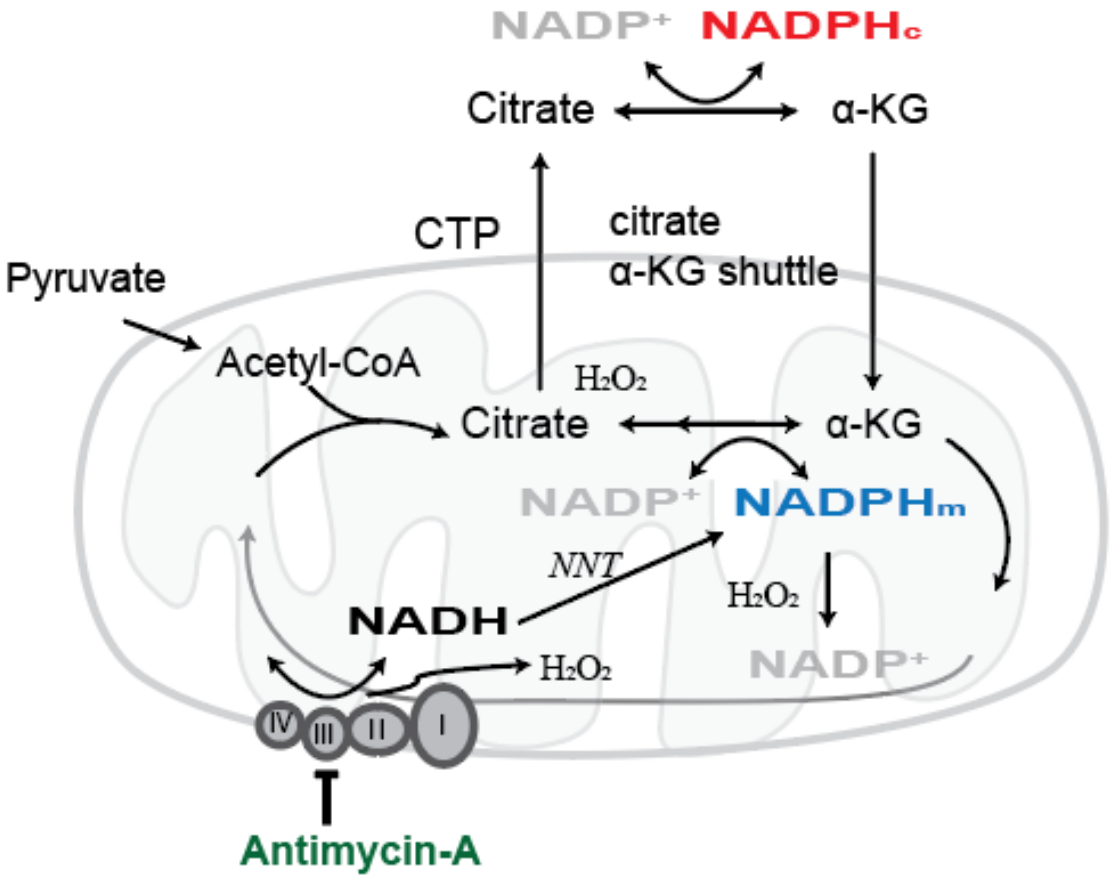

Figure 6.10. Schematics representing a mitochondrial dysfunctional system caused by inhibition of electron transport chain complex III by antimycin-A. One of the consequence of inhibition is accumulation of mitochondrial NADH and generation of H_2O_2.

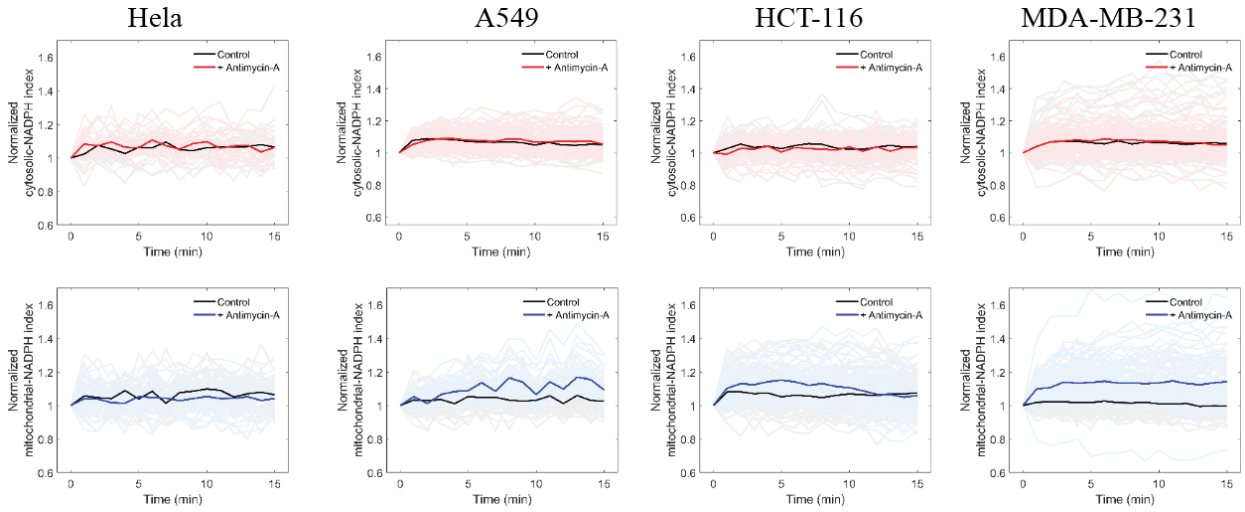

Figure 6.11. Dynamics of cytosolic and mitochondrial NADPH levels upon treatment of antimycin-A across different cancer cell lines.

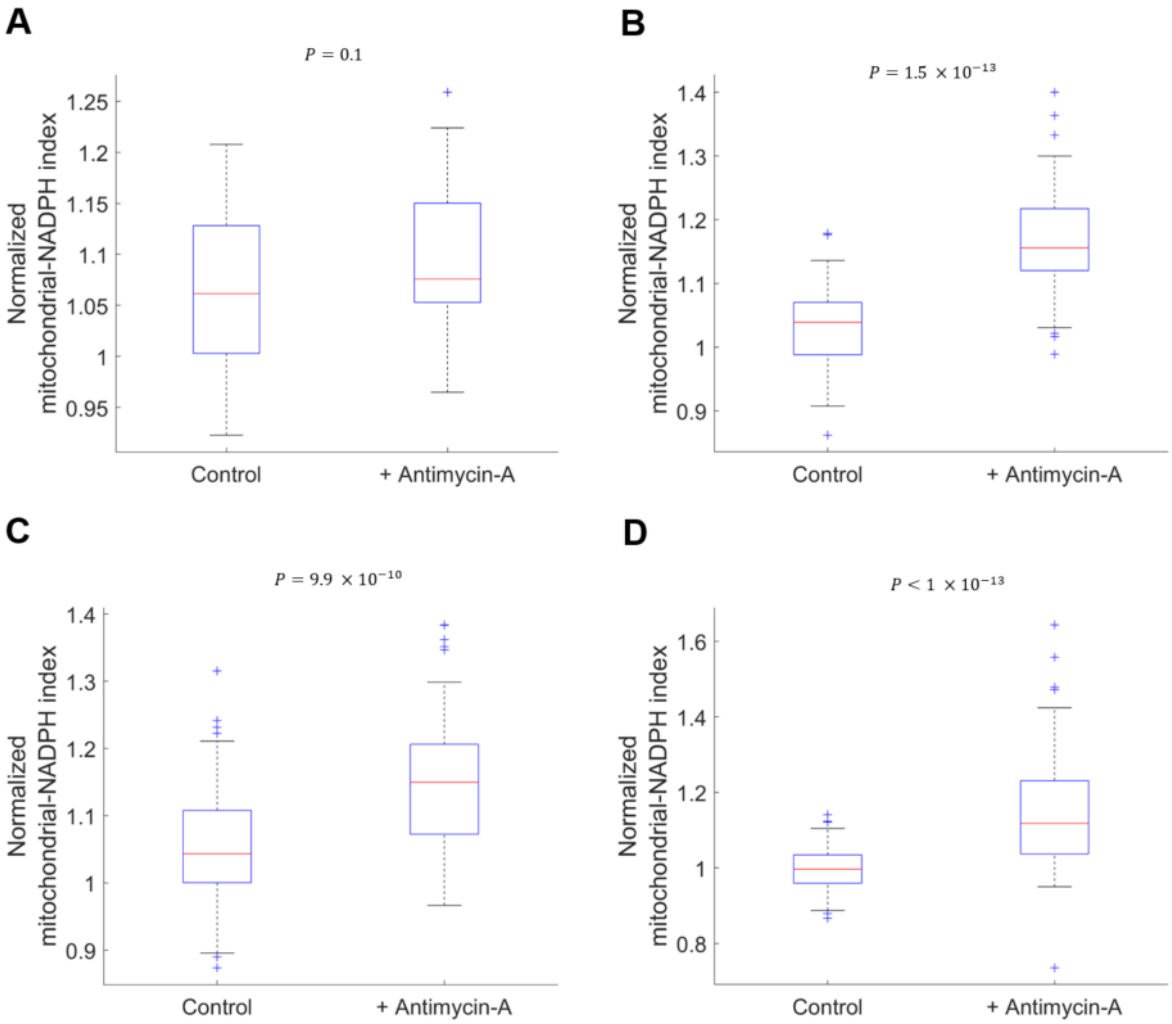

Figure 6.12. Box plots represent a distribution of mitochondrial NADPH indices at a time that exhibits a peak difference between experimental and control conditions. (A) Box plot represents a distribution of mitochondrial-NADPH index of Hela cell after 16 minutes, (B) of A549 cells after 8 minutes, (C) of HCT 116 cells after 5 minutes, and (D) MDA-MB-231 cells after 16 minutes.

6.4.5. Inhibition of citrate transporter and electron transport chain complex III perturbs both cytosolic and mitochondrial NADPH levels

Next, we tested how the co-treatment of citrate transport inhibitor and antimycin-A influences the cytosolic and mitochondrial NADPH dynamics (**Figure 6.13**). It was previously shown that citrate transporter inhibition decreased cytosolic NADPH levels, whereas antimycin-A treatment

increased the mitochondrial NADPH levels. Once the cells are challenged with these two small molecules, cytosolic NADPH levels decreased throughout the cell lines just as treatment of CTPI-2 alone (**Figure 6.14**). In particular, the cytosolic NADPH levels decreased by nearly 7, 13, 7, 5 % across Hela, A549, HCT-116, and MDA-MB-231 cells (**Figure 6.15**). Compared to the CTPI-2 only condition, in which the cytosolic NADPH levels decreased by 10, 8, 7, 6% compared to the control across the above cell lines, co-treatment did not make much difference across the cell lines.

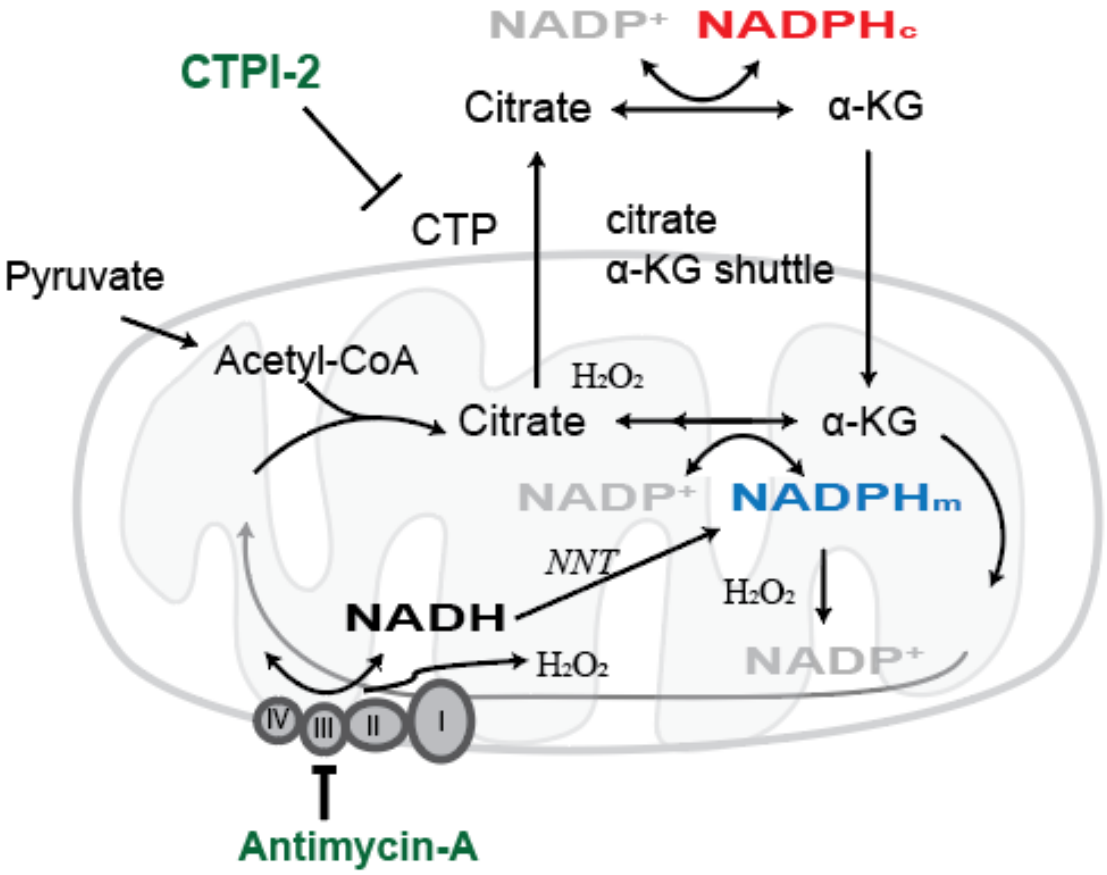

Figure 6.13. Schematics representing a mitochondrial dysfunctional system caused by inhibition of electron transport chain complex III by antimycin-A and inhibition of citrate transporter with CTPI-2.

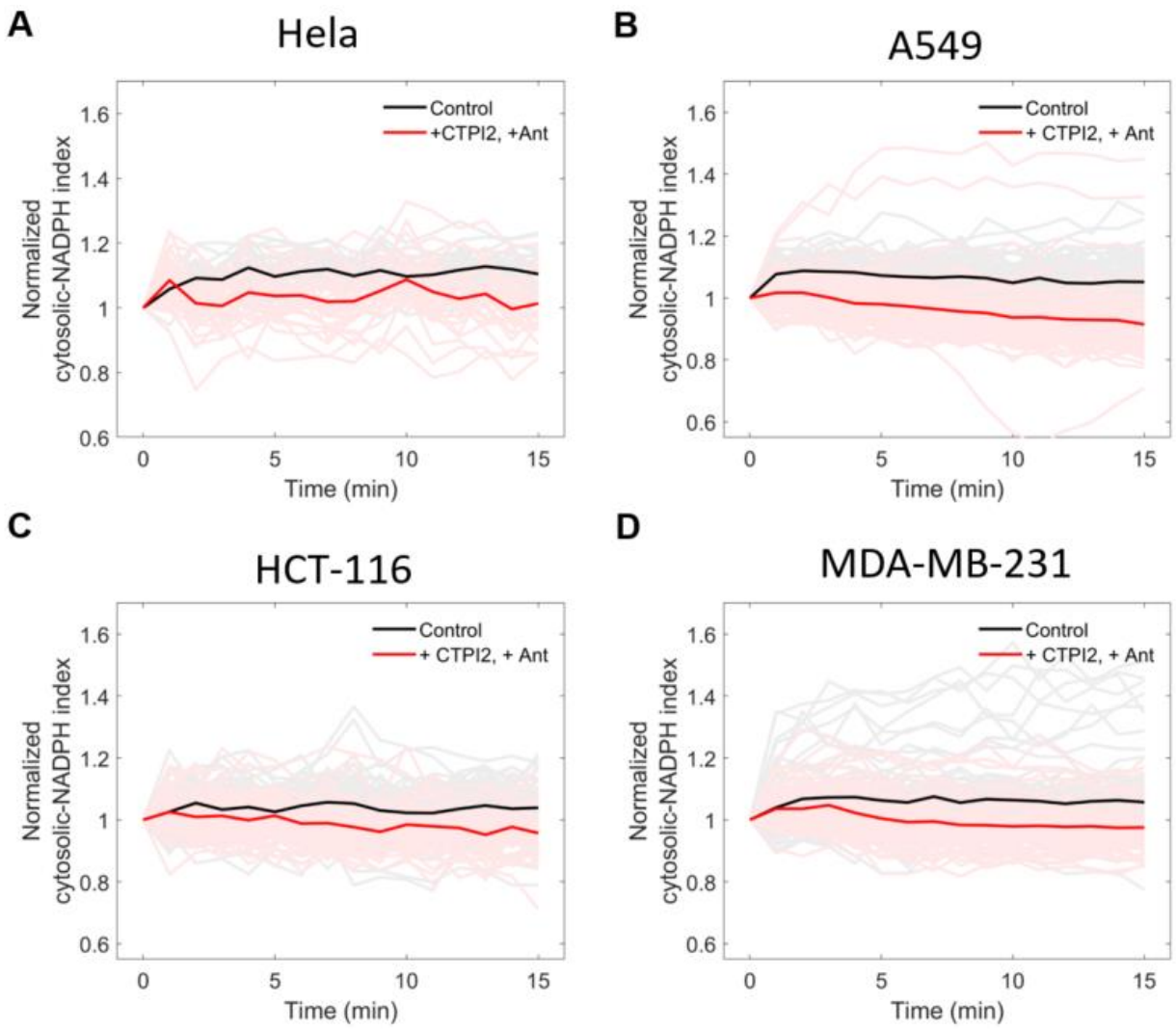

Figure 6.14. Dynamics of cytosolic NADPH levels upon co-treatment of CTPI-2 and antimycin-A across different cancer cell lines.

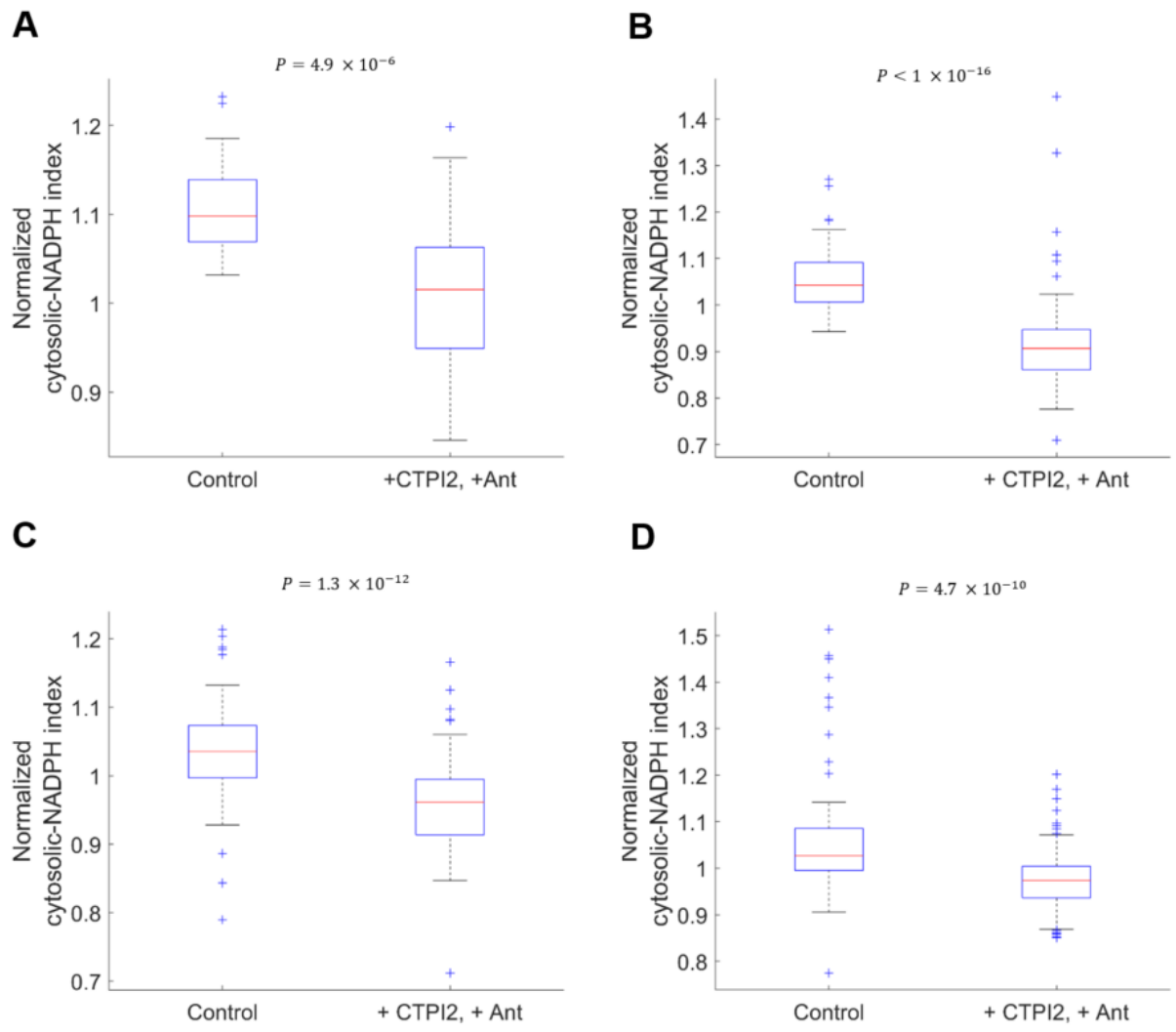

Figure 6.15. Box plots represent a distribution of mitochondrial NADPH indices at a time that exhibits a peak difference between experimental and control conditions. (A) Box plot represents a distribution of mitochondrial-NADPH index of Hela cell after 16 minutes, (B) of A549 cells after 8 minutes, (C) of HCT 116 cells after 5 minutes, and (D) MDA-MB-231 cells after 16 minutes.

In regards to the mitochondrial NADPH dynamics, co-treatment elevated the mitochondrial NADPH indices similar to antimycin-A condition, but the co-treatment started to decrease the mitochondrial NADPH index after the peak throughout the cell lines except Hela cells. NADPH index peaked after 10 minutes by increasing the NADPH index around 10 % compared to the control and started decreasing to end at 1 % greater than the control. For HCT-116 cell lines, mito-NADPH index increased by 16 % compared to the control after 5 minutes

and readily decreased to end with 15 % down compared to the control. For MDA-MB-231 cell lines, mito-NADPH index increased by 6 % compared to the control after 3 minutes and readily decreased to end with 13 % down compared to the control (**Figure 6.16**).

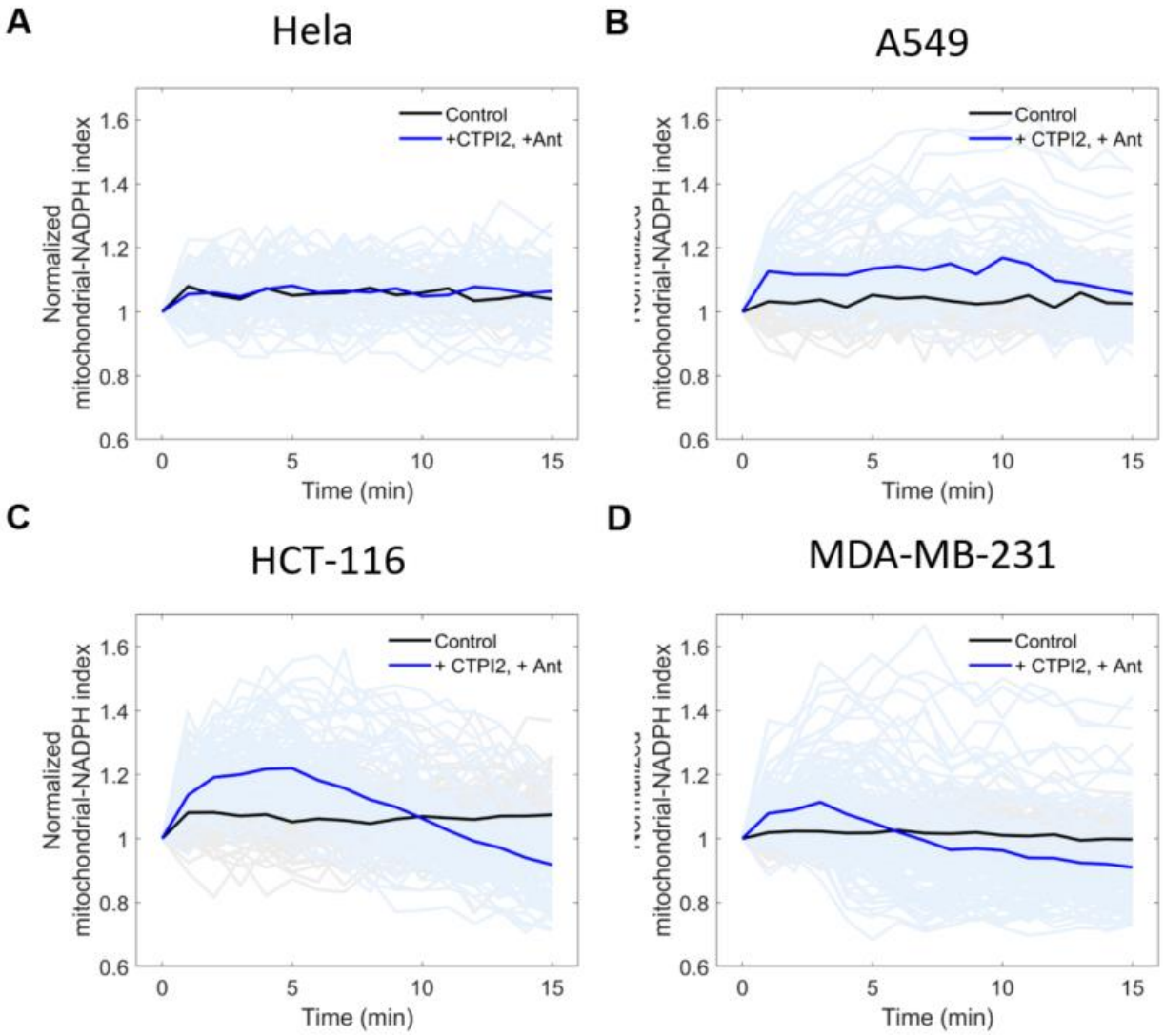

Figure 6.16. Dynamics of mitochondrial NADPH levels upon co-treatment of CTPI-2 and antimycin-A across different cancer cell lines.

6.4.6. Influence of SMER-3 small molecule to compartmentalized NADPH levels

Besides antimycin-A that was widely characterized and known to generate mitochondrial stress, we also generated mitochondrial stress using SMER-3 small molecule. SMER-3 was a molecular known to generate H_2O_2 mainly in mitochondria but also in cytosol at higher dose[28]. Although the exact mechanism of action was not yet fully discovered, we used this molecule to generate oxidative stress and monitored how generation of stress and inhibition of citrate transporter influence cytosolic and mitochondrial NADPH metabolism. First, we selected SMER-3, which was found to be generating mitochondrial H_2O_2, as a molecule to perturb the redox system. When we titrated SMER-3, we observed that despite the role in generating H_2O_2 mainly in mitochondria, we noticed the SMER-3 perturbed the cytosolic NADPH as well (**Figure 6.17**).

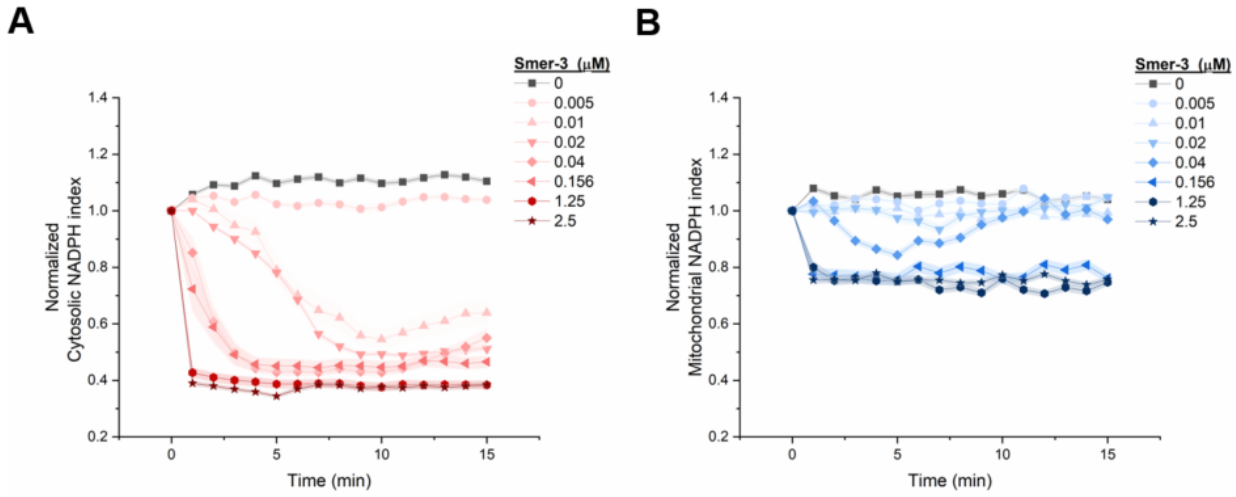

Figure 6.17. Time-course measurement of (A) cytosolic and (B) mitochondrial NADPH indices upon addition of SMER-3 molecules to Hela-iNap or Hela-mito-iNap cell lines.

At 40 nM dose, we observed that both cytosolic and mitochondrial NADPH decreased. For cytosolic NADPH, the index decreased by 47 % after 9 minutes and by 40 % after 15 minutes compared to the control. In terms of concentration, it decreased from 2.5 µM to 0.7 µM. Similarly, when we measured the mitochondrial NADPH index, the index decreased by 16 %

after 5 minutes and recovered up to 105% after 12 minutes and started decreasing again reaching 97 % compared to the initial index after 15 minutes. The dynamics of mitochondrial NADPH was interesting in a way that it decreased and starting to recover. The recovery rate was higher for mitochondrial NADPH index than the cytosolic NADPH (**Figure 6.18A-B**).

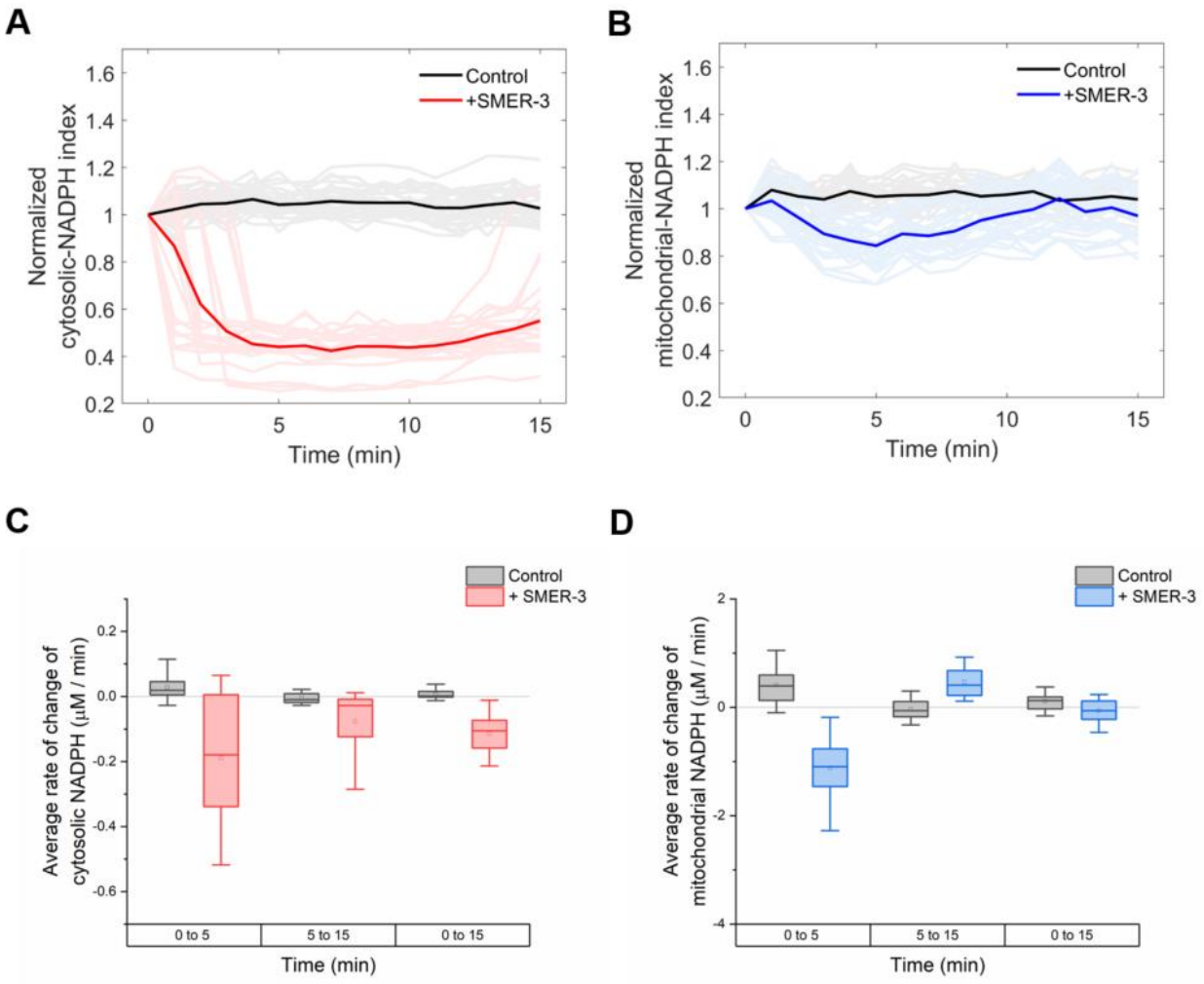

Figure 6.18. Time-course measurement of cytosolic and mitochondrial NADPH levels and their average rates. (A) Cytosolic and (B) NADPH index was monitored over 15 minutes under 40 nM SMER-3 addition. The average rate of change of (C) cytosolic NADPH and (D) mitochondrial NADPH were estimated over different time spans.

In terms of rate, we observed an interesting trend. For the first 5 minutes, both cytosolic and mitochondrial NADPH rate was negative due to a rapid oxidation of NADPH in antioxidant reaction networks to clear H_2O_2. The absolute rate of cytosolic NADPH change was -0.19, whereas the mitochondrial NADPH rate of change was -1.1 μM /min for the first 5 minutes. However, after 5 minutes, the cytosolic NADPH rate was still -0.06, whereas the mitochondrial NADPH was +0.32, showing an increase. Potentially, the recovery of NADPH in mitochondria after 5 minutes indicated the reaction was apparently making some effect (**Figure 6.18C-D**).

When we considered the change of rate in the beginning and the end-point at 15 minutes, the cytosolic NADPH rate was -0.12 and the mitochondrial NADPH was -0.06. As previous literature showed evidence that oxidative stress altered the directionality of citrate-a-KG shuttle such that IDH2 mediated NADPH generation in mitochondria would prevent the accumulation of oxidative species in mitochondria. If this was indeed the case, we expected an increase of mitochondrial NADPH due to the transport and transient decrease of cytosolic NADPH. Based on our measurement, we expected that the increase of mitochondrial NADPH could be due to the transfer of cytosolic NADPH, which was thereby decreased as result and not increasing, but balanced out.

To further elucidate the role of citrate transporter in mediating cytosolic and mitochondrial NADPH, we co-treated cells with both SMER-3 and the CTPI-2. If the shuttle system behaved in transporting citrated to mitochondria during mitochondrial oxidative stress, we expected to see that the inhibition of citrate transporter would limit the immediate supply of NADPH from cytosol to mitochondria. This prevented further decrease of cytosolic NADPH but not mitochondrial NADPH. Indeed, a decrease of cytosolic NADPH was minimized upon inhibition of citrate transporter. The NADPH index decreased by 20 % at most and 10 % after 15

minutes. The end NADPH index was 9 % lower compared to the control (**Figure 6.19A and C**). For mitochondrial NADPH index, the decrease of mitochondrial NADPH index was also reduced compared to the SMER-3 treatment only up to 10 minutes. However, after 10 minutes, the mitochondrial NADPH did not increase as shown in SMER-3 treated case, but rather the mitochondrial NADPH index remained flat, lowering the index by 6 % compared to the initial value. Compared to the control, the mitochondrial NADPH index after 15 minutes decreased by nearly 10% upon co-treatment, but for SMER-3 only, mito-NADPH index decreased by 7%. Overall there was a slight decrease of mitochondrial NADPH index upon mitochondrial oxidative stress (**Figure 6.19B and D**).

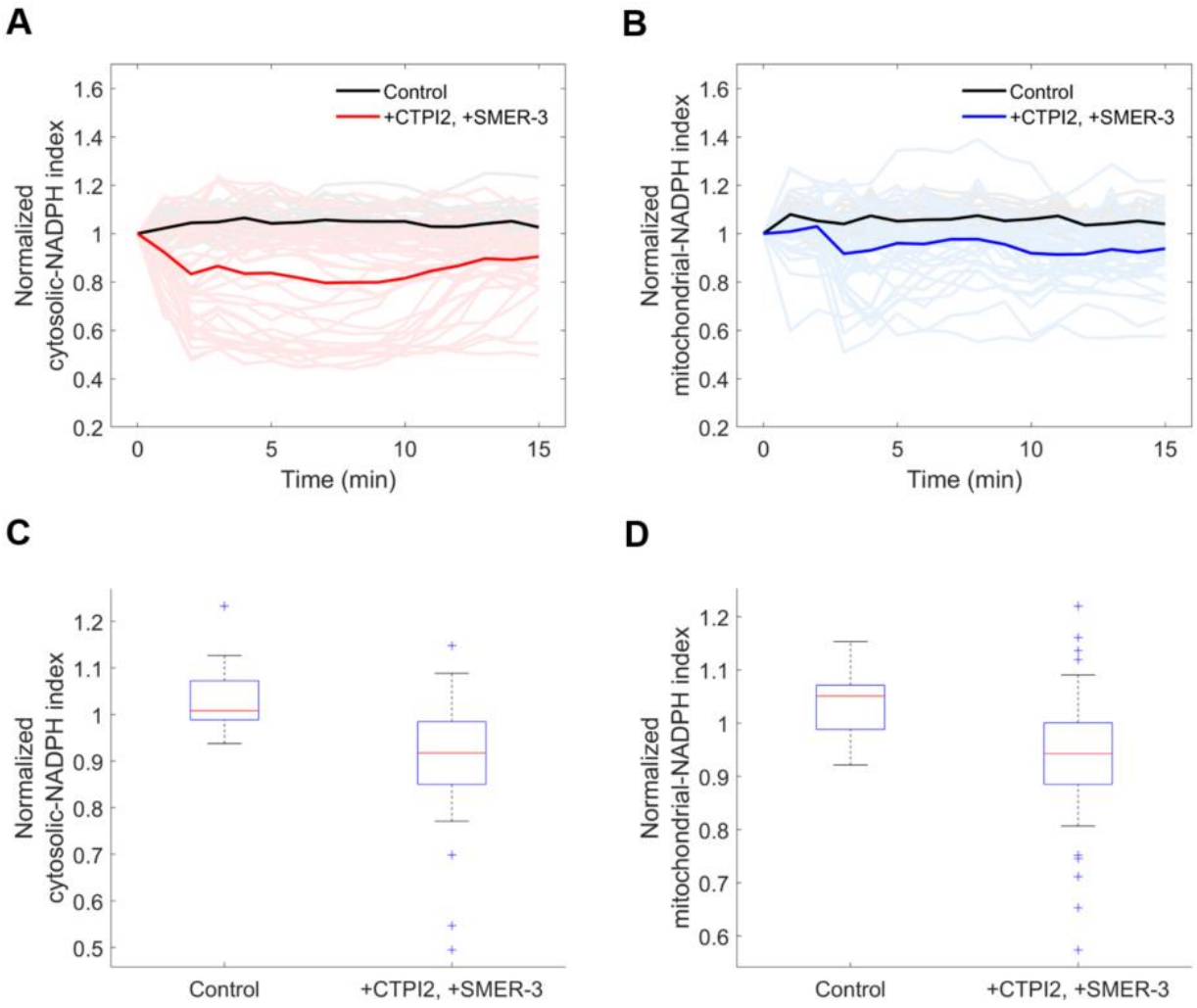

Figure 6.19. Cytosolic and mitochondrial NADPH dynamics upon inhibition of citrate transporter and SMER-3. Kinetics of (A) cytosolic and (B) mitochondrial NADPH indices normalized to the initial index at t = 0 min. Box plots represent a distribution of normalized (C) cytosolic and (B) mitochondrial NADPH indices at t = 15 minutes.

6.5. Discussion

SLC25 genes encoded proteins that facilitate transport of small molecules, inorganic molecules, and amino acids in and out of mitochondria. Here, we implemented essentiality and co-essentiality analysis to evaluate key SLC25 genes that were important for cell growth and determined their functions in metabolism. Further, our genome-scale metabolic model simulation

predicted that SLC25A1 gene, which encoded citrate transport (CTP), was critical in maintaining NADPH homeostasis. With these computational analysis, we examined the cytosolic and NADPH dynamics in the context of citrate αKG shuttle system. Inhibition of citrate transporter decreased cytosolic NADPH, whereas mitochondrial NADPH remained robust for most of the cell lines. It was previously shown that citrate transporter inhibition or knockout allowed accumulation of citrate within mitochondria and lack of citrate in cytosol mediate increased glycolysis6.

We expected that inhibition of CTP would increase mitochondrial NADPH and do not alter cytosolic NADPH pools. However, upon inhibition, we observed that cytosolic NADPH pools decreased immediately for all the cell lines tested. A decrease of cytosolic NADPH pools was not by decreased amount of citrate in cytosol as addition of citrate did not rescue cytosolic NADPH pools upon inhibition of citrate transport inhibition. Although further examinations were needed to understand why cytosolic NADPH decreased in response to inhibition of citrate transporter, it might be due to citrate transporter inhibition causing cytosolic oxidative stress and lowering NDAPH levels. Increased glycolysis by citrate transporter inhibition could lead to activation of glycerol-3-phosphate dehydrogenase (GPDH), which was known to be a source of H_2O_2 that was comparable to the generation of H_2O_2 in electron transport chain complex III in mitochondria[29]. Another possibility was that the small molecule CTPI-2 might have non-specific binding to other proteins which might elevate cytosolic oxidative stress, leading to decrease of cytosolic NADPH. Inhibition of citrate transporter, however, did not perturb much change in mitochondria, suggesting inhibition of citrate transporter influenced cytosolic NADPH pools more than the mitochondrial NADPH pools in short time scale.

Spheroids or cell growing detached from extracellular matrix were shown to import citrate from cytosol to mitochondria, enhancing NADPH buffering capacity in mitochondria to combat against mitochondrial oxidative stress[6,7,9]. To test whether citrate was imported into mitochondria and facilitated NADPH production in mitochondria, we generated mitochondrial oxidative stress through treatment of antimycin-A, an electron transport chain complex (ETC) III inhibitor. Antimycin-A mediated ETCIII inhibition was associated with increased electron leakages and generation of H_2O_2 more than other ETC sites[26,30,31]. Inhibition of ETCIII also caused elevation of mitochondrial NADH[27].

We determined antimycin-A caused an increase of mitochondrial NADPH levels, indicating that NADH elevation might induce activation of NNT enzymes to balance NADH by pushing the reaction forward, transferring the electrons to $NADP^+$ and reproducing NADPH. Although Antimycin-A caused generation of both mitochondrial and cytosolic H_2O_2, within the 15 minutes time-scales the generation of H_2O_2 might not be sufficient to cause significant decrease of NADPH. Indeed, antimycin-A started causing significant H_2O_2 generation primarily to mitochondrial matrix and some extent to cytosol after 10 minutes time scale[32]. We also observed that mitochondrial NADPH levels increased over 6 hours time-scale and started to decrease after 24 hours (data not shown). Although we expected that cytosolic NADPH may start decrease in latter time point due to mitochondrial oxidative stress, if the assumption was correct about the direction of citrate transport, we did not observe a significant change of cytosolic NADPH dynamics upon mito-stress caused by antimycin-A within 15 minute time span.

From the co-treatment experiments with antimycin-A and citrate transporter inhibitor, we monitored both cytosolic and mitochondrial NADPH dynamics changed. Cytosolic NADPH indices decreased by the effect of citrate transporter and the mitochondrial NADPH indices

increased by the antimycin-A. Interestingly, we observed that after an increase of mitochondrial NADPH indices, it started to decrease sharply after a few to ten minute time span. It might be due to the inhibition of citrate transporter allow cells generating more of mitochondrial H_2O_2. It was also shown that citrate transport knockout or inhibition caused increased of mitochondrial H_2O_2[6,9,33].

Although we started evaluating the directionality of citrate αKG NADPH shuttle system at basal and under mitochondrial oxidative stress conditions, we were unable to resolve the direction of this shuttle system using the cytosolic and mitochondrial NADPH dynamics studies. However, we still determined how cytosolic and mitochondrial NADPH dynamics vary upon inhibition of citrate transporter inhibition. Although we focused on citrate transporter, there existed other SLC25 genes that encoded other transporters that facilitate NADPH shuttles between mitochondria and cytosol. There might be a compensatory activation of these other shuttle systems when one shuttle system collapsed, or studying other shuttle systems might reveal detailed mechanistic findings regarding NADPH shuttle systems.

6.6. References

1. Goodman, R. P., Calvo, S. E. & Mootha, V. K. Spatiotemporal compartmentalization of hepatic NADH and NADPH metabolism. *J. Biol. Chem.* **293**, 7508–7516 (2018).

2. Ying, W. NAD^+/NADH and $NADP^+$/NADPH in Cellular Functions and Cell Death: Regulation and Biological Consequences. *Antioxid. Redox Signal.* **10**, 179–206 (2008).

3. Palmieri, F. The mitochondrial transporter family (SLC25): Physiological and pathological implications. *Pflugers Arch. Eur. J. Physiol.* **447**, 689–709 (2004).

4. Palmieri, F., Scarcia, P. & Monné, M. Diseases caused by mutations in mitochondrial carrier genes SLC25: A review. *Biomolecules* **10**, 1–32 (2020).

5. Majd, H., King, M. S., Smith, A. C. & Kunji, E. R. S. Pathogenic mutations of the human mitochondrial citrate carrier SLC25A1 lead to impaired citrate export required for lipid, dolichol, ubiquinone and sterol synthesis. *Biochim. Biophys. Acta - Bioenerg.* **1859**, 1–7 (2018).

6. Tan, M. *et al.* Inhibition of the mitochondrial citrate carrier, Slc25a1, reverts steatosis, glucose intolerance, and inflammation in preclinical models of NAFLD/NASH. *Cell Death Differ.* **27**, 2143–2157 (2020).

7. Fernandez, H. R. *et al.* The mitochondrial citrate carrier, SLC25A1, drives stemness and therapy resistance in non-small cell lung cancer. *Cell Death Differ.* **25**, 1239–1258 (2018).

8. Palmieri, F. & Monné, M. Discoveries, metabolic roles and diseases of mitochondrial carriers: A review. *Biochim. Biophys. Acta - Mol. Cell Res.* **1863**, 2362–2378 (2016).

9. Jiang, L. *et al.* Reductive carboxylation supports redox homeostasis during anchorage-independent growth. *Nature* **532**, 255–258 (2016).

10. Iacobazzi, V. *et al.* Mitochondrial carriers in inflammation induced by bacterial endotoxin and cytokines. *Biol. Chem.* **398**, 303–317 (2017).

11. Xiao, H. *et al.* A Quantitative Tissue-Specific Landscape of Protein Redox Regulation during Aging. *Cell* **180**, 968-983.e24 (2020).

12. Nutt, L. K. *et al.* Metabolic regulation of oocyte cell death through the CaMKII-mediated phosphorylation of caspase-2. *Cell* **123**, 89–103 (2005).

13. MacDonald, M. J. Feasibility of a mitochondrial pyruvate malate shuttle in pancreatic islets.

Further implication of cytosolic NADPH in insulin secretion. *Journal of Biological Chemistry* vol. 270 20051–20058 (1995).

14. Mette V. Jensen, 1 Jamie W. Joseph, 2 Sarah M. Ronnebaum, 1 Shawn C. Burgess, 3 A. Dean Sherry, 3 and Christopher B. Newgard. Metabolic cycling in control of glucose-stimulated insulin secretion. *Am. J. Physiol. Metab.* **295**, E1287–E1297 (2008).

15. Liu, L. *et al.* Malic enzyme tracers reveal hypoxia-induced switch in adipocyte NADPH pathway usage. *Nat. Chem. Biol.* **12**, 345–352 (2016).

16. Cheng, T. *et al.* Pyruvate carboxylase is required for glutamine-independent growth of tumor cells. *Proc. Natl. Acad. Sci. U. S. A.* **108**, 8674–8679 (2011).

17. Zhou, X., Paredes, J. A., Krishnan, S., Curbo, S. & Karlsson, A. The mitochondrial carrier SLC25A10 regulates cancer cell growth. *Oncotarget* **6**, 9271–9283 (2015).

18. Mizuarai, S., Miki, S., Araki, H., Takahashi, K. & Kotani, H. Identification of dicarboxylate carrier Slc25a10 as malate transporter in de Novo fatty acid synthesis. *J. Biol. Chem.* **280**, 32434–32441 (2005).

19. Xiao, W. & Loscalzo, J. Metabolic Responses to Reductive Stress. *Antioxid. Redox Signal.* **00**, 1–18 (2019).

20. Veech, H. A. K. and R. L. Pyridine nucleotide interrelations.

21. Wang, T. *et al.* Identification and characterization of essential genes in the human genome. *Science (80-.).* **350**, 1096–1101 (2015).

22. Wang, T. *et al.* Gene Essentiality Profiling Reveals Gene Networks and Synthetic Lethal Interactions with Oncogenic Ras. *Cell* **168**, 890-903.e15 (2017).

23. Mi, H., Muruganujan, A., Huang, X., Guo, X. & Thomas, P. D. Protocol Update for large-scale genome and gene function analysis with the PANTHER. *Nat. Protoc.* (2016) doi:10.1038/s41596-019-0128-8.

24. Robinson, J. L. *et al.* An atlas of human metabolism. *Sci. Signal.* **13**, 1–12 (2020).

25. Schober, F. A. *et al.* The one-carbon pool controls mitochondrial energy metabolism via complex I and iron-sulfur clusters. *Sci. Adv.* **7**, (2021).

26. Chen, Q., Vazquez, E. J., Moghaddas, S., Hoppel, C. L. & Lesnefsky, E. J. Production of reactive oxygen species by mitochondria: Central role of complex III. *J. Biol. Chem.* **278**, 36027–36031

(2003).

27. Chen, W. W., Freinkman, E., Wang, T., Birsoy, K. & Sabatini, D. M. Absolute Quantification of Matrix Metabolites Reveals the Dynamics of Mitochondrial Metabolism [mito]. *Cell* **166**, 1324-1337.e11 (2016).

28. Hao, Y., Langford, T. F., Moon, S. J., Eller, K. A. & Sikes, H. D. Screening compound libraries for H(2)O(2)-mediated cancer therapeutics using a peroxiredoxin-based sensor. *Cell Chem. Biol.* (2021) doi:10.1016/j.chembiol.2021.09.003.

29. Mráček, T., Drahota, Z. & Houštěk, J. The function and the role of the mitochondrial glycerol-3-phosphate dehydrogenase in mammalian tissues. *Biochim. Biophys. Acta - Bioenerg.* **1827**, 401–410 (2013).

30. Turrens, J. F. & Boveris, A. Generation of superoxide anion by the NADH dehydrogenase of bovine heart mitochondria. *Biochem. J.* **191**, 421–427 (1980).

31. Boveris, A., Oshino, N. & Chance, B. The cellular production of hydrogen peroxide. *Biochem. J.* **128**, 617–630 (1972).

32. Hoehne, M. N. *et al.* Spatial and temporal control of mitochondrial H 2 O 2 release in intact human cells . *EMBO J.* 1–16 (2022) doi:10.15252/embj.2021109169.

33. Jiang, L. *et al.* Quantitative metabolic flux analysis reveals an unconventional pathway of fatty acid synthesis in cancer cells deficient for the mitochondrial citrate transport protein. *Metab. Eng.* **43**, 198–207 (2017).

Chapter 7

NADPH composite index relates cytosolic and mitochondrial NADPH indices to growth

7.1. Abstract

Several metabolites shuttle systems allowed redistribution of reducing equivalents of NADPH between cytosol and mitochondria. For instance, to meet the biosynthetic demands during lipogenesis, reducing equivalents of NADPH were transferred to cytosol from mitochondria. On the other hand, excessive generation of mitochondrial reactive oxygen species promoted a transfer of reducing equivalents of NADPH from cytosol to mitochondria for maintenance of mitochondrial antioxidant network. These shuttling effects indicated NADPH pools were not completely isolated between these two compartments.

In this chapter, we defined a NADPH composite index to combine cytosolic and mitochondrial NADPH indices using a contribution factor. The contribution factor was calculated based on an assumption that the change of NADPH indices were highly correlated with growth rate. We determined that cancer cells with higher contribution factor were more sensitive to cytosolic NADPH perturbation, whereas cancer cells with lower contribution factor was more sensitive to mitochondrial NADPH perturbation. Thus, using NADPH composite index and contribution factor, we obtained insight on cytosolic and mitochondrial NADPH states of cancer cells and how these differences could be used for selective inhibition of cancer cells.

7.2. Introduction

This chapter was an extension of the **Chapter 5**, **Chapter 6** and the detailed introduction were described in the previous chapter.

Reducing equivalents of NADPH in cytosol could be shuttled into mitochondria via several metabolite shuttle systems[1]. These shuttle systems were mainly constituted by proteins

that are encoded by *SLC25* gene family[2]. A detailed review on *SLC25* gene family was described in the previous chapter. In brief, reducing equivalents of NADPH could be shuttled between cytosol and mitochondria through citrate-αKG metabolite shuttle systems, and malate-pyruvate shuttle systems[3,4]. Mitochondrial oxidative stress allowed citrate-αKG metabolite shuttles to operate in a way to transfer reducing equivalents of cytosolic NADPH to mitochondria[5]. For pyruvate-malate shuttle systems, pancreatic cells used these shuttle systems to generate cytosolic NADPH readily upon insulin stimulation[6].

A major consumption pathway of NADPH was for fatty acid synthesis[7]. For instance, synthesis of one mole of palmitate, a major component of lipid bilayers, require fourteen moles of NADPH[8]. This indicated that rapidly proliferating cells, such as cancers, enhanced NADPH generation pathway to meet the demands of lipid synthesis. Availability of NADPH was directly linked to lipid synthesis capabilities and biomass generation[9,10]. In this case, NADPH could be shuttled from mitochondria to cytosol to meet the demand. Therefore, we attempted to combine the cytosolic and mitochondrial NADPH indices by defining NADPH composite index term, using contribution factor f. With the factor f, we correlated the composite index and growth rate to investigate how different cancer cells exhibited cytosolic and mitochondrial NADPH relations for growth. These differences could be used for inhibition of growth rates of difference cancer cells.

7.3. Materials and Methods

7.3.1. Determination of NADPH, $NADP^+$, and NADPH/$NADP^+$

Approximately 5e5 cells were seeded per each of well in 6-well dish with 2 ml of DMEM, supplemented with 10% dialyzed FBS. The medium was aspirated and placed on ice. The cells were washed twice with 2 mL of ice-cold PBS. Then, an ice-cold 1:1 mixture of PBS and 1% dodecyltrimethylammonium bromide in 0.2 M NaOH was added to the wells, and cells were collected by scraping for 20 seconds and transferred to the ice-cold 1.5 mL centrifuge tube. The cell lysates were split to two with an equal volume of 200 μL. One aliquot was left untreated, while the other aliquot was treated with 100 μL of 0.4 M HCl. Both aliquots were placed in an incubator with 60 °C for 20 minutes. NADPH and $NADP^+$ levels were measured with Promega NADP+/NADPH-Glo kits according to the manufacturer's instructions. The concentration was estimated after developing a calibration curves.

7.3.2. Measurement of cell growth

Cells were plated at 2e4 cells per well for A549 and Hela, or 4e4 cells for MDA-MB-231 cells per each well of 6-well plates. After a day, media was aspirated, washed twice with 2 mL PBS. New media with appropriate nutrient compositions were added and grown for two more days. Cells were trypsinized and counted and this initial cell count was used as an initial number of cell. After two days, final cell counts were measured using a Cellometer. The following formula was used to calculate proliferation rate: Doublings per day = 1/time x ln(final cell number/initial cell number).

7.4. Results

7.4.1. Highly proliferating cells increase production rates of NADPH levels

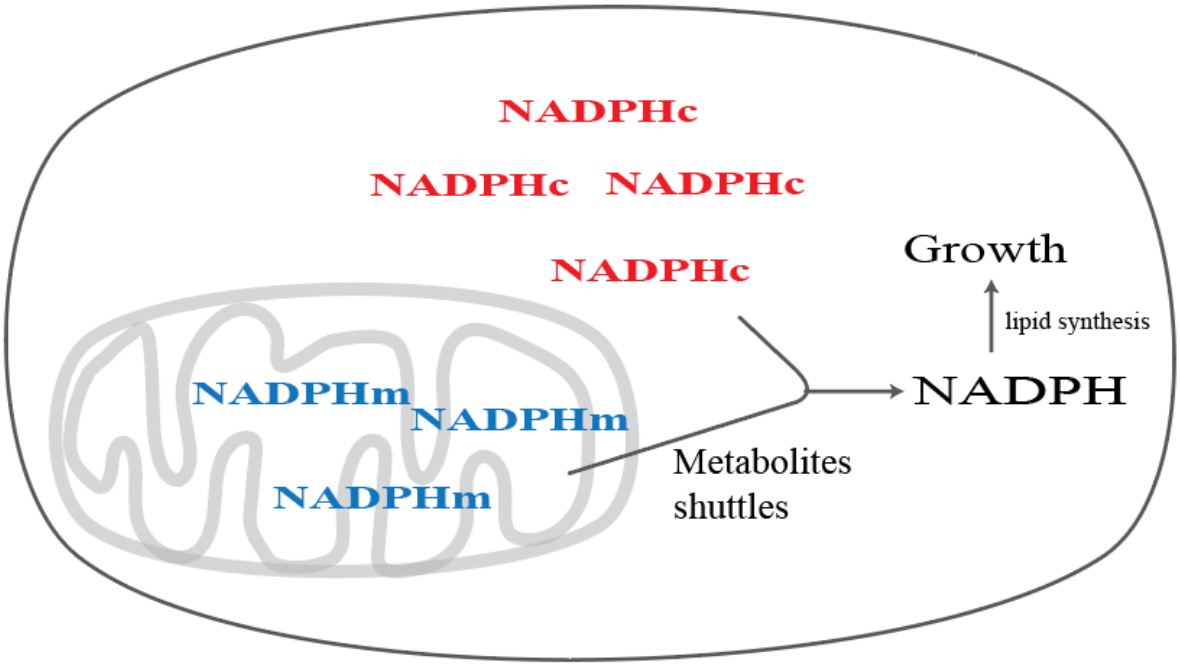

Figure 7.1. Schematics representing cytosolic and mitochondrial NADPH are combined to cellular NADPH and its consumption through lipid synthesis, which is linked growth.

The cellular NADPH pools reflected both cytosolic and mitochondrial NADPH pools. This combined NADPH pools were effectively used for lipid synthesis in cytosol, and fatty acids synthesis was required for tumor growth[9,10] (**Figure 7.1**).

First, we measured the cellular NADPH levels under varying nutrient conditions to test whether NADPH availability decreased in absence of key substrates that are important for NADPH generation. As expected, for proliferating cells, the generation rates of NADPH was about 8 μM hr^{-1} $cell^{-1}$, but for lack of either glucose or glutamine showed no increase of NADPH generation. In absence of serine, the generation rate of cellular NADPH was still positive with a value of 3 μM hr^{-1} $cell^{-1}$. When there was no glucose and glutamine available, the net generation

of cellular NADPH turned negative values with -1.1 (**Figure 7.2**). We also measured the $NADP^+$ levels. The $NADP^+$ levels were maintained from 20 to 50 µM per cell for conditions with 51 µM for control case. However, the concentrations increased statistically significant in absence of glucose or in absence of glucose and glutamine conditions. In absence of glucose condition, $NADP^+$ increased to 180 µM. The average NADPH concentration for control was 867 µM per cell and decreased to 430 for absence of glucose condition and 276 in absence of both glucose and glutamine (**Figure 7.3A).** In regards to the ratio, the control showed quite a variability and the average ratio was 23. In absence of glucose, it decreased to 2.3 and 0.9 in absence glucose and glutamine (**Figure 7.3B)**.

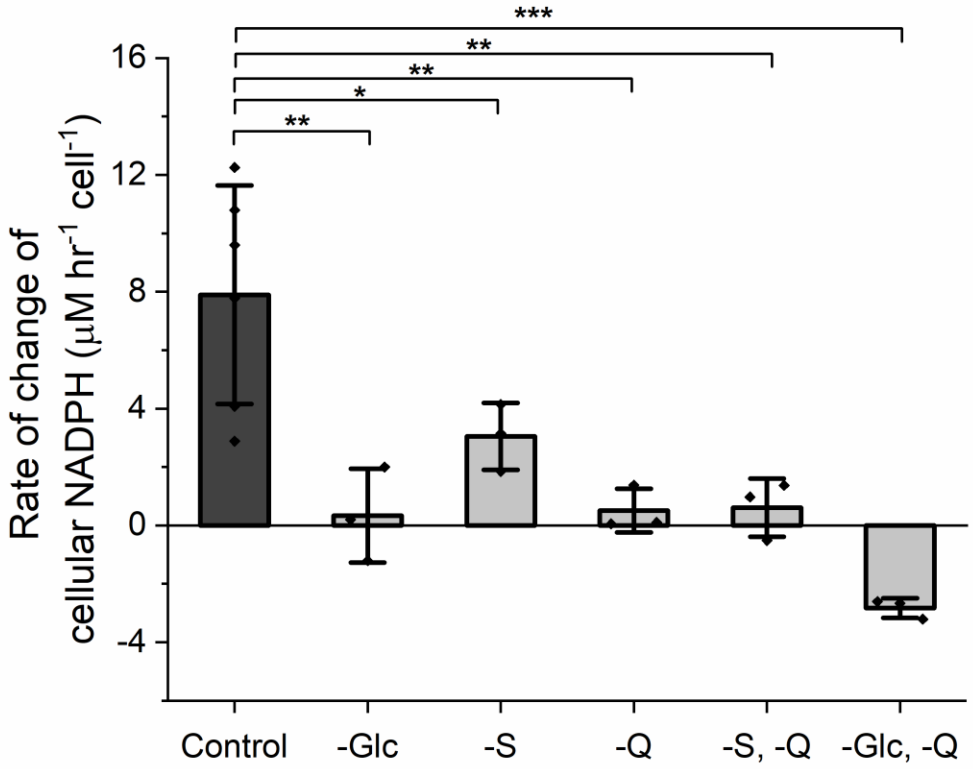

Figure 7.2. Generation rate of cellular NADPH under varying nutrient conditions. Control is for cells grown under a regular growth media, which contains glucose, serine, and glutamine. The other bars represents a condition in absence of glucose, serine (S), glutamine (Q), or combination of amino acids and glucose.

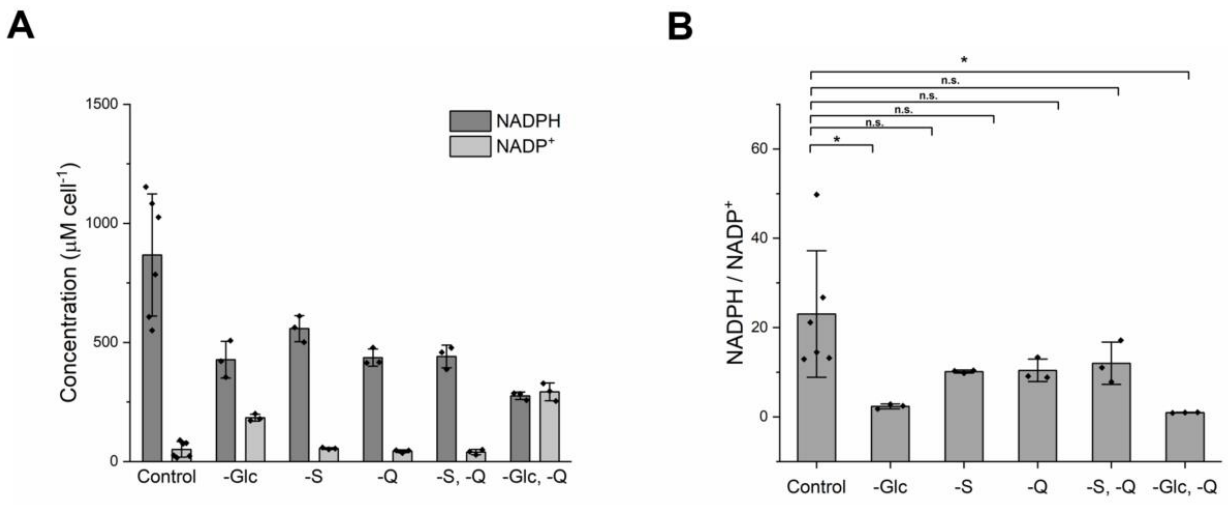

Figure 7.3. Concentration of NADPH, $NADP^+$, and the ratio at 96 hours.

Next, we measured the growth rate under varying nutrient conditions and examine how the nutrient conditions influence the growth rate. For control, the mean growth rate was 0.0.035 hr^{-1} and decreased to 0.013 and 0.008 for glucose deprived or glucose and glutamine deprived conditions. In absence of serine, the growth was partially compromised as the rate decreased to 0.02 and without glutamine the rate decreased to 0.017 (**Figure 7.5**). Next, we correlated the growth rate and the cellular NADPH rate change to find out that there was a high linear correlation between these two parameters (**Figure 7.5**). This confirmed that highly proliferating cells boosted NADPH production to meet the demands of lipid synthesis that was a part of macromolecule composition of biomass.

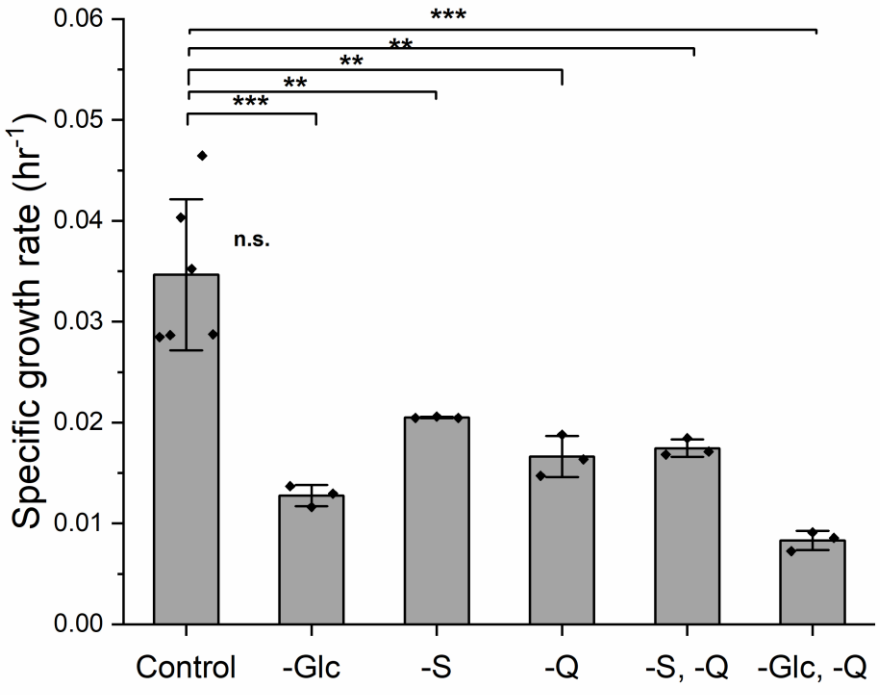

Figure 7.4. Specific growth rate under varying nutrient conditions.

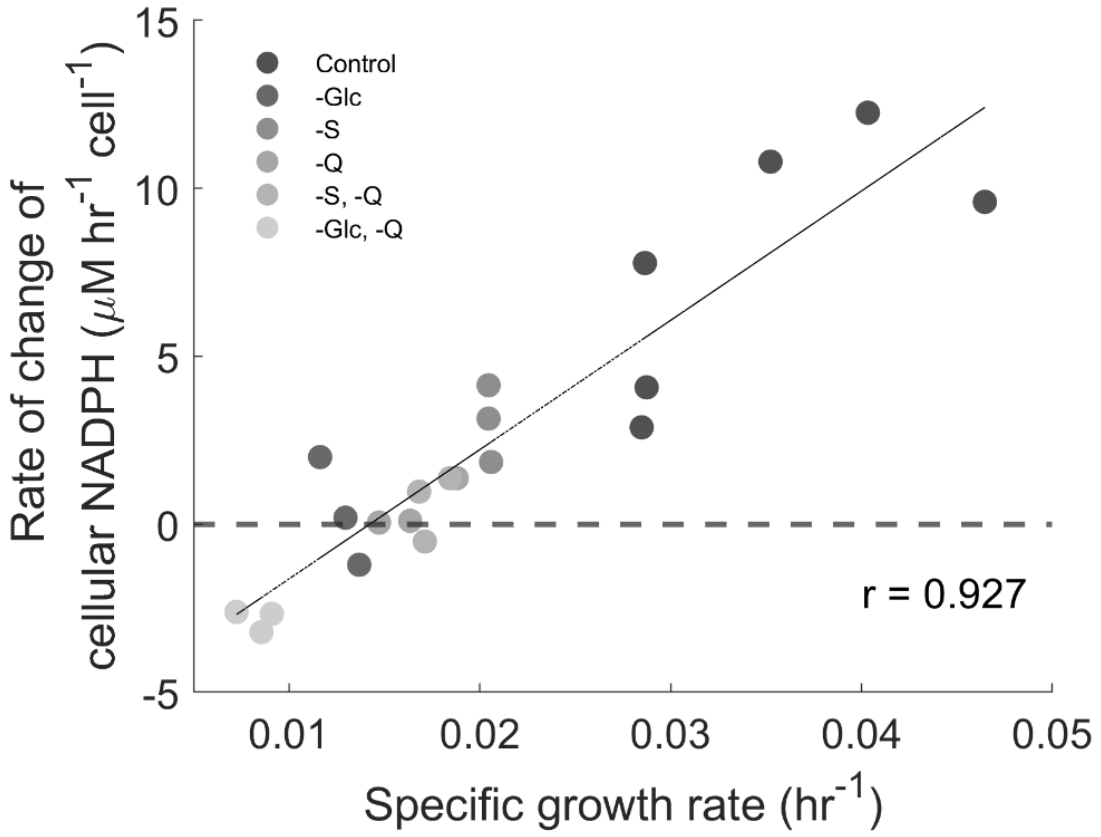

Figure 7.5. Rate of change of cellular NADPH vs. Specific growth rate.

7.4.2. NADPH composite index represents contribution of cytosolic and mitochondrial NADPH indices to cell growth

Cell growth was reflected by increase in cell biomass and lipids were one of the major biological macromolecules. Lipid synthesis occurred in cytosol and supply of cytosolic NADPH was important to drive the reductive biosynthesis. To test whether our assumption that the change of NADPH index was related to growth rate, we measured the change of cytosolic NADPH to cell growth and found out that there was positive correlation between these two parameters with a Pearson's correlation of 0.73 (**Figure 7.6A**). When we compared the change of mitochondrial NADPH indices to the growth rate, the correlation was not as high as those with the cytosolic

NADPH index to growth rate. The Pearson's correlation was 0.58 (**Figure 7.6B**). Next, we defined a NADPH composite index (**Equation 1)**, which was a combination of cytosolic and mitochondrial NADPH indices with a contribution factor f. $\Delta \boldsymbol{I'_{composite}}$ indicated the change of NADPH composite index relative to the value at initial time point. f represented a contribution factor that ranges from 0 to 1. $\Delta \boldsymbol{I'_{cyto}}$ represented a change of cytosolic NADPH index relative to the value at initial time point. $\Delta \boldsymbol{I'_{mito}}$ represented a change of mitochondrial NADPH index relative to the value at initial time point.

$$\Delta \boldsymbol{I'_{composite}} = \boldsymbol{f}\Delta \boldsymbol{I'_{cyto}} + (\mathbf{1} - \boldsymbol{f})\Delta \boldsymbol{I'_{mito}} \quad \textbf{(1)}$$

Next, assuming the growth rate was proportional to the availability of cellular NADPH levels, or in our case the change of composite index, we estimated how the change of factor f influenced the correlation between the changes of NADPH composite index to the growth. When f equaled to 1, the linear correlation coefficient was 0.73. When f equaled to 0, the linear correlation coefficient was 0.58. When f equaled to 0.57, the correlation coefficient was highest, with the value of 0.81 (**Figure 7.6C**). We used the factor that provided the highest correlation and the relation between the composite index and the growth rate was plotted **(Figure 7.6D).** The factor of 0.57 indicated NADPH composite index was comprised by 57 % of cytosolic NADPH change and 43 % of mitochondrial NADPH index change.

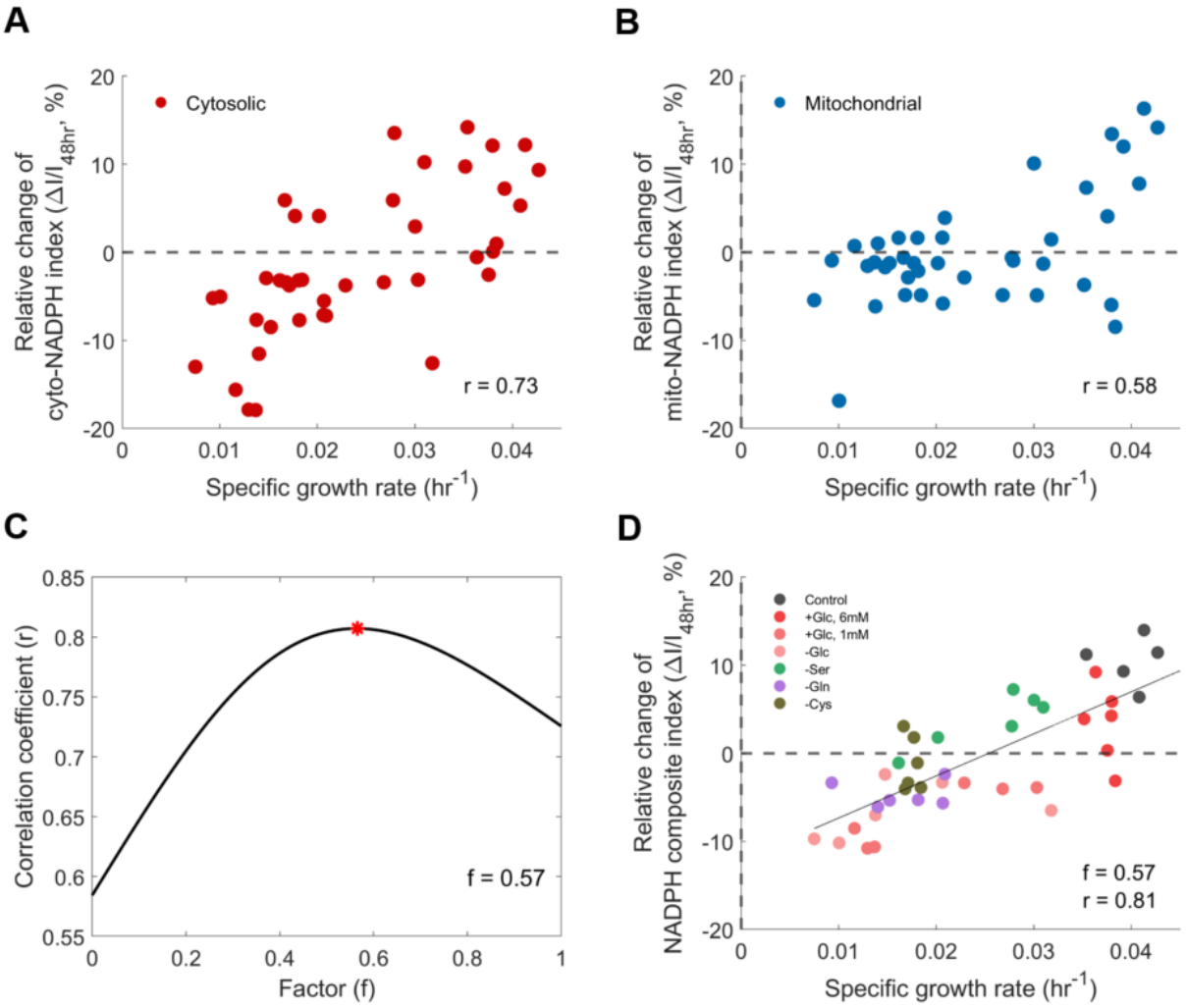

Figure 7.6. Correlation between the cytosolic and mitochondrial NADPH indices to growth rate. A correlation between (A) cytosolic and (B) mitochondrial NADPH indices. (C) Correlation coefficient between the two parameters vary as a function of contribution factor, which ranges from 0 to 1. (D) The correlation plot between the changes of NADPH composite index to the growth rate.

To test whether other cell lines revealed similar contribution factors and NADPH-growth relationships, we plotted cytosolic and mitochondrial NADPH indices against growth rate across different cancer cell lines. Despite the change of varying growth rate, both cytosolic and mitochondrial NADPH indices did not show positive correlation to growth rates for A549. Both cytosolic and mitochondrial NADPH indices showed a poor correlation coefficient to growth rate. For HCT-116 cell lines, there was no significant linear relationships were observed as well.

The correlation coefficient was -0.16 for cytosolic NADPH change and -0.47 for mitochondrial NADPH index change. Both showed a negative correlation between the change of NADPH indices and the growth rate, with mitochondrial NADPH indices showing higher correlation. Lastly, MDA-MB-231 cells showed similar correlation pattern with Hela, in which the cytosolic NADPH index change had correlation coefficient of 0.87 against growth rate, whereas the mitochondrial NADPH index change showed correlation coefficient of 0.38 (**Figure 7.7**).

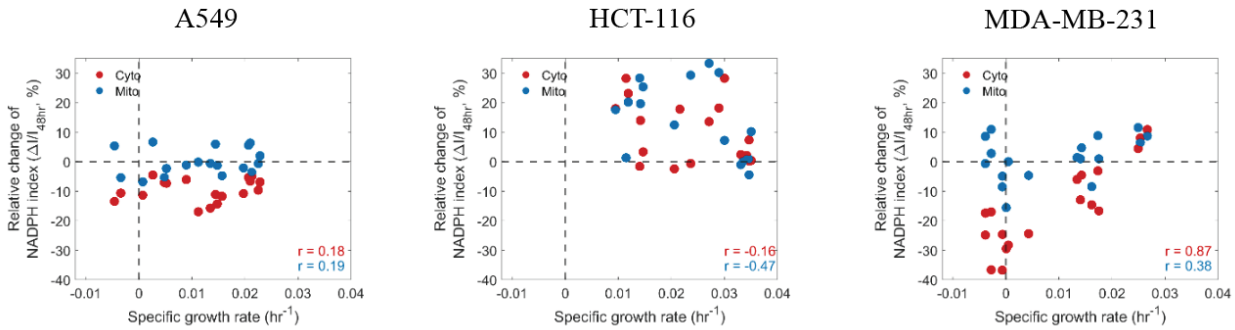

Figure 7.7. Relative change of cytosolic or mitochondrial NADPH indices against growth rate in A549, HCT-116, and MDA-MB-231 cell lines.

Next, using the NADPH composite index equation, we determined how the correlation coefficient between the NADPH composite index and growth rate changed. For A549, as cytosolic and mitochondrial NADPH indices had low correlation coefficient at the start, the highest correlation coefficient was only about 0.24 with a factor of 0.53. For HCT-116, the highest correlation coefficient was observed when the factor was 0.31, with the correlation coefficient of -0.5. For MDA-MB-231, the highest correlation was observed to be 0.87 with a contribution factor of 1 (**Figure 7.8**).

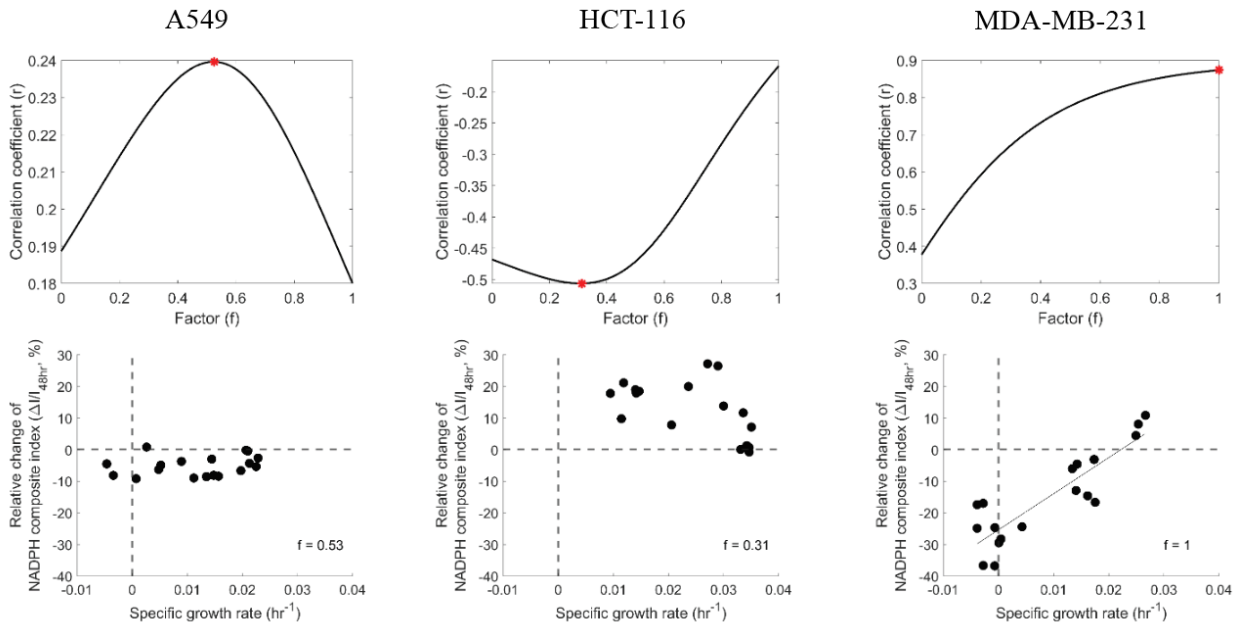

Figure 7.8. The correlation coefficients are estimated against different contribution factor values (f) across different cancer cell lines. The change of NADPH composite index against growth rate are plotted.

Finally, we tested whether the NADPH composite index could be used to guide in perturbing either cytosolic or mitochondrial NADPH levels was effective in limiting cell growth. We hypothesized that cancer cells with higher contribution factor would be more sensitive to cytosolic NADPH perturbation because higher factor implied that this cell line showed higher growth relation to cytosolic NADPH change. On the other hand, if the contribution factor was closer to 0, meaning NADPH composite index was reflective more of mitochondrial NADPH index and correlated with growth rate, a perturbation of mitochondrial NADPH pools would be more effective in limiting the growth rate.

It turned out that MDA-MB-231 cell line with an index coefficient of 1 turned out to be more sensitive to an inhibitor that perturbed cytosolic NADPH production, whereas HCT-116 cell line with an index coefficient of 0.31 was more sensitive to a small molecule that perturbed mitochondrial NADPH (**Figure 7.9A-B**).

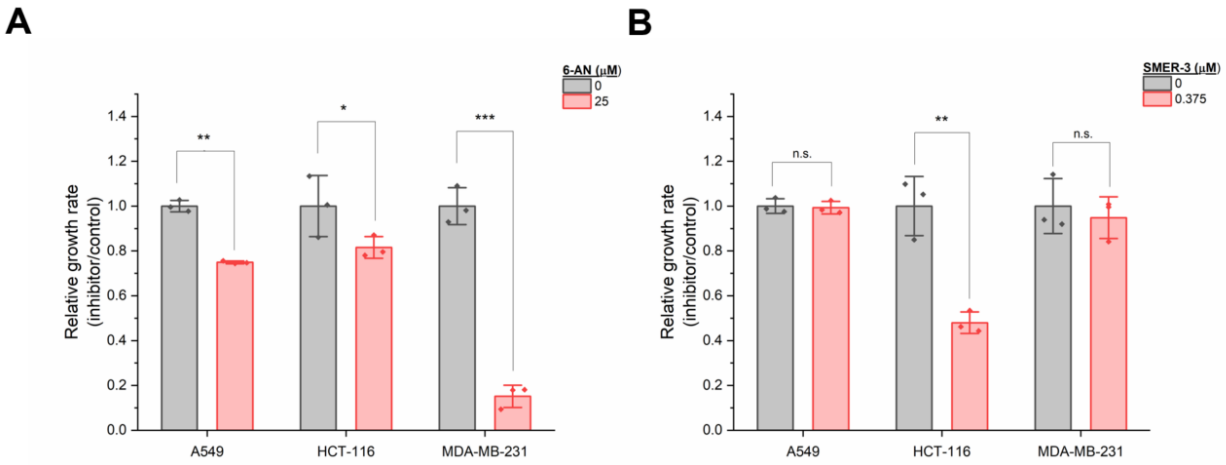

Figure 7.9. Relative growth rate upon treatment of 6-AN or SMER-3 across A549, HCT-116, and MDA-MB-231 cell lines. **(A)** 6-AN is an inhibitor of G6PD enzyme, which is a major contributor of NADPH generation in cytosol. **(B)** SMER-3 is known to generate oxidative stress mainly in mitochondria and decreases mitochondrial NADPH levels.

7.5. Discussion

Reducing equivalents of NADPH played a key role in lipid biosynthesis. Although NADPH pools in cytosol and mitochondria were different due to its impermeability to mitochondrial membrane, reducing equivalents of NADPH could be shuttled between the two compartments through metabolite shuttle systems such as citrate-αKG, and pyruvate-malate. Through these shuttle systems, electrons from one compartment were shuttled to the other compartments depending on conditions such as lipogenesis, gluconeogenesis, and mitochondrial oxidative stress.

Here, we determined the extent of the contribution of cytosolic and mitochondrial NADPH redox states by correlating the composite index with the growth rate. First, we measured the change of cytosolic and mitochondrial NADPH pools under several nutrient conditions. Next,

we combined the cytosolic and mitochondrial NADPH indices by defining a NADPH composite index, which was a linear combination of cytosolic and mitochondrial NADPH indices with a contribution factor f. The factor represented that some cell lines were more sensitive to cytosolic NADPH perturbations, whereas another cell line was more sensitive to mitochondrial NADPH perturbation. Thus, NADPH composite index elucidated a link between the cytosolic and mitochondrial NADPH to growth, which was difficult to estimate with traditional biochemical methods in living cells, and further provided how the differences in contribution factor could be used to selectively inhibit the growth rates of cancer cells.

7.6. References

1. Ying, W. NAD $^{+}$ /NADH and NADP $^{+}$ /NADPH in Cellular Functions and Cell Death: Regulation and Biological Consequences. *Antioxid. Redox Signal.* **10**, 179–206 (2008).

2. Palmieri, F. & Monné, M. Discoveries, metabolic roles and diseases of mitochondrial carriers: A review. *Biochim. Biophys. Acta - Mol. Cell Res.* **1863**, 2362–2378 (2016).

3. MacDonald, M. J. Feasibility of a mitochondrial pyruvate malate shuttle in pancreatic islets. Further implication of cytosolic NADPH in insulin secretion. *Journal of Biological Chemistry* vol. 270 20051–20058 (1995).

4. Veech, H. A. K. and R. L. Pyridine nucleotide interrelations.

5. Jiang, L. *et al.* Reductive carboxylation supports redox homeostasis during anchorage-independent growth. *Nature* **532**, 255–258 (2016).

6. Jensen, M. V. *et al.* Metabolic cycling in control of glucose-stimulated insulin secretion. *Am. J. Physiol. - Endocrinol. Metab.* **295**, 1287–1297 (2008).

7. Heiden, M. G. Vander *et al.* Understanding the Warburg Effect : Cell Proliferation. *Science (80-.).* **324**, 1029 (2009).

8. Lunt, S. Y. & Vander Heiden, M. G. Aerobic Glycolysis: Meeting the Metabolic Requirements of Cell Proliferation. *Annu. Rev. Cell Dev. Biol.* **27**, 441–464 (2011).

9. Keibler, M. A. *et al.* Metabolic requirements for cancer cell proliferation. *Cancer Metab.* **4**, 1–16 (2016).

10. Mullen, A. R. *et al.* Reductive carboxylation supports growth in tumour cells with defective mitochondria. *Nature* **481**, 385–388 (2012).

Chapter 8

Nicotinamide nucleotide transhydrogenase (NNT) for mitochondrial NADPH homeostasis

8.1. Abstract

Recent studies provided evidence that NADH/NAD^+ redox states was constrained in cancers and decreasing NADH/NAD^+ redox state rescued proliferation by promoting nucleotide synthesis for mitochondrial dysfunctional cells [1–3]. Mitochondrial NADH/NAD^+ redox states were closely linked to NADPH/$NADP^+$ via Nicotinamide nucleotide transhydrogenase (NNT), a proton-translocating transhydrogenase embedded in mitochondrial membrane. This enzyme was a key contributor of mitochondrial NADPH for protection of cells against oxidative stress [4]. However, it still remained unknown about the dynamic roles of NNT enzymes and its contribution to the generation of mitochondrial NADPH compared to other well-known enzymes including MTHFD2, IDH2, and GLUD2. Furthermore, recent discoveries of NAD transport along with citrate transport posed interest of whether NNT enzyme shared the functions with transporters.

Our lab has previously demonstrated that NNT coordinated reductive carboxylation and glucose and glutamine catabolism for survival in Vhl deficient renal cell carcinoma and melanomas. More recently, researchers in other labs demonstrated that knockout of NNT inhibited tumorigenesis of liver and gastric cancers [5,6]. Structure of NNT by cryo-electron microscopy revealed a potential opportunities of developing NNT inhibitors, which could be used for therapeutic purposes in cancers as well as ischemia reperfusion injury and metabolic diseases [7].

The main goal of this project was to investigate the role of NNT enzyme in mitochondria dysfunctional cells and cancer models with high expression of NNT such as lung cancers. I aimed to understand the extent of an impact of a knockout of NNT to cell growth. Growing evidence suggested that under hypoxic conditions and mitochondrial dysfunctions caused by inhibitions of electron transport chains increased NADH/NAD ratio. I hypothesized that NNT

enzyme generated NADPH in mitochondria to drives reductive carboxylation via isocitrate dehydrogenase 2 in mitochondria and dissipated the reductive stress caused imbalance of $NADH/NAD^+$.

8.2. Introduction

Maintaining mitochondrial NAD(P)H redox state was important to prevent accumulation of reactive oxygen specifies and programmed cell death[8,9]. Imbalance of mitochondrial redox states was associated with disease models such as cancer, neurodegeneration, and heart failure[10]. Several metabolic enzymes played an important role in maintaining mitochondrial NADPH levels. It included isocitrate dehydrogenase 2 (IDH2), malic enzyme 3 (ME3), Methylenetetrahydrofolate dehydrogenase 2 (MTHFD2), glutamate dehydrogenase 1 (GLUD1) and nicotinamide nucleotide transhydrogenase (NNT). Of these, NNT played an important role in alleviating mitochondrial stress characterized by dysfunctional mitochondria. Mitochondrial disease models or hypoxic conditions were known to perturb the redox state in mitochondria by elevating the NADH/NAD+ level. NNT mitigated the redox stress by converting the excess NADH to NAD+ while regenerating NADPH, as well as which can be used for antioxidant defense.

Furthermore, it was suggested that cell lineage influenced cancer metabolism and thus understanding the lineage-specific metabolic vulnerabilities could be effective in developing metabolic targeting drugs [11]. One carbon and serine metabolism contributed a production of precursors for nucleotides and NADPH for antioxidant defense [12]. Growing evidence suggested that serine catabolism occurred in mitochondria and thus provide NADH or NADPH with higher

catabolic rates in Myc-driven breast cancers under hypoxic conditions [13,14]. It was unknown to which extent NADH or NADPH was regulated or coordinated by NNT enzymes. Therefore, with evidence that supported NNT played a critical roles in tumorigenesis *in vivo* and its coordination with glucose and glutamine metabolism, we endeavored to extend our previous work to its function related to serine metabolism in different cancer types.

The extent of NNT in mitochondrial NADPH homeostasis under varying nutrient conditions was not evaluated in detail. We hypothesized that a knockout of NNT promoted the redox stress by increasing NADH and reducing NADP+, making it more vulnerable to oxidative stress as well as reductive stress. To test the hypothesis, I knockout NNT out and measured the change NADPH using the sensors. Our work explored the metabolic adaptations occurred by NNT to glucose, glutamine, or serine metabolism, and how NNT regulated the hydrogen peroxide levels in mitochondria via antioxidant networks.

8.3. Materials and Methods

8.3.1. Media formulation

Several media were prepared to grow cells under varying nutrient conditions. First, DMEM without sodium bicarbonates, amino acids, glucose, pyruvic acid, and phenol red powder was purchased from biological Life Science. We prepared the MEM solution by diluting the DMEM powder. To add non-essential amino acids, we diluted MEM amino acids solution (Thermo, 11130) to the previously made solution. For addition of non-essential amino acids, we further added MEM non-essential amino acids solution (Thermo, 11140).

8.3.2. Bioinformatics survey

For essentiality and co-essentiality analysis, a detailed method was described in **Chapter 6**.

8.4. Results

8.4.1. Bioinformatics and computational analysis reveals increased NNT reaction rate upon mitochondrial oxidative stress

Mutations in NNT enzyme was known to cause familial glucocorticoid deficiency[15]. To analyze the NNT status in cancer cell, we implemented bioinformatics survey based on the Cancer Genome Atlas database. It was found that lung squamous cells had most affected NNT enzymes, which included approximately 10% of amplification and 2 % of the mutations, followed by Stomach Adenocarcinoma, Esophageal Adenocarcinoma, and Lung Adenocarcinoma (**Figure 8.1**). We further evaluated the mutation and amplification frequencies across other NADPH generating enzymes in TCGA database and found out that NNT gene had most mutations or amplifications in the samples tested except IDH1 reaction, which showed higher mutations rates in glioma cells (**Table 8.1**).

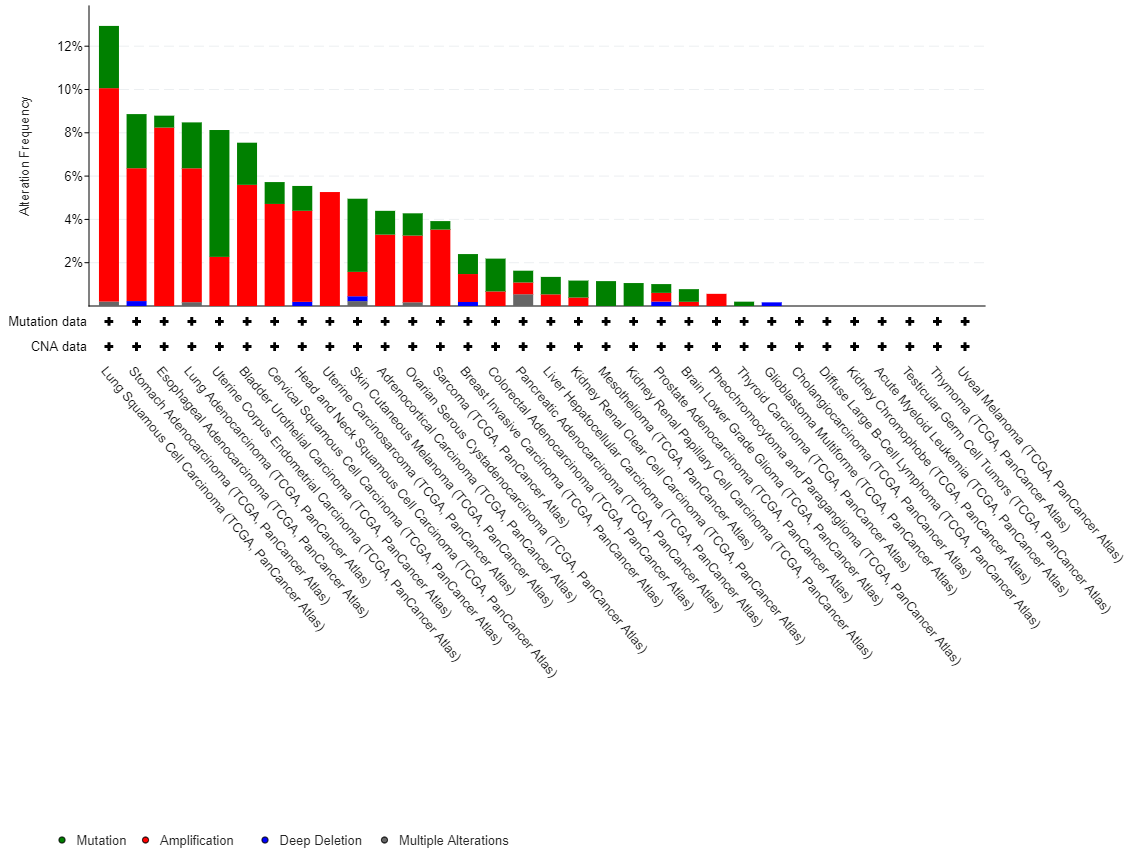

Figure 8.1. Frequency of mutations and amplification observed in NNT enzyme based on the Cancer Genome Atlas database. Lung squamous cell carcinoma showed more than 13 % of affected NNT enzyme. About 2 % of NNT gene was mutated and 10% are amplified. Many of NNT enzymes were amplified through the cancer types. A total of 10967 samples and 10953 patients in 32 studies. The graph was generated from the cBioProtal website.

Table 8.1. TCGA PanCancer Atlas studies on NADPH generating enzymes and their mutation frequencies.

Genes	Mutation and amplification frequency (case)	Of Cases	Cancer Type	Cancer Study

NNT	12.94 (63)	487	Lung Squamous Cell Carcinoma (TCGA, PanCancer Atlas)	Undifferentiated Stomach Adenocarcinoma
MTHFD1	6.06 (27)	444	Skin Cutaneous Melanoma (TCGA, PanCancer Atlas)	Melanoma
MTHFD2	4.17% (1)	48	Diffuse Large B-cell Lymphoma	Mature B-Cell Neoplasms
MTHFD2L	4.4% (4)	91	Adrenocortical Carcinoma (TCGA, PanCancer Atlas)	Adrenocortical Carcinoma
GLUD1	4.25% (21)	494	Prostate Adenocarcinoma (TCGA, PanCancer Atlas)	Cervical Adenocarcinoma
GLUD2	6.62% (36)	529	Uterine Corpus Endometrial Carcinoma (TCGA, PanCancer Atlas)	Undifferentiated Stomach Adenocarcinoma
G6PD	10.42% (5)	48	Diffuse Large B-cell Lymphoma	Mature B-Cell Neoplasms
PGD	5.63 (25)	444	Skin Cutaneous Melanoma (TCGA, PanCancer Atlas)	Melanoma
ME1	9.23 (41)	444	Skin Cutaneous Melanoma (TCGA, PanCancer Atlas)	Melanoma
ME3	8.73 (51)	584	Ovarian Serous Cystadenocarcinoma (TCGA, PanCancer Atlas)	Ovarian Epithelial Tumor
IDH1	76.85 (395)	514	Brain Lower Grade Glioma (TCGA, PanCancer Atlas)	Diffuse Glioma

IDH2	10.5 (21)	200	Acute Myeloid Leukemia (TCGA, PanCancer Atlas)	Leukemia

When we implemented the gene essentiality analysis on NNT enzyme *in vitro*, a knockout out of NNT genes did not influence growth significantly (**Figure 8.2**). Our computational and bioinformatics analysis provided evidence of greater role of NNT in regulation of mitochondrial NADPH pools during mitochondrial oxidative stress (**Figure 8.3).** First, we used publicly available mRNA-seq databased generated by Broad Institute to determine which of the cancer cell types were highly expressing NNT enzymes. The cell types that expressed high levels of NNT enzymes included cervix, hematopoietic and lymphoid, skin, and lung cancers (**Figure 8.3A**).

Next, we implemented a genome-scale flux balance analysis, in which we artificially created mitochondrial dysfunctional states by increasing a steady state generation of H_2O_2 generation rates up to five times. A relative steady state rate distribution of NADPH producing enzymes in mitochondria at basal condition showed that NNT generated about 8% of mitochondrial NADPH **(Figure 8.3B).** As we artificially induced mitochondrial oxidative stress by increasing the hydrogen peroxide generation rate up to five times higher, we found that the change of the rate was most significant for NNT enzyme **(Figure 8.3C).** The rate increased by nearly 38 %, whereas the rate of IDH2 reaction decreased by 20 %. At the same time, the simulation predicted that IDH1 reaction increased by 19 % in cytosol as well as 15 % increase of 6PGD enzyme. These change suggested that despite compartmentalization of NADPH levels in cytosol and mitochondria, the mitochondrial stress caused by increased H_2O_2 generation not only perturbed the mitochondrial NADPH metabolism but also influenced the cytosolic NADPH metabolic pathways.

We further implemented a co-essentiality analysis as described in Chapter 6 for NNT enzyme. It revealed that NNT enzyme had a high likelihood of interacting with the mitochondrial isoform of NAD kinase (NADK2) and SLC25A1, which was a citrate transporter and has been known for the indirect transporter for NADPH **(Figure 8.3D)**.

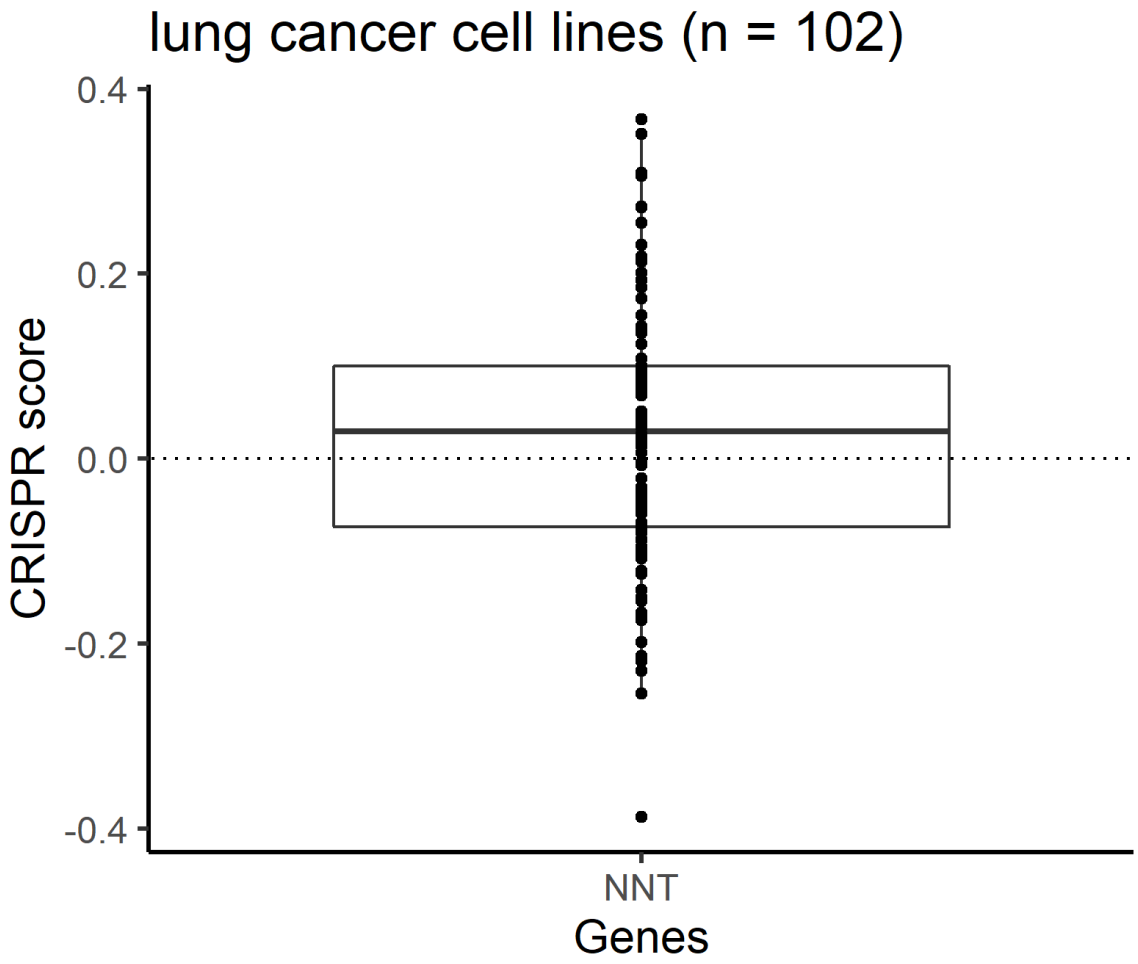

Figure 8.2. CRISPR score for lung cancer cell lines based on essentiality database generated by Broad Institute.

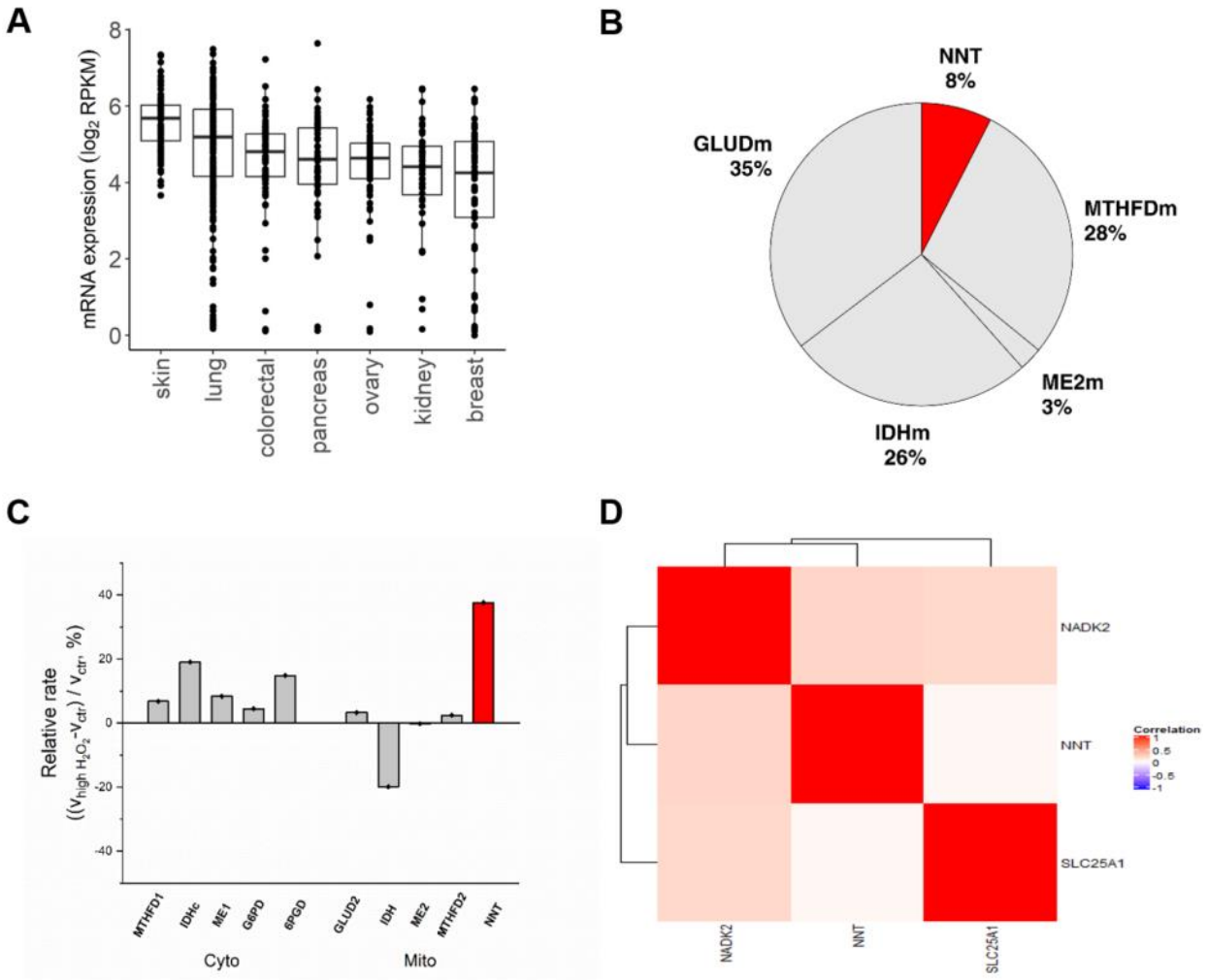

Figure 8.3. Genome-scale flux balance analysis and co-essentiality analysis reveals an importance of NNT enzyme when mitochondria exhibit increased H_2O_2 generation rates. (A) The pie chart represents the relative flux percentages among NADPH generating enzymes localized in mitochondria. (B) In response to the elevation of superoxide dismutase enzyme rate up to five times, the flux distributions to through mitochondrial cytosolic enzymes are graphed. Of 10 widely known cytosolic and mitochondrial enzymes, NNT enzyme colored in red showed the largest flux change, which is about 37%. (C) The co-essentiality analysis reveals that NNT enzyme is closely linked to NADK2 enzyme and additionally the SLC25A1, a citrate transport that has been known to participate in regulation of mitochondrial NADPH redox state. (D) A genome-scale flux balance analysis reveals that transporter fluxes are changing most highly when the level of hydrogen peroxide is increased.

Additionally, a flux distributions on TCA cycle demonstrated an increased fluxes on mitochondrial transporters **(Figure 8.4)**. This indicated that when mitochondria were challenged by oxidative stress, transporter mechanisms other than the traditional glycolytic and oxidative phosphorylation pathways played greater roles. *SLC25A1* gene encoded a citrate transporter and was known to regulate NADPH homeostasis in mitochondria. *SLC25A10* encoded malate transporter and transport of malate was fueled for malic enzyme reactions. Lastly, I conducted a proteomic research to determine whether NNT enzyme had cysteine reside that was vulnerable to oxidation. Based on the analysis, I found about 2% of cysteine groups in NNT enzyme, and two regions show the pattern that was vulnerable to oxidation **(Figure 8.5).** Additionally, we performed sequence alignment analysis across different organelles to find that the reactive cysteine residues were conserved for mammalian cells (**Table 8.2**).

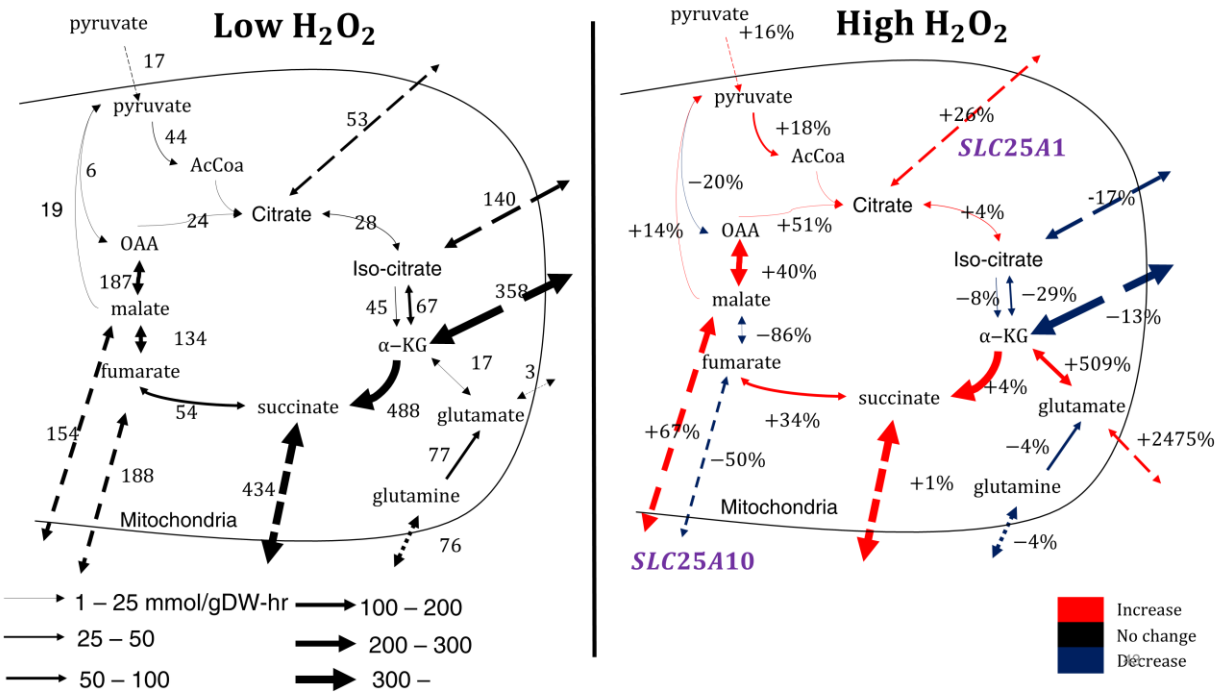

Figure 8.4. Flux distributions in reactions in TCA cycle for cases with low and high hydrogen peroxide generation rate.

A

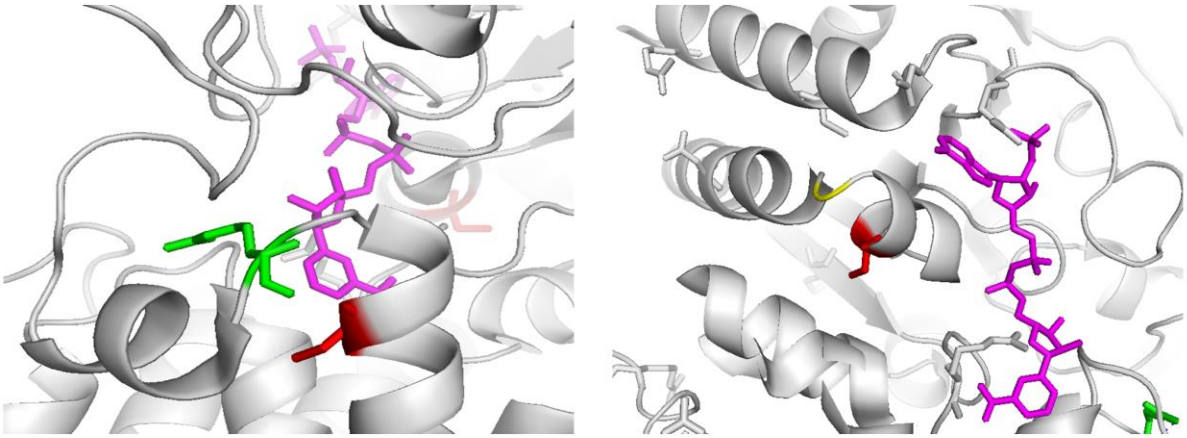

B

-5	-4	-3	-2	-1	834	+1	+2	+3	+4	+5	+6
L	S	I	Y	M	C	V	A	M	N	R	S

-5	-4	-3	-2	-1	893	+1	+2	+3	+4	+5	+6
P	G	Y	G	L	C	A	A	K	Q	Y	P

Figure 8.5. A part of NNT enzyme where the purple ligands represent NADPH, green for arginine and yellow K for lysine. The red represents the cysteine group. Based on the pKa values and oxidation states (Xiao, Chouchani, 2020), cysteine groups close to lysine or arginine within five base pairs are tendency for oxidation.

Table 8.2. Reactive cysteine residue is highly conserved in mammalian NNT enzymes. The sequence was aligned using the Molecular Evolutionary Genetics Analysis (MEGA) with sequences imported from Uniprot database.

							83													89						
Organisms							4													3						
Homo sapiens - Q13423	I	L	S	Y	I	M	C	V	A	M	N	R	S	T	P	G	Y	G	L	C	A	A	K	A	Q	Y
Bos taurus - P11024	I	L	S	Y	I	M	C	V	A	M	N	R	S	T	P	G	Y	G	L	C	A	A	K	A	Q	Y

Ovis aries - W5PFI3	I	L	S	Y	I	M	C	V	A	M	N	R	S	T	P	G	Y	G	L	C	A	A	K	A	Q	Y
Mus musculus - Q61941	I	L	S	Y	I	M	C	V	A	M	N	R	S	T	P	G	Y	G	L	C	A	A	K	A	Q	Y
Escherichia coli - P0AB67	I	L	S	Y	I	M	C	K	A	M	N	R	S	T	P	G	Y	G	M	A	V	A	Q	A	Q	Y
Rhodospirillum rubrum - P0C188	I	L	S	Y	I	M	C	K	G	M	N	R	S	V	P	G	Y	G	M	A	V	A	Q	A	Q	H
Shigella flexneri - P0AB70	I	L	S	Y	I	M	C	K	A	M	N	R	S	T	P	G	Y	G	M	A	V	A	Q	A	Q	Y
Haemophilus influenzae- P43010	I	L	S	Y	I	M	C	K	A	M	N	R	S	T	P	G	Y	G	M	A	V	A	Q	A	Q	Y

8.4.2. Prepare NNT knockout cell lines using a CRISPR knockout system.

In order to investigate the role of NNT enzyme, I knocked out NNT enzyme (**Figure 8.6)**. We also re-expressed the NNT enzyme to the knockout cells to use it as another control (**Figure 8.7**).

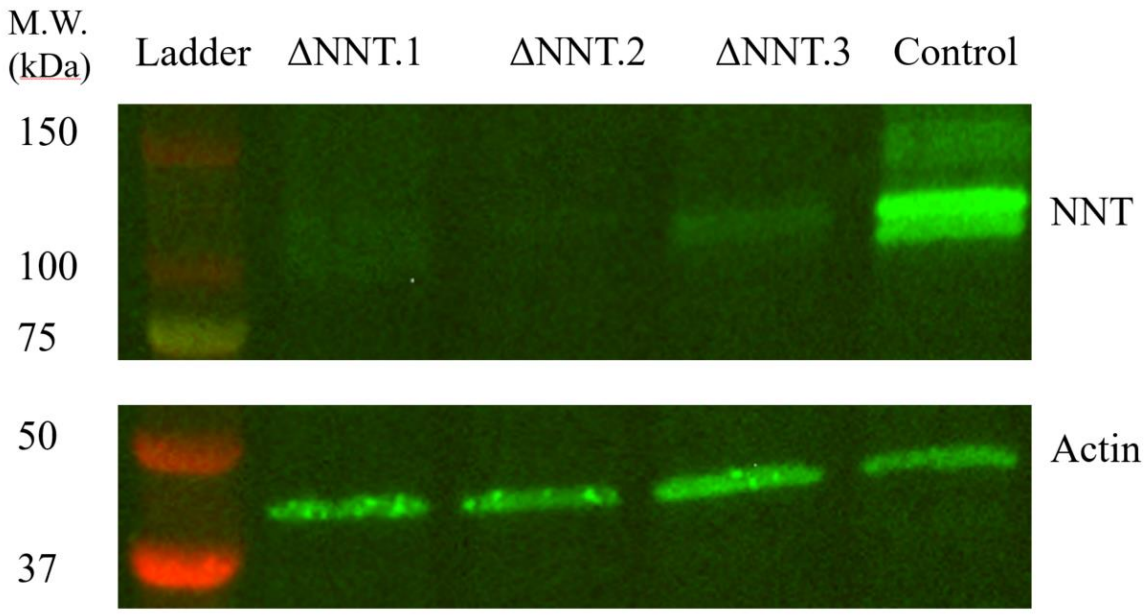

Figure 8.6. CRISPR knockout of NNT enzyme for Hek cells. Three distinct sgRNAs were construct for knockout the genes. Each population was emanated from a single cell as suggested in Ran, Zhang's Nature protocol.

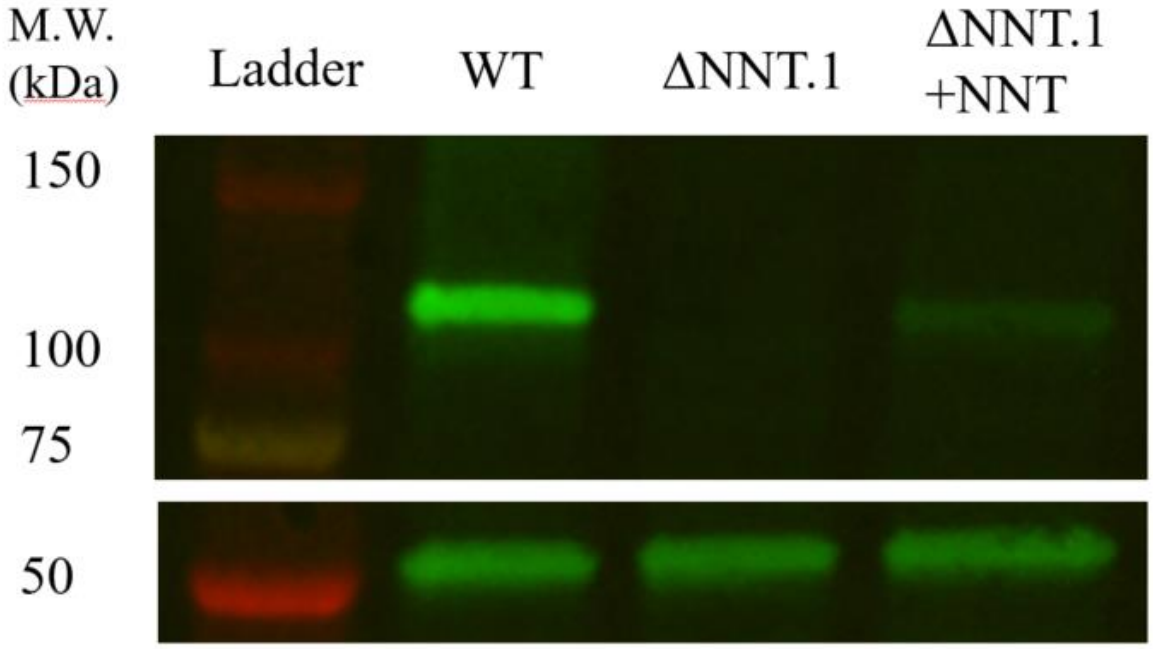

Figure 8.7. A western blot representing knockout cell lines as well as re-expression of NNT enzyme.

8.4.3. NNT knockout cells increase glucose oxidation but are vulnerable to mitochondrial oxidative stress

Next, we investigated glucose metabolic pathway activities of NNT wild type and NNT knockout Hek cells. First, we cultured respective cells under [U-13C]glucose tracers and measured the isotopologues of central carbon metabolites after two days of incubation. As previously reported, we confirmed that the NNT knockout cells increase glucose oxidation under normoxic conditions. However, the extent of increase was less than what was previously reported, in which the labeling fraction increased by approximately 4 %. For Hek cells, M+2 isotopologues increased by nearly 1 to 3 % for central carbon metabolites and also M+3 labeling increased by 1 to 2 % (**Figure 8.8**) . We further studied the oxidative pentose phosphate pathway activity using [1,2-13C]glucose tracer to find out that there was no statistically significant differences between the HEK and HEK-ΔNNT cells. The median fraction of M+1 of lactate was about 6.8 and 6.5 % for HEK and HEK-ΔNNT cells (**Figure 8.9**).

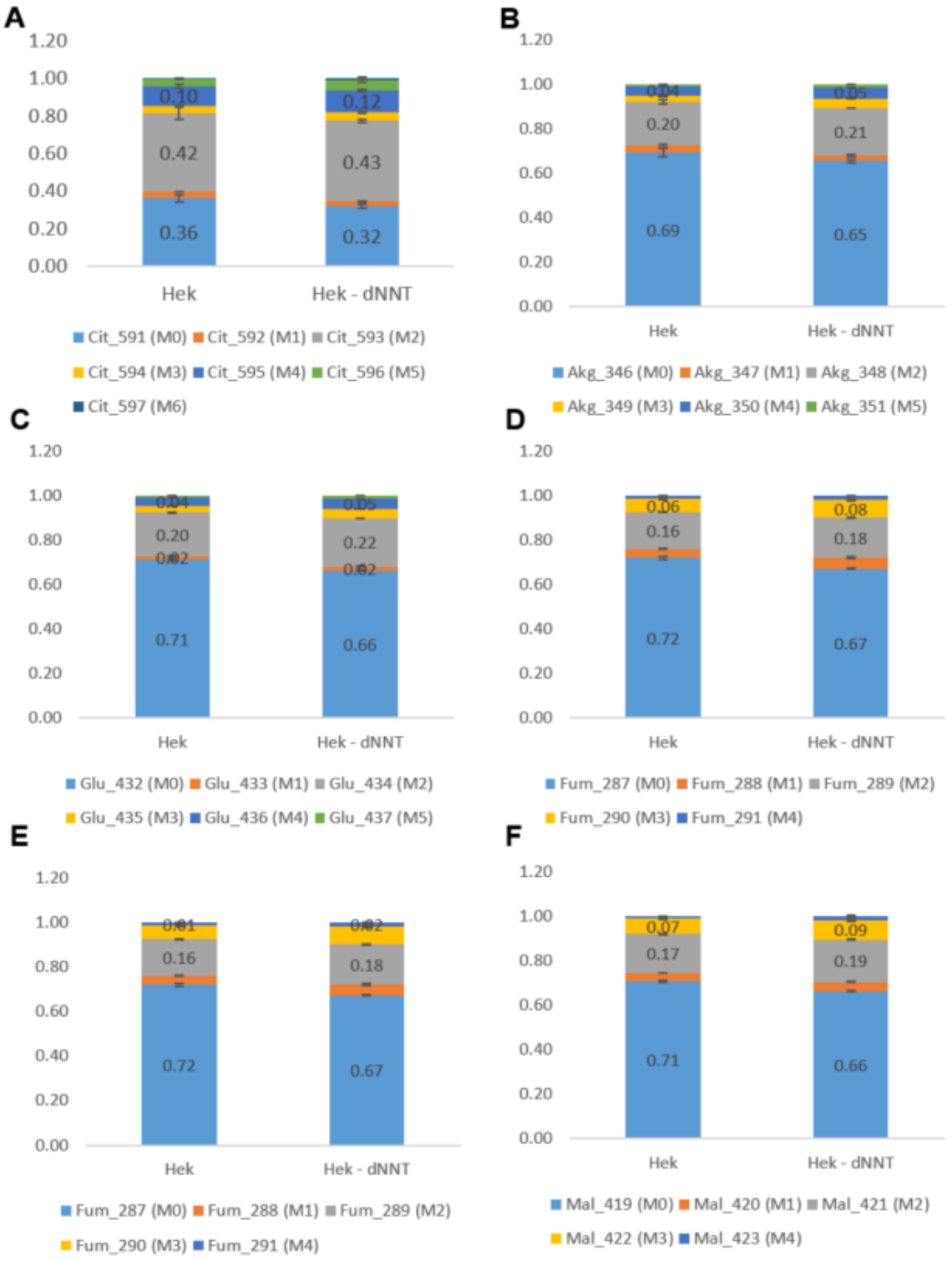

Figure 8.8. TCA cycle metabolites isotopologues profiling for Hek and Hek-ΔNNT cell lines. Hek and NNT knockout Hek cells grew in [U-13C]glucose for two days and the isotopologue profiling was measured for (A) citrate, (B) αKG, (C) glutamate, (D) succinate, (E) fumarate, and (F) malate.

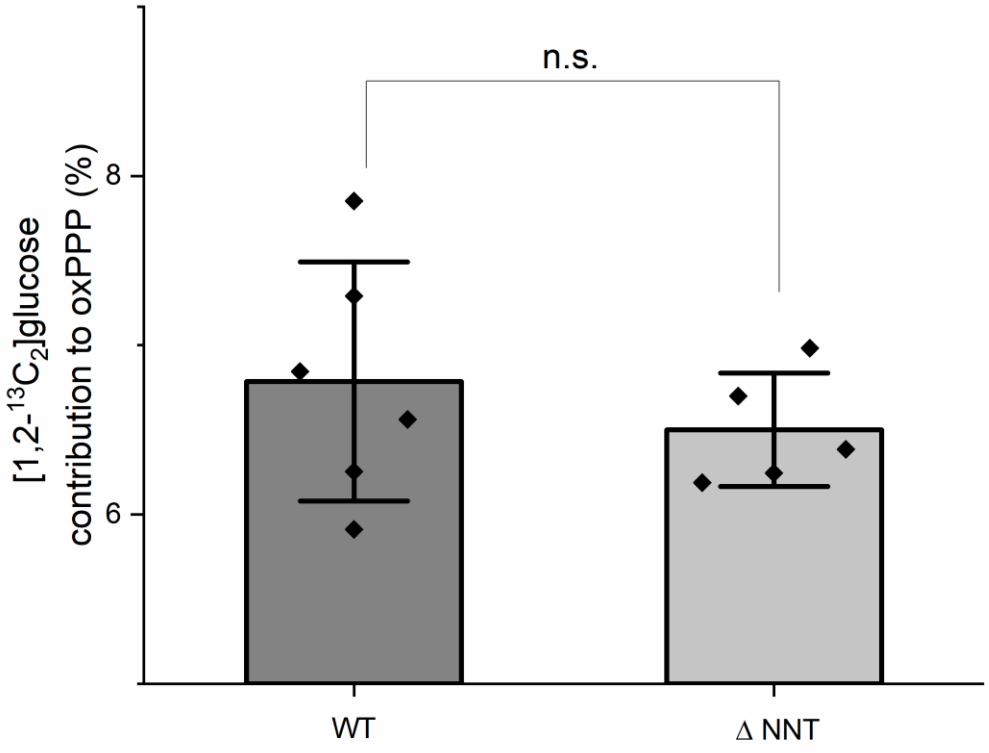

Figure 8.9. [1,2-$^{13}C_2$]glucose tracer reveals an activity of pentose phosphate pathway by glucose. There is no difference between the pentose phosphate pathway usage between HEK and HEK-ΔNNT cells.

Next, we tested whether the NNT knockout cells were vulnerable to oxidative stress. It was previously shown that NNT play a role in maintaining mitochondrial NADPH redox states[15–18] . These researches revealed that NNT knockout down cells showed higher ROS in mitochondria using MitoSox chemical dye[5,15]. Here, we used mitochondrial specific H_2O_2 generation using the mitoPQ and monitored whether the NNT knockout cells were indeed more sensitive to mitochondrial oxidative stress. We treated cells with mitoPQ, which generated mitochondrial H_2O_2 by interfering complex I but did not influence the oxidative phosphorylation is maintained (**Figure 8.10**). Given NNT knockout cells were more sensitive to mitochondrial

oxidative stress, we tested whether the mitochondrial stress induced oxidative pentose phosphate pathway under mitochondrial oxidative stress in one hour. However, when we measured the oxidative pentose phosphate pathway activity after 1 hour, we did not observe significant increase of the oxPPP (**Figure 8.11**).

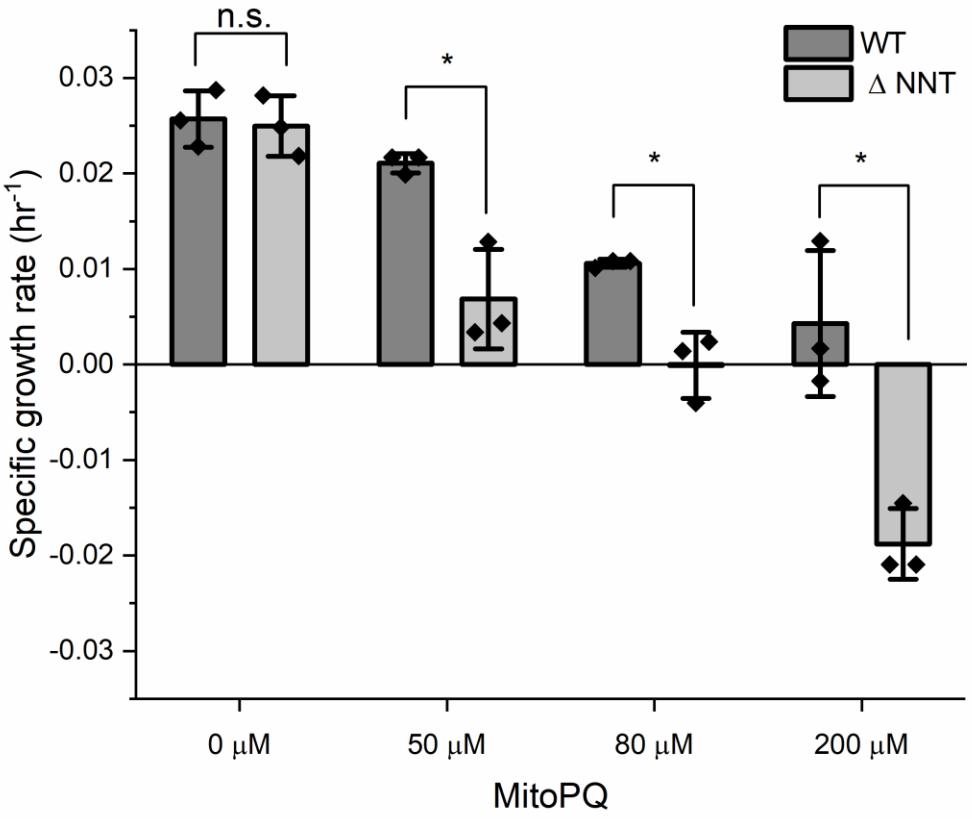

Figure 8.10. NNT knockout cells are vulnerable to mitochondrial oxidative stress.

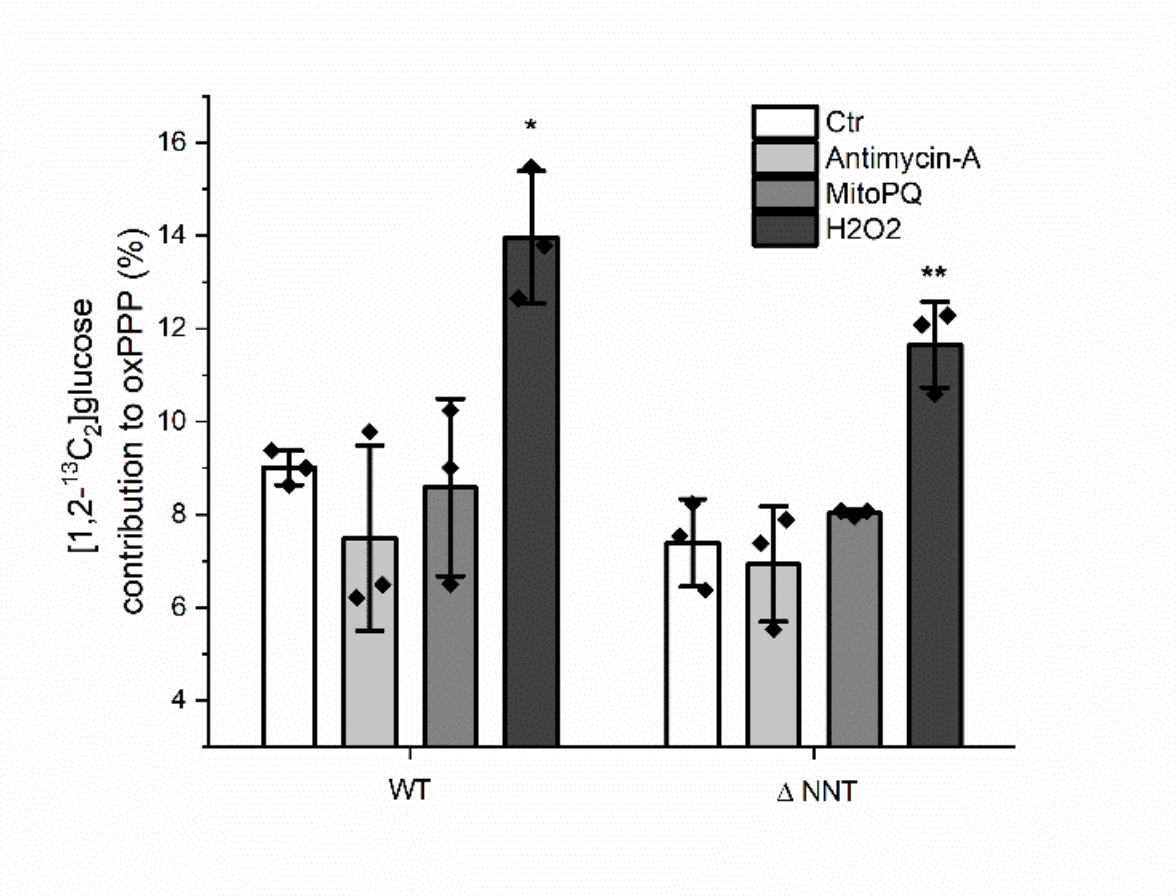

Figure 8.11. Glucose contribution to oxidative pentose phosphate pathway upon mitochondrial oxidative stress in 1 hour.

8.4.4. Determination of essential components in media for NNT knockout cells

Next, we tested whether the NNT knockout cells relied on certain amino acids or metabolites in media for growth under nutrient limited conditions. When we cultured the cells in MEM media, we found out the growth was inhibited. The growth rate under MEM media was 0.028 hr^{-1}, whereas the NNT knockout cells had proliferation rate of 0.022 hr^{-1}, which is about 22 % slower growth than the wild-type. The NNT rescued cells exhibited a similar growth rate compared to the wild type, with a growth rate of 0.027 hr^{-1}. When we cultured cells in MEM media with non-essential amino acids or RPMI, the growth rate decreased by 5 and 7 %, respectively and these

were not statistically significant (**Figure 8.12**). Next, we tested which of the non-essential amino acids were important for maintaining cell growth for NNT knockout cells. Of several non-essential amino acids, we reasoned that serine be an important source, because we previously observed that absence of serine generally slowed down the growth rate. When we added either serine or glycine in media, we found out that the growth was rescued (**Figure 8.13**).

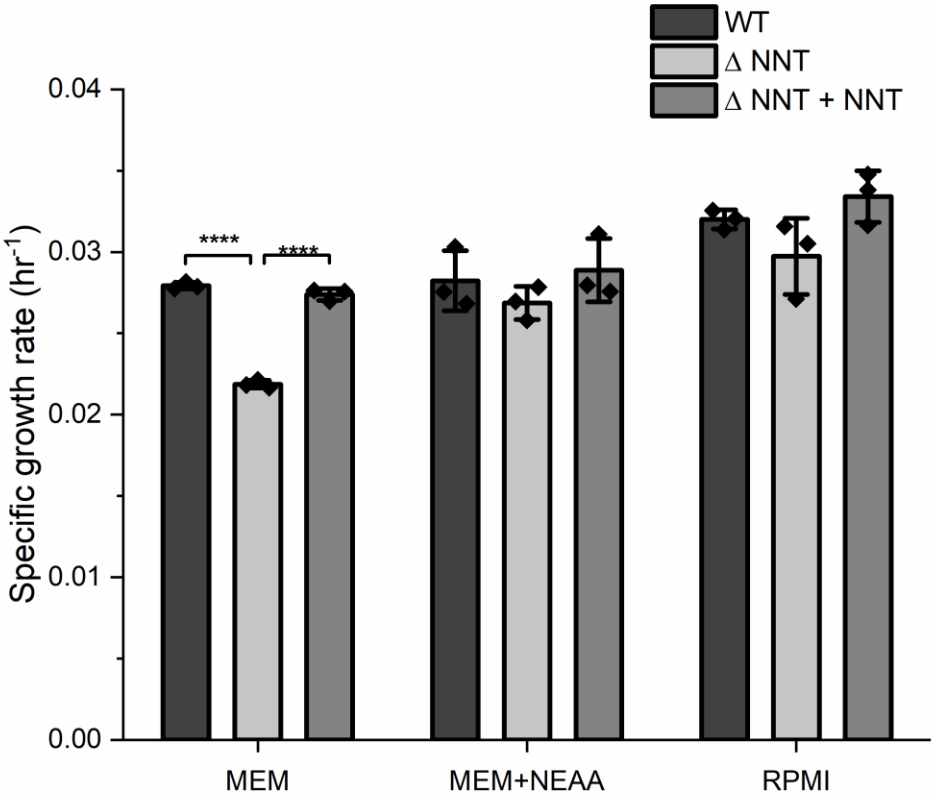

Figure 8.12. NNT knockout cells grow slower in MEM media, which lacks non-essential amino acids (NEAA) including alanine, asparagine, aspartate, cysteine, glutamate, glutamine, glycine, proline, serine, tyrosine, arginine, and histidine.

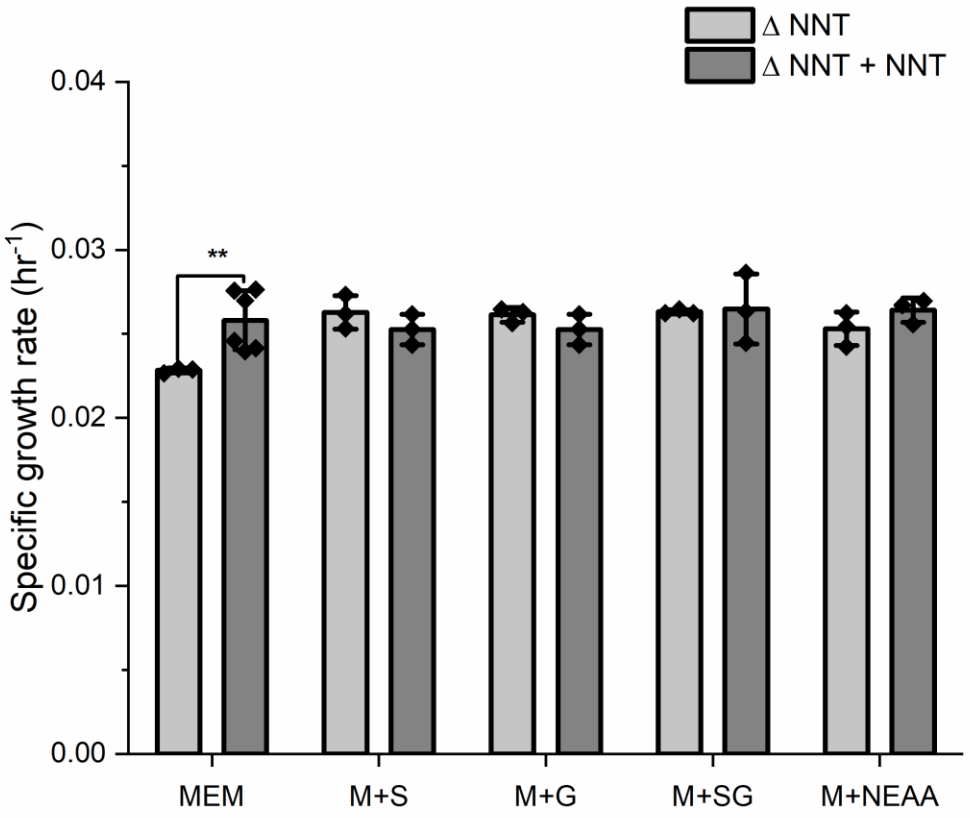

Figure 8.13. Serine and glycine supports cell growth in NNT knockout cells. S represents serine and G represent glycine. NEAA represents non-essential amino acids.

8.4.5. Bioinformatics analysis reveals a functional relationship between NNT and OXCT1 gene for ketone body metabolism

In the previous sections, we confirmed that NNT knockout cells were vulnerable to oxidative stress. Then, we also found out that NNT knockout cells have limited growth rate in absence of non-essential amino acids, particularly serine and glycine. This could be that NNT knockout cells may have limited capacity in generating mitochondrial NADPH and thus it is essential to supply serine and glycine to maintain mitochondrial NADPH redox homeostasis.

To explore a possibility of NNT's other functions in metabolism, I implemented co-essentiality analysis on NNT enzyme based on CRISPR genetic screen data publicly available by Broad Institute. Based on 17645 genes across 990 cell lines, co-essentiality analysis shows OXCT gene, a rate-limiting enzyme in ketone catabolism pathway, was highly correlated with NNT in functionality (**Figure 8.14**). The expression levels of OXCT1 gene was low in liver but higher across other tissues[19]. Mechanistically, acetoacetate (AcAc) was converted to AcAc-CoA through exchange of a CoA from succinyl-CoA to Acetoacetate through succinyl-CoA:3-oxoacid-CoA transferase, which is encoded by OXCT1 gene[20].

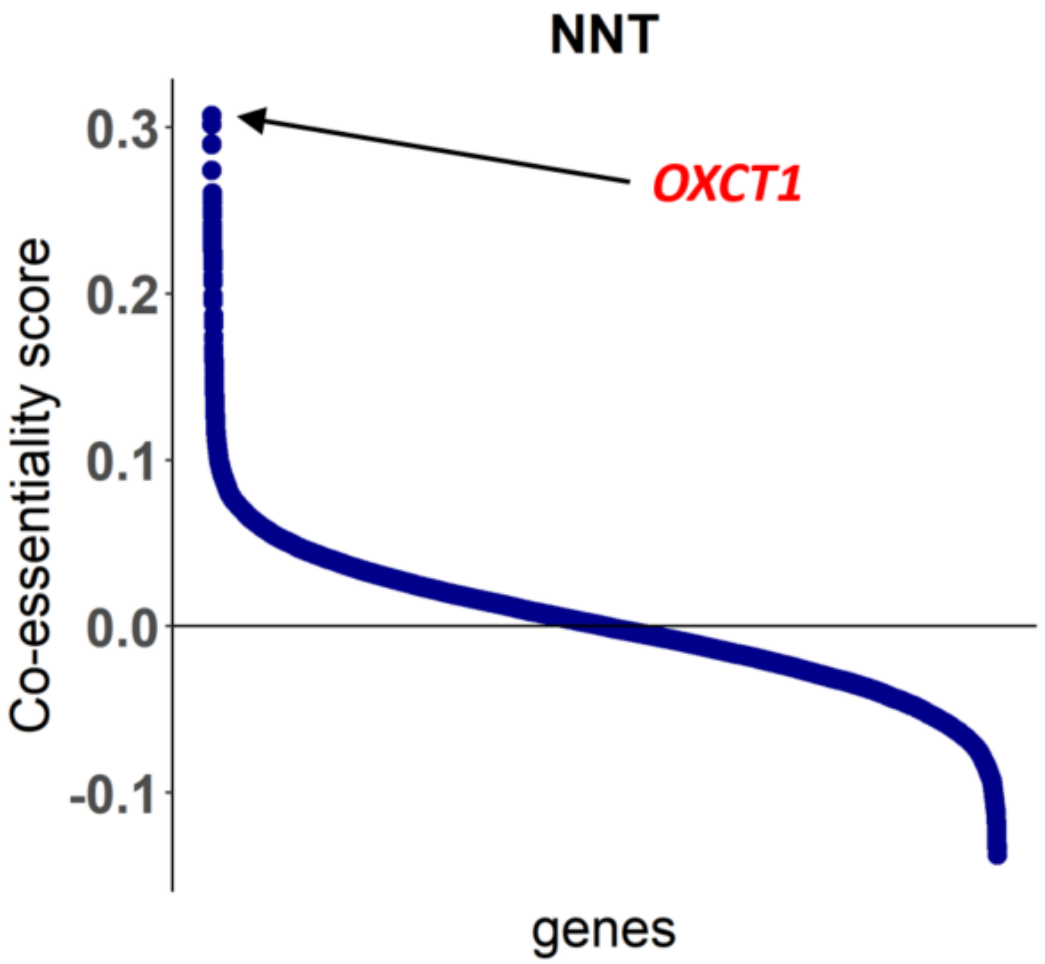

Figure 8.14. Co-essentiality analysis with NNT gene. A total of 17645 query genes were used to correlate with NNT gene across 990 cell lines. Each dot represents a correlation coefficient value between NNT gene and a query gene across 990 cell lines. The CRISPR screening data is freely available by Broad Institute.

Next, we also implemented bioinformatics analysis to assess whether the OXCT1 gene and NNT genes were functionally related. OXCT1 gene encodes SCOT enzyme, which converted acetoacetate to acetocaetyl-CoA (AcAc-CoA) was subsequently converted to acetyl-CoA, which participates TCA cycle by reacting with oxaloacetate to make citrate. D-βOHB dehydrogenase (BDH1) was a first step that catabolizes beta-hydroxybutyrate (βOHB) making acetoacetate while using NAD^+ (**Figure 8.15**). βOHB dehydrogenase was at near equilibrium

with NADH/NAD^{+}[21]. We hypothesized that NNT played a role in ketone body metabolism by converting NADH to NAD^{+} allowing oxidation of βOHB to AcAc and as found in the co-essentiality analysis, SCOT enzyme, which was encoded by OXCT1 gene, allowed subsequent reaction process to supply acetyl-CoA, fueling TCA cycle.

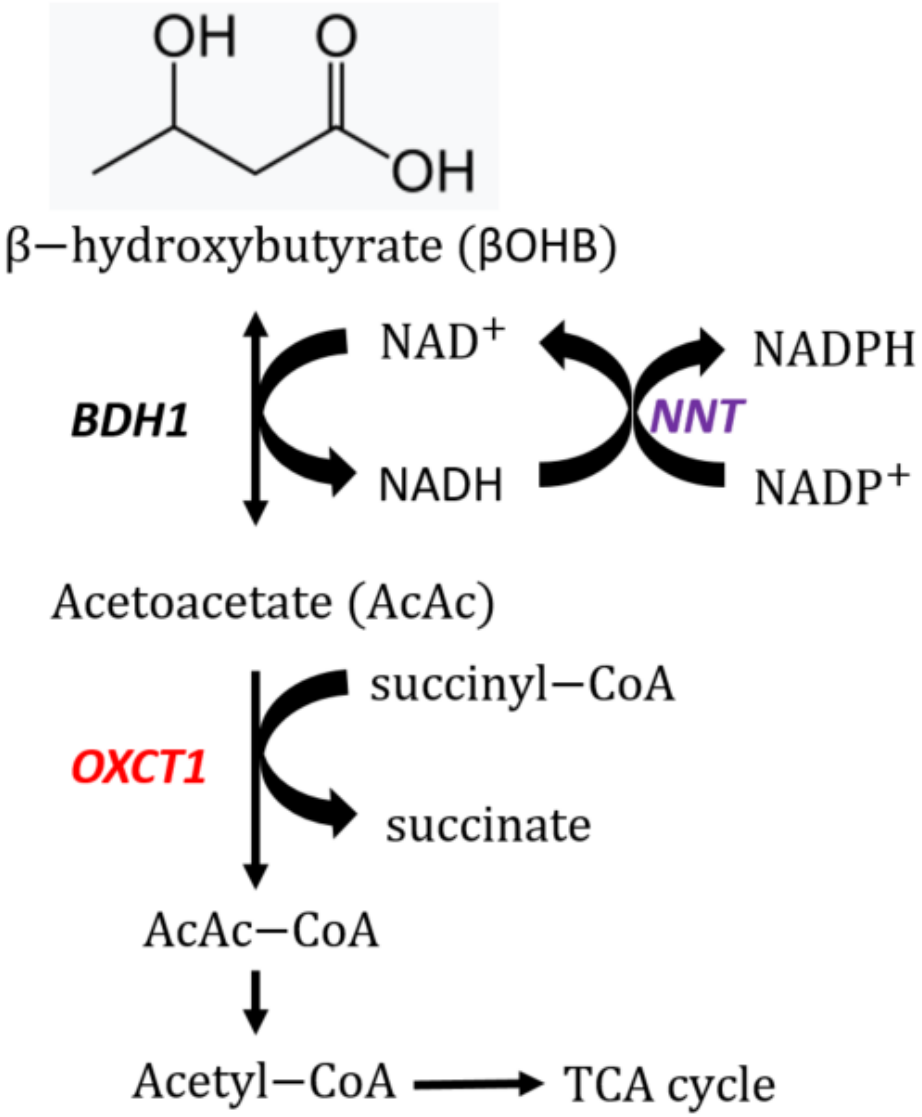

Figure 8.15. Functional relationship between NNT and OXCT1 genes. OXCT1 gene encodes SCOT enzyme, which converts acetoacetate to acetocaetyl-CoA (AcAc-CoA) is subsequently converted to acetyl-CoA, which participates TCA cycle by reacting with oxaloacetate to make citrate. D-βOHB dehydrogenase (BDH1) is a first step that catabolizes beta-hydroxybutyrate (βOHB) making acetoacetate while using NAD^{+}.

Additionally, I evaluated which of genes have high correlation with NNT in regards to mRNA expression levels in cancer cells. Based on the CCLE database, which consisted of the mRNA gene expression levels of 19177 genes and 1379 cell lines, I found out that OXCT1 gene ranked the top in correlation with NNT genes. Next to OXCT1 gene, MAPRE2 gene encoded a microtubule-associated protein that was necessary for spindle formation. TMEM265 gene encoded a protein related to transcription coactivator activity and histone acetyltransferase activity. ALOXE3 gene encoded a lipoxygenase enzyme that catabolize arachidonic acid-derived compounds (**Figure 8.16**).

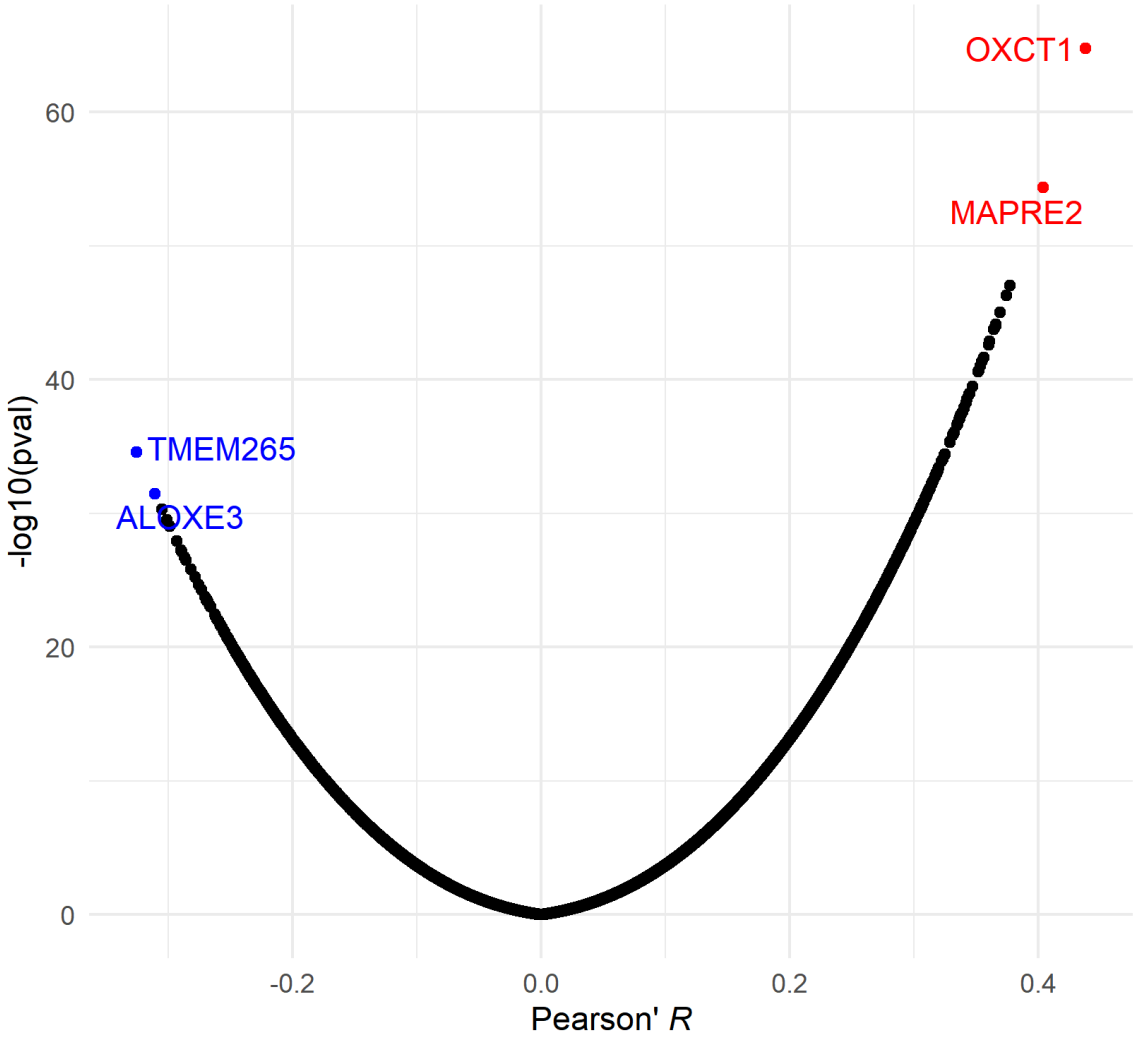

Figure 8.16. A volcano plot representing Pearson's correlation with NNT genes and 19177 genes from 1379 cell lines based on the CCLE database. Transcriptomics data based on CCLE (Cancer cell-line encyclopedia) reveals a strong positive correlation between the expression levels of NNT and OXCT1.

Further, I implemented gene expression correlation analysis based on The Cancer Genome Atlas (TCGA) database to see whether there existed a high correlation between NNT genes and OXCT1 genes based on patients' samples. The Cancer Genome Atlas (TCGA) database further demonstrated a high correlation between the expression levels of NNT and OXCT1 in kidney cancer. The Pearson correlation coefficient was 0.8 (**Figure 8.17**).

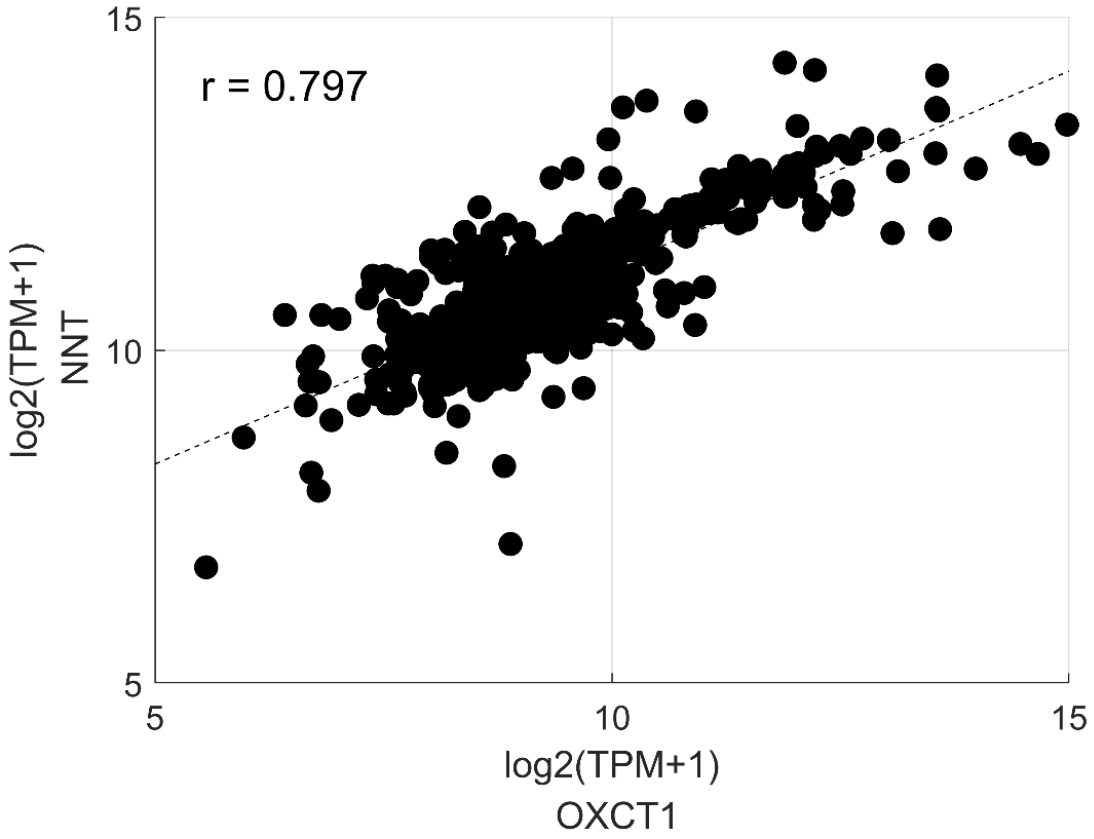

Figure 8.17. Gene expression correlation analysis between OXCT1 and NNT genes reveal a high correlation in kidney renal clear cell carcinoma (KIRC) based on 606 patient samples.

Next, I also evaluated the prognostic values of a particular gene, in which the patients were grouped to either high or low expression of a specific gene. The two patient groups were compared with Kaplan-Meier survival plot with the hazard ratio of 95 % confidence intervals and log rank P value were estimated. I evaluated the NNT and OXCT1 genes for KIRC cohorts to find out that high expressions of NNT and OXCT1 genes helped patient survival. Instead, the lower expression of these genes showed lower survival probability (**Figure 8.18**).

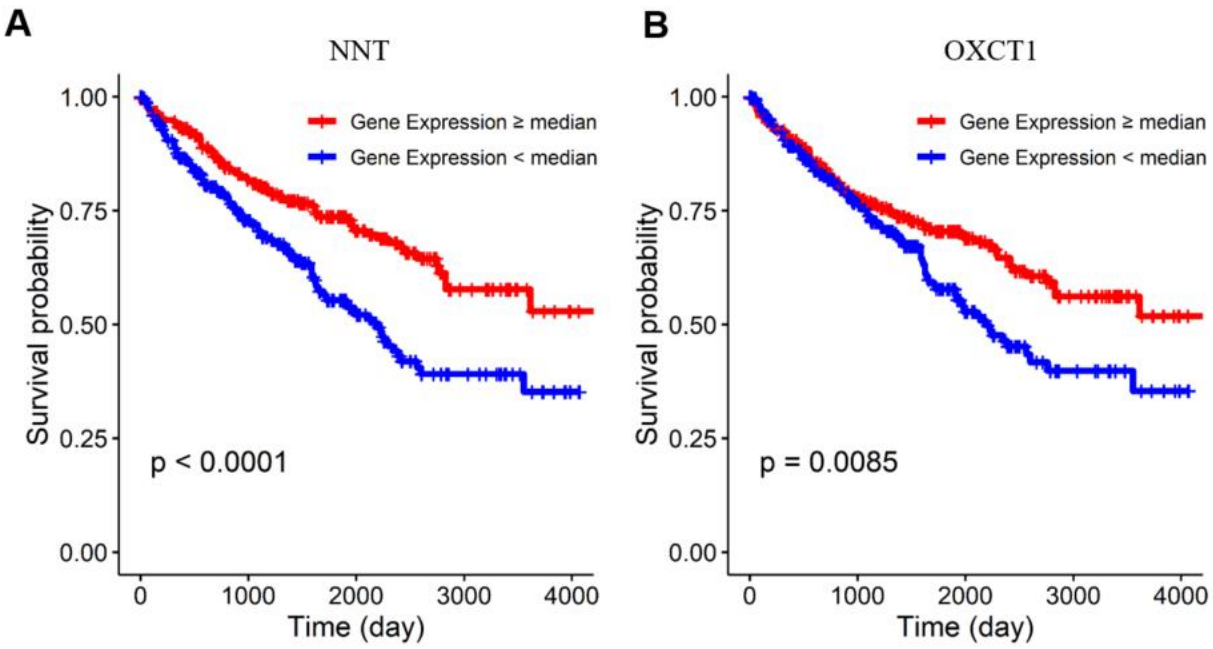

Figure 8.18. Kaplan-Meier survival plot on NNT and OXCT1 genes based on kidney renal clear cell carcinoma (KIRC) of TCGA database.

8.4.6. NNT facilitates catabolism of beta-hydroxybutyrate (βOHB) under glucose limited conditions

To understand whether NNT served in ketone body metabolism by mediating ketone body catabolism such as beta-hydroxybutyrate (βOHB), I cultured HEK and HEK with NNT knockout on βOHB in either glucose deficient or sufficient conditions. I hypothesized that under glucose deprived condition, βOHB oxidation activity increased to fuel TCA cycle, but knockout NNT impaired the catabolic step of BDH1 and slowed down proliferation by disrupting TCA cycle (**Figure 8.19**).

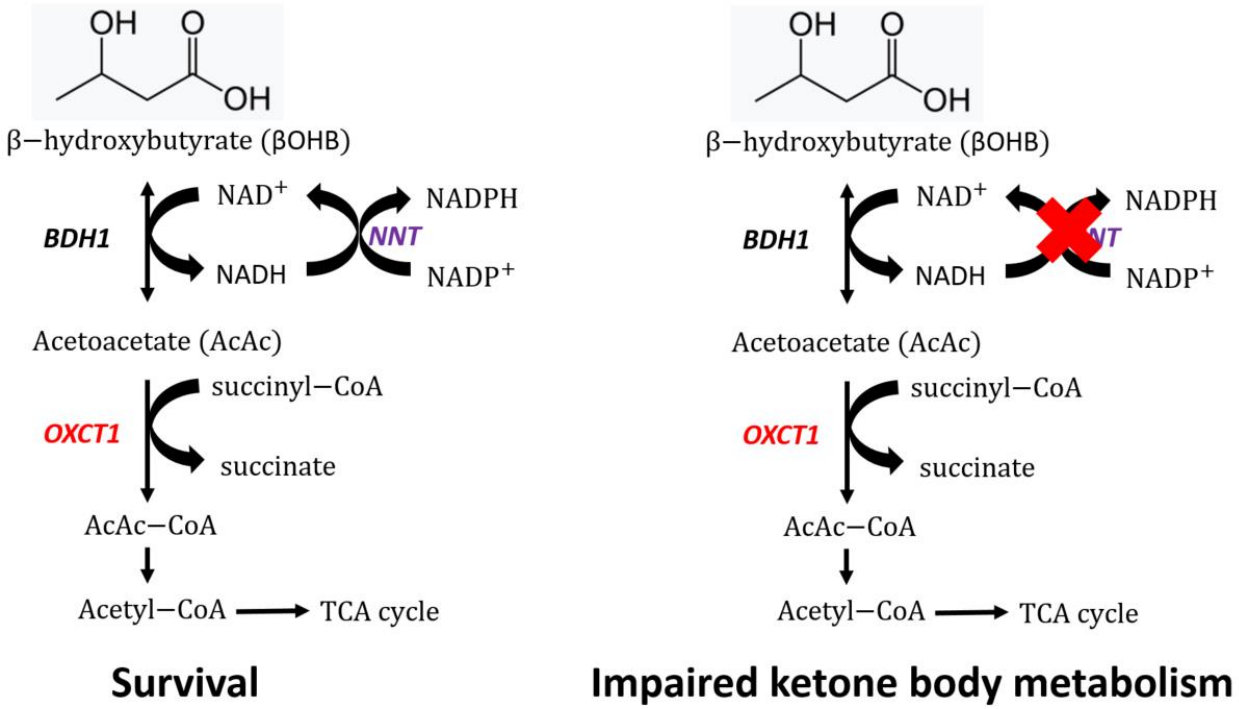

Figure 8.19. Data-driven hypothesis generation for a role of NNT in ketone body metabolism. NNT maintains NAD^+/NADH redox states to facilitate βOHB catabolism. Under glucose deprived condition, ketone body metabolism is known to increase. In glucose deprived condition, cells may use βOHB as a carbon course to fuel TCA cycle. However, upon knockout or dysfunctional NNT enzyme, βOHB cannot be effectively catabolized and impairs ketone body metabolism.

To test the hypothesis, I cultured cells in absence or presence of βOHB under glucose sufficient or deprived conditions. First, under regular MEM with 5.6 mM glucose conditions, I found out that the presence or absence of βOHB did not influence growth rates of both HEK and HEK-ΔNNT cells. The reduced growth rate was consistent with the previous experiments in which HEK-ΔNNT cells proliferated slowly in MEM media. Growth rate decreased by approximately 16 % for NNT knockout cells in MEM media, in which the growth rate decreased from 0.029 hr^{-1} to 0.024. In MEM with βOHB, the growth rate for control was 0.029^{-1} but decreased to 0.023^{-1} for NNT knockout cells (**Figure 8.20**).

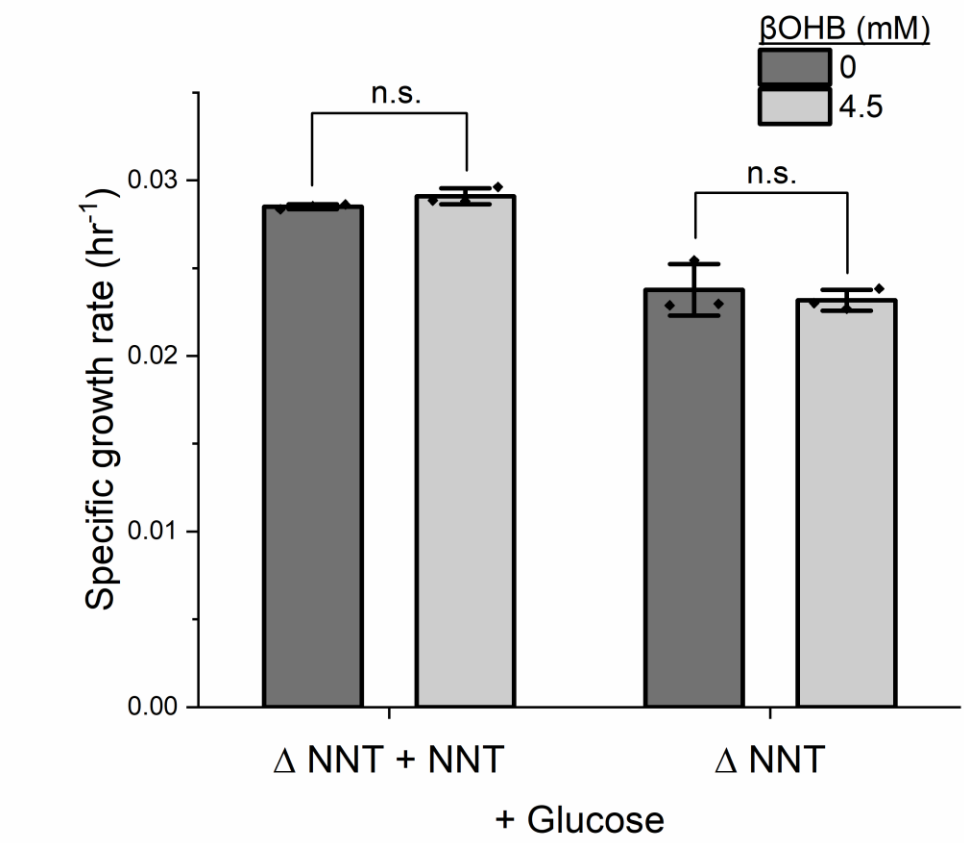

Figure 8.20. Growth rate for HEK and HEK-ΔNNT cells grown in MEM media with 5.6 mM glucose and 0 or 4.5 mM βOHB.

Next, we cultured cells in glucose deprived conditions with or without βOHB. During starvation, cells shifted their glucose metabolism to ketone body catabolism to support homeostasis and the serum βOHB levels were known to increase up to 6 mM[20,22]. When I cultured cells in glucose deprived condition without βOHB, the growth rate for control was 0.027 hr^{-1} and 0.024 hr^{-1} for NNT knockout cells. It was shown that HEK cells maintained similar growth rates regardless the presence of glucose at least in this experimental setting. When βOHB was introduced, the cell growth increased by nearly 10 % from going 0.027 to 0.03 hr^{-1}. On the other hand, HEK-ΔNNT cells decreased proliferation rate from 0.024 hr^{-1} to 0.021 hr^{-1}, which is about 10 % decrease (**Figure 8.21**).

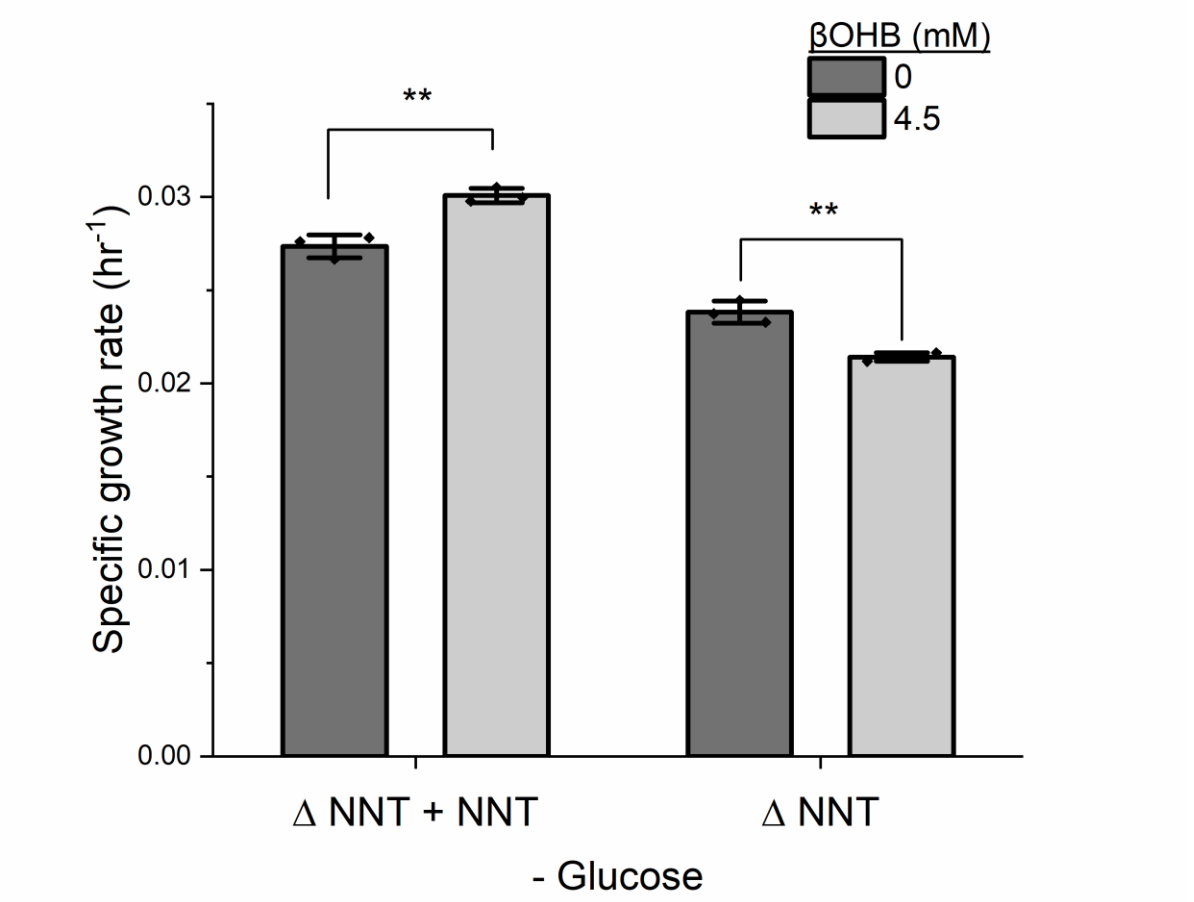

Figure 8.21.Growth rate for HEK and HEK-ΔNNT cells grown in MEM media with 0 mM glucose and 0 or 4.5 mM βOHB.

Further, I prepared A549 and A549-ΔNNT cells and tested whether the extent of influence of βOHB in glucose deprived condition was similar. When we cultured cells in glucose sufficient media, growth rate of the wild type was 0.029 and knockout cells was 0.025 hr^{-1}, indicating the knot out of NNT decreased the growth rate by 13 % in MEM media. When βOHB was added, the growth for wild type was 0.027 and the NNT knockout cells was 0.024 hr^{-1}. Presence of βOHB decreased the proliferation rate by 5 and 7 % relative to the absence of βOHB conditions, but statistically not significant (**Figure 8.22A**). In glucose depleted condition, the growth rate decreased for wild type and NNT knockout cells. The rate was 0.022 and 0.017 hr^{-1}, which was approximately 21 and 32 % decrease. Indeed, the absence of glucose slowed the

growth more significantly for NNT knockout cells. When we treated βOHB in glucose deprived media, the growth rate did not change much compared to the βOHB absent condition (**Figure 8.22B**), indicating A549 did not catabolize βOHB as much as HEK cells.

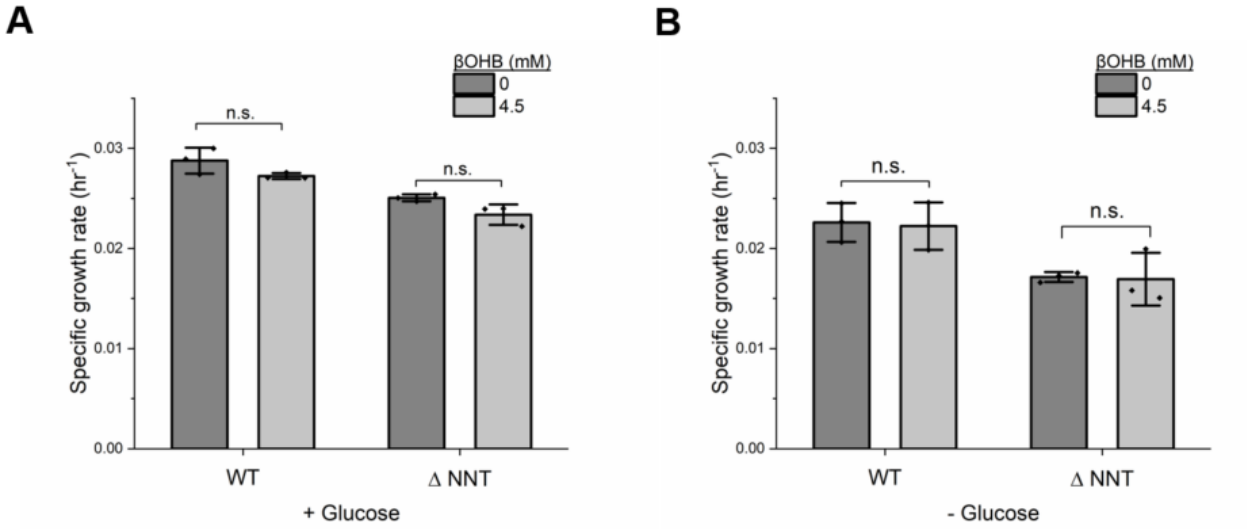

Figure 8.22. Growth rate for A549 and A549-ΔNNT cells grown in MEM media with 0 mM glucose and 0 or 4.5 mM βOHB.

8.5. Discussion

Nicotinamide nucleotide transhydrogenase (NNT) was a mitochondrial membrane localized enzyme that regulated mitochondrial NADPH and NADH redox states. NNT was known to maintain the mitochondrial NAD(P)H redox homeostasis. A knockdown of NNT in cancer cells decreased reductive carboxylation and stimulated glucose catabolism. I hypothesized that a knockout of NNT promoted pentose phosphate pathway to compensate NADPH in mitochondria during mito-stress. Upon generation of mitochondrial oxidative stress, I found out NNT knockout cells were more vulnerable to such stress as the growth rate decreased. Although I expected the PPP be activated for NNT knockout cells under extensive mitochondrial oxidative

stress, mitochondrial oxidative stress did not activate the oxPP pathway in one hour. Additionally, there was no difference between the NNT intact or knockout cells in usage of oxPPP.

Further, I explore whether NNT knockout cells relied more on specific nutrient compositions in media to complement the functions that NNT knockout cells were unable to achieve. Under DMEM or RPMI media, NNT knockout cells proliferated as much as NNT intact cells. However, when NNT knockout cells were grown in MEM media, the growth rate was compromised. Supplementation of non-essential amino acids, particularly serine and glycine rescued the growth rate.

Lastly, I assessed the bioinformatics data to find that NNT might play an important role in ketone body metabolism. Based on co-essentiality analysis and gene expression correlation analysis, I determined that NNT enzyme shared the same pathway with OXCT1 gene, which was a rate-limiting enzyme in ketone body catabolic pathway. Indeed, I found out that a growth of NNT knockout cells slowed down by approximately 10 % in presence of βOHB under glucose deprived conditions, whereas NNT intact cells maintained the growth rate.

8.6. References

1. Titov, D. V. *et al.* Complementation of mitochondrial electron transport chain by manipulation of the NAD+/NADH ratio. *Science (80-.).* **352**, 231–236 (2016).

2. Diehl, F. F., Lewis, C. A., Fiske, B. P. & Vander Heiden, M. G. [supple] Cellular redox state constrains serine synthesis and nucleotide production to impact cell proliferation. *Nat. Metab.* **1**, 861–867 (2019).

3. Sullivan, L. B. *et al.* Supporting Aspartate Biosynthesis Is an Essential Function of Respiration in Proliferating Cells. *Cell* **162**, 552–563 (2015).

4. Rydström, J. Mitochondrial NADPH, transhydrogenase and disease. *Biochim. Biophys. Acta - Bioenerg.* **1757**, 721–726 (2006).

5. Ho, H. Y., Lin, Y. T., Lin, G., Wu, P. R. & Cheng, M. L. Nicotinamide nucleotide transhydrogenase (NNT) deficiency dysregulates mitochondrial retrograde signaling and impedes proliferation. *Redox Biol.* **12**, 916–928 (2017).

6. Li, S. *et al.* Nicotinamide nucleotide transhydrogenase-mediated redox homeostasis promotes tumor growth and metastasis in gastric cancer. *Redox Biol.* **18**, 246–255 (2018).

7. Kampjut, D. & Sazanov, L. A. Structure and mechanism of mitochondrial proton-translocating transhydrogenase. *Nature* **573**, 291–295 (2019).

8. Sullivan, L. & Chandel, N. Mitochondrial reactive oxygen species and cancer. *Cancer Metab.* (2014) doi:10.1186/2049-3002-2-17.

9. Handy, diane & Loscalzo, J. Redox regulation of mitochondrial function. *Oxidative Stress Redox Regul.* **16**, 343–357 (2012).

10. Panieri, E. & Santoro, M. M. ROS homeostasis and metabolism: a dangerous liason in cancer cells. *Cell Death Dis.* **7**, e2253 (2016).

11. Vander Heiden, M. G. & DeBerardinis, R. J. Understanding the Intersections between Metabolism and Cancer Biology. *Cell* **168**, 657–669 (2017).

12. Yang, M. & Vousden, K. H. Serine and one-carbon metabolism in cancer. *Nat. Rev. Cancer* **16**, 650–662 (2016).

13. Minton, D. R. *et al.* Serine Catabolism by SHMT2 Is Required for Proper Mitochondrial

Translation Initiation and Maintenance of Formylmethionyl-tRNAs. *Mol. Cell* **69**, 610-621.e5 (2018).

14. Ye, J. *et al.* Serine catabolism regulates mitochondrial redox control during hypoxia. *Cancer Discov.* **4**, 1406–1417 (2014).

15. Meimaridou, E. *et al.* Mutations in NNT encoding nicotinamide nucleotide transhydrogenase cause familial glucocorticoid deficiency. *Nat. Genet.* **44**, 740–742 (2012).

16. DeBerardinis, R. J. *et al.* Beyond aerobic glycolysis: Transformed cells can engage in glutamine metabolism that exceeds the requirement for protein and nucleotide synthesis. *Proc. Natl. Acad. Sci. U. S. A.* **104**, 19345–19350 (2007).

17. Yin, F., Sancheti, H. & Cadenas, E. Silencing of nicotinamide nucleotide transhydrogenase impairs cellular redox homeostasis and energy metabolism in PC12 cells. *Biochim. Biophys. Acta - Bioenerg.* **1817**, 401–409 (2012).

18. Santos, L. R. B. *et al.* NNT reverse mode of operation mediates glucose control of mitochondrial NADPH and glutathione redox state in mouse pancreatic β-cells. *Mol. Metab.* **6**, 535–547 (2017).

19. Huang, D. *et al.* Hepatocellular carcinoma redirects to ketolysis for progression under nutrition deprivation stress. *Cell Res.* **26**, 1112–1130 (2016).

20. Puchalska, P. & Crawford, P. A. Multi-dimensional Roles of Ketone Bodies in Fuel Metabolism, Signaling, and Therapeutics. *Cell Metab.* **25**, 262–284 (2017).

21. Krebs, H. A. W. The redox state of nicotinamide adenine dinucleotide in the cytoplasm and mitochondria of rat liver. *Adv. Enzyme Regul.* **5**, 409–434 (1967).

22. George, F. C. Fuel metabolism in starvation. *Annu. Rev. Nutr.* **26**, 1–22 (2006).

Chapter 9

Expanding palettes of genetically encoded sensors for NADP and NADPH

9.1. Abstract

Current NADPH sensor was based on circularly permuted yellow fluorescent protein (cpYFP). Here, I improved a current NADPH sensor design by replacing a cpYFP to circularly permuted red fluorescent protein (cpRFP) with a goal of measuring NADPH dynamics in mitochondria and cytosol simultaneously. In addition to a development of cpRFP based NADPH sensor, I developed a GFP-RFP FRET based NADP sensor, allowing more accessibility of researchers to measure $NADP^+$ levels in cells without using a currently available NADPH sensor that required an advanced customized fluorescence microscope.

9.2. Introduction

Development of genetically encoded sensors advanced knowledge in basic biology[1]. These type of sensors were expressed in cells and allow monitoring target molecules in living cells. Over the past decades, a wide range of sensors were developed to answer biological questions such as calcium signaling processes, Akt signaling processes, and NADH metabolic states under varying metabolic conditions[2–6].

Current $NADP^+$ sensor required a specialized microscope setting, limiting its accessibility[7]. Additionally, simultaneous measurement of NADPH levels in cytosol and mitochondria was currently lacking. Lastly, there still did not exist NADPH/$NADP^+$ sensor available. Currently, the only genetically encoded sensor for $NADP^+$ was an Apollo sensor[7]. However, Apollo sensor required a specially customized microscope setting, limiting its accessibility to researchers that have access to simple fluorescence microscope. In brief, the Apollo sensor was based on the engineered G6PD protein attached with a yellow fluorescent protein. Using a Homo-FRET technique with perpendicular and parallel components of emission

setting, one determined the extent of $NADP^+$ levels in cells. Another motivation of developing a $NDAP^+$ sensor was that Apollo sensor had a low dynamic range. Based on the Homo-FRET technique, the dynamic range was about 7 %. Upon addition of diamide, the 2P anisotropy changed from 0.42 to 0.38. Although the error bars were small, it was useful if one could develop another sensor. Therefore, for a new sensor design, we switched a YFP to GFP and RFP and make a clover-eG6PD-mRuby fusion sensor protein. As the eG6PD enzyme dimerized based on NADP concentration, FRET efficiency between green and red fluorescent protein would change accordingly.

9.3. Materials and Methods

9.3.1. Cloning and transformation of iNapRed

A total of three iNapRed variants was constructed. First, iNapRed was constructed by replacing the cpYFP to cpRFP with a Gibson assembly technique. Next, using the overlap extension PCR technique, I constructed an iNapRed1, which had an extended linker length of one more serine compared to the original construct and an iNapRed2 which had two more amino acids in the linker, which involved with serine and glycine for iNapRed2. The DNA templates were integrated into a pET28b vector and transformed into BL-21 *E. coli* for protein expression.

9.3.2. Protein expression of iNapRed

BL-21 *E. coli* containing iNapRed plasmids is cultured in LB-kan media overnight at 37 °C. Next day, the cell cultures were transferred to 500 mL baffled flask with TB-kan media and incubated until OD_{600} reaches to near 0.6. Then, IPTG was introduced to the media and the

temperature drops to 20 °C, allowing stable expression of proteins for 16 – 20 hours. After expression, cell pellets were collected by centrifugation at 4000 xg for 10 minutes at 4 °C.

9.3.3. Purification of His-tagged iNapRed sensors

Cell pellets were equilibrated with a Tris buffer and lysed with sonicator. Once the cells were lysed, the crude cell lysates were centrifuged at 15,000 xg for 30 minutes and solution fraction was collected. The solution was sterile filtered with 20 / 40 µm membrane filter. Using the Immobilized metal affinity chromatography system, the filtered solution that contains iNapRed sensors are passed through the HisTrap FF column that contains Ni Sepharose. His-iNapRed are attached to the column and after loading the samples, the purified sensors are eluted with a buffer that contains 500 mM imidazole. The imidazole containing solution is removed by using the spin column filters that contains PBS buffer for at least three times.

9.4. Results

9.4.1. Clover-eG6PD-mRuby sensor monitors the change of $NADP^+$ in living cells

We first constructed a fusion protein based on clover-eG6PD-mRuby through overlap extension PCR method. Once we confirmed the sequence was correct, we inserted the fragment into the pCDNA vector using EcoRI and XhoI restriction sites. After a plasmid construction, we transiently expressed the sensors in Hela cells using Lipofectamine 2000 transfection system. We confirmed that the sensors were successfully expressed in Hela cells as cells emitted

fluorescence when excited at 488 nm and emission photons were collected at 525 and 625 nm. When we also excited at 560 nm, we were able to measure the fluorescence at 625 nm.

Diamide was an oxidizing reagent that could oxidize NADPH to $NADP^+$. To validate whether the sensor responded to oxidative stress, we treated cells with diamide. Upon addition of 200 µM diamide, the emission at 525 nm upon excitation at 488 nm increased to nearly 11 % within a minute. For control it slightly increased over time to 4.5 % after 15 minutes. After two minutes, the fluorescence steadily decreased over time reaching to 5 % after 15 minutes (**Figure 9.1A**). Next, we also measured the fluorescence at 625 nm to determine whether the FRET occur. If the FRET occurred, we would expect the fluorescence at 625 would decrease compared to control. Indeed, we observed that immediately after a minute, the fluorescence decreased by 4 % (**Figure 9.1B**). After a minute, the fluorescence started increase to be at 3 % increase compared to the initial fluorescence intensity. When we measured the fluorescence ratio between the emission fluorescence at 525 and 625 nm, we found that there was a dose-responsive change of fluorescence ratio. For control, we observed that the fluorescence ratio steadily decreased to be 10 % lower compared to the initial fluorescence ratio. On the other hand, upon 20 µM diamide addition, we observed that the fluorescence ratio increased by nearly 10 % and steadily decrease to 4 % lower compared to the initial fluorescence ratio. When we provided more challenge to cells with 200 µM diamide, we observed the fluorescence ratio increased to 15 % and steadily decreased to be at 2 % above the initial value (**Figure 9.1C**).

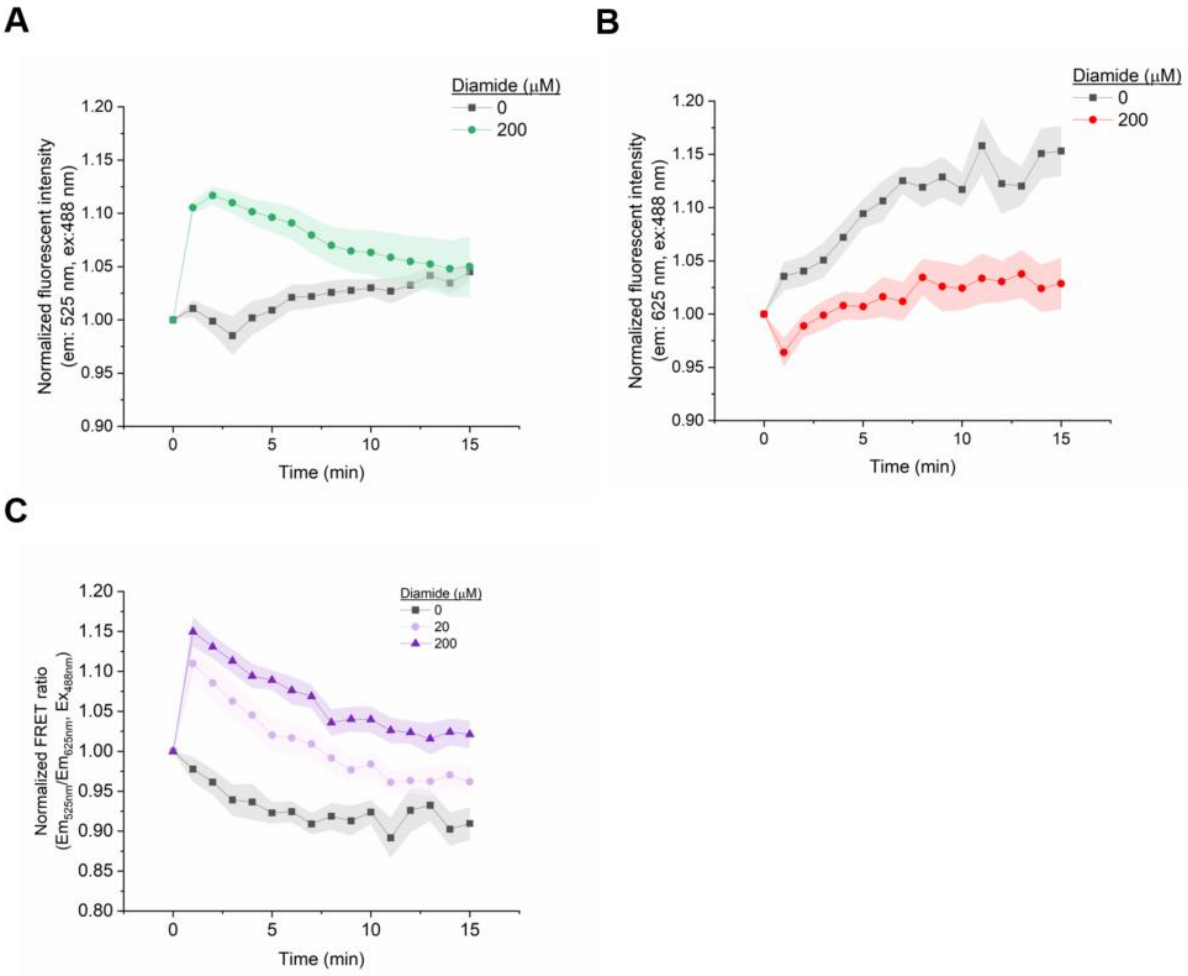

Figure 9.1. Fluorescence intensities emitted by the clover-eG6PD-mRuby sensor and its ratio. (A) The fluorescence intensity at 525 nm was measured after excitation at 488 nm in Hela cells that express Clover-eG6PD-mRuby sensor upon addition of diamide. (B) The fluorescence intensity at 625 nm was measured after excitation at 488 nm. (C) The fluorescence ratio between emission wavelength at 525 nm and 625 nm after excitation at 488 nm.

We further tested whether the dynamics of NADPH change was consistent with the change of $NADP^+$ observed from the clover-eG6PD-mRuby sensor. To test the change of NADPH under the same condition, we used Hela-iNap cell lines and challenged cells with 20 μM diamide. After a minute, we observed a sharp decrease of cytosolic NADPH followed by recover and reached to the initial value around 10 minutes. This recovery rate was similar to the clover-eG6PD-mRuby sensor, in which the NADP reached to the initial value after 8 minutes.

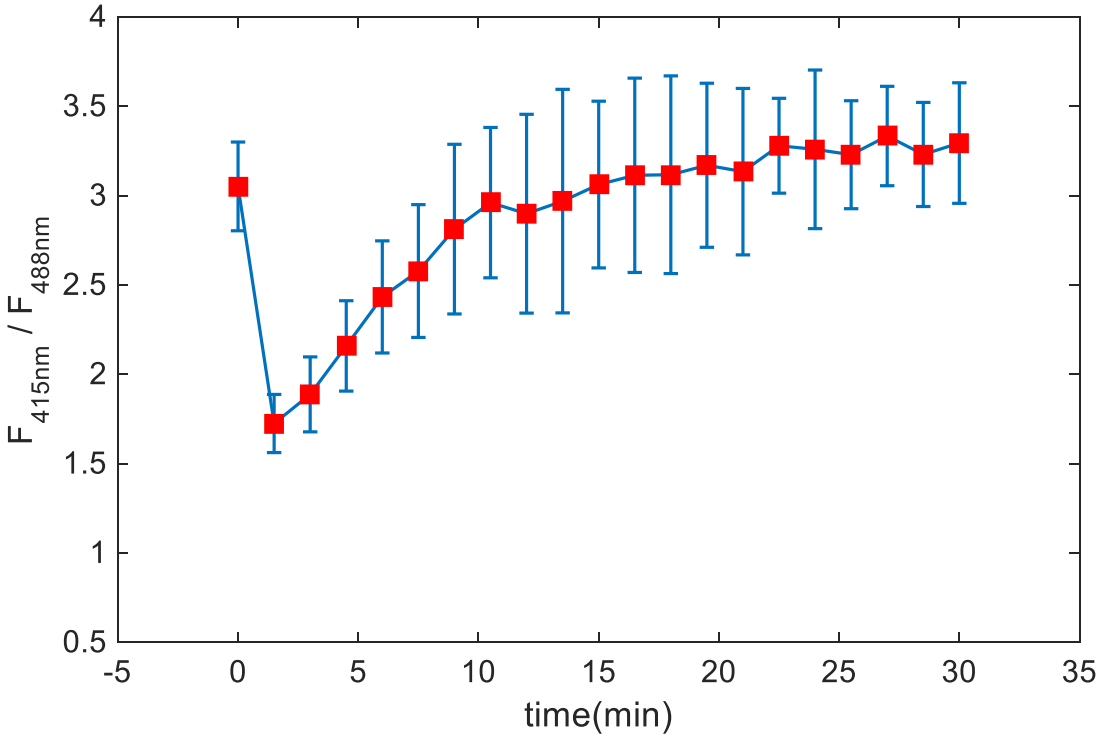

Figure 9.2. Fluorescence ratio change upon addition of 20 μM diamide in Hela cells stably expressing NADPH sensor.

9.4.2. Purified iNapRed sensor responds to the change of NADPH levels

With a goal of developing an iNap sensor with another fluorescent protein for simultaneous measurement, I replaced the circularly permuted yellow fluorescent (cpYFP) of the iNap sensor to the circularly red fluorescent protein (cpRFP). This new iNap variant was expected to function simultaneously with the original iNap as the fluorescence spectra of these two fluorescent proteins overlapped minimally.

Once I completed a construction of iNapRed, I implemented protein purification step and characterization as follows. When we implemented the excitation scan, we observed that the peak was observed around 570 nm, which was as expected based on the cpRFP fluorescence properties (**Figure 9.4A**)[8]. Additionally, we implemented an emission scan while fixing the

excitation wavelength at 550 nm (**Figure 9.4B**). The fluorescence intensity increased about 56 % upon addition of 1.4 mM NADPH and 29 % for 0.7 mM compared to the control (**Figure 9.4C**)

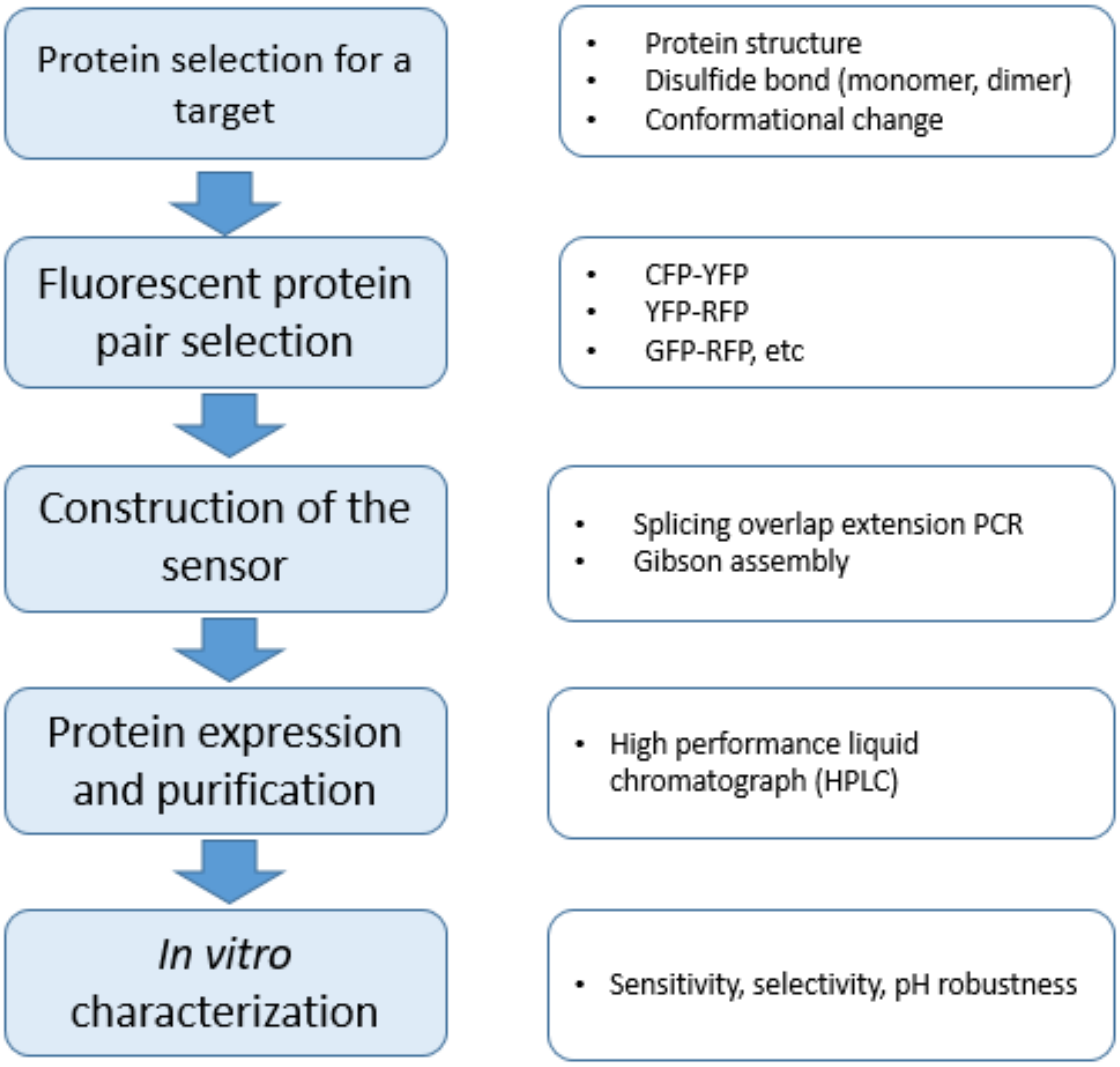

Figure 9.3. Scheme of designing and constructing a sensor.

A

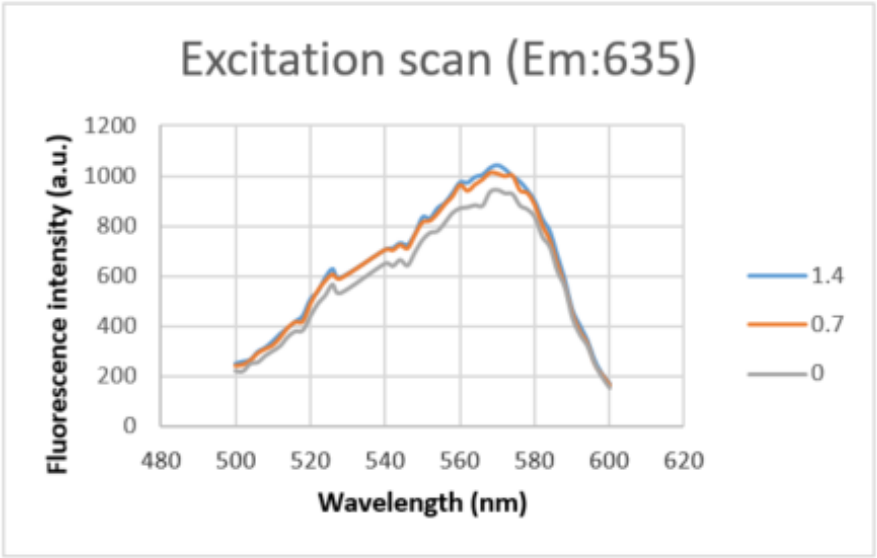
Excitation scan (Em:635)
Fluorescence intensity (a.u.)
1200
1000
800
600
400
200
0
480
500
520
540
560
580
600
620
Wavelength (nm)
1.4
0.7
0

B

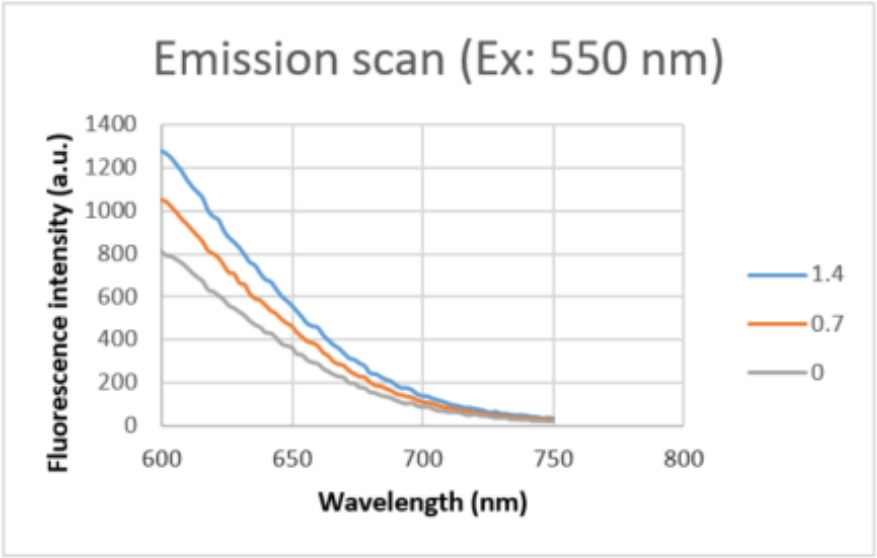
Emission scan (Ex: 550 nm)
Fluorescence intensity (a.u.)
1400
1200
1000
800
600
400
200
0
600
650
700
750
800
Wavelength (nm)
1.4
0.7
0

C

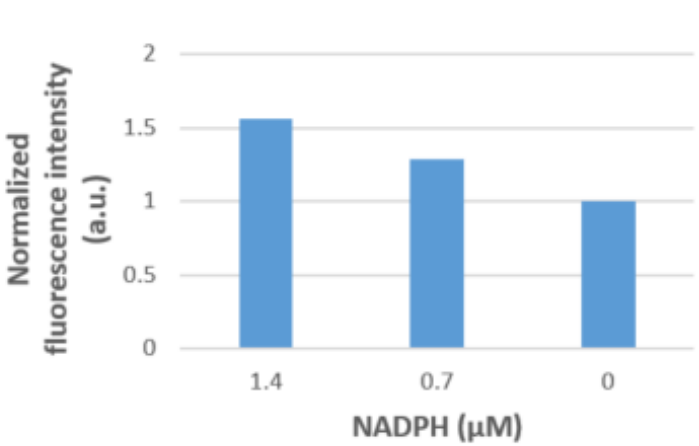
Normalized fluorescence intensity (a.u.)
2
1.5
1
0.5
0
1.4
0.7
0
NADPH (µM)

Figure 9.4. Excitation and emission spectrum of purified iNap-red. **(A)** Purified iNap-red sensor is prepared at final concentration of 4.4 μM and incubated with 1.4, 0.7, and 0 mM NADPH and the excitation spectrum with emission set at 635 nm was initiated. The peak is at 570 nm. **(B)** The emission scan is performed while setting the excitation at 550 nm. We did not set 570 nm because the excitation wavelength is too close to the emission wavelength at 600 nm. We modulated the excitation at lower wavelength to measure the peak emission intensity wavelength. Indeed, we were able to confirm that the maximum peak of the iNap-red is at 598 nm upon excitation at lower wavelength. In this case, we used 527 nm excitation wavelength (**Figure 9.5A**). Fluorescence intensity increased only about 10 % upon addition of NADPH with 360 μM.

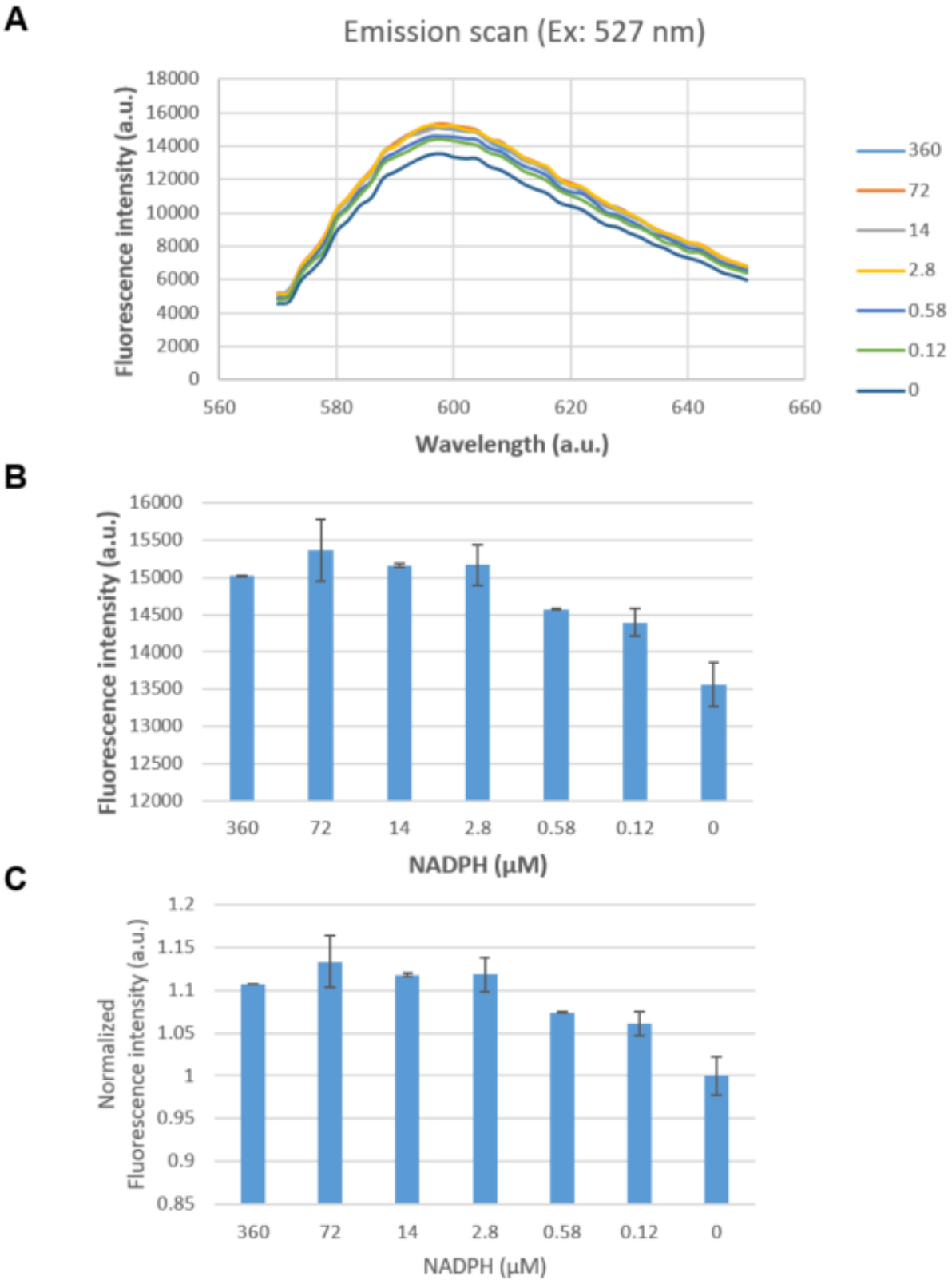

Figure 9.5. Emission spectra of purified iNap-red**. (A)** Purified iNap-red is prepared at a final concentration of 4.4 µM and incubated with 360, 72, 14, 2.8, 0.58, 0.12 µM of NADPH. (**B**) The

fluorescence intensity at 598 nm upon excitation of 527 nm. **(C)** Normalized fluorescence intensity with excitation at 527 nm and the emission fixed at 600.

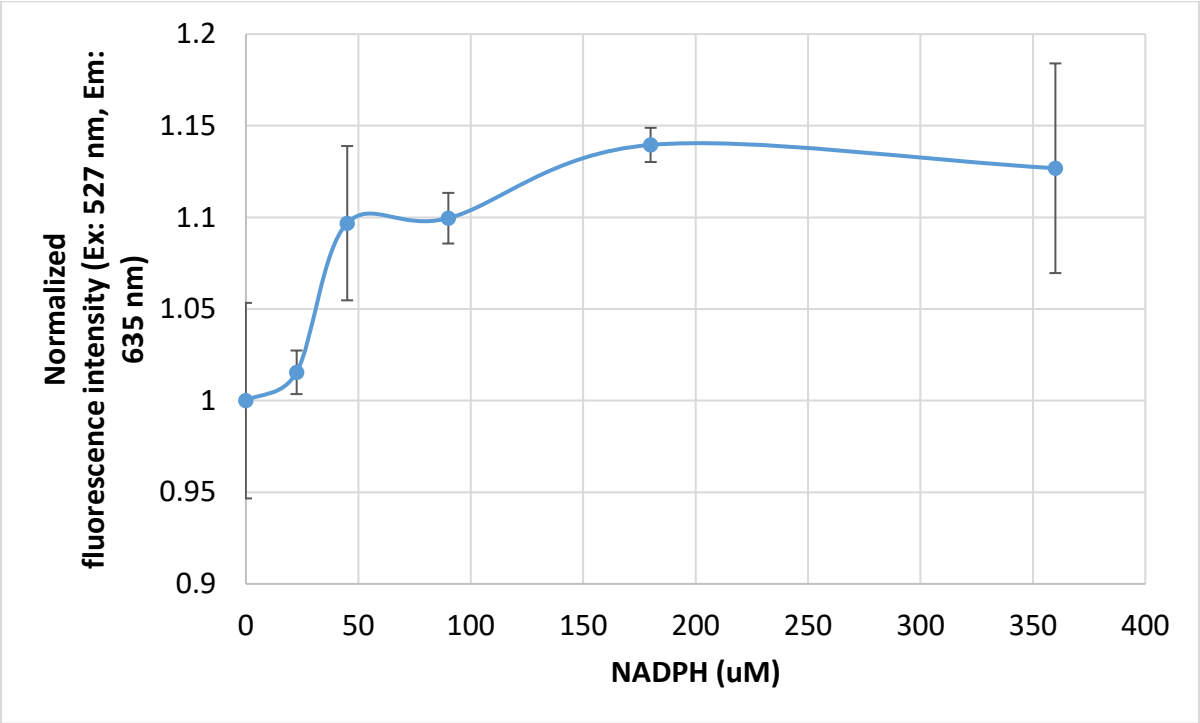

Figure 9.6. Normalized fluorescence intensity with excitation at 527 nm and emission set at 635 nm.

Further, I used a different excitation wavelength and observe whether there was a dose-dependent change of fluorescence intensity. Similarly, although I used an excitation wavelength at 527 nm, the emission fluorescence intensity tended to increase with respect to increased presence of NADPH in buffer. Upon 360 µM of NADPH, the fluorescence increased by 13 %, whereas it increased by only 2 % upon addition of 22.4 µM (**Figure 9.6**).

To determine whether we could increase the fluorescence intensity, I modulated the linker length between the cpRFP and the Trex (190-211) DNA template. iNapRed1 had glycine-serine linker and iNapRed2 has glycine-serine-glycine linker. We chose the linker length between these two templates as the binding pocket was near these regions (**Figure 9.7**). Upon

addition of different concentration of NADPH from 0 to 760 µM, the iNapRed1 and iNapRed2 did not show much change in fluorescence intensities upon excitation (**Figure 9.8**).

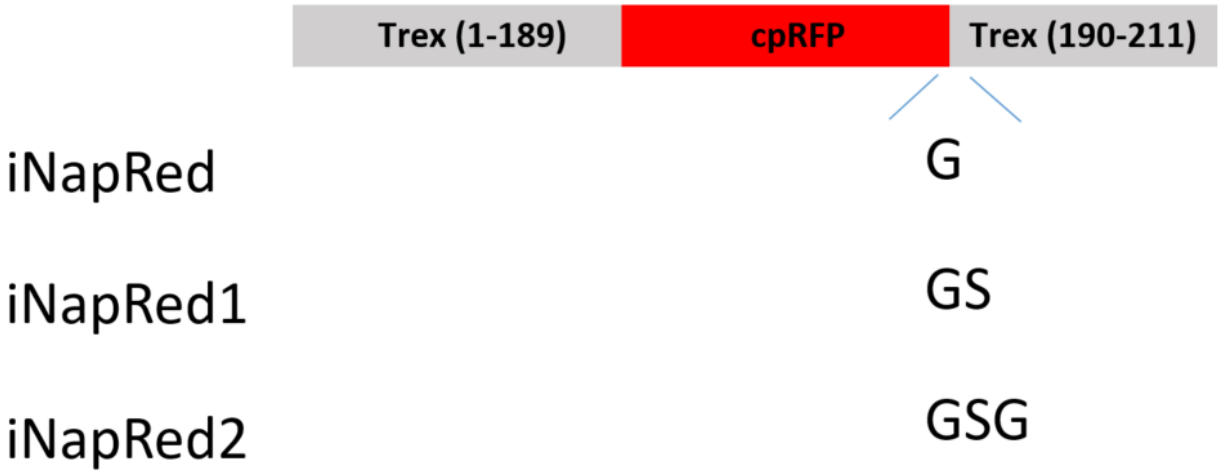

Figure 9.7. iNapRed variants**.** iNapRed1 and iNapRed2 were designed to test whether increasing the linker length allows increase of fluorescence intensity.

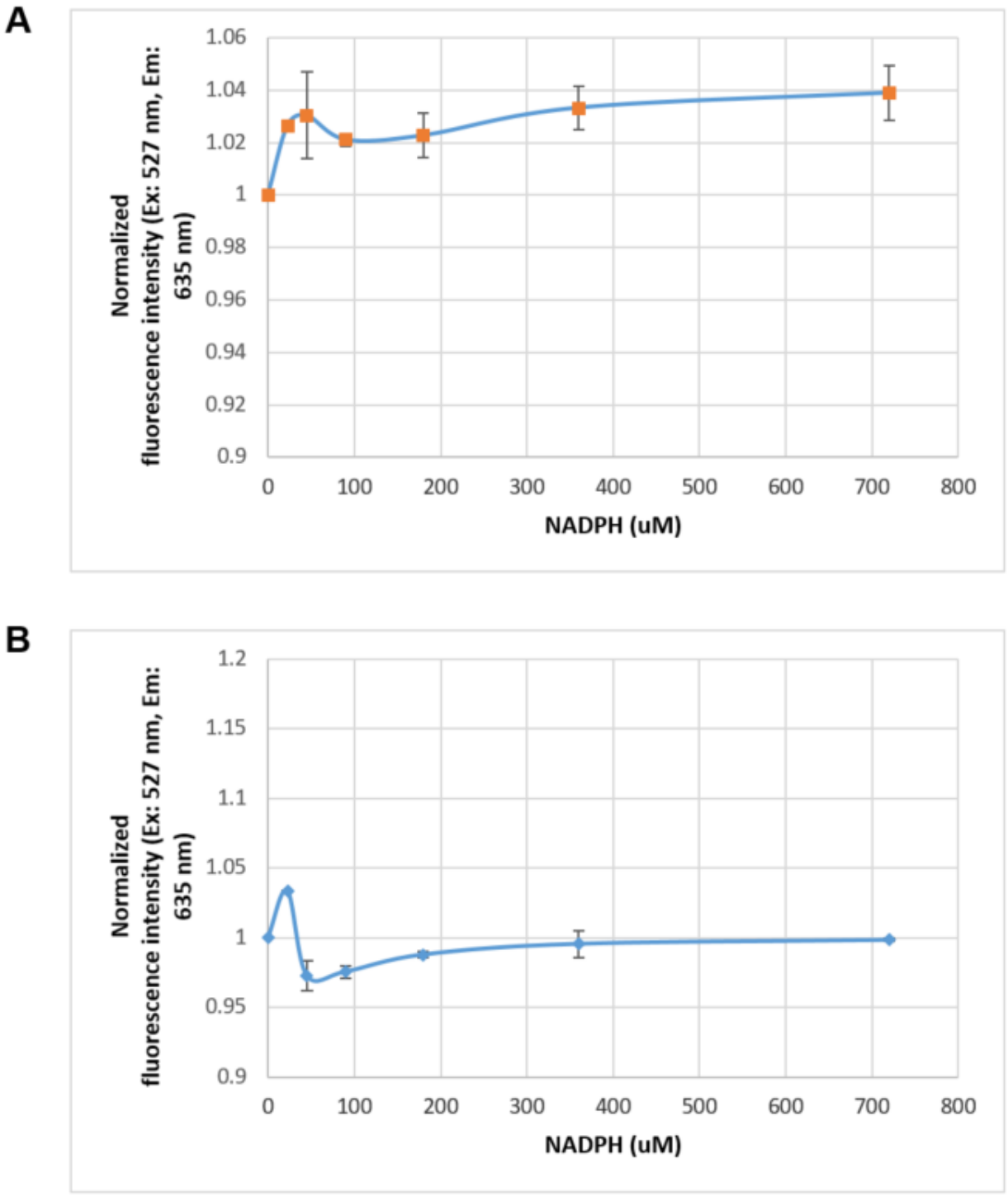

Figure 9.8. Normalized fluorescence intensity upon addition of NADPH for iNapRed2 and iNapRed3 sensors. (A) iNapRed1 sensor and (B) iNapRed2 sensor shows no greater change upon increase of NADPH levels.

9.5. Discussion

Genetically encoded sensors are powerful in monitoring specific target molecules in living cells. Here, we attempt to improve a currently available $NADP^+$ sensor by changing the fluorescent proteins such that a new construct can be easily used by scientists who do not have a specialized but a generic fluorescence microscope. The FRET-based $NADP^+$ sensor responds to the change of $NADP^+$ levels by addition of diamide and the green and red channels alter in opposite direction, providing a direct evidence of the FRET.

Secondly, I try to improve an original iNap sensor by replacing the cpYFP to cpRFP with a goal of expressing both sensors simultaneously for measurement of cytosolic and mitochondrial NADPH levels in a same cell. As the fluorescence spectrum does not overlap with one another, it will be useful to measure the change of NADPH levels in different organelles by expressing each of the sensor constructs to respective organelle. Of the three constructs I have developed, the iNapRed1 increases its fluorescence intensity upon increase of NADPH concentration with a maximum increase of 12 %, which is still not a dramatic increase compared to the original iNap construct. Further studies are needed to improve the dynamics range of the iNapRed sensors.

9.6. References

1. Tsien, R. Y. & Harootunian, A. T. Practical design criteria for a dynamic ratio imaging system. *Cell Calcium* **11**, 93–109 (1990).

2. Berg, J., Hung, Y. P. & Yellen, G. A genetically encoded fluorescent reporter of ATP:ADP ratio. *Nat. Methods* **6**, 161–166 (2009).

3. Hung, Y. P., Albeck, J. G., Tantama, M. & Yellen, G. Imaging Cytosolic NADH-NAD+ Redox State with a Genetically Encoded Fluorescent Biosensor. *Cell Metab.* **14**, 545–554 (2011).

4. Hung, Y. P. *et al.* Akt regulation of glycolysis mediates bioenergetic stability in epithelial cells. *Elife* **6**, 1–25 (2017).

5. Tao, R. *et al.* Genetically encoded fluorescent sensors reveal dynamic regulation of NADPH metabolism. *Nat. Methods* **14**, 720–728 (2017).

6. Zhao, Y. *et al.* SoNar, a Highly Responsive NAD+/NADH Sensor, Allows High-Throughput Metabolic Screening of Anti-tumor Agents. *Cell Metab.* **21**, 777–789 (2015).

7. Cameron, W. D. *et al.* Apollo-NADP+: A spectrally tunable family of genetically encoded sensors for NADP+. *Nat. Methods* **13**, 352–358 (2016).

8. Ermakova, Y. G. *et al.* Red fluorescent genetically encoded indicator for intracellular hydrogen peroxide. *Nat. Commun.* **5**, (2014).

Chapter 10

Conclusions and future directions

10.1. Abstract

This thesis explored cytosolic and mitochondrial NADPH dynamics and NADPH dependent metabolic pathways in cancer cells using NADPH sensors, isotopic tracers, and a mathematical model[1]. In regards to sensors, future directions included an application of redox sensors to study in other disease models such as *in-vivo* models. Further, these sensors could be utilized for high-throughput screening to find small molecules that could potentially alter NADPH redox states in cancer cells and be used for redox cancer therapies. With respect to isotopic tracer studies, deuterium tracers that probed NADPH generation pathways other than oxidative pentose phosphate pathway could be utilized in combination with sensors to relate the change of NADPH levels and pathway activities simultaneously. Third, in addition to a kinetic model used to estimate NADPH related parameter values, other computational models such as curated genome-scale metabolic model for human cells could be adopted for comprehensive and quantitative understanding of compartmentalized NADPH metabolic network. In addition, the kinetic model could be further expanded to connect with other kinetic models in other subcellular organelles, making a complete redox network in cells. Lastly, along with all these improvements, other –omics data could be incorporated to relate how the NADPH redox metabolic pathways were altered across varying cancer cell lines.

10.2. Summary and concluding remarks

This thesis explored cytosolic and mitochondrial NADPH dynamics and NADPH dependent metabolic pathway activities under mitochondrial oxidative stress and varying nutrient conditions in cancer cells. To complete the task, we used NADPH sensors with live-cell imaging techniques, isotopic tracers, and mathematical models that included a kinetic model and genome-

scale metabolic model. Our work provided an insight on how cytosolic and mitochondrial NADPH levels varied during a variety of physiologically relevant and pathological conditions and the variabilities across different cancer cell lines. Additionally, our integrated approach provided a basis of how these types of sensors could be incorporated to study cancer redox metabolism as well as how mathematical models provided valuable biological insights that could be obtained using other biochemical assays.

In **Chapter 2**, we evaluated the influence of mitochondria derived oxidative stress to cytosolic and mitochondrial NADPH dynamics. By expressing a mitochondria localized D-amino acid oxidase, we controlled the generation rates of mitochondrial H_2O_2 by modulating the concentration of D-alanine substrate. Increased mitochondrial H_2O_2 rate decreased mitochondrial NADPH levels in a dose-dependent manner, whereas mitochondrial H_2O_2 generation minimally influenced the cytosolic NADPH levels. Similar patterns were observed for cytosolic and mitochondrial NADPH dynamics upon modulating cytosolic H_2O_2 generation rates.

In **Chapter 3,** we assessed the NADPH generation pathways, including pentose phosphate pathway in cytosol and the change of TCA cycle metabolites turn-over rates in mitochondria using ^{13}-C isotopic glucose tracers during the mitochondrial oxidative stress. Mitochondrial oxidative stress elevated the activity of cytosolic pentose phosphate pathway and increased glucose oxidation, enriching TCA cycle metabolites. NADPH regenerated in cytosol was transported into mitochondrial via indirect NADPH shuttle system, and TCA cycle metabolites were used to make NADPH in mitochondria through several NADPH generating enzymatic reactions.

In **Chapter 4,** we estimated the mitochondrial NADPH/$NADP^+$ using a kinetic model based on the mitochondrial antioxidant network. We used a system of ordinary differential

equations based on the mitochondrial antioxidant network that comprises 23 reactions and 23 redox species, and implemented the least square methods to fit the experimental data on the model system, determining the four unknown parameter values. Based on a model simulation, we found0 mitochondrial NADPH/ $NADP^+$ decreased up to 67-fold under mitochondrial oxidative stress going from 13.4 to 0.2. Second, we documented an indirect NADPH shuttle system was activated during mitochondrial oxidative stress to maintain mitochondrial NADPH pools in response to mitochondrial oxidative stress.

In **Chapter 5,** we analyzed the influence of nutrient conditions to cytosolic and mitochondrial NADPH dynamics across different cancer cell lines. In previous chapters, we focused on how mitochondrial derived influenced cytosolic and mitochondrial NADPH dynamics and relevant NADPH generation pathways. Here, we evaluated how environmental factors influenced compartmentalized NADPH dynamics. We measured cytosolic and mitochondrial NADPH levels in absence of glucose, serine, and glutamine. Both glucose and glutamine decreased cytosolic and mitochondrial NADPH levels, whereas cytosolic NADPH was maintained in absence of serine. Further, we found cancer cell lines responded differently to nutrient stress. HCT-116 cells were robust in maintaining both cytosolic and mitochondrial NADPH indices during nutrient stress, whereas cytosolic and mitochondrial NADPH indices changed greatly for MDA-MB-231, A549, and Hela cells. Based on mRNA expression data, we found HCT-116 cells showed lower expression levels of oxidative pentose phosphate pathway genes but increased serine synthesis pathways and related NADPH generation pathways compared to other cell lines. This indicated that HCT-116 cells was robust in maintaining NADPH homeostasis under varying nutrient stress conditions.

In **Chapter 6,** we focused on mitochondrial carriers to understand which of proteins were important for regulating a transfer of electrons from NADPH across the mitochondrial membranes. We implemented essentiality, co-essentiality analysis, followed by genome-scale metabolic model simulations to find out that SLC25A1 gene, which encoded citrate transporter, was one of the important transporters in maintaining cytosolic and mitochondrial NADPH redox states. Moreover, we monitored cytosolic and mitochondrial NADPH dynamics upon inhibition of citrate transporter under regular and mitochondrial stress conditions. Inhibition of citrate transporter mainly influenced cytosolic NADPH pools in short term but impacted both NADPH pools after a day. Further, inhibition of citrate transporter and mitochondrial stress influenced both cytosolic and mitochondrial NADPH pools.

In **Chapter 7**, we attempted to relate cytosolic and mitochondrial NADPH to growth. We defined a NADPH composite index to estimate a relative contribution of cytosolic and mitochondrial NADPH to growth. Based on the calculation, some cancer cell lines such as MDA-MB-231 had higher correlation of cytosolic NADPH change to growth, whereas another cancer cell line, HCT-116 cell, showed higher correlation of mitochondrial NADPH change to growth. Using these differences, we found MDA-MB-231 cells were more sensitive to cytosolic NADPH perturbation, whereas HCT-116 cells were more sensitive to mitochondrial NADPH perturbation.

In **Chapter 8,** we investigated a role of nicotinamide nucleotide transhydrogenase (NNT) in mitochondrial NADPH redox homeostasis. Throughout the bioinformatics and computational analysis used in previous chapters, we found out that NNT played a greater role in maintaining mitochondrial NADPH metabolism. First, based on genome-scale metabolic model, we found that a rate through NNT enzyme increased most upon increase of H_2O_2 generation in

mitochondria. Second, we found NNT was functionally linked to SLC25A1 and NADK2 genes based on the co-essentiality analysis. Third, we predicted that NNT and OXCT1 gene, which was a rate-limiting enzyme for beta-hydroxybutyrate in ketone metabolism, were functionally linked based on co-essentiality analysis. We confirmed that NNT was essential for cell survival upon mitochondrial oxidative stress. Moreover, we found that growth of NNT knockout cells were hampered in absence of serine and glycine, indicating that NNT was important in modulating serine and glycine mediated NAD(P)H homeostasis and growth. Lastly, NNT knockout cells were slower in growth during glucose deprivation and did not metabolize beta-hydroxybutyrate. In conclusion, in combination of data-driven hypothesis generation and subsequent experimental validation revealed a new role of NNT in cell growth.

Lastly, in **Chapter 9**, we improved $NADP^+$ and NADPH sensors by changing sensor designs. For $NADP^+$ sensors, we replaced the currently existing $NADP^+$ sensor to FRET-based format, allowing a tracking of $NADP^+$ with a generic fluorescent microscope. For NADPH sensor, we replaced the circularly yellow fluorescent protein to red fluorescent protein, allowing a possibility to measure NADPH levels in cytosol and mitochondria simultaneously.

10.3. Suggestions for future work

10.3.1. Application of NADPH sensors to other disease models and organisms

In this thesis, related to **Chapter 5, 6, and 7,** I mainly focused on applying NADPH sensors to study four different cancer cell lines, including Hela (cervical), A549 (lung), HCT-116 (colorectal), and MDA-MB-231 (breast). Expression of these sensors to other cell lines could provide more quantitative information about the differences between cancer cell lines.

Understanding the differences would guide better therapeutic design that targets redox metabolism[2–4].

Additionally, these type of genetically encoded sensors could be used in other diseases models that have been associated with perturbed NADPH metabolism. This includes Leigh syndrome model that had dysfunctional mitochondria or heart failure that had higher oxidative stress[5,6]. Moreover, one could induce the NADPH sensors to non-transformed cells and observed how NADPH redox states varied during disease progression and whether inhibition of these changes might slow down disease progression[7]. Lastly, as NADPH sensors could be used to monitor the NADPH dynamics in living cells, the sensors could be applied to study a circadian rhythm system and how the NADPH could vary during days and nights[8].

Moreover, NADPH sensor could be useful in studying plant metabolism[9]. Photosynthesis in plant provided NADPH to drive the Calvin cycle. Additionally, nitric oxide generated from NADPH oxidase was a key signaling molecule for plant growth. Thus, understanding how NADPH redox pool sizes and its dynamics influenced these pathways and whether modulating NADPH redox states led to different plan phenotypes was of an interesting topic.

10.3.2. Role of NNT enzyme in ketone body metabolism

Related to **Chapter 8,** our computational and proliferation analysis on NNT knockout cells revealed that NNT played an important role in ketone body metabolism[10]. The future work remained on validating whether NNT indeed played an important role in ketone body metabolism by serving as NADH regenerator and related mechanistic studies. For instance, we could perform a beta-hydroxybutyrate (βOHB) isotopic tracer study to track whether βOHB consumption was increased in glucose deprived condition and decreased for NNT knockout

cells. Additionally, double knockout of OXCT1 gene and NNT could provide an evidence of the functionality of these genes in pathways.

Another direction was the role of NNT in serine derived one carbon metabolism. We found the growth was inhibited for NNT knockout cells in absence of serine and glycine, indicating that serine and glycine played an important role in NNT knockout cells. A compensatory uptake of serine and glycine was to provide a proper NAD(P)H states in mitochondria for cells that lack NNT enzymes. Serine deuterium tracers could be used to test whether serine was indeed consumed to provide NADPH in mitochondria.

These studies could provide new insight on the role of NNT enzyme, which was reported in literature. A future direction also included finding a right system where NNT played a critical roles particularly in ketone body metabolism. In our bioinformatics survey, role of NNT in kidney appear important but other tissues such as brain might be an important system where NNT played a pivotal role in maintaining ketone body metabolism.

10.3.3. Characterization of FRET-based $NADP^+$ sensor and iNapRed NADPH sensor

Related to **Chapter 9,** we improved a sensor design by developing a FRET-based NADP sensor and iNapRed NADPH sensor. For FRET-based $NADP^+$ sensor, we confirmed that the FRET efficiency varied upon modulation of $NADP^+$ levels. However, the sensor was not characterized in vitro. We had difficulties in expressing the $NADP^+$ sensor. A further direction included an in vitro characterization.

Regarding the iNapRed sensor, the sensor was purified and characterized for some extent in vitro. However, a further characterization was needed such as testing the selectivity and sensitivity of the sensors. Once the characterization was confirmed, sensors could be co-

expressed with iNap sensors and simultaneous measurement of cytosolic and mitochondrial NADPH dynamics could be measured. This co-measurement would allow one to explore the compartmentalized NADPH dynamics more effectively.

10.3.4. Improvement of a kinetic model and application of a genome-scale metabolic model

In **Chapter 4**, we used a kinetic model based on the mitochondrial antioxidant reaction network[11,12]. We were able to fit our model to the experimental data, finding mitochondrial NADPH/$NADP^+$ and H_2O_2 generation rates that is considered to be excessive. The next step was to combine the mitochondrial and cytosolic kinetic model and include mitochondrial carrier parameter values. A combined antioxidant network system would provide a comprehensive view of the network kinetics. To make the system robust, measurement of not just NADPH but $NADP^+$, H_2O_2, GSH, and other redox species would enhance the model validation and prediction.

In **Chapter 6**, we applied a curated human genome-scale metabolic model to estimate the flux differences between different cancer cell lines. However, the model prediction was not as expected. The model prediction could be enhanced if we were able to validate the model by measuring pathway fluxes through experiments such as labeling studies[12,13]. With these validation, we might be able to constraint the model and allow better predictions. Additionally, incorporation of thermodynamics database would make the model more physiologically relevant. Altogether, a more careful curation of the genome-scale metabolic models would be useful in designing patient's specific metabolic models that could be used for designing cancer therapies that target metabolic pathways.

10.4. References

1. Moon, S. J., Dong, W., Stephanopoulos, G. N. & Sikes, H. D. Oxidative pentose phosphate pathway and glucose anaplerosis support maintenance of mitochondrial NADPH pool under mitochondrial oxidative stress. *Bioeng. Transl. Med.* 1–18 (2020) doi:10.1002/btm2.10184.

2. Gorrini, C., Harris, I. S. & Mak, T. W. Modulation of oxidative stress as an anticancer strategy. *Nat. Rev. Drug Discov.* **12**, 931–47 (2013).

3. Trachootham, D., Alexandre, J. & Huang, P. Targeting cancer cells by ROS-mediated mechanisms: a radical therapeutic approach? *Nat. Rev. Drug Discov.* (2009) doi:10.1038/nrd2803.

4. Vander Heiden, M. G. Targeting cancer metabolism: A therapeutic window opens. *Nat. Rev. Drug Discov.* **10**, 671–684 (2011).

5. Nickel, A. G. *et al.* Reversal of mitochondrial transhydrogenase causes oxidative stress in heart failure. *Cell Metab.* **22**, 472–484 (2015).

6. Patgiri, A. *et al.* An engineered enzyme that targets circulating lactate to alleviate intracellular NADH:NAD+ imbalance. *Nat. Biotechnol.* **38**, 309–313 (2020).

7. Hayes, J. D., Dinkova-Kostova, A. T. & Tew, K. D. Oxidative Stress in Cancer. *Cancer Cell* **38**, 167–197 (2020).

8. Estrella, M. A. *et al.* The metabolites NADP+ and NADPH are the targets of the circadian protein Nocturnin (Curled). *Nat. Commun.* **10**, 1–10 (2019).

9. Pochekailov, S., Black, R. R., Chavali, V. P., Khakhar, A. & Seelig, G. A Fluorescent Readout for the Oxidation State of Electron Transporting Proteins in Cell Free Settings. *ACS Synth. Biol.* **5**, 662–671 (2016).

10. Puchalska, P. & Crawford, P. A. Multi-dimensional Roles of Ketone Bodies in Fuel Metabolism, Signaling, and Therapeutics. *Cell Metab.* **25**, 262–284 (2017).

11. Stein, K. T., Moon, S. J., Nguyen, A. N. & Sikes, H. D. Kinetic modeling of H2O2 dynamics in the mitochondria of HeLa cells. *PLoS Comput. Biol.* **16**, 1–21 (2020).

12. Robinson, J. L. *et al.* An atlas of human metabolism. *Sci. Signal.* **13**, 1–12 (2020).

13. Shalem, O. *et al.* Genome-scale CRISPR-Cas9 knockout screening in human cells. *Science (80-.).* **343**, 84–87 (2014).